Universal scaling dynamics at non-thermal fixed points in multi-component Bose gases far from equilibrium

Christian-Marcel Schmied

2020

Dissertation

submitted to the

Combined Faculties of the Natural Sciences and Mathematics

of the Ruperto-Carola-University of Heidelberg, Germany

for the degree of

Doctor of Natural Sciences

Put forward by

Christian-Marcel Schmied

born in: Gummersbach, Germany

Oral examination: 20.05.2020

Universal scaling dynamics at non-thermal fixed points in multi-component Bose gases far from equilibrium

Referees: Prof. Dr. Thomas Gasenzer
Prof. Dr. Jörg Jäckel

Abstract

Far from equilibrium, comparatively little is known about the possibilities nature reserves for the structure and states of quantum many-body systems. A potential scenario is that these systems can approach a non-thermal fixed point and show universal scaling dynamics. The associated spatio-temporal self-similar evolution of correlations is characterized by universal scaling functions and scaling exponents. In this thesis, we investigate the universal scaling behavior of multi-component bosonic quantum gases from a theoretical point of view. In particular, we perform numerical simulations of spin-1 Bose gases in one and two spatial dimensions. To enable universal scaling dynamics, we prepare far-from-equilibrium initial configurations by making use of instabilities arising from a parameter quench between different phases of the spin-1 model. The subsequent universal scaling at the non-thermal fixed point is driven by the annihilation and dissolution of (quasi)topological excitations. In addition, we make analytical predictions for the non-thermal fixed point scaling of $U(N)$-symmetric models which we corroborate with numerical simulations of a $U(3)$-symmetric Bose gas in three spatial dimensions. We find that the scaling behavior at the fixed point is dominated by the conserved redistribution of collective excitations. Furthermore, we introduce prescaling as a generic feature of the evolution of a quantum many-body system towards a non-thermal fixed point. During the prescaling evolution, some well-measurable properties of spatial correlations already scale with the universal exponents of the fixed point while others still show scaling violations. We illustrate the existence of prescaling by means of numerical simulations of a three-dimensional $U(3)$-symmetric Bose gas. The research presented in this thesis contributes to a deeper understanding of universal scaling dynamics far from equilibrium. In particular, it unravels important key aspects for establishing out-of-equilibrium universality classes. Furthermore, the introduced concept of prescaling allows bridging the gap in the time evolution from the initial state to the associated non-thermal fixed point.

Zusammenfassung

Vergleichsweise wenig ist bekannt darüber, welche Möglichkeiten die Natur für die Stuktur und die Zustände von Quantenvielteilchensystemen fernab vom Gleichgewicht bereit hält. Ein mögliches Szenario ist, dass sich diese Systeme einem nicht-thermischen Fixpunkt nähern und universelle Skalierungsdynamik zeigen. Die damit verbundene selbstähnliche Entwicklung von Korrelationen in Raum und Zeit wird durch universelle Skalenfunktionen und Skalenexponenten charakterisiert. In der vorliegenden Arbeit untersuchen wir universelles Skalierungsverhalten in mehrkomponentigen bosonischen Quantengasen unter theoretischen Gesichtspunkten. Im Speziellen simulieren wir Spin-1 Bose Gase in ein und zwei räumlichen Dimensionen. Um universelle Skalierungsdynamik während der Zeitentwicklung zu ermöglichen, präparieren wir Anfangskonfigurationen fernab vom Gleichgewicht, indem wir uns Instabilitäten zu Nutze machen, die als Folge einer schnellen Parameterveränderung zwischen verschiedenen Phasen des Spin-1 Modelles entstehen. Das sich daraus ergebende universelle Skalieren am nicht-thermischen Fixpunkt ist getrieben von Annihilationen und dem Auflösen (quasi)topologischer Anregungen. Außerdem machen wir analytische Vorhersagen für das Skalieren von $U(N)$-symmetrischen Modellen am nicht-thermischen Fixpunkt, die wir mit Hilfe numerischer Simulationen eines $U(3)$-symmetrischen Bose Gases in drei räumlichen Dimensionen untermauern. Wir stellen fest, dass das Skalierungsverhalten am Fixpunkt von der erhaltenen Umverteilung kollektiver Anregungen dominiert wird. Darüber hinaus führen wir Präskalieren als eine generische Eigenschaft der Zeitentwicklung eines Quantenvielteilchensystems hin zum nicht-thermischen Fixpunkt ein. Während der Präskalierungsentwicklung skalieren einige gut messbare Eigenschaften räumlicher Korrelationen bereits mit den universellen Exponenten des Fixpunktes, wohingegen andere noch Verletzungen des Skalierens aufweisen. Wir illustrieren die Existenz von Präskalieren anhand numerischer Simulationen eines dreidimensionalen $U(3)$-symmetrischen Bose Gases. Die in der vorgelegten Arbeit präsentierte Forschung trägt zu einem tieferen Verständnis universeller Skalierungsdynamik fernab vom Gleichgewicht bei. Im Speziellen zeigt sie wichtige Schlüsselaspekte für das Aufstellen von Universalitätsklassen fernab des Gleichgewichts auf. Außerdem ermöglicht das eingeführte Konzept des Präskalierens es, die Lücke in der Zeitentwicklung vom Anfangszustand bis hin zum damit verbundenen nicht-thermischen Fixpunkt zu schließen.

Publications

This thesis contains discussions and results from the publications listed below.

1. **Observation of universal dynamics in a spinor Bose gas far from equilibrium**
   M. Prüfer, P. Kunkel, H. Strobel, S. Lannig, D. Linnemann, C.-M. Schmied, J. Berges, T. Gasenzer and M. K. Oberthaler, Nature **563**, 217–220 (2018)

2. **Prescaling in a far-from-equilibrium Bose gas**
   C.-M. Schmied, A. N. Mikheev, T. Gasenzer, Phys. Rev. Lett. **122**, 170404 (2019)

3. **Low-energy effective theory of non-thermal fixed points in a multicomponent Bose gas**
   A. N. Mikheev, C.-M. Schmied, T. Gasenzer, Phys. Rev. A **99**, 063622 (2019)

4. **Non-thermal fixed points: Universal dynamics far from equilibrium**
   C.-M. Schmied, A. N. Mikheev, T. Gasenzer, Int. J. Mod. Phys. A **34**, 1941006 (2019)

5. **Bi-directional universal dynamics in a spinor Bose gas close to a non-thermal fixed point**
   C.-M. Schmied, M. Prüfer, M. K. Oberthaler, T. Gasenzer, Phys. Rev. A **99**, 033611 (2019)

6. **Violation of single-length-scaling dynamics via spin vortices in an isolated spin-1 Bose gas**
   C.-M. Schmied, T. Gasenzer, P. B. Blakie, Phys. Rev. A **100**, 033603 (2019)

7. **Stability analysis of ground states in a one-dimensional trapped spin-1 Bose gas**
   C.-M. Schmied, T. Gasenzer, M. K. Oberthaler, P. G. Kevrekidis, CNSNS **83**, 105050 (2020)

These publications represent the result of collaborative research. The following statement summarizes my contributions to each of the above listed projects in order to clearly separate them from the work done by other co-authors.

Statement of contribution to jointly authored works

I contributed to the writing of the manuscripts of all listed publications.

1. I performed complementary numerical simulations (not shown in the paper) supporting the experimental observations and elaborated on the theoretical concepts.

2. I carried out all numerical simulations and analyzed the data. All authors developed the general concept of prescaling and the methods to extract it from the numerical data.

3. I performed all numerical simulations. All analytical calculations were done by A. N. Mikheev.

4. This overview article gives an introduction to the concept of non-thermal fixed points summarizing analytical and numerical work that has been carried out over the last decade. Among other work, it contains material of publications 2 and 3 of the above stated list. I assembled sections 1-3 and 5-8. Section 4 has been done by A. N. Mikheev.

5. I performed all numerical simulations and analyzed the data.

6. I carried out all numerical simulations and the subsequent data analysis.

7. I implemented all numerical methods and generalized the mentioned algorithms to multi-component systems.

Contents

1. Introduction **1**

I. Theoretical background 5

2. Theoretical concepts **7**
2.1. The concept of non-thermal fixed points 7
2.2. Theoretical description of non-equilibrium quantum many-body systems 12
2.3. Ultracold Bose gases 13
2.3.1. Multi-component Bose gases as a tool to study universal scaling dynamics 14
2.3.2. Collective and topological excitations of Bose gases 17

3. Theoretical models **21**
3.1. $U(N)$-symmetric Bose gas 21
3.1.1. The model 21
3.1.2. Low-energy effective field theory 22
3.1.3. Observables 25
3.2. Spin-1 Bose gas 26
3.2.1. The model 27
3.2.2. Mean-field phase diagram 28
3.2.3. Observables 29
3.3. Numerical methods 30
3.4. Hydrodynamic formulation 32

II. Non-thermal fixed points dominated by topological excitations 35

4. Generating far-from-equilibrium states via quenches **39**
4.1. Bogoliubov excitations in a homogeneous spin-1 system 40
4.1.1. Excitations about the polar state 40
4.1.2. Excitations about the antiferromagnetic state 42
4.1.3. Excitations about the easy-plane state 43
4.1.4. Excitations about the easy-axis state 44
4.2. The one-dimensional trapped spin-1 Bose gas 44
4.3. Ground states and phase diagram of the trapped spin-1 Bose gas 45
4.3.1. Time-independent equations of motion 46
4.3.2. Continuous-time Nesterov scheme 47
4.3.3. Numerical results 50

4.4. Stability analysis of the trapped spin-1 Bose gas . . . 52
4.4.1. Determining the wave functions of stationary states within the (δ, q)-plane using an exact Newton method . . . 52
4.4.2. Bogoliubov de-Gennes equations . . . 53
4.4.3. Numerical results . . . 56
4.5. Summary and outlook . . . 66

5. Bidirectional universal scaling dynamics in a one-dimensional spin-1 Bose gas 69
5.1. Numerical methods and parameter quench . . . 69
5.2. Bidirectional universal scaling . . . 71
5.3. Scaling regime . . . 75
5.4. Spatial correlation function . . . 76
5.5. Departure from the scaling regime . . . 77
5.6. Discussion of scaling exponents . . . 78
5.7. Comparison to experimental observations . . . 79
5.8. Summary and outlook . . . 80

6. Violation of single-length-scaling dynamics via spin vortices in a two-dimensional spin-1 Bose gas 83
6.1. Numerical methods and parameter quench . . . 83
6.2. Spin vortices . . . 85
6.3. Detection of spin vortices . . . 85
6.4. Universal decay laws of spin vortices . . . 87
6.5. Violation of single-length scaling . . . 89
6.6. Summary and outlook . . . 94

III. Non-thermal fixed points dominated by collective excitations 97

7. Universal scaling dynamics in a $U(N)$-symmetric Bose gas 99
7.1. Analytical predictions for the $U(N)$-symmetric Bose gas . . . 99
7.1.1. From Kadanoff-Baym to kinetic equations in a nutshell . . . 100
7.1.2. Spatio-temporal scaling in the large-N limit . . . 100
7.1.3. Relation between the scaling of particle and quasiparticle distributions . . . 103
7.2. Numerical simulation of the $U(3)$-symmetric Bose gas . . . 103
7.2.1. Numerical parameters . . . 103
7.2.2. Spatio-temporal scaling . . . 104
7.3. Summary and outlook . . . 109

8. Prescaling 113
8.1. Motivation and introduction . . . 114
8.2. Position-space correlations . . . 115
8.3. Extraction of prescaling . . . 117
8.4. Discussion of numerical results . . . 119
8.5. Conservation laws during prescaling . . . 120

8.6. Scaling function and scaling violations 121
8.7. Summary and outlook 124

IV. Concluding Remarks **127**

9. Summary **129**

10. Outlook **131**

Bibliography **133**

List of Figures

2.1. Schematics of a non-thermal fixed point 8
2.2. Sketch of self-similar scaling in time and space 10

3.1. Mean-field phase diagram of the spin-1 Bose gas 28

4.1. Gound state wave functions of a trapped spin-1 Bose gas 50
4.2. Mode frequencies of the polar state 54
4.3. Comparison of the energy spectrum of the polar state in a trapped and homogeneous setting 55
4.4. Maximal growth rates of eigenmodes of the polar state 57
4.5. Mode frequencies of the antiferromagnetic state 58
4.6. Maximal growth rates of the eigenmodes of the antiferromagnetic state . 59
4.7. Mode frequencies of the easy-plane state 60
4.8. Maximal growth rates of the eigenmodes of the easy-plane state 61
4.9. Mode frequencies of the easy-axis state 62
4.10. Maximal growth rates of the eigenmodes of the polar state for increased strength of the spin coupling 63
4.11. Maximal growth rates of the eigenmodes of the polar state for increased normalized trap strength 64
4.12. Maximal growth rates of the eigenmodes of the polar state for decreased normalized trap strength 65

5.1. Space-time evolution of the transversal spin in the one-dimensional spin-1 Bose gas 71
5.2. Bidirectional self-similar evolution of the structure factor 72
5.3. Scaling exponents as a function of the reference time 75
5.4. Spatial correlation function of the transversal spin within the temporal scaling regime 76
5.5. Time evolution of the structure factor indicating the departure from the scaling regime 77
5.6. Time evolution of the characteristic IR and UV scale 78

6.1. Snapshot of a single realization of the two-dimensional spin-1 Bose gas within the scaling regime 86
6.2. Vortex number as a function of time within the universal scaling regime for $q = 0.15\,q_0$ 87
6.3. Vortex number as a function of time within the universal scaling regime for $q = 0.3\,q_0$ and $q = 0.05\,q_0$ 88
6.4. Universal scaling dynamics of the structure factor of the transversal spin 90
6.5. Momentum distributions derived from the hydrodynamic decomposition of the kinetic energy density 92
6.6. Hydrodynamic decomposition of the kinetic energy density 93

7.1. Universal scaling of the occupation number distribution and the correlator measuring the spatial fluctuations of the relative phases 105
7.2. Scaling exponents of the $U(3)$-symmetric Bose gas in three spatial dimensions 106
7.3. Time evolution of the zero-momentum mode of the single-component occupation number 107
7.4. Hydrodynamic decomposition of the flow pattern encoded in the phase-angle field 108
7.5. Universal scaling dynamics of the occupation numbers representing parts of the hydrodynamic decomposition 109

8.1. Time evolution of the first- and second-order coherence functions of a $U(3)$-symmetric Bose gas 116
8.2. Prescaling of position-space correlations 118
8.3. Enlarged representation of the infrared prescaling evolution of the single-component occupation number 122

1. Introduction

Comparatively little is known about the structure and states of quantum many-body systems far from equilibrium. To reveal potential out-of-equilibrium phenomena, the dynamics of isolated quantum many-body systems quenched far from equilibrium has been an object of intensive study during recent years. Examples range from the post-inflationary early universe [1, 2], via the dynamics of quark-gluon matter created in heavy-ion collisions [3, 4] to the evolution of ultracold atomic systems following a sudden quench of, e.g., an interaction parameter [5, 6]. Yet, despite great efforts, there are many open questions remaining about possible pathways for the evolution of such systems. Various scenarios have been discussed for and observed in ultracold atomic quantum gases, including integrable dynamics [7–10], prethermalization [11–15], generalized Gibbs ensembles [16–20], critical and prethermal dynamics [21–24], many-body localization [25, 26], relaxation after quantum quenches [27, 28], wave turbulence [29–31], decoherence and revivals [32], universal scaling dynamics associated with a non-thermal fixed point [33–36], as well as prescaling [37]. The rich spectrum of different possible phenomena highlights the capabilities of ultracold quantum gases, as well as the gain obtained with quantum systems as compared to classical statistical ensembles.

Out of the plethora of non-equilibrium phenomena listed above, this thesis is devoted to the investigation of universal scaling dynamics associated with non-thermal fixed points in ultracold bosonic quantum gases far from equilibrium. The major goal is to unravel the underlying key features that characterize the universal scaling behavior near the fixed point. This knowledge can then be used to address the overarching question of establishing out-of-equilibrium universality classes.

Universal scaling dynamics associated with a non-thermal fixed point is characterized by a self-similar scaling evolution of correlation functions in time and space. This leads to a dramatic reduction of the complexity of the non-equilibrium time evolution of the quantum many-body system as the dynamics of correlations can be captured by universal scaling functions and scaling exponents. Global conservation laws strongly constrain the non-local transport associated with the self-similar evolution and impose scaling relations between the exponents. The scaling exponents together with the scaling function allow determining the universality class associated with the fixed point [34, 38]. However, a full classification is lacking so far such that establishing out-of-equilibrium universality classes is subject to ongoing research. In the style of equilibrium universality classes, one expects underlying symmetries of the system to be relevant for the observable universal dynamics and thus for the associated out-of-equilibrium universality class.

The universal scaling behavior can emerge from rather different underlying physical configurations and processes. For example, the dynamics can be either driven by the conserved redistribution of collective excitations or by the reconfiguration and annihilation of topological excitations populating the system. Universal scaling dynamics at non-thermal fixed points with reference to topological excitations has been discussed in Refs. [36, 39–45], whereas scaling behavior not subject to such excitations has been

investigated in Refs. [33–35, 46–51].

The spatio-temporal scaling of correlation functions in isolated systems is associated with the loss of information about the details of the initial condition and microscopic system properties. Nonetheless, a common key ingredient for the occurrence of self-similar dynamics is an extreme out-of-equilibrium initial state. Such a state can, for example, be generated by means of an instantaneous change of a Hamiltonian parameter which we refer to as a parameter quench.

The universal properties of the scaling behavior allow us to look for common characteristics in the non-equilibrium dynamics of rather different physical systems with typical energy scales ranging over nearly twenty orders of magnitude. If two such systems belong to the same out-of-equilibrium universality class, the concept of universality may enable us to use one physical system to predict dynamical properties of another system that is, for example, hard to access in experiments. Such a correspondence has been theoretically shown to exist between a non-equilibrium plasma of highly occupied gluon fields and scalar Bose fields modelling the respective dynamics of an ultracold Bose gas [38]. Starting from an extreme out-of-equilibrium initial condition, the distribution functions of both systems feature universal dynamics characterized by the same set of scaling exponents. The investigated so-called quark-gluon plasma, produced at a temperature of $T \simeq 10^{12}$ K, is a short living stage after an ultra-relativistic heavy-ion collision. The dynamical evolution of this stage is very hard to observe experimentally as the detectors can only measure the final distribution of hadrons after the system has cooled down. From this distribution, one has to infer the dynamical properties of the quark-gluon plasma. Hence, the experimental extraction of time-resolved correlation functions, which then show universal scaling properties, is unfeasible. The experimental accessibility of universal scaling dynamics changes dramatically when we consider ultracold atomic quantum gases at temperatures of $T \simeq 10^{-9}$ K. The major advantage of these systems is that they are well-controlled in experiments and can thus be utilized as toy models to study fundamental questions of quantum many-body physics. In contrast to the quark-gluon plasma, the non-equilibrium time evolution can be directly monitored experimentally. Furthermore, the high degree of control allows repeating the experiment many times under comparable conditions which is essential for the extraction of correlation functions that show universal scaling behavior at a non-thermal fixed point. In addition, using experimental manipulation techniques, it is possible to vary the interactions between the atoms or to generate a variety of different far-from-equilibrium initial configurations, which opens a window to reveal key ingredients of universal scaling dynamics. These unique characteristics are thus the main motivations for studying universal scaling dynamics by means of investigating the non-equilibrium dynamics in experiments with ultracold quantum gases as well as in the associated theoretical models. To finally provide a full picture, we need a combined experiment-theory effort making use of experimental platforms as well as numerical simulations and analytical predictions.

In this thesis, we consider universal scaling dynamics associated with non-thermal fixed points in ultracold Bose gases from a theoretical point of view. In particular, we present numerical and analytical studies of multi-component Bose gases quenched far out of equilibrium. When possible, we compare our findings to experimental observations. We explore strong cooling quenches as well as magnetic field quenches that lead to the growth of unstable momentum modes which subsequently drive the system far from equilibrium within the early stage of the time evolution. As aforementioned, the

emerging spatio-temporal scaling behavior can be governed by rather different underlying physical configurations and processes. We find that multi-component Bose gases offer the possibility to investigate both, non-thermal fixed point scaling dominated by topological as well as collective excitations. Which type of excitation determines the observed scaling behavior appears to crucially depend on the dimensionality of the system.

Numerical simulations of a spin-1 Bose gas in one spatial dimension reveal bidirectional universal scaling, which is prototypical for the spatio-temporal evolution at a non-thermal fixed point. The bidirectional self-similar scaling is caused by the redistribution and reshaping of quasi-topological excitations. While a scaling evolution is not expected in one-dimensional single-component gases, we show that the multi-component system features a spin degree of freedom which enables universal scaling dynamics in one spatial dimension. In two spatial dimensions, we find that the system can be simultaneously attracted to two non-thermal fixed points with distinctly different scaling exponents and scaling functions. This results from the presence of two types of topological excitations in the spin degree of freedom which is a peculiar property subject to the multiple components. The numerically extracted scaling dynamics, which is characterized by the simultaneous growth of two macroscopic length scales, has not been observed and described before in the context of non-thermal fixed points. This finding raises interesting questions concerning the classification of universal scaling out of equilibrium.

Numerical and analytical treatments additionally enable us to extract universal scaling dynamics dominated by collective excitations in $U(N)$-symmetric Bose gases. The associated relevant low-energy degree of freedom is identified to be characterized by relative-phase excitations. The $U(N)$-symmetric model further allows us to extract how the system approaches the non-thermal fixed point during the time evolution from a far-from-equilibrium initial configuration. Performing numerical simulations of a $U(3)$-symmetric Bose gas in three spatial dimensions, we are able to show the existence of prescaling, a new out-of-equilibrium phenomenon that we propose as a generic feature of the time evolution of a quantum many-body system towards a non-thermal fixed point.

The research presented in this thesis contributes to a deeper understanding of universal scaling dynamics far from equilibrium and unravels important key aspects for establishing out-of-equilibrium universality classes. In particular, we find that the dimensionality, as well as the nature and interaction of potential excitations of the system play a decisive role for the classification of universal scaling dynamics out of equilibrium. Especially, the reported variety of universal scaling properties of spin-1 Bose gases suggests that such a classification requires more than underlying symmetries of the investigated model. Additionally, we introduce and illustrate prescaling as an out-of-equilibrium phenomenon describing the evolution towards a non-thermal fixed point, which allows us to bridge the conceptual gap in the time evolution from the initial state to the associated fixed point.

Organization of this thesis

This thesis is organized in four parts that cover different overarching thematic aspects.

The first part contains information about the theoretical background.

In Chpt. 2, we introduce the basic theoretical concepts. We start with the theory of non-thermal fixed points followed by a discussion of the theoretical description of non-equilibrium quantum many-body systems. Then, we comment on the capabilities of multi-component Bose gases as platforms to study universal scaling dynamics.

In Chpt. 3, we elaborate on the theoretical models of the multi-component Bose gases investigated in the course of this thesis. In this context, we discuss the basic properties of $U(N)$-symmetric and spin-1 Bose gases. Furthermore, we present a hydrodynamic description of the models which allows us to identify the role of different types of excitations in the universal scaling regime by means of a decomposition of the kinetic energy.

In the second part, we consider universal scaling dynamics at non-thermal fixed points dominated by topological excitations. We illustrate this type of scaling behavior by numerical simulations of spin-1 Bose gases.

In Chpt. 4, we present scenarios for the generation of far-from-equilibrium initial configurations in spin-1 Bose gases. These scenarios are based on using instabilities that arise from parameter quenches between different phases of the model. We identify potential instabilities by means of investigating the dynamical stability of pre-quench states within the post-quench phase. The stability properties are studied by means of Bogoliubov theory which we apply to homogeneous as well as trapped one-dimensional spin-1 systems. To analyze the stability properties of the trapped system, we introduce suitable numerical tools and elaborate on their generalization to multi-component systems.

In Chpt. 5, we present numerical results showing bidirectional universal scaling in a one-dimensional spin-1 Bose gas driven by quasi-topological excitations such as spin textures and kink-like defects.

In Chpt. 6, we report on universal scaling involving the growth of two macroscopic length scales determined by the mutual annihilation of two types of spin vortices in a two-dimensional spin-1 Bose gas.

In the third part, we focus on universal scaling dominated by collective excitations.

In Chpt. 7, we illustrate this type of non-thermal fixed point scaling by investigating the non-equilibrium dynamics of a $U(N)$-symmetric Bose gas. Taking the large-N limit of the model and making use of a low-energy effective field theory description, we elaborate on analytical predictions of the spatio-temporal scaling of the $U(N)$-symmetric Bose gas within a kinetic theory approach. We corroborate our analytical predictions with numerical simulations of a $U(3)$-symmetric Bose gas in three spatial dimensions.

In Chpt. 8, we introduce prescaling as a generic feature of the evolution of a quantum many-body system towards a non-thermal fixed point. To illustrate the concept and the existence of prescaling, we consider a $U(3)$-symmetric Bose gas in three spatial dimensions. We outline the extraction of prescaling from numerically calculated position-space correlation functions and elaborate on conservation laws obeyed during the prescaling evolution of the system.

In the final part, we summarize (Chpt. 9) and give an outlook to future research (Chpt. 10).

Part I.

Theoretical background

2. Theoretical concepts

In this chapter, we present the theoretical concepts that set the framework to study universal scaling dynamics in quantum many-body systems far from equilibrium. We aim at giving a conceptual overview which summarizes the key ideas underlying the non-equilibrium physics investigated in the course of this thesis. We start with introducing the concept of non-thermal fixed points in Sect. 2.1. Then, we elaborate on the theoretical description of non-equilibrium quantum many-body systems, where we illustrate analytical and numerical approaches in Sect. 2.2. With this at hand, we discuss the capabilities of multi-component Bose gases as platforms to study universal scaling in Sect. 2.3. Furthermore, we point to potential low-energy excitations of these systems as they play a decisive role for the observed scaling behavior.

2.1. The concept of non-thermal fixed points

The main focus of this thesis is to study universal scaling dynamics at non-thermal fixed points in quantum many-body systems far from equilibrium. Therefore, we aim at giving a detailed introduction to the concept of non-thermal fixed points in this section. We present the key features characterizing such a fixed point including an illustration of the associated dynamics by reference to an ultracold Bose gas. This section is taken and adapted from Ref. [52].

The theory of non-thermal fixed points in the real-time evolution of, foremost closed, non-equilibrium systems, is inspired by the concepts of equilibrium and near-equilibrium renormalization-group theory [53–55]. The basic concept of such out-of-equilibrium fixed points is motivated by universal critical scaling of correlation functions in equilibrium. When using a renormalization-group approach, a physical system is basically studied through a microscope at different resolutions. Close to a phase transition, one observes that the correlations look self-similar, i.e., the same no matter which resolution is used. In this case, shifting the spatial resolution by a multiplicative scale parameter s causes correlations between points with distance x, denoted by $C(x;s)$, to be rescaled according to $C(x;s) = s^{\zeta} f_s(x/s)$. Hence, the correlations are solely characterized by the universal scaling function f_s and a universal exponent ζ. When a change of the scale s does not change C by any means, a fixed point of the renormalization-group flow is reached. In that case, the scaling function takes the form of a pure power law $f_s(x) \sim x^{-\zeta}$. In a realistic physical system, the scaling function f_s is, in general, not a pure power law but retains information of characteristic scales such as a correlation length ξ. Thus, the system may only approximately reach the fixed point.

Taking the time t as the scale parameter, the renormalization-group idea can be extended to the time evolution of systems (far) away from equilibrium. The corresponding fixed point of the renormalization-group flow is called non-thermal fixed point. In Fig. 2.1, we show a schematic illustration, where the non-thermal fixed point is indicated as a transient phenomenon in the evolution of a quantum many-body system towards equilibrium. In the scaling regime near a non-thermal fixed point, the evo-

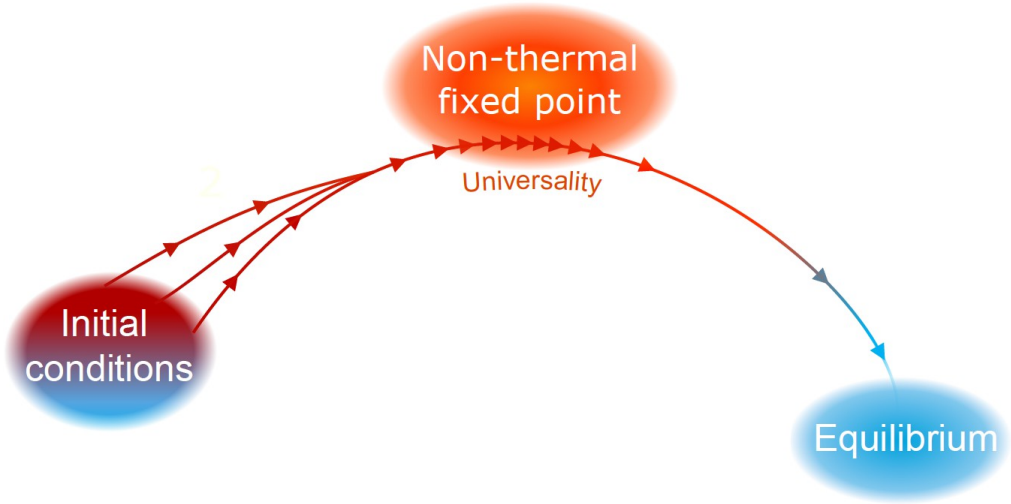

Figure 2.1.: Schematics of a non-thermal fixed point [33] based on the ideas of a renormalization group flow. Depending on the initial condition, an out-of-equilibrium system can approach a non-thermal fixed point during the time evolution. In the vicinity of such a fixed point, the system experiences critical slowing down (indicated by the tightly packed red arrows). As a consequence, correlation functions $C(k,t)$ show scaling behavior in space and time according to $C(k,t) = t^{\alpha} f_s(t^{\beta}k)$, with a universal scaling function f_s. The associated self-similar evolution is characterized by non-zero universal scaling exponents α and β. Universal scaling close to a non-thermal fixed point is understood to occur as a transient phenomenon on the way to equilibrium (indicated by the trajectory leading away from the fixed point). Figure taken and adapted from Ref. [35].

lution of the time-dependent version of the correlations discussed above is determined by $C(x,t) = t^{\alpha} f_s(t^{-\beta}x)$, with two universal exponents α and β which assume, in general, non-zero values. Such a time-dependent scaling relation for the correlations is also termed dynamical scaling hypothesis. The associated correlation length of the system changes as a power of time, $\xi(t) \sim t^{\beta}$. Commonly, the universal scaling properties are extracted from the associated momentum-space correlator $C(k,t)$, which also obeys the dynamical scaling hypothesis and evolves according to $C(k,t) = t^{\alpha} f_s(t^{\beta}k)$ within the scaling regime.

Note that the time evolution taking power-law characteristics is equivalent to critical slowing down, which in this case occurs in real time. We remark that, depending on the sign of β, increasing the time t can correspond to either a reduction or an increase of the microscope resolution. Furthermore, we stress that the spatio-temporal scaling behavior at the fixed point leads to a dramatic reduction in the complexity of the non-equilibrium time evolution as the correlation function only depends on the product of space and time and not on each of the variables individually.

The scaling exponents α and β together with the scaling function f_s allow determining the universality class associated with the fixed point [34, 38]. While a full such classification is still lacking, underlying symmetries of the system are expected to be relevant for the observable universal dynamics and thus for the associated universality class. If it is possible to establish out-of-equilibrium universality classes, the evolution of very different physical systems far from equilibrium can be categorized by means of their possible

kinds of scaling behavior. In the course of this thesis, we will see that the presence and configuration of excitations plays a crucial role for the realized scaling exponents and scaling functions suggesting that a quantum many-body system can even be attracted to different non-thermal fixed points depending on the type of excitation that dominates the scaling evolution. Such findings have to be taken into account in order to provide a full classification of universal dynamics out of equilibrium.

Whether a physical system can approach a non-thermal fixed point and show universal scaling dynamics, and, if so, which particular fixed point is reached, generally depends on the class of chosen initial conditions. Within each class, sometimes referred to as the attractive basin of a non-thermal fixed point, the subsequent scaling dynamics is independent of the details of the initial configuration. A common key ingredient for the occurrence of self-similar dynamics is an extreme out-of-equilibrium initial state. Such a state can, for example, be characterized by a strong overpopulation of the particle number distribution as compared to the equilibrium case.

To illustrate the conceptual idea of non-thermal fixed points and the associated universal scaling dynamics, we consider the time evolution of a dilute Bose gas in three spatial dimensions after a strong cooling quench [56]. For a simplified representation of the time evolution of the particle number distribution see Fig. 2.2 as well as Refs. [34, 57–59]. An extreme version of such a cooling quench can be achieved by first cooling the system adiabatically such that its chemical potential is $0 < -\mu \ll k_B T$, where the temperature $T \gtrsim T_c$ is just above the critical temperature T_c separating the normal and the superfluid phase of the Bose gas. In a next step, one removes all particles with energy higher than $\sim |\mu|$. This leads to a particle number distribution that drops abruptly above a momentum scale Q (see Fig. 2.2). If the corresponding energy is on the order of the ground-state energy of the post-quench fully condensed gas, meaning that $(\hbar Q)^2/(2M) \simeq |\mu| \simeq g\rho$, with the coupling parameter $g = 4\pi\hbar^2 a/M$ quantified by the scattering length a and atom mass M, then the energy of the entire gas after the quench is concentrated at the scale $Q \simeq k_\xi$, with characteristic healing-length momentum scale $k_\xi = \sqrt{8\pi a\rho}$.

Most importantly, such a strong cooling quench leads to an extreme initial condition for the subsequent dynamics. The post-quench particle number distribution is strongly over-occupied at momenta $k \lesssim Q$ as compared to the final equilibrium distribution. This initial overpopulation of modes with energies $\sim (\hbar Q)^2/2M$ induces inverse particle transport to lower momenta while energy is transported to higher wavenumbers [34, 57, 58] as indicated by the arrows in Fig. 2.2. The rescaling is thus characterized by a bidirectional, in general non-local redistribution of particles and energy. In contrast to the case of a weak cooling quench leading to a scaling evolution in which weak wave turbulence is typically induced [56, 60], here the inverse transport is characterized by a different, strongly non-thermal power-law form of the scaling function in the infrared momentum region.

While the spatio-temporal scaling provides the "smoking gun" for the approach of a non-thermal fixed point, the steep power-law scaling of the momentum distribution, $n(k) \sim k^{-\zeta}$, reflects the character of the underlying transport. The evolution during the scaling period is universal in the sense that it becomes mainly independent of the precise initial conditions set by the cooling quench as well as of the particular values of the physical parameters characterizing the system.

In the vicinity of the non-thermal fixed point, the momentum distribution of the Bose gas rescales self-similarly, within a certain range of momenta, according to $n(k,t) = (t/t_{\mathrm{ref}})^\alpha f_s([t/t_{\mathrm{ref}}]^\beta k)$, with some reference time t_{ref}. The distribution shifts to lower mo-

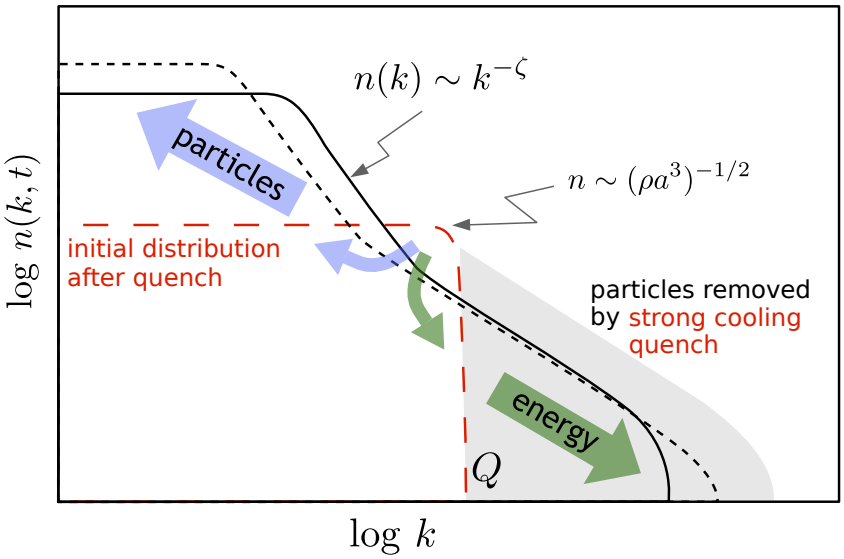

Figure 2.2.: Self-similar scaling in time and space close to a non-thermal fixed point. The sketch shows, on a double-logarithmic scale, the time evolution of the single-particle momentum distribution $n(k,t)$ of a Bose gas for two different times t (solid and short-dashed line). Starting from an extreme initial distribution marked by the red long-dashed line, being the result of a strong cooling quench, a bidirectional redistribution of particles in momentum space occurs as indicated by the arrows. Particle transport towards zero momentum as well as energy transport to large momenta are characterized by self-similar scaling evolutions in space and time according to $n(k,t) = (t/t_{\mathrm{ref}})^{\alpha} f_s([t/t_{\mathrm{ref}}]^{\beta} k)$, with universal scaling exponents α and β, in general, different for both directions. Here, t_{ref} is some reference time within the temporal scaling regime. The infrared transport (blue arrow) conserves the particle number which is concentrated at small momenta. In contrast, the energy, being concentrated at high momenta, is conserved in the redistribution of short-wavelength fluctuations (green arrow). See main text for details. Figure taken and adapted from Ref. [52].

menta for $\beta > 0$, while transport to larger momenta occurs in the case of $\beta < 0$. A bidirectional scaling evolution is, in general, characterized by two different sets of scaling exponents. One set describes the inverse particle transport towards low momenta whereas the second set quantifies the transport of energy towards large momenta.

Global conservation laws – applying within an extended regime of momenta – strongly constrain the redistribution underlying the self-similar dynamics in the vicinity of the non-thermal fixed point. Hence, they play a crucial role for the possible scaling evolution as they impose scaling relations between the scaling exponents. For example, particle number conservation in the infrared regime of long wavelengths requires that $\alpha = d\beta$ in d spatial dimensions.

The aforementioned transport in momentum space can emerge from rather different underlying physical configurations and processes. For example, the dynamics can either be driven by the conserved redistribution of collective excitations such as in weak wave turbulence [34, 56] or by the reconfiguration and annihilation of topological excitations populating the system [45, 57]. If topological excitations are subdominant or absent

at all, which can, for example, be realized in multi-component systems, the strongly occupied modes exhibiting scaling near the fixed point [34, 56] typically reflect strong phase fluctuations not subject to an incompressibility constraint [61]. The associated scaling exponents are generically different for both types of dynamics, with and without topological excitations [34, 42, 45].

The existence and significance of strongly non-thermal momentum power laws, requiring a non-perturbative description reminiscent of wave turbulence, was proposed by Rothkopf, Berges and collaborators in the context of reheating after early-universe inflation [33, 46], generalized by Scheppach, Berges, and Gasenzer to scenarios of strong matterwave turbulence [47], and to the case of topological excitations by Nowak, Sexty, Erne, Gasenzer et al. [39–42, 57], see also Refs. [43–45, 62–65]. Universal scaling at a non-thermal fixed point in both space and time was studied by Piñeiro Orioli, Boguslavski, and Berges for relativistic $O(N)$-symmetric models [34, 66], see also Refs. [50, 67], and discussed in the context of heavy-ion collisions [4, 38, 49, 68] as well as axionic models [64]. First experimental observations of universal scaling dynamics close to a non-thermal fixed point were made by Prüfer et al. [35] as well as Erne et al. [36] in ultracold atomic quantum gases.

For clarification, we remark that the concept of non-thermal fixed points includes scaling dynamics which exhibits coarsening and phase-ordering kinetics [69] following the creation of defects and nonlinear patterns that occur after a quench across an ordering phase transition. However, we emphasize that coarsening and phase-ordering kinetics in most cases are being discussed within an open-system framework, considering the system to be coupled to a heat bath. Moreover, most theoretical treatments of these phenomena do not take non-linear dynamics and transport into account. In this framework, the universal scaling exponents are deduced from the underlying dynamics of (quasi)topological excitations, the dimensionality of the system and the presence/absence of the conservation of the order-parameter field in the post-quench phase.

We further remark that the scaling behavior at non-thermal fixed points is reminiscent of the transport and scaling characterizing wave-turbulent cascades. In these cascades, analogously to fluid turbulence, universal scaling is expected in a certain interval of momenta, termed the inertial range. Within the inertial range of a wave-turbulent cascade, transport occurs locally, from momentum shell to momentum shell, leaving the transported quantity within such a momentum shell constant in time. The transport is commonly uni-directional, either from large to small characteristic scales or vice versa. This is in contrast to self-similar scaling at non-thermal fixed points where the transport is bidirectional and non-local. However, note that bidirectional transport can also be found in turbulence. One example is Kraichnan turbulence in two spatial dimensions [70]. In this case, two formal inertial ranges give rise to an inverse energy cascade and a direct enstrophy cascade. Using the concept of kinetic time [71] further allows distinguishing between wave-turbulent cascades and universal scaling dynamics at non-thermal fixed points. While the kinetic time diverges in the scaling limit at a non-thermal fixed point reflecting the critical slowing down, the kinetic time decreases within the wave-turbulent cascade [56].

To summarize, a common property of the universal evolutions is scaling behavior with evolution time as scaling parameter. The associated scaling is reminiscent of equilibrium criticality at a continuous phase transition [54, 55, 72]. The system rescales in space with some power of the evolution time, which looks like zooming in or out the field of view of a microscope in real time. To a certain extent, slowed-down dynamics and scaling in

the evolution time can be seen as analogues of the universality in equilibrium critical phenomena in non-equilibrium systems [53, 69, 73–75].

2.2. Theoretical description of non-equilibrium quantum many-body systems

In the previous section, we have outlined the basic ideas of non-thermal fixed points, a phenomenon that occurs in the dynamical evolution of a non-equilibrium quantum many-body system. For studying such fixed points theoretically, we can make use of analytical as well as numerical tools.

For a general analytical treatment of non-thermal fixed points, we need to be able to calculate the time evolution of a quantum many-body system out-of equilibrium. Suitable techniques are provided by the framework of non-equilibrium quantum field theory (QFT). Using a path integral formulation, all information about the time-evolving quantum system is contained in the so-called Schwinger-Keldysh non-equilibrium generating functional [76]. Correlation functions, which show universal scaling at a non-thermal fixed point, can be obtained by functional differentiation of the generating functional with respect to corresponding sources. To calculate such observables at some instant in time, the system is evolved along a Schwinger-Keldysh closed time path which reflects the nature of non-equilibrium QFT as an initial value problem. This is in contrast to equilibrium QFT, where only asymptotic input and output states are used. The technique was first introduced by Julian Schwinger in 1961 [77] and further developed by Mahanthappa and Bakshi [78–80], who were focussing on bosonic systems. The initial configuration of the out-of equilibrium system is contained in the initial density matrix entering the generating functional. In the majority of cases, it is sufficient to choose the initial density matrix to be Gaussian. Calculating the non-equilibrium generating functional in its most general formulation is highly non-trivial.

To study the universal scaling behavior at non-thermal fixed points, one generally focusses on the evolution of two-point correlators. From these, e.g., (quasi)particle occupation numbers in momentum space can be derived. Taking the Schwinger-Keldysh description, one derives dynamical equations for unequal-time two-point correlators, called Kadanoff-Baym equations [81]. These equations describe the non-equilibrium dynamics exactly but are as non-trivial to solve as the computation of the non-equilibrium generating functional entering these equations is. One is thus held to reduce the complexity of the problem and to obtain approximate dynamical equations that are capturing the physics relevant at a non-thermal fixed point.

It turns out that a kinetic theory approach provides such an approximation, see, e.g., Refs. [50, 76, 82]. Using a kinetic-theory description enables us to perform a scaling analysis from which the scaling exponents associated with the non-thermal fixed point can be predicted analytically. Within this description, the time evolution of correlation functions is determined by a generalized quantum Boltzmann equation involving a scattering integral that characterizes the properties of the interacting quantum many-body system via the so-called scattering T-matrix. As we are generally dealing with highly correlated systems, occupation numbers grow large at low momentum scales which renders the scattering properties to be non-perturbative.

These properties can be taken into account by means of a non-perturbative coupling resummation scheme based on the two-particle irreducible (2PI) effective action, see

Sect. 2.3.1 for details. Alternatively, one can think of the idea to reformulate the theory in terms of new degrees of freedom in the first place, such that the resulting description becomes more easy to treat in non-perturbative regions. Since the non-perturbative behavior appears at low momentum scales, it is suggestive to use a low-energy effective field theory (LEEFT) approach [83, 84]. This typically implies a choice of suitable degrees of freedom describing the physics occurring below a chosen energy scale. We will outline such an approach for $U(N)$-symmetric multi-component Bose gases in Sect. 3.1.2.

We remark that the above stated analytical treatments generally do not take into account the influence of non-linear and topological excitations onto the scaling behavior. This results from the fact that including such excitations in out-of-equilibrium analytical frameworks is highly non-trivial. Thus, we expect the analytical predictions to capture the scaling properties of quantum many-body systems where non-linear and topological excitations are absent or subdominant, whereas deviations are expected to arise in cases where these excitations play a dominant role in the non-equilibrium time evolution of the system.

Numerical simulations allow us to corroborate the analytical predictions but are additionally able to unravel phenomena beyond analytics. In particular, we can study universal scaling behavior arising from non-linear or topological excitations by means of numerical simulations as they can either be generated within the non-equilibrium time evolution of the system or put in by hand into the initial configuration. As the scaling behavior occurs in a regime of strongly occupied modes, the time evolution can be computed by means of semi-classical simulation methods. For a justification of the semi-classical approximation in the framework of path integrals, we refer to Ref. [85]. Using the so-called truncated Wigner approximation [86, 87], we follow the evolution, starting from a noisy initial configuration, by evaluating many trajectories according to the classical equations of motion. Correlation functions are then obtained by averaging the trajectories. The number of trajectories is chosen in a way that the statistical error arising from run-to-run fluctuations is small. This crucially depends on the dimensionality of the system, the number of grid points used for the numerical simulation and the numerical grid spacing. Extracting the scaling function and the scaling exponents associated with the non-thermal fixed point, especially in the low momentum regime of the correlators, requires a huge number of trajectories that are calculated up to very long evolution times. Hence, we make use of high performance parallel computing techniques to calculate the time evolution of the systems under consideration. In particular, the equations of motion are solved on high level graphical processing units (GPUs) which allow us to highly parallelize the required computations using the large number of provided streaming multiprocessors.

This thesis mainly contains results obtained from numerical simulations supported by selected analytical calculations. For more technical descriptions of the analytical treatments stated above at various levels of detail see Refs. [50, 52, 56, 61, 76, 88].

2.3. Ultracold Bose gases

An intensively studied class of quantum many-body systems far-from-equilibrium are ultracold Bose gases. A major advantage of these systems is their high level of controllability. Making use of high precision experimental techniques, it is possible to engineer various types of interactions between the atoms ranging from short range contact interactions to long range dipolar interactions. In addition, they allow for experiments that

are well isolated from the environment and feature long coherence times which makes them suitable to investigate universal scaling dynamics out of equilibrium [35, 36]. Furthermore, a high repetition rate enables studying higher-order correlation functions, the building blocks of any quantum-field-theory description of many-body systems [89, 90].

To highlight some conceptual aspects, let us assume for now, that we have a non-relativistic ultracold Bose gas in the superfluid regime below the critical temperature for Bose condensation. Superfluidity is generally associated with a complex order-parameter field ψ and results from breaking a global symmetry at sufficiently low temperatures. This means that the expectation value $\langle\psi(\mathbf{x},t)\rangle$ assumes non-zero values below the critical temperature. Being in the superfluid regime, the order-parameter field can be expressed in density-phase representation according to $\langle\psi(\mathbf{x},t)\rangle = \sqrt{\rho(\mathbf{x},t)}\exp\{i\theta(\mathbf{x},t)\}$, with $\rho(\mathbf{x},t) = |\langle\psi(\mathbf{x},t)\rangle|^2$ being the space-time dependent density and $\theta(\mathbf{x},t)$ being the phase of the field. Additionally, we keep the system isolated such that the total particle number $N = \int d\mathbf{x}\rho(\mathbf{x},t)$ is fixed during the time evolution. This is different from relativistic systems or systems coupled to an environment where the total particle number can change due to pair-creation processes or exchange with the environment.

Naturally, ultracold Bose gases are dilute systems characterized by the mean inter-particle distance being much larger than the respective length scale associated with the interactions. Dilute gases are generally referred to as being weakly interacting. We note that, as the diluteness of the system is quantified by both the density and the interactions, the above stated correspondence has to be taken with care in the limit of low densities.

2.3.1. Multi-component Bose gases as a tool to study universal scaling dynamics

Apart from being many-body quantum systems, ultracold Bose gases can feature internal degrees of freedom such as different hyperfine states. This renders them to become multi-component systems where the individual components are labeled by the respective hyperfine magnetic quantum numbers. Among other processes, atoms can be redistributed between the different components leading to much richer non-equilibrium dynamics as compared to a single-component system.

A major advantage of multi-component Bose gases is the possibility to investigate universal scaling under various aspects. On the one hand, we can employ experiments with multi-component ultracold bosonic quantum gases. On the other hand, we can make use of analytical and numerical tools to study respective theoretical models.

In the course of this thesis, we investigate the dynamics of multi-component Bose gases from a theoretical point of view. In particular, we focus on two types of multi-component systems, namely $U(N)$-symmetric and spin-1 Bose gases. Before we introduce the specific theoretical models of these multi-component systems, we comment on the capabilities of multi-component Bose gases to study universal scaling dynamics at non-thermal fixed points. This discussion allows us to conceptually motivate the chosen model systems.

The strength of a theoretical description lies in the freedom to choose the particular model system. While experimental systems might feature rather complex types of interactions, it can be useful to reduce the complexity and try to identify some overarching properties from a much simpler theoretical model. In that light, one could think of the idea to start with a model that has interactions compatible with the maximum possible symmetry of the underlying fundamental fields. By adding more complex types of

interactions, one gradually breaks this overall symmetry.

In the context of non-relativistic N-component Bose gases, such a simple model is characterized by quartic interactions between the complex bosonic fields and is subject to a $U(N)$ symmetry. From an analytical point of view, the model is well-suited to make predictions for the scaling behavior at a non-thermal fixed point by means of a non-perturbative resummed kinetic theory approach. Making use of a non-perturbative large-N approximation [76, 91] allows for an analytical description of universal scaling of the $U(N)$-symmetric model at the non-thermal fixed point [47, 56]. The applied scheme is based on analytical work employing N-component relativistic scalar models that are $O(N)$-symmetric under orthogonal transformations in the space of field components, see Refs. [33, 34, 48, 50]. Note that the analytical predictions of the scaling behavior of $O(N)$-symmetric models at non-thermal fixed points have been corroborated by numerical simulations of an $O(4)$- and $O(8)$-symmetric relativistic scalar field theory [33, 64].

At this point, it is worthwhile to explain the suitability of the $U(N)$-symmetric model for the analytical treatments. Therefore, it is essential to briefly review the key ideas of the above stated resummation procedure, see Refs. [56, 76, 92, 93] for details.

The applied resummation scheme is based on the two-particle-irreducible (2PI) effective action. The 2PI effective action is defined as the double Legendre transform of the generating functional of connected correlation functions with respect to a local and bilocal source term. Hence, it is a functional of the field expectation value and the full propagator. This implies that the graphs in the 2PI effective action, which are termed skeleton diagrams, are built from the dressed propagator instead of the bare one. In a diagrammatic form, the action contains those types of connected loop diagrams that cannot be split apart when cutting two propagator lines. We stress that the propagator is an object defined by the time-ordered two-point correlators of the fundamental fields of the respective model. In case of complex bosonic fields, it is a 2×2 Hermitian matrix resembling the four possible combinations of two-point correlators. The 2PI effective action provides a self-consistent set of dynamical equations for the field expectation value and the propagator. The solutions to these equations preserve conservation laws associated with global symmetries of the investigated theory. Hence, in case of the $U(N)$-symmetric model, the solutions will obey particle-number conservation due to an underlying global $U(1)$ symmetry.

To study the universal scaling dynamics at a non-thermal fixed point within a kinetic theory approach, one commonly first derives a kinetic equation from the dynamical equation of the propagator. In a second step, one analyzes scaling solutions of the kinetic equation to determine the scaling exponents describing the evolution of equal-time two-point correlators at the fixed point.

The respective dynamical equations involve the proper self-energy which has to be deduced from contributions to the 2PI effective action beyond one-loop. As the 2PI effective action consists of an infinite number of 2PI diagrams, one has to make approximations to the action in order to be able to compute the self-energy. Recall that without any approximations, the 2PI effective action contains the complete information about the quantum theory. Expanding the 2PI effective action in a small parameter provides a controlled and systematic approximation. In case of a weak coupling, it might be intuitive to think of an expansion of the effective action in powers of the small coupling of the model. However, when mode occupations become large within the momentum regime subject to the scaling evolution, in particular on the order of the inverse coupling,

the coupling expansion (as well as so-called loop expansions of the 2PI effective action) break down as higher order contributions will become significantly relevant. In other words, this means that the scattering properties of the system become non-perturbative. For an N-component field theory, it turns out that a controlled expansion parameter for the 2PI effective action within the non-perturbative regime is given by the inverse of the number of components. Limiting the contributions from higher orders of the expansion requires N to be sufficiently large. To go beyond a mean-field type approximation, the expansion is taken to next-to-leading order (NLO) in $1/N$.

We stress that the NLO contribution is given by the resummation of an infinite number of diagrams. The crucial property, resulting from the $U(N)$ symmetry of the model, is that solely one class of diagrams appears at NLO. Performing the resummation of this class of diagrams simply boils down to evaluating a geometrical sum providing an analytical expression for the approximated 2PI effective action, see Refs. [56, 93, 94]. This finally allows us to analytically compute the associated self-energy within the given approximation. To ultimately deduce the scaling behavior of the model within a kinetic theory description, one takes the large-N limit in the resulting expressions. Performing this limit is essential to identify the scaling of the dispersion relation characterizing the scattering terms in the kinetic equation.

In this thesis, we use a different analytical approach by means of deriving a low-energy effective field theory for the $U(N)$-symmetric Bose gas anticipating that the scaling behavior at the fixed point occurs in the regime of low momenta. The treatment can be viewed as first rewriting the theory in the relevant low-energy degrees of freedom and then deducing the scaling properties within a kinetic theory framework. In some sense, this approach is more intuitive as it reduces the complexity of the problem before analyzing the universal scaling behavior. Note that the low-energy effective field theory approach in principle does not rely on N being large. Hence, we can also make analytical predictions for the scaling behavior in the limiting case of $N = 1$ [61].

As $U(N)$-symmetric systems are also well-tractable by means of numerical simulations, it is possible to corroborate the analytical predictions with numerical results. Remarkably, the scaling properties extracted from numerical simulations of a $U(1)$-symmetric non-relativistic Bose gas are in good agreement with the analytical predictions derived within the large-N limit of the model [34]. In that light, it is of particular interest to also compare numerical simulations of the $U(N)$-symmetric model for cases with $N > 1$ to the analytical predictions. To do so, we numerically employ the case of $N = 3$, which allows for a comparison with large-N predictions from both, the low-energy effective field theory description as well as the 2PI resummed kinetic theory approach. Furthermore, numerical simulations are capable of unraveling phenomena beyond the scope of the analytical treatment such as the role of topological excitations which are not included in the schemes discussed above.

While investigating the scaling behavior of the $U(N)$-symmetric model provides general properties of universal scaling dynamics possible within the realm of non-relativistic Bose gases, we are also interested in studying the scaling properties of models that are realized in experiments with ultracold bosonic quantum gases.

Spinor Bose gases are one such class of multi-component systems, where the $U(N)$ symmetry is broken due to spin interaction terms. They are well-controlled in experiments and feature long coherence times which makes them eminently suited for studying non-equilibrium phenomena [95–99]. Note that analytical predictions for the scaling behavior of spinor Bose gases by means of kinetic theory approaches are lacking so far.

However, using experimental platforms and numerical simulations allows us to investigate universal scaling dynamics far from equilibrium.

A particularly interesting platform are spin-1 Bose gases, where the three different components account for the magnetic sublevels of the $F = 1$ hyperfine manifold of the atoms forming the gas. Universal scaling dynamics has recently been observed experimentally in a ferromagnetic spin-1 Bose gas in a near-1D geometry [35]. Numerical studies have shown that universal scaling can occur in the ordering process of one- and quasi-two-dimensional spin-1 Bose gases after a parameter quench into an ordered phase [100–109]. We discuss the scaling behavior reported in Refs. [102, 109] in detail in the course of this thesis and compare the results to the experimental observation in Ref. [35].

2.3.2. Collective and topological excitations of Bose gases

Starting from a far-from-equilibrium initial state, both $U(N)$-symmetric and spin-1 Bose gases show universal scaling dynamics associated with a non-thermal fixed point. However, we will find the underlying physical processes causing the scaling behavior to be distinctly different in both systems. While the scaling evolution of the spin-1 Bose gas is determined by the dissolution and annihilation of (quasi)topological excitations, the scaling evolution of the $U(N)$-symmetric system is dominated by the redistribution of (incoherent) collective excitations. Note that, strictly speaking, topological excitations can be also viewed as coherent collective excitations. However, throughout this thesis we solely refer to sound-like or quasiparticle excitations as collective excitations.

Due to their significant role in the universal dynamics, we briefly elaborate on general properties of common collective and topological excitations of ultracold Bose gases at this point. Note that we deliberately leave the discussion on a conceptual level. We go into more detail when discussing the scaling dynamics of both $U(N)$-symmetric and spin-1 Bose gas in the second and third part of this thesis.

A dilute, interacting non-relativistic Bose gas within the superfluid phase generally allows for different types of low-energy excitations on top of the condensate.

Collective excitations

One type of excitation that exists in interacting Bose gases are collective excitations or quasiparticles. They are low-lying excited states on top of the condensed gas. One class of collective excitations in Bose gases are Bogoliubov quasiparticles which are characterized by a sound-like dispersion relation at low momenta [110]. Depending on the number of components of the Bose gas, they can, for example, be sound waves (phonons) and/or spin waves (magnons). Such excitations arise from fluctuations on top of the condensed background gas. They can be theoretically described within the framework of Bogoliubov theory, see Chpt. 4 for details.

For the $U(N)$-symmetric Bose gas we find two types of collective excitations in the low-energy regime. Whereas one type has a Bogoliubov-like dispersion and is associated with the total phase of all components, the other type is a Goldstone mode with free-particle dispersion associated with relative phases between different components.

Topological excitations

While non-interacting Bose gases are described by linear equations of motion, interaction terms cause the equations to become non-linear. These non-linearities generally

allow for (quasi)topological solutions. Such coherent solutions have particle-like properties such that we can speak of them as being solitary excitations of the system [111]. The topology comes from the fact that these objects cannot be continuously deformed into a pure ground state solution when we impose boundary conditions to the system. The presence of topological excitations causes the Bose gas to be strongly correlated even though the interaction between the atoms is commonly weak. Note that there are also other types of non-linear excitations that do not feature topological properties [112]. Although the underlying model may allow for a variety of topological excitations, only a few of them are actually dynamically stable. The stability of the objects generally depends on the dimensionality of the system. There are two types of (quasi)topological excitations that are of interest in this thesis - solitons and vortices.

To get a flavor of these excitations, we start by discussing basic properties arising in single-component Bose gases. We then elaborate on more complex structures of topological excitations in multi-component systems.

Solitons are quasi-topological defects which generally travel with a fixed velocity but are non-dispersive, i.e., stationary in shape and stable in $d = 1$ dimension. This is possible due to a special interplay of the dispersion and the non-linearity such that spreading of the soliton is prevented through the non-linear interaction. Note that in a quantum-field-theoretical framework, solitons are commonly associated with so-called kink solutions. For repulsive interactions, the defects are termed dark solitons as they are characterized by a localized suppression of the background condensate density [113, 114]. The depth of the density suppression is quantified by the continuous grayness parameter which is directly proportional to the solitons velocity. If the density drops to zero, the soliton is called black and does not move. The quasi-topology of dark solitons results from a phase jump $\Delta\theta$ of the complex bosonic field at its center. A black soliton features the largest possible phase jump given by $\Delta\theta = \pi$. In case of attractive interactions, one finds bright solitons characterized by a localized density peak due to the absence of a background condensate. Unlike dark solitons, bright solitons show a linearly varying phase instead of a phase jump and move in form of a localized wave packet along with its carrier wave. In $d > 1$ dimensions, solitons become unstable due to so-called snaking instabilities [115, 116].

Vortices are topologically stable solutions in $d > 1$ dimensions which form the superfluid analogies of eddy flows in classical fluids. In general, vortices have a defect core where the density of the condensate drops to zero, $\rho(\mathbf{x}) \to 0$ as $|\mathbf{x}| \to 0$. The phase of the complex field winds around the vortex core with integer multiples of 2π. This integer multiple is called the winding number and defines the charge of the vortex. A configuration with positive charge is termed vortex, a configuration with negative charge anti-vortex. In general, only singly-quantized vortices with charge ± 1 are stable configurations. A vortex and an anti-vortex can mutually annihilate releasing unstable solitary waves that propagate through the system. In $d = 3$ dimensions, point vortices extend to vortex lines or loops around which the fluid rotates.

Multi-component systems allow for various combinations of the above stated, so to say, elementary topological excitations in the different components. In one-dimensional systems one thus observes so-called vector solitons. One particular example is that of dark-bright solitons [117–120], where one of the components forms a potential well where the absence of atoms causes its filling by atoms of a different component. If the atoms of the second component solely populate that region, we talk of a dark-bright solitonic state. Note that we assume the first component to also feature the phase jump

associated with a dark soliton. In case of three-component systems, excitations such as dark-bright-bright (DBB) and dark-dark-bright (DDB) solitons have been discussed theoretically [121, 122] as well as observed experimentally [123]. Such types of vector solitons give rise to interesting phenomena as it is possible to redistribute the population among the components by means of mutual collisions. For spin-1 systems in two spatial dimensions, a plethora of spin vortices has been found in numerical studies [104–109, 124]. Such spin vortices are composed out of vortices in each of the individual components. The composition is realized in a way that a vortex is also present in the spin degree of freedom of the system.

3. Theoretical models

In this chapter, we introduce the theoretical models of the multi-component Bose gases investigated in the course of this thesis. We start with discussing the basic properties of $U(N)$-symmetric Bose gases in Sect. 3.1. Then, we elaborate on the theoretical description of spin-1 Bose gases in Sect. 3.2. For both systems, we further comment on suitable observables to extract the scaling behavior at non-thermal fixed points. In Sect. 3.3, we discuss the numerical methods used to simulate the dynamics of the $U(N)$-symmetric and spin-1 Bose gas. In Sect. 3.4, we finally make use of a hydrodynamic formulation to analyze different contributions to the kinetic energy of the systems which allows us to identify the role of different types of excitations in the universal scaling regime.

3.1. $U(N)$-symmetric Bose gas

In this section, we discuss the basic properties of $U(N)$-symmetric Bose gases, where the parameter N denotes the number of components. For the numerical simulations we will later restrict ourselves to the case of $N = 3$. Nonetheless, we elaborate on the general case here to highlight some generic characteristics of the model. Furthermore, we study the model within the large-N limit in order to make analytical predictions for the scaling behavior at the non-thermal fixed point.

We start in Sect. 3.1.1 by introducing the Hamiltonian and the equations of motion that govern the time evolution of the system. In Sect. 3.1.2, we derive a low-energy effective field theory for the $U(N)$-symmetric model which is based on identifying the relevant degrees of freedom below a certain energy scale. The resulting low-energy description allows us to directly infer the scattering properties needed to make analytical predictions for the scaling behavior of the system at the non-thermal fixed point within a kinetic theory approach. Finally, we comment on the observables used to study universal scaling dynamics in Sect. 3.1.3.

3.1.1. The model

The spatially uniform $U(N)$-symmetric Bose gas consists of identical particles distinguished only by a single property such as the hyperfine magnetic quantum numbers of the atoms forming the gas. The system in d spatial dimensions is described by a $U(N)$-symmetric Gross-Pitaevskii (GP) model with quartic contact interaction in the total density,

$$H = \int \mathrm{d}\mathbf{x} \left[-\psi_a^\dagger \frac{\hbar^2}{2M} \nabla^2 \psi_a + \frac{g}{2} \psi_a^\dagger \psi_b^\dagger \psi_b \psi_a \right] , \tag{3.1}$$

where M is the particle mass and space-time field arguments are suppressed. Further, we sum over the Bose fields, $a, b = 1, ..., N$, obeying commutators $[\psi_a(\mathbf{x}, t), \psi_b^\dagger(\mathbf{y}, t)] = \delta_{ab}\delta(\mathbf{x}-\mathbf{y})$. The gases are thus assumed to occupy the same space and be subject to identical inter- and intra-species contact interactions quantified by g. In $d = 3$ dimensions

the coupling reads

$$g = \frac{4\pi\hbar^2 a}{M}, \tag{3.2}$$

with a being the respective s-wave scattering length characterizing the contact interactions in the low-energy regime of the model.

In a sense, the $U(N)$-symmetric model features the most simple interaction term in analogy to standard ϕ^4 interactions in $O(N)$-symmetric relativistic scalar field theory models. This makes the model appealing for analytical treatments and offers the possibility to extract general properties of universal scaling dynamics expected in non-relativistic Bose gases as discussed in Sect. 2.3.1.

The time evolution of the $U(N)$-symmetric model is given by the coupled Gross-Pitaevskii equations (GPEs)

$$i\hbar\partial_t\psi_a = \left(-\frac{\hbar^2}{2M}\nabla^2 + g\psi_b^\dagger\psi_b\right)\psi_a. \tag{3.3}$$

Note that all numerical simulations of the model presented in this thesis are performed for the three-dimensional $U(3)$-symmetric case obtained by setting $N = 3$ and $d = 3$.

3.1.2. Low-energy effective field theory

For the $U(N)$-symmetric model, we aim to make analytical predictions for the universal scaling expected at the non-thermal fixed point within a kinetic theory approach. Since we anticipate the scaling behavior to take place at low momentum scales, we make use of a low-energy effective field theory approach. This allows us to rewrite the theory in terms of the relevant low-energy degrees of freedom. Deriving the associated low-energy effective action of the model enables us to directly infer the form of the scattering terms that enter the kinetic equations.

We make use of the effective action when discussing analytical predictions for the universal scaling behavior of the $U(N)$-symmetric Bose gas in Sect. 7.1. This subsection is taken and adapted from Refs. [37, 52]. For a detailed derivation of the effective action see Ref. [61]. Note that we use units of $\hbar = 1$ in the following.

The key observation for deriving a low-energy effective field theory is, that the $U(N)$-symmetric Gross-Pitaevskii model offers a natural separation of scales which allows us to identify relevant low-energy degrees of freedom. This is generally done by comparing the influence of fluctuations of different degrees of freedom of the model below a certain energy scale. We then integrate out all degrees of freedom whose contributions are suppressed at low momenta such that we end up with an effective low-energy description of the system in terms of the relevant degrees of freedom. For the $U(N)$-symmetric Bose gas, we find phase excitations to dominate in the low-energy regime.

The derivation of the low-energy effective field theory, in a path-integral language, makes use of the representation of the fluctuating Bose fields ψ_a in terms of the particle densities ρ_a and phase angles θ_a,

$$\psi_a(\mathbf{x}, t) = \sqrt{\rho_a(\mathbf{x}, t)}\, \exp\left\{i\theta_a(\mathbf{x}, t)\right\}. \tag{3.4}$$

With this, the Lagrangian of the model in Eq. (3.3) reads

$$\mathcal{L} = -\sum_a \left\{ \rho_a \partial_t \theta_a + \frac{1}{2M} \left[\rho_a (\nabla \theta_a)^2 + (\nabla \sqrt{\rho_a})^2 \right] \right\} - \frac{g}{2} \rho^2 \,, \tag{3.5}$$

with total density $\rho = \sum_a \rho_a$. As a first step, we consider density fluctuations $\delta\rho_a$ and phase fluctuations $\delta\theta_a$ about the uniform ground-state densities $\rho_a^{(0)} = \langle \psi_a^\dagger(\mathbf{x}) \psi_a(\mathbf{x}) \rangle$ and phases $\theta_a^{(0)} = 0$. Hence, we write $\rho_a = \rho_a^{(0)} + \delta\rho_a$ and $\theta_a = \delta\theta_a$ and expand the Lagrangian in Eq. (3.5) up to second order in the fluctuations. The corresponding linearized equations of motion are given by

$$\partial_t \theta_a = \frac{1}{4M\rho_a^{(0)}} \nabla^2 \delta\rho_a - g \sum_b \delta\rho_b \,, \tag{3.6}$$

$$\partial_t \delta\rho_a = -\frac{\rho_a^{(0)}}{M} \nabla^2 \theta_a \,. \tag{3.7}$$

Going to Fourier space, the equations of motion read

$$\partial_t \theta_a(\mathbf{k}, t) = -\frac{\mathbf{k}^2}{4M\rho_a^{(0)}} \delta\rho_a(\mathbf{k}, t) - g \sum_b \delta\rho_b(\mathbf{k}, t) \,, \tag{3.8}$$

$$\partial_t \delta\rho_a(\mathbf{k}, t) = \frac{\rho_a^{(0)}}{M} \mathbf{k}^2 \theta_a(\mathbf{k}, t) \,. \tag{3.9}$$

Taking a further time derivative, we can combine Eq. (3.8) and (3.9) to obtain a Bogoliubov-type matrix wave equation for the θ_a,

$$\partial_t^2 \theta_a(\mathbf{k}, t) + \frac{\mathbf{k}^2}{2M} \left(\frac{\mathbf{k}^2}{2M} \delta^{ab} + 2g\rho_b^{(0)} \right) \theta_b(\mathbf{k}, t) = 0 \,, \tag{3.10}$$

where Einstein's sum convention is implied. While, for $N = 1$, we recover the Bogoliubov dispersion, for general N, diagonalization of the coefficient matrix yields the eigenfrequencies of $N - 1$ Goldstone (G) and one Bogoliubov (B) mode. The respective dispersion relations, given by the square roots of the eigenvalues of the coefficient matrix, read

$$\omega_{\mathrm{G}}(\mathbf{k}) = \frac{\mathbf{k}^2}{2M} \,, \tag{3.11}$$

$$\omega_{\mathrm{B}}(\mathbf{k}) = \sqrt{\frac{\mathbf{k}^2}{2M} \left(\frac{\mathbf{k}^2}{2M} + 2g\rho^{(0)} \right)} \,. \tag{3.12}$$

From the corresponding eigenvectors, we find that the Goldstone excitations with a free-particle-like dispersion correspond to relative phases between different components, whereas the Bogoliubov quasiparticle mode is related to the total phase.

Note that the Goldstone theorem [125] predicts, due to the spontaneous breaking of $U(N) \to U(N-1)$, $2N - 1$ gapless Goldstone modes. However, only N of these modes are independent because of the absence of Lorentz invariance and thus particle-hole symmetry [126, 127]. Hence, to take account of this fact and distinguish the modes, we only refer to the quadratic modes as Goldstone ones, whereas the linear one will be

addressed as Bogoliubov mode.

Similarly to Eq. (3.10), one can derive an evolution equation for the density fluctuations $\delta\rho_a(\mathbf{k},t)$. From the solutions of the respective equation, we obtain that the time derivative of the density fluctuations is dominated by the Bogoliubov mode at low momenta $k \ll k_\Xi$, such that

$$\partial_t \delta\rho_a(\mathbf{k},t) \sim \omega_B(\mathbf{k})\delta\rho_a(\mathbf{k},t)\,. \tag{3.13}$$

Here, $k_\Xi = [2M\rho^{(0)}g]^{1/2}$ is the healing-length momentum scale associated with the total condensate density $\rho^{(0)} = \sum_a \rho_a^{(0)}$.

Plugging the relation stated in Eq. (3.13) into Eq. (3.9) and expanding the Bogoliubov dispersion relation at low momenta yields

$$\frac{\delta\rho_a(\mathbf{k})}{\rho^{(0)}} \sim \frac{|\mathbf{k}|}{k_\Xi}\theta_a(\mathbf{k}) \ll \theta_a(\mathbf{k}) \qquad \text{for} \quad k \ll k_\Xi\,. \tag{3.14}$$

Hence, density fluctuations are suppressed in the regime of low momenta as compared to phase fluctuations, which we identify as the relevant low-energy degree of freedom of the model.

Integrating out the suppressed density fluctuations $\delta\rho_a$ at quadratic order of the expansion of the Lagrangian in Eq. (3.5), we arrive at the low-energy effective action $S_{\text{eff}} = S_{\text{eff,G}} + S^{(3)}_{\text{eff,nG}} + S^{(4)}_{\text{eff,nG}}$, with Gaussian (quadratic) as well as three- and four-wave interaction parts

$$\begin{aligned} S_{\text{eff,G}}[\theta] = \int_{\mathbf{k}} \frac{1}{2}\Bigg\{ & \frac{1}{g_{\text{G}}(\mathbf{k})}\left(\delta^{ab} - \frac{k_{\Xi,a}k_{\Xi,b}/k_\Xi^2}{1+\mathbf{k}^2/2k_\Xi^2}\right)\partial_t\theta_a(\mathbf{k},t)\partial_t\theta_b(-\mathbf{k},t) \\ & - \frac{\rho^{(0)}\mathbf{k}^2}{M}\theta_a(\mathbf{k},t)\theta_a(-\mathbf{k},t)\Bigg\}, \end{aligned} \tag{3.15}$$

$$\begin{aligned} S^{(3)}_{\text{eff,nG}}[\theta] = \int_{\mathbf{k}\mathbf{k}'} & \frac{1}{N^{1/2}}\frac{1}{g_{\text{G}}(\mathbf{k})}\left(\delta^{ab} - \frac{k_{\Xi,a}k_{\Xi,b}/k_\Xi^2}{1+\mathbf{k}^2/2k_\Xi^2}\right)\frac{k_\Xi}{k_{\Xi,b}}\frac{\mathbf{k}'(\mathbf{k}'-\mathbf{k})}{2M} \\ & \times \partial_t\theta_a(-\mathbf{k},t)\theta_b(\mathbf{k}',t)\theta_b(\mathbf{k}-\mathbf{k}',t)\,, \end{aligned} \tag{3.16}$$

$$\begin{aligned} S^{(4)}_{\text{eff,nG}}[\theta] = \int_{\mathbf{k}\mathbf{k}'\mathbf{k}''} & \frac{1}{2N}\frac{1}{g_{\text{G}}(\mathbf{k})}\left(\frac{\delta^{ab}k_\Xi^2}{k_{\Xi,a}^2} - \frac{1}{1+\mathbf{k}^2/2k_\Xi^2}\right)\frac{\mathbf{k}'(\mathbf{k}'+\mathbf{k})}{2M}\frac{\mathbf{k}''(\mathbf{k}''-\mathbf{k})}{2M} \\ & \times \theta_a(\mathbf{k}',t)\theta_a(-\mathbf{k}-\mathbf{k}',t)\theta_b(\mathbf{k}'',t)\theta_b(\mathbf{k}-\mathbf{k}'',t)\,. \end{aligned} \tag{3.17}$$

Here, $\int_{\mathbf{k}} \equiv \int \mathrm{d}^d k/(2\pi)^d$, and $k_{\Xi,a} = [2M\rho_a^{(0)}g]^{1/2}$ is a momentum scale taking the form of the inverse healing length of a single component.

We find that the Gaussian part has Luttinger-liquid form [128], with momentum-dependent coupling function $g_{\text{G}}(\mathbf{k}) = Ng\mathbf{k}^2/(2k_\Xi^2)$. Note that the interaction terms in Eq. (3.16) and Eq. (3.17) result from a basic three vertex between two phase-angle fields and one $\delta\rho_a$, arising in the expansion of the quadratic kinetic term in the model in Eq. (3.3), while the cubic and quartic terms in the density fluctuations arising from the original non-linear term are being neglected. We emphasize that the above stated effective action allows us to predict scaling exponents for any finite $N \geq 1$.

For simplicity, we consider the large-N limit where we obtain [61]

$$
\begin{aligned}
S_{\text{eff}}[\theta] = &\int_{\mathbf{k}} \frac{1}{2g_{\text{G}}(\mathbf{k})}\,\theta_a(\mathbf{k},t)\,\left(-\partial_t^2-(\mathbf{k}^2/2M)^2\right)\theta_a(-\mathbf{k},t)\\
&-\int_{\{\mathbf{k}_i\}}\frac{k_{\Xi,a}^2}{k_\Xi^2}\frac{N\mathbf{k}_1\cdot\mathbf{k}_2}{2M\,g_{\text{G}}(\mathbf{k}_3)}\,\theta_a(\mathbf{k}_1,t)\,\theta_a(\mathbf{k}_2,t)\,\partial_t\theta_a(\mathbf{k}_3,t)\,\delta\Big(\sum_{i=1}^{3}\mathbf{k}_i\Big)\\
&+\int_{\{\mathbf{k}_i\}}\frac{k_{\Xi,a}^2}{k_\Xi^2}\frac{N(\mathbf{k}_1\cdot\mathbf{k}_2)\,(\mathbf{k}_3\cdot\mathbf{k}_4)}{8M^2\,g_{\text{G}}(\mathbf{k}_1-\mathbf{k}_2)}\,\theta_a(\mathbf{k}_1,t)\cdots\theta_a(\mathbf{k}_4,t)\,\delta\Big(\sum_{i=1}^{4}\mathbf{k}_i\Big)\,. \qquad (3.18)
\end{aligned}
$$

Here, $\int_{\{\mathbf{k}_i\}}$ denotes an integral over all momenta $\mathbf{k}_i$ with $i\in\{1,2,3\}$ for the three-wave interaction part and $i\in\{1,2,3,4\}$ for the four-wave interaction part, respectively. The low-energy effective action contains interaction terms with momentum-dependent couplings showing that the resulting theory is non-local in nature, as expected for such type of effective descriptions [61]. Note that the index G of the coupling refers to the relevant Goldstone excitations in the large-N limit.

We stress that the derivation of the low-energy effective field theory naturally covers the non-perturbative scattering regime due to the momentum-depending coupling $g_{\text{G}}(\mathbf{k})$ which remarkably coincides with the universal coupling obtained in the non-perturbative resummation within the 2PI formalism [56]. Moreover, taking the large-N limit, the effective action becomes diagonal in component space to leading order in $1/N$ and thus breaks up into N independent replicas. This means that the phases θ_a of the different components decouple in the limit of large N.

The three- and four-wave interaction parts of the effective action in Eq. (3.18) define the interactions between the phase excitations and will be used later to describe the scaling behavior of the time-evolving correlation functions at the non-thermal fixed point within a kinetic theory approach.

3.1.3. Observables

To make analytical predictions for the scaling exponents within a kinetic theory approach, we analyze the scaling behavior of the two-point correlator of the phase-excitation quasiparticles given by

$$f_a(\mathbf{k},t)=\langle\theta_a(\mathbf{k},t)\theta_a(-\mathbf{k},t)\rangle\,. \qquad (3.19)$$

To numerically study the universal scaling dynamics of the $U(3)$-symmetric model, we make use of two different correlation functions motivated by the capabilities of experimental settings, where one does not have direct access to the phase correlator of the fundamental Bose fields stated in Eq. (3.19).

A general choice for such models are the occupation number distributions of the components in momentum space given by

$$n_a(\mathbf{k},t)=\langle|\psi_a(\mathbf{k},t)|^2\rangle\,, \qquad (3.20)$$

with $\langle\dots\rangle$ denoting the average over different runs of the numerical simulation which will become clear from the discussion in Sect. 3.3. However, as Goldstone excitations

associated with the relative-phase degree of freedom become dominant in the large-N limit, we expect the scaling behavior to be predominantly seen in observables that contain information about relative phases. Such information is absent in the occupation number distribution. Therefore, we additionally study the momentum-space correlator

$$C_{ab}(\mathbf{k}, t) = \langle |(\psi_a^\dagger \psi_b)(\mathbf{k}, t)|^2 \rangle \tag{3.21}$$

measuring the spatial fluctuations of the relative phases $\theta_a - \theta_b$ between different components a and b. We stress that such a correlator is accessible in experiments as it measures coherences between different Bose fields.

To extract prescaling from the numerical data, we study two types of position-space correlators, namely the first- and second-order spatial coherence function. The first-order coherence function

$$g_a^{(1)}(\mathbf{r}, t) = \langle \psi_a^\dagger(\mathbf{x} + \mathbf{r}, t)\, \psi_a(\mathbf{x}, t) \rangle \tag{3.22}$$

is obtained as the Fourier transform of the occupation number $n_a(\mathbf{k}, t)$. As the first-order coherence function is insensitive to the relative phases, which are expected to become more and more relevant in the system as we increase the number of components N, we additionally study the second-order coherence function

$$g_{ab}^{(2)}(\mathbf{r}, t) = \langle \psi_a^\dagger(\mathbf{x} + \mathbf{r}, t)\, \psi_b(\mathbf{x} + \mathbf{r}, t)\, \psi_b^\dagger(\mathbf{x}, t)\, \psi_a(\mathbf{x}, t) \rangle \,. \tag{3.23}$$

Note that this observable is a four-point correlation function in the fundamental Bose fields ψ_a and results from a Fourier transform of $C_{ab}(\mathbf{k}, t)$.

Due to the isotropy of the numerical system, we compute angle-averaged correlation functions in $d = 3$ dimensions such that the correlators solely depend on the radial momentum $k = |\mathbf{k}|$ or distance $r = |\mathbf{r}|$, respectively.

3.2. Spin-1 Bose gas

In this section, we focus on spin-1 Bose gases and discuss the basic properties of this type of multi-component system. We start by introducing the Hamiltonian and the equations of motion that govern the time evolution of the system in Sect. 3.2.1. As compared to the $U(N)$-symmetric case, the spin-1 model contains interactions that break the $U(N)$-symmetry. Due to these interactions, the spin-1 system features different phases that are characterized by means of the respective energetically favored spin configuration. The presence of such phases offers the possibility to generate far-from-equilibrium configurations by means of instabilities arising from parameter quenches between different phases. To set the stage for a thorough discussion of potential parameter quenches and to highlight the rich spin physics of the spin-1 model, we review the mean-field phase diagram of the spin-1 Bose gas in Sect. 3.2.2. This further allows us to motivate and identify in Sect. 3.2.3 all those observables, which we will use to study universal scaling dynamics in spin-1 Bose gases.

3.2.1. The model

A d-dimensional spin-1 Bose gas with atomic mass M is described by the Hamiltonian [99]

$$H = \int \mathrm{d}\mathbf{x} \left[\boldsymbol{\psi}^\dagger \left(-\frac{\hbar^2}{2M}\nabla^2 + V(\mathbf{x}) + q f_z^2 \right) \boldsymbol{\psi} + \frac{c_0}{2}\rho^2 + \frac{c_1}{2}|\mathbf{F}|^2 \right] , \tag{3.24}$$

where $\boldsymbol{\psi} = (\psi_1, \psi_0, \psi_{-1})^T$ is a three-component bosonic spinor field whose components account for the magnetic sublevels $m_F = 0, \pm 1$ of the $F = 1$ hyperfine manifold. Note that we suppress space-time arguments of the fields to shorten the notation. The parameter q is the quadratic Zeeman energy shift which is proportional to an external magnetic field along the z-direction. It leads to an effective detuning of the $m_F = \pm 1$ components with respect to the $m_F = 0$ component. We are working in a frame where a homogeneous linear Zeeman shift has been absorbed into the definition of the fields.

Spin-independent contact interactions are described by the term $c_0\rho^2$, where $\rho = \boldsymbol{\psi}^\dagger\boldsymbol{\psi} \equiv \sum_m \psi_m^\dagger \psi_m$ is the total density. Spin-dependent interactions are characterized by the term $c_1|\mathbf{F}|^2$, where $\mathbf{F} = \boldsymbol{\psi}^\dagger \mathbf{f} \boldsymbol{\psi}$ is the spin density and $\mathbf{f} = (f_x, f_y, f_z)$ is a vector that contains the spin-1 matrices in the fundamental representation

$$f_x = \frac{1}{\sqrt{2}}\begin{pmatrix} 0 & 1 & 0 \\ 1 & 0 & 1 \\ 0 & 1 & 0 \end{pmatrix}, \quad f_y = \frac{i}{\sqrt{2}}\begin{pmatrix} 0 & -1 & 0 \\ 1 & 0 & -1 \\ 0 & 1 & 0 \end{pmatrix}, \quad f_z = \begin{pmatrix} 1 & 0 & 0 \\ 0 & 0 & 0 \\ 0 & 0 & -1 \end{pmatrix}. \tag{3.25}$$

The spin-dependent term accounts, among others, for the redistribution of atoms between the three hyperfine levels via spin-changing collisions [99]. In $d = 3$ dimensions, the coupling constants c_0 and c_1 are given by

$$c_0 = \frac{4\pi\hbar^2 (a_0 + 2a_2)}{3M}, \quad c_1 = \frac{4\pi\hbar^2 (a_2 - a_0)}{3M}, \tag{3.26}$$

with the s-wave scattering lengths a_0 and a_2 of the symmetric spin channels with total spin 0 and 2.

The spin interaction term and the quadratic Zeeman energy shift break the $U(N)$ symmetry of the Hamiltonian. Both contributions can be viewed as competing energy scales whose quantitative relation favors different spin configurations. This causes the spin-1 Bose gas to feature distinct phases within the two-dimensional plane spanned by the parameters c_1 and q. The presence of different phases allows for much richer dynamics as compared to $U(N)$-symmetric Bose gases and further offers the possibility to generate far-from-equilibrium configurations by means of parameter quenches between different phases. In case of $c_1 = q = 0$, Eq. (3.24) reduces to the $U(N)$-symmetric model stated in Eq. (3.1) with $N = 3$.

In experimental systems, the atoms are confined by means of an external trapping potential $V(\mathbf{x})$ which is typically harmonic. This causes the density of the condensed gas to become position-dependent as compared to the homogeneous case, $V(\mathbf{x}) = 0$, where the background density is constant.

The time evolution of the spin-1 system is given by the coupled Gross-Pitaevskii equations (GPEs)

$$i\hbar\partial_t\boldsymbol{\psi} = \left(-\frac{\hbar^2}{2M}\nabla^2 + V(\mathbf{x}) + q f_z^2 + c_0\rho + c_1 \mathbf{F}\cdot\mathbf{f} \right) \boldsymbol{\psi}. \tag{3.27}$$

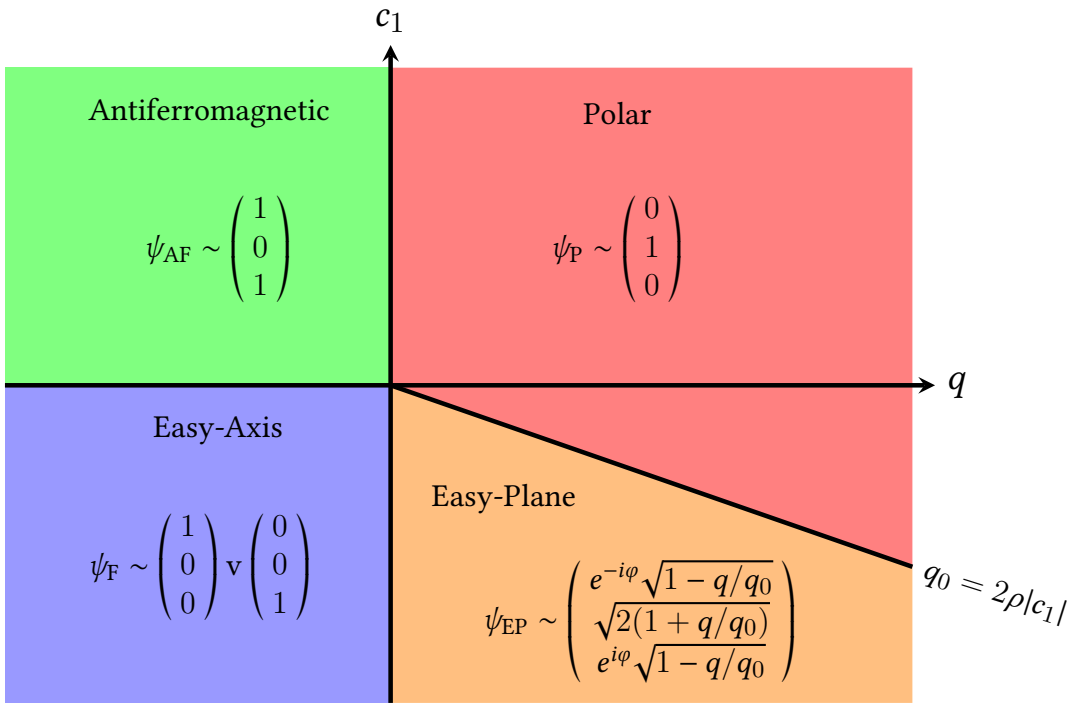

Figure 3.1.: Mean-field phase diagram of the spin-1 Bose gas in absence of a trapping potential ($V = 0$) for vanishing z-component of the magnetization (we are implicitly accounting here for the fact that the ground state in the easy-axis phase is degenerate). For $c_1 > 0$, we obtain two different phases. For $q > 0$, the system is in the polar phase whereas for $q < 0$, the system is in the antiferromagnetic phase. The phase transition occurs at $q = 0$. For $c_1 < 0$, three phases exist. In case of $q > 2\rho|c_1|$, the system is in the polar phase, for $0 < q < 2\rho|c_1|$, it is in the easy-plane phase and for $q < 0$, it is in the easy-axis phase. A quantum phase transition (QPT) occurs at $q = 2\rho|c_1|$. The phase transition between the easy-plane and easy-axis phase is at $q = 0$. Note that $q_0 = 2\rho|c_1|$ and ρ is the homogeneous total density. For details on the ground states see main text. Figure caption taken and adapted from Ref. [129].

3.2.2. Mean-field phase diagram

To enable universal scaling dynamics, it is essential to prepare the system in an extreme out-of-equilibrium initial configuration. As aforementioned, such a configuration can be generated in spin-1 Bose gases by means of instabilities arising from parameter quenches between the different phases of the model. To set the stage for a thorough discussion of this procedure, we briefly review the mean-field phase diagram of the homogeneous spin-1 Bose gas, see Ref. [130] for details.

For a mean-field description, we replace the bosonic field operators in Eq. (3.24) by complex functions resembling the respective field expectation values. The phase diagram is obtained by minimizing the mean-field energy functional of the spin-1 system in absence of a trapping potential within the (c_1, q)-plane. For each phase, we also elaborate on the associated mean-field ground state and potential properties of the order-parameter fields. A schematic plot of the phase diagram is shown in Fig. 3.1. This subsection is taken and adapted from Ref. [129].

(i) *polar phase* – For $c_1 > 0$, the spin interaction is antiferromagnetic. If $q > 0$ additionally, the system is in the polar phase. The ground state is unmagnetized and is given by the state vector

$$\psi_{\mathrm{P}} = e^{i\phi}\sqrt{\rho}\begin{pmatrix}0\\1\\0\end{pmatrix}. \tag{3.28}$$

Here, ρ is the homogeneous total density of the system and ϕ is a global phase distinguishing different realizations of the spontaneous symmetry breaking.

(ii) *antiferromagnetic phase* – If $q < 0$, but $c_1 > 0$, the system is in the antiferromagnetic phase. The ground state is again unmagnetized and its state vector reads

$$\psi_{\mathrm{AF}} = \sqrt{\rho}\begin{pmatrix}e^{i\phi_1}\\0\\e^{i\phi_{-1}}\end{pmatrix}. \tag{3.29}$$

Here, $\phi_{\pm1}$ are arbitrary phases of the $m_{\mathrm{F}} = \pm1$ components. The first-order phase transition separating the antiferromagnetic and polar phase is at $q = 0$.

(iii) *easy-axis phase* – For $c_1 < 0$, the spin interaction is ferromagnetic. If $q < 0$ additionally, the system is in the easy-axis ferromagnetic phase. The two degenerate ground states emerge by an explicit symmetry breaking in the $m_{\mathrm{F}} = \pm1$ components. This leads to a state which is either fully magnetized in $+z$ or $-z$ direction, i.e., $f_z = (\rho_1 - \rho_{-1})/\rho = \pm1$. The corresponding state vectors are given by

$$\psi_{\mathrm{F}} = e^{i\phi}\sqrt{\rho}\begin{pmatrix}1\\0\\0\end{pmatrix} \quad \text{or} \quad \psi_{\mathrm{F}} = e^{i\phi}\sqrt{\rho}\begin{pmatrix}0\\0\\1\end{pmatrix}. \tag{3.30}$$

At $q = 0$, a first-order phase transition occurs in the system.

(iv) *easy-plane phase* – For $c_1 < 0$ and $0 < q < q_0$, with $q_0 = 2\rho|c_1|$, the system is in the easy-plane ferromagnetic phase in which the mean-field ground state reads

$$\psi_{\mathrm{EP}} = \sqrt{\rho}\frac{e^{i\phi}}{2}\begin{pmatrix}e^{-i\varphi}\sqrt{1-q/q_0}\\\sqrt{2(1+q/q_0)}\\e^{i\varphi}\sqrt{1-q/q_0}\end{pmatrix}, \tag{3.31}$$

where φ denotes the angle with respect to the spin-x-axis. The complex order-parameter field in the easy-plane phase is the transversal spin

$$F_\perp = F_x + iF_y = \sqrt{2}\left(\psi_0^*\psi_1 + \psi_{-1}^*\psi_0\right). \tag{3.32}$$

The ground state gives rise to the mean spin vector lying in the transversal spin plane, with magnetization $|f_\perp| = |F_\perp|/\rho = [1-(q/q_0)^2]^{1/2}$. At $q = q_0$, the system exhibits a quantum phase transition (QPT) that breaks the full spin symmetry of the ground state. For $q > q_0$, the system is again in the polar phase with the unmagnetized ground state given by Eq. (3.28).

3.2.3. Observables

While we discuss the generation of far-from-equilibrium states via quenches for all types of spin interactions, we subsequently solely consider universal scaling dynamics in fer-

romagnetic ($c_1 < 0$) spin-1 Bose gases. We investigate the scaling behavior of the system after a parameter quench into the easy-plane ferromagnetic phase. We take the transversal spin $F_\perp$, as defined in Eq. (3.32), as our main observable to study the spatio-temporal scaling evolution of the spin-1 model.

In order to get a qualitative impression of the non-equilibrium dynamics, we show single realizations of the transversal spin. Potential non-linear and (quasi)topological excitations are most easily identified when going into the amplitude-phase representation of the complex order-parameter field. Therefore, we write $F_\perp = |F_\perp| e^{i\theta_{F_\perp}}$ and depict both amplitude and phase separately. However, in order to distinguish different types of spin vortices in the two-dimensional setting, we additionally make use of single realizations of the fundamental fields $\psi_{m_\mathrm{F}} = |\psi_{m_\mathrm{F}}| e^{i\theta_{m_\mathrm{F}}}$ of the different m_F-components. While different types of spin vortices look the same in the transversal spin degree of freedom, they are composed of a different structure of topological excitations in the three m_F-components, see Chpt. 6 for details.

For a quantitative analysis of the universal scaling dynamics, we consider averaged correlations of the transversal spin. Since our system is translationally invariant, we evaluate these correlations in momentum space by means of the structure factor

$$S(\mathbf{k}, t) = \langle |F_\perp(\mathbf{k}, t)|^2 \rangle \,, \tag{3.33}$$

with $\langle \dots \rangle$ denoting the average over different runs of the numerical simulation which will become clear from the discussion in Sect. 3.3. Note that due to the isotropy of the numerical system, we compute angle-averaged correlation functions in $d > 1$ dimensions such that the correlators solely depend on the radial momentum $k = |\mathbf{k}|$.

Within the scaling regime, the structure factor obeys the scaling form

$$S(\mathbf{k}, t) = (t/t_\mathrm{ref})^\alpha \, f_\mathrm{s}\left([t/t_\mathrm{ref}]^{\,\beta} \, \mathbf{k} \right) \,, \tag{3.34}$$

where f_s is a universal scaling function depending on a single variable only. The corresponding scaling exponents α and β define the evolution of the single characteristic length $L(t) \sim t^{\,\beta}$. The time scale t_ref denotes some reference time within the temporal scaling regime.

If the scaling behavior is caused by the mutual annihilation of topological excitations, a common phenomenon in two-dimensional systems, universality of the process is generally encoded in the decay laws of these excitations. In that case, the decaying number of topological excitations is inversely proportional to the power-law growth of the characteristic length $L(t)$ which can be associated with the effective mean distance between such excitations. Thus, we can deduce the universal scaling exponent β by extracting the power-law decay of the mean number of topological excitations as a function of the evolution time, see Chpt. 6 for details.

3.3. Numerical methods

As we are interested in the non-equilibrium dynamics of the $U(3)$-symmetric and spin-1 Bose gas within a regime of strongly occupied modes, we compute the time evolution by means of semi-classical simulation methods.

In presence of strong mode occupations, it has been shown that the dynamical evolution is well described by classical fields [85–87, 131]. Replacing the bosonic field opera-

tors in the GPEs in Eq. (3.1) and (3.27) by classical complex fields results in the respective classical equations of motion. Solving these equations for a fixed initial configuration leads to a mean-field description of the time evolution.

Making use of the semi-classical truncated Wigner approximation allows us to compute the time evolution beyond mean-field level as we include quantum statistical fluctuations in the initial field configurations, which are then evolved according to the classical equations of motion. Observables, such as correlation functions, are obtained by averaging over many trajectories of the numerical simulation. For details on the truncated Wigner approximation see Refs. [86, 87].

At this point, it is worthwhile to mention that the GPEs particularly provide an adequate description of the dynamics of dilute gases [110]. Recall that the Bose gas is called dilute when its inter-particle distance, set by the mean density in the numerical simulation, is much larger than the respective s-wave scattering length characterizing the contact interactions. This condition has to be ensured by an appropriate choice of the numerical density and the interaction parameter.

We numerically solve the equations of motion for both, the $U(3)$-symmetric and spin-1 Bose gas, by means of a spectral split-step algorithm. The method is based on treating the term involving the second-order derivative separately from the other terms in the equations of motion within each discrete numerical time step. While the derivative term becomes diagonal and thus simple to evaluate in momentum space, the other terms are treated in real space. Hence, the split-step algorithm involves a number of Fourier transformations. We can speed up the computations significantly by performing parallelized discrete fast Fourier transforms on graphical processing units (GPUs). While the nonlinearity in the $U(N)$-symmetric model is straightforwardly evaluated when solving the coupled GPEs in Eq. (3.1), one needs a more refined treatment for the spin-interaction part in Eq. (3.27) when dealing with the spin-1 model. For details and different implemented versions of the split-step algorithm for the spin-1 model see Refs. [132–134].

We remark that in order to solve the equations of motion numerically, we have to discretize space on a lattice with a given number of grid points in each of the dimensions. This means that quantities like time, length or densities are measured in units of the numerical grid spacing. Afterwards we can assign a physical length to the grid spacing which then defines the physical system that corresponds to our numerical simulation. In many cases, one simply goes the opposite way, i.e., we take a given physical system and adjust the grid spacing in a way that we are able to resolve all characteristic scales of the system in our numerics. Keeping that in mind, it is obvious that we do not have to start our computation with the dimensionful coupled GPEs, as stated in Eq. (3.1) and (3.27), but we can consistently rescale the GPEs to rewrite the equations in the task-related most convenient form.

Throughout this thesis, we use different rescaled versions of the spin-1 GPEs stated in Eq. (3.27). For example, it can be useful to rescale the equations in a way that only the ratio between the density and spin coupling remains in the equations of motion. This is particularly relevant in cases where we want to directly study the influence of the coupling ratio onto the properties of the system. No matter which type of rescaling is chosen, one can always transform all quantities back to physical units which allows for a direct comparison of all numerical results. In order to avoid potential confusion, we will clearly state how time, length and densities are measured in the respective numerically studied spin-1 systems in Chpts. 4–6.

3.4. Hydrodynamic formulation

Apart from using a description by means of Gross-Pitaevskii theory, the physics of ultracold Bose gases can be equivalently captured in a hydrodynamical formulation, where the equations are expressed in terms of macroscopic observable physical quantities such as densities and mass currents. Making use of such a formulation allows decomposing the kinetic energy density of the system into different hydrodynamic contributions.

In particular, we are able to separate contributions to the flow field arising from compressible and incompressible excitations populating the system. While the compressible part is determined by sound-like collective excitations, the incompressible part contains information about the topological excitations. Note that the incompressible contribution to the flow field is only present in $d > 1$ spatial dimensions. The decomposition of the kinetic energy density provides information about the dominating type of excitation at a non-thermal fixed point and furthermore gives insights into the power-law behavior of the universal scaling function characterizing the fixed point distribution.

In this section, we present a brief definition of the hydrodynamic decomposition of the spin-1 Bose gas in $d > 1$ spatial dimensions. The derivation of the decomposition is analogous for the $U(3)$-symmetric model. For details of the decomposition see also Refs. [61, 135]. This section is taken and adapted from Ref. [109].

For simplicity of the expressions, we use units of $\hbar = 1$. In a hydrodynamic formulation [135], the spin-1 system is described by the total density ρ, the spin vector f_μ and the nematic tensor $n_{\mu\nu}$,

$$\rho = \sum_m \psi_m^\dagger \psi_m \tag{3.35}$$

$$f_\mu = \frac{1}{\rho} \sum_{m,m'} \psi_m^\dagger \left(\mathrm{f}_\mu\right)_{mm'} \psi_{m'} , \tag{3.36}$$

$$n_{\mu\nu} = \frac{1}{\rho} \sum_{m,m'} \psi_m^\dagger \left(\mathrm{n}_{\mu\nu}\right)_{mm'} \psi_{m'} , \tag{3.37}$$

$\mu = x, y, z$, with f_μ being the spin-1 matrices in the fundamental representation, and the nematic or quadrupole tensor representation $\mathrm{n}_{\mu\nu} = (\mathrm{f}_\mu \mathrm{f}_\nu + \mathrm{f}_\nu \mathrm{f}_\mu)/2$. The superfluid velocity field $\mathbf{v}$ is then given by

$$\mathbf{v} = \frac{-i}{2M\rho} \sum_m \left[\psi_m^\dagger \left(\nabla \psi_m\right) - \left(\nabla \psi_m^\dagger\right) \psi_m\right] . \tag{3.38}$$

For expressing the hydrodynamic energy, it is useful to define the generalized velocities corresponding to the quantum-pressure (q), the spin (s), the nematic (n), the incompressible (i) and compressible (c) parts,

$$\begin{aligned} \mathbf{w}^{(q)} &= M^{-1} \nabla \sqrt{\rho} , & \mathbf{w}^{(i,c)} &= \sqrt{\rho}\, \mathbf{v}^{(i,c)} , \\ \mathbf{w}_\mu^{(s)} &= (2M)^{-1} \sqrt{\rho}\, \nabla f_\mu , & \mathbf{w}_{\mu\nu}^{(n)} &= (2M)^{-1} \sqrt{2\rho}\, \nabla n_{\mu\nu} . \end{aligned} \tag{3.39}$$

Here, $\mathbf{v}^{(i,c)}$ are obtained by a Helmholtz decomposition of the velocity field $\mathbf{v} = \mathbf{v}^{(i)} + \mathbf{v}^{(c)}$, with the incompressible part having a vanishing divergence, $\nabla \cdot \mathbf{v}^{(i)} = 0$, and the compressible part a vanishing curl, $\nabla \times \mathbf{v}^{(c)} = 0$.

Using the hydrodynamic variables, we can express the energy as

$$E = E_{\text{kin}} + \int d\mathbf{x} \left[\frac{c_0}{2}\rho^2 + \frac{c_1}{2}\rho^2 f_\mu^2 + q\rho n_{zz} \right] . \tag{3.40}$$

In the $U(3)$-symmetric model, the last two terms are absent as $c_1 = q = 0$ in this case. However, as we are interested in the decomposition of the kinetic part of the energy, E_{kin}, the following treatment is equivalent for the spin-1 and $U(3)$-symmetric Bose gas. For both types of systems the kinetic part reads

$$\begin{aligned} E_{\text{kin}} =& \frac{1}{2M} \int d\mathbf{x} \left[(\nabla\sqrt{\rho})^2 + \frac{\rho}{4} \left(\nabla f_\mu \right)^2 + \frac{\rho}{2} \left(\nabla n_{\mu\nu} \right)^2 \right] \\ &+ \frac{M}{2} \int d\mathbf{x}\, \rho \mathbf{v}^2 . \end{aligned} \tag{3.41}$$

Hence, in Fourier space, the kinetic-energy spectrum is given by the correlation functions of the generalized velocities

$$\varepsilon_{\text{kin}}(k) = \varepsilon^{(q)}(k) + \varepsilon^{(c)}(k) + \varepsilon^{(i)}(k) + \varepsilon^{(s)}(k) + \varepsilon^{(n)}(k) , \tag{3.42}$$

averaged over the orientation of the momentum vector,

$$\varepsilon^{(\delta)}(k) = \frac{M}{2} \int d\Omega_{\mathbf{k}} \langle |\mathbf{w}^{(\delta)}(\mathbf{k})|^2 \rangle , \quad (\delta = q, i, c) \tag{3.43}$$

$$\varepsilon^{(s)}(k) = \frac{M}{2} \int d\Omega_{\mathbf{k}} \langle \mathbf{w}_\mu^{(s)}(\mathbf{k}) \cdot \mathbf{w}_\mu^{(s)}(\mathbf{k}) \rangle , \tag{3.44}$$

$$\varepsilon^{(n)}(k) = \frac{M}{2} \int d\Omega_{\mathbf{k}} \langle \mathbf{w}_{\mu\nu}^{(n)}(\mathbf{k}) \cdot \mathbf{w}_{\mu\nu}^{(n)}(\mathbf{k}) \rangle , \tag{3.45}$$

where Einstein's sum convention is implied. The respective total energies are obtained as $E^{(\delta)} = \int d\mathbf{x} \int dk\, k^{d-1}\, \varepsilon^{(\delta)}(k)$. The spectrum of the kinetic energy can then be used to calculate corresponding occupation numbers using the relation

$$n^{(\delta)}(k) = 2M\, k^{-2} \varepsilon^{(\delta)}(k) , \tag{3.46}$$

where $\delta = q, i, c, s, n$. The total occupation number, which is the sum of the occupation numbers of the different components, is then approximately given by

$$n_{\text{tot}}(k) \approx \sum_\delta n^{(\delta)}(k) = 2M\, k^{-2} \varepsilon_{\text{kin}}(k) . \tag{3.47}$$

We remark that the total occupation number n_{tot} and $2M\, k^{-2} \varepsilon_{\text{kin}}(k)$ deviate from each other in the regime of infrared momenta below the inverse healing length scale due to additional contributions from four-point correlations of the fundamental fields contributing to the kinetic energy density, see the discussion in the Appendix of Ref. [40].

Part II.

Non-thermal fixed points dominated by topological excitations

In the first part of this thesis, we set the basis for discussing universal scaling dynamics at non-thermal fixed points in multi-component Bose gases far from equilibrium. In the remainder, we present two classes of fixed points where the scaling behavior is caused by different excitations of the investigated systems. In this part, we consider universal scaling dynamics which is dominated by topological excitations whereas we focus on non-thermal fixed point scaling dominated by collective excitations in the final part of the thesis.

To illustrate universal scaling dominated by topological excitations, we investigate the non-equilibrium dynamics of spin-1 Bose gases. In Chpt. 4, we elaborate on the generation of out-of-equilibrium configurations in spin-1 systems by means of parameter quenches. Such configurations are a key feature to enable spatio-temporal scaling of correlations in the subsequent dynamical evolution of the system. We then present numerical results showing bidirectional universal scaling in a one-dimensional spin-1 Bose gas driven by quasi-topological excitations such as spin textures and kink-like defects in Chpt. 5. We finally discuss universal scaling involving the growth of two macroscopic length scales determined by the mutual annihilation of two types of spin vortices in a two-dimensional spin-1 Bose gas in Chpt. 6.

In order to embed our numerical studies into the broader research context, we briefly review previous work on universal scaling dynamics dominated by topological excitations. We focus on scaling phenomena reported in single-component and spin-1 Bose gases which set the appropriate framework for the numerical studies in the remainder of this part.

Universal ordering processes characterized by the underlying dynamics of (quasi)topological excitations were commonly discussed in dissipative systems, where they are referred to as coarsening or phase ordering dynamics [69, 136–142]. Coarsening is a specific type of universal scaling evolution, generically associated with the phase-ordering kinetics of a system coupled to a temperature bath, and exhibiting an ordering phase transition [69]. Typically, the coarsening evolution following a quench into the ordered phase only involves a single characteristic length which fixes the scale of the correlations and evolves as a power law in time. Such a growing length scale can be associated with, e.g., the coarsening of magnetic domains in the ordered phase. The associated scaling exponents are determined by the underlying dynamics of the topological excitations and potential conservation laws [69]. As already mentioned in Sect. 2.1, the concept of non-thermal fixed points generalizes such universal scaling dynamics to isolated systems far from equilibrium.

There are numerous experimental and numerical works that study universal scaling dynamics at non-thermal fixed points where the scaling behavior is governed by the dynamics of topological excitations. First investigations were made by numerical simulations of single-component Bose gases in two and three spatial dimensions [39, 40, 42]. In these cases, the non-thermal fixed point was identified by a steep infrared momentum-space power-law distribution of the particle number distribution. Performing a hydrodynamic decomposition of the flow field further revealed the dominant role of topological excitations in such systems. By changing the out-of-equilibrium initial configuration of the system, it was possible to either make the system approach a non-thermal fixed point during its subsequent time evolution or directly equilibrate [40]. Recent numerical studies of a single-component Bose gas in two spatial dimensions uncovered that a quantum many-body system can be attracted to multiple non-thermal fixed points with different scaling exponents [45]. It was shown that the initial arrangement and quan-

tization of vortices can lead to two distinct types of universal scaling behavior. If the configuration was chosen in a way that the vortices tend to cluster during the time evolution, slowed scaling with exponent $\beta \simeq 1/5$ was extracted from the numerical data as compared to the case of free vortices characterized by $\beta \simeq 1/2$. The observed strongly slowed scaling can be interpreted as being due to mutual defect annihilation following three-vortex collisions and has recently been found consistent with experimental data [143–145]. The first experimental observation of universal scaling dynamics dominated by (quasi)topological excitations has been made in a one-dimensional single-component Bose gas [36]. In this case, the scaling evolution with exponent $\beta \simeq 1/10$ is governed by the redistribution of solitonic excitations that emerge from shock cooling of the atomic gas.

Within recent years, spin-1 Bose gases have become of particular research interest for universal scaling dynamics as they can be well-controlled in experiments. The rich phase diagram of the system further allows for a plethora of scaling phenomena. Motivated by experiments in two spatial dimensions, where domain coarsening of spin textures, without reference to universal scaling, has been observed in the long-time dynamics after a parameter quench [146], several numerical studies of two-dimensional spin-1 Bose gases have been carried out. Quenching the spin-1 system into the easy-plane ferromagnetic phase starting from a polar condensate, universal scaling dynamics was found to be characterized by the annihilation of spin vortices with unmagnetized core [104, 105]. In case of antiferromagnetic spin interactions, nematic ordering caused by half-quantum vortices could be extracted [107]. In all these works, only a single vortex type determined the universal scaling evolution of the system. The scaling reported in Chpt. 6 is very different in nature although it also results from the annihilation of spin vortices. However, due to the presence of two types of spin vortices with distinctly different decay laws, the system features the growth of two macroscopic length scales leading to a violation of single-length scaling. Such a multiple-faceted scaling behavior has later also been found in a one-dimensional spin-1 Bose gas with antiferromagnetic interactions [103]. Apart from this, unconventional universal scaling occurred in a one-dimensional spin-1 Bose-Hubbard model in the superfluid regime which is closely related to the spin-1 Bose gas [100]. In this case, the scaling results from merging of one-dimensional spin domains. In addition, studying the non-equilibrium time evolution of the spin-1 Bose-Hubbard model in one spatial dimension with antiferromagnetic spin interactions revealed universal scaling dynamics with scaling exponent $\beta \simeq 1/3$ [101]. In this case, the scaling of a single macroscopic scale is characterized by the pair annihilation of magnetic solitons by forming Flemish strings. In Chpt. 5, we report bidirectional universal scaling dynamics in a one-dimensional spin-1 Bose gas. In contrast to the cases mentioned above, the scaling is characterized by a growing macroscopic scale and a simultaneously decreasing microscopic scale. Such an evolution, prototypical for scaling dynamics at a non-thermal fixed point, is usually not observed in numerical simulations as the build-up of a thermal tail generally spoils the scaling behavior in the ultraviolet regime of momenta.

4. Generating far-from-equilibrium states via quenches

In order to approach a non-thermal fixed point during the time evolution, we have to prepare the system in an extreme out-of-equilibrium configuration. Such a configuration can be generated by means of a fast change of a Hamiltonian parameter of the system, which we refer to as a quench. We already discussed the example of a strong cooling quench, where one removes all atoms above a certain momentum scale to create the far-from-equilibrium initial state of the Bose gas (see Sect. 2.1).

In this chapter, we discuss potential scenarios that can be employed to generate far-from-equilibrium initial configurations in spin-1 Bose gases. Due to the rich phase diagram, spin-1 Bose gases offer the possibility to drive the system out of equilibrium by performing a sudden parameter quench across a phase transition. Such a protocol leads to instabilities that generate far-from-equilibrium configurations in a controlled fashion during the early-time dynamics of the system. Note that the short-time dynamics following quenches between different phases of the spin-1 model has also been investigated in experiments [97, 98].

Whether the system features an instability depends on the state of the system prior to the quench. Such pre-quench states are commonly chosen to be the ground states of a particular spin-1 phase as they are easily prepared in experimental settings. We infer the presence of an instability after a parameter quench between different phases from investigating the dynamical stability of the respective pre-quench state in the post-quench phase.

The stability properties can be studied by means of Bogoliubov theory which has been carried out in detail for homogeneous spin-1 systems in Ref. [130]. As we later make use of instabilities to generate far-from-equilibrium states in one- and two-dimensional homogeneous spin-1 Bose gases, which set the stage for the subsequent universal scaling dynamics, we briefly review the results obtained from Bogoliubov theory in the homogeneous spin-1 system in Sect. 4.1.

However, far less is known about what happens in the presence, e.g., of an external trap, as it is commonly the case in experiments [110, 147]. Hence, a major part of this chapter is devoted to the investigation of the influence of a trapping potential onto the stability properties of the spin-1 Bose gas. In order to keep the numerical computations feasible, we consider spin-1 Bose gases in one spatial dimension. We start by refining the definition of the spin-1 model and by introducing a set of numerical units that is most suitable for the stability discussion in Sect. 4.2. In order to investigate the stability properties of the ground states in presence of a trapping potential, we first need to map out the corresponding mean-field phase diagram, which is presented in Sect. 4.3. To do so, we make use of a, so-called, continuous-time Nesterov method. We present an extension of the method, which has been previously applied to one-component systems, to our multi-component system in Sect. 4.3.2. Subsequently, we solve numerically the Bogoliubov de-Gennes equations in order to analyze the stability of the ground states of

the trapped spin-1 system in Sect. 4.4. Finally, we summarize the results and comment on potential future research in Sect. 4.5.

The content of this chapter is taken and adapted from Ref. [129]. I stress that most of the parts are taken verbatim from the publication. However, I rearranged the structure of the presentation. I further added and/or modified formulations to embed the work into the broader context of this thesis.

4.1. Bogoliubov excitations in a homogeneous spin-1 system

In the following, we give a brief summary of the Bogoliubov theory for the spin-1 ground states in absence of a trapping potential. The results are summarized in Table 4.1. A detailed analysis of the homogeneous theory can be found in Ref. [130].

To obtain the Bogoliubov excitation spectra, one first expands the Hamiltonian up to second order in small fluctuations about a particular mean-field state of the system which we take to be one of the spin-1 ground states as introduced in Sect. 3.2.2. This procedure then leads to the so-called Bogoliubov de-Gennes equations. Solving the eigenvalue problem one obtains the Bogoliubov excitation spectra which then enable us to determine the dynamical stability of the ground states in different phases. We outline this procedure for the trapped spin-1 system in detail in Sect. 4.4.

Whenever the mode energies of the determined Bogoliubov spectra become imaginary, a dynamical instability occurs as relevant momentum modes will grow exponentially in time. In that case, the growth rates of the unstable modes can be calculated from the excitation spectra (i.e., from the imaginary parts of the corresponding eigenfrequencies). We will use the Bogoliubov predictions made for the homogeneous system for a later comparison to numerical results obtained for the trapped system.

The following discussion refers to the mean-field phase diagram of the spin-1 system introduced in Sect. 3.2.2. For the numerical treatment in this chapter, we will use a unit system where we normalize the interactions of the model by the spin-independent coupling c_0 such that we replace the spin-dependent coupling c_1 by the coupling ratio $\delta = c_1/c_0$. For details on the unit system see Sect. 4.2. To avoid confusion between densities of the homogeneous and the trapped system, we denote the homogeneous total density by ρ_h throughout this chapter.

4.1.1. Excitations about the polar state

Diagonalizing the Bogoliubov Hamiltonian for a small perturbation about the polar state $\psi \sim (0,1,0)^T$ in a homogeneous spin-1 system, one obtains one phonon mode and two modes corresponding to excitations in the transverse spin direction.

The spectrum of the phonon mode is given by

$$E^\mathrm{P}_\mathrm{ph}(k) = \sqrt{\epsilon_k(\epsilon_k + 2\rho_\mathrm{h} c_0)}, \tag{4.1}$$

with mode energy $\epsilon_k = k^2/2$ and ρ_h being the homogeneous total density. This mode is stable irrespective of the parameters q and δ.

State	Energy spectrum	Stability properties in ...phase			
		AF	P	EA	EP
P	$E^{\mathrm{P}}_{\mathrm{ph}}(k)=\sqrt{\epsilon_k(\epsilon_k+2\rho_{\mathrm{h}}c_0)}$	S	S	S	S
	$E_{\mathrm{s}}(k)=\sqrt{(\epsilon_k+q)\,(\epsilon_k+q+2\rho_{\mathrm{h}}\delta)}$	U $\gamma_{\mathrm{s}}(\tilde{k})=\left\lvert\Im\left(\sqrt{q\,(q+2\rho_{\mathrm{h}}\delta)}\right)\right\rvert$ for $0<-q<\rho_{\mathrm{h}}\delta$ $\gamma_{\mathrm{s}}(\tilde{k})=\rho_{\mathrm{h}}\lvert\delta\rvert$ for $\rho_{\mathrm{h}}\delta\leq -q$	S	U $\gamma_{\mathrm{s}}(\tilde{k})=\rho_{\mathrm{h}}\lvert\delta\rvert$	U $\gamma_{\mathrm{s}}(\tilde{k})=\left\lvert\Im\left(\sqrt{q\,(q+2\rho_{\mathrm{h}}\delta)}\right)\right\rvert$ for $-\rho_{\mathrm{h}}\delta<q<-2\rho_{\mathrm{h}}\delta$ $\gamma_{\mathrm{s}}(\tilde{k})=\rho_{\mathrm{h}}\lvert\delta\rvert$ for $0\leq q\leq-\rho_{\mathrm{h}}\delta$
AF	$E^{\mathrm{AF}}_{\mathrm{ph}}(k)=\sqrt{\epsilon_k(\epsilon_k+2\rho_{\mathrm{h}}c_0)}$	S	S	S	S
	$E_{\mathrm{m}}(k)=\sqrt{\epsilon_k(\epsilon_k+2\rho_{\mathrm{h}}\delta)}$	S	S ($\delta>0$), U ($\delta<0$) $\gamma_{\mathrm{m}}(\tilde{k})=\rho_{\mathrm{h}}\lvert\delta\rvert$	U $\gamma_{\mathrm{m}}(\tilde{k})=\rho_{\mathrm{h}}\lvert\delta\rvert$	U $\gamma_{\mathrm{m}}(\tilde{k})=\rho_{\mathrm{h}}\lvert\delta\rvert$
	$E_{\mathrm{g}}(k)=\sqrt{(\epsilon_k-q)^2+2\rho_{\mathrm{h}}\delta\,(\epsilon_k-q)}$	S	U $\gamma_{\mathrm{g}}(\tilde{k})=\left\lvert\Im\left(\sqrt{q\,(q-2\rho_{\mathrm{h}}\delta)}\right)\right\rvert$ for $q<\rho_{\mathrm{h}}\delta$ and $\delta>0$ $\gamma_{\mathrm{g}}(\tilde{k})=\rho_{\mathrm{h}}\lvert\delta\rvert$ for $q\geq\rho_{\mathrm{h}}\delta$ and $\delta>0$	S ($q<2\rho_{\mathrm{h}}\delta$), U ($q>2\rho_{\mathrm{h}}\delta$) $\gamma_{\mathrm{g}}(\tilde{k})=\rho_{\mathrm{h}}\lvert\delta\rvert$ for $\rho_{\mathrm{h}}\delta<q<0$ $\gamma_{\mathrm{g}}(\tilde{k})=\left\lvert\Im\left(\sqrt{q\,(q-2\rho_{\mathrm{h}}\delta)}\right)\right\rvert$ for $2\rho_{\mathrm{h}}\delta<q\leq\rho_{\mathrm{h}}\delta$	U $\gamma_{\mathrm{g}}(\tilde{k})=\rho_{\mathrm{h}}\lvert\delta\rvert$
EP	$E_0=\sqrt{\epsilon_k\,(\epsilon_k+q)}$	U $\gamma_0(\tilde{k})=\lvert q\rvert/2$	S	U $\gamma_0(\tilde{k})=\lvert q\rvert/2$	S
EA	$E^{\mathrm{EA}}_{\mathrm{ph}}=\sqrt{\epsilon_k\left[\epsilon_k+2\,(1+\delta)\,\rho_{\mathrm{h}}\right]}$	S	S	S ($\delta\geq-1$), U ($\delta<-1$) $\gamma^{\mathrm{EA}}_{\mathrm{ph}}(\tilde{k})=\sqrt{3}\lvert(1+\delta)\rvert\,\rho_{\mathrm{h}}$	S ($\delta\geq-1$), U ($\delta<-1$) $\gamma^{\mathrm{EA}}_{\mathrm{ph}}(\tilde{k})=\sqrt{3}\lvert(1+\delta)\rvert\,\rho_{\mathrm{h}}$

Table 4.1.: Stability properties of the spin-1 ground states derived within homogeneous Bogoliubov theory. The abbreviations P, AF, EP, EA stand for polar, antiferromagnetic, easy-plane, and easy-axis. Stable regimes of the listed excitation spectra are marked with S, unstable regimes with U. In case of an instability, the maximal growth rate $\gamma(\tilde{k})$, with $\tilde{k}$ being the respective most unstable momentum mode, is stated. The instabilities used in Chpt. 5 and Chpt. 6 to generate far-from-equilibrium configurations which subsequently lead to universal scaling dynamics are highlighted in blue. Table taken and adapted from Ref. [129].

The spectrum of the transverse spin excitations reads

$$E_{\mathrm{s}}(k) = \sqrt{(\epsilon_k + q)\,(\epsilon_k + q + 2\rho_{\mathrm{h}}\delta)}. \tag{4.2}$$

This mode is dynamically unstable whenever the parameters q and δ are chosen in a way that the expression under the square root becomes negative.

(i) *antiferromagnetic phase* – In case of $q < 0$ and $\delta > 0$, i.e., in the antiferromagnetic phase, three different instability regimes exist. For $0 < -q < \rho_{\mathrm{h}}\delta$, momentum modes up to an ultraviolet (UV) cutoff $k_{\mathrm{UV}} = \sqrt{-2q}$ are unstable. The most unstable mode is $\tilde{k} = 0$ with growth rate

$$\gamma_{\mathrm{s}}\left(\tilde{k}\right) = \left|\Im\left(E_{\mathrm{s}}(0)\right)\right| = \left|\Im\left(\sqrt{q\,(q + 2\rho_{\mathrm{h}}\delta)}\right)\right|, \tag{4.3}$$

where the symbol $\Im$ denotes the imaginary part of a complex number. For $\rho_{\mathrm{h}}\delta \leq -q$, the most unstable mode is $\tilde{k} = \sqrt{-2(q + \rho_{\mathrm{h}}\delta)}$ with growth rate

$$\gamma_{\mathrm{s}}\left(\tilde{k}\right) = \rho_{\mathrm{h}}\,|\delta|\,. \tag{4.4}$$

In case of $2\rho_{\mathrm{h}}\delta < -q$, an additional infrared (IR) cutoff of the instability region occurs at $k_{\mathrm{IR}} = \sqrt{-(q + 2\rho_{\mathrm{h}}\delta)}$.

The same scenario as discussed above is present for $\delta < 0$.

(ii) *easy-plane phase* – For $0 < q < -2\rho_{\mathrm{h}}\delta$, i.e, in the easy-plane phase, the first two of the above stated instability regimes can be found. In case of $-\rho_{\mathrm{h}}\delta < q < -2\rho_{\mathrm{h}}\delta$, the most unstable mode is $\tilde{k} = 0$ with growth rate given by Eq. (4.3). For parameters $0 \leq q \leq -\rho_{\mathrm{h}}\delta$, the most unstable mode occurs at $\tilde{k} = \sqrt{-2(q + \rho_{\mathrm{h}}\delta)}$. The corresponding growth rate is stated in Eq. (4.4).

We make use of this instability in Chpt. 5 to generate a far-from equilibrium initial configuration in a one-dimensional homogeneous spin-1 Bose gas. The broad range of unstable momentum modes at $q \simeq \rho_{\mathrm{h}}\delta$ is well-suited to initialize bidirectional universal scaling dynamics of the non-equilibrium system.

(iii) *easy-axis phase* – Moving to $q < 0$, i.e., entering the easy-axis phase, the additional IR cutoff of the instability region occurs as mentioned above. The most unstable mode is $\tilde{k} = \sqrt{-2(q + \rho_{\mathrm{h}}\delta)}$ with growth rate given by Eq. (4.4).

4.1.2. Excitations about the antiferromagnetic state

Diagonalizing the Bogoliubov Hamiltonian for a small perturbation about the antiferromagnetic state $\psi \sim (1, 0, 1)^T$ in a homogeneous spin-1 system, one obtains one stable uncoupled phonon mode given by

$$E_{\mathrm{ph}}^{\mathrm{AF}}(k) = \sqrt{\epsilon_k(\epsilon_k + 2\rho_{\mathrm{h}}c_0)}. \tag{4.5}$$

In addition, an uncoupled magnon mode with spectrum

$$E_{\mathrm{m}}(k) = \sqrt{\epsilon_k(\epsilon_k + 2\rho_{\mathrm{h}}\delta)} \tag{4.6}$$

exists. The magnon mode exhibits unstable momentum modes up to a UV cutoff of $k_{\mathrm{UV}} = \sqrt{-4\rho_{\mathrm{h}}\delta}$ in case of $\delta < 0$. Irrespective of the parameter q, the most unstable

momentum mode is $\tilde{k} = \sqrt{-2\rho_{\mathrm{h}}\delta}$ with corresponding growth rate

$$\gamma_{\mathrm{m}}\left(\tilde{k}\right) = \rho_{\mathrm{h}}\left|\delta\right| . \tag{4.7}$$

Hence, one finds unstable modes showing the same maximal growth rate within the polar, easy-plane and easy-axis phase associated with ferromagnetic spin interactions.

Furthermore, a quadratic mode described by

$$E_{\mathrm{g}}(k) = \sqrt{\left(\epsilon_k - q\right)^2 + 2\rho_{\mathrm{h}}\delta\left(\epsilon_k - q\right)} \tag{4.8}$$

is present in the system.

(i) *polar phase* – For $\delta > 0$ and $q > 0$, i.e., in the polar phase for antiferromagnetic spin interactions, we find two different instability regimes. In case of $q < \rho_{\mathrm{h}}\delta$, the most unstable mode occurs at $\tilde{k} = 0$. Its growth rate reads

$$\gamma_{\mathrm{g}}\left(\tilde{k}\right) = \left|\Im\left(\sqrt{q\left(q - 2\rho_{\mathrm{h}}\delta\right)}\right)\right| . \tag{4.9}$$

The second regime emerges for $q \geq \rho_{\mathrm{h}}\delta$ where the most unstable mode becomes $\tilde{k} = \sqrt{2(q - \rho_{\mathrm{h}}\delta)}$. The growth rate is given by

$$\gamma_{\mathrm{g}}\left(\tilde{k}\right) = \rho_{\mathrm{h}}\left|\delta\right| . \tag{4.10}$$

For $\delta < 0$ and $q > -2\rho_{\mathrm{h}}\delta$, i.e., in the polar phase for ferromagnetic spin interactions, the quadratic mode is stable.

(ii) *easy-plane and easy-axis phase* – For $\delta < 0$ and $\rho_{\mathrm{h}}\delta < q < -2\rho_{\mathrm{h}}\delta$, i.e., in the easy-plane phase and parts of the easy-axis phase, the most unstable mode is $\tilde{k} = \sqrt{2(q - \rho_{\mathrm{h}}\delta)}$ with growth rate according to Eq. (4.10). A second instability regime occurs within the easy-axis phase for $2\rho_{\mathrm{h}}\delta < q \leq \rho_{\mathrm{h}}\delta$. Here, $\tilde{k} = 0$ is the most unstable mode with growth rate given by Eq. (4.9). For values $q < 2\rho_{\mathrm{h}}\delta$, the quadratic mode is dynamically stable.

We make use of this type of instability in the easy-plane phase in Chpt. 6 to generate a far-from-equilibrium initial configuration in a two-dimensional homogeneous spin-1 Bose gas. The subsequent universal scaling dynamics is much richer than simply using the respective instability arising from the expansion about the polar state due to the presence of multiple spin vortices.

4.1.3. Excitations about the easy-plane state

Diagonalizing the Bogoliubov Hamiltonian for a small perturbation about the easy-plane state $\psi \sim \left(\sqrt{1 - q/q_0}, \sqrt{2(1 + q/q_0)}, \sqrt{1 - q/q_0}\right)^T$ in a homogeneous spin-1 system, where $q_0 = -2\rho_{\mathrm{h}}\delta$, one obtains one gapless mode given by

$$E_0 = \sqrt{\epsilon_k\left(\epsilon_k + q\right)}. \tag{4.11}$$

This mode is dynamically unstable for $q < 0$ irrespective of the spin interaction δ. The most unstable mode is $\tilde{k} = \sqrt{-q}$ with growth rate

$$\gamma_0\left(\tilde{k}\right) = \frac{|q|}{2}. \tag{4.12}$$

We remark that, in addition to the above stated gapless mode, there are two further Bogoliubov modes that will not be discussed in this thesis.

4.1.4. Excitations about the easy-axis state

Diagonalizing the Bogoliubov Hamiltonian for a small perturbation about the easy-axis state $\psi \sim (1,0,0)^T$ or $\psi \sim (0,0,1)^T$ respectively in a homogeneous spin-1 system, one obtains two single-particle like modes which are stable. The system exhibits an additional phonon mode with spectrum

$$E_{\mathrm{ph}}^{\mathrm{EA}} = \sqrt{\epsilon_k \left[\epsilon_k + 2\left(1+\delta\right)\rho_{\mathrm{h}}\right]}. \tag{4.13}$$

This mode is dynamically unstable for $\delta < -1$.
The most unstable mode is $\tilde{k} = \sqrt{-2(1+\delta)\rho_{\mathrm{h}}}$ with growth rate given by

$$\gamma_{\mathrm{ph}}^{\mathrm{EA}}\left(\tilde{k}\right) = \sqrt{3}\,|(1+\delta)|\,\rho_{\mathrm{h}}. \tag{4.14}$$

As we are studying experimentally realistic parametric regimes in the following, the spin coupling $|\delta|$ is on the order of $\sim 10^{-2}$ so we expect to find no dynamically unstable modes for the easy-axis state irrespective of the parameter q and the sign of δ.

4.2. The one-dimensional trapped spin-1 Bose gas

Having summarized the key results obtained from Bogoliubov theory of the spin-1 Bose gas in absence of a trapping potential, we use the remainder of this chapter to investigate the stability properties in presence of a trapping potential as it is commonly the case in experimental systems.

In Sect. 3.2, we introduced the d-dimensional spin-1 Bose gas with arbitrary trapping potential $V(\mathbf{x})$. Here, we consider a one-dimensional (1D) spin-1 Bose gas in a highly anisotropic harmonic trap with longitudinal ($\omega_{\parallel}$) and transverse ($\omega_{\perp}$) trapping frequencies chosen such that $\omega_{\parallel} \ll \omega_{\perp}$. In that case, the wave functions can be separated into a longitudinal and transverse part. The transverse wave function is the ground state of the respective harmonic oscillator and can be integrated out to obtain the following system of coupled 1D mean-field equations for the longitudinal part of the wave function

$$i\hbar\partial_t\psi_{\pm1} = \mathcal{H}_0\psi_{\pm1} + \tilde{q}\psi_{\pm1} + c_1^{(1\mathrm{D})}\left(|\psi_{\pm1}|^2 + |\psi_0|^2 - |\psi_{\mp1}|^2\right)\psi_{\pm1} + c_1^{(1\mathrm{D})}\psi_0^2\psi_{\mp1}^*, \tag{4.15}$$

$$i\hbar\partial_t\psi_0 = \mathcal{H}_0\psi_0 + c_1^{(1\mathrm{D})}\left(|\psi_1|^2 + |\psi_{-1}|^2\right)\psi_0 + 2c_1^{(1\mathrm{D})}\psi_{-1}\psi_0^*\psi_1. \tag{4.16}$$

Here, $\psi_{\pm1}$ and ψ_0 are the classical complex bosonic spinor fields and the asterisk denotes the complex conjugate of the corresponding field. The spin-independent part of the Hamiltonian is given by

$$\mathcal{H}_0 = -[\hbar^2/(2M)]\partial_x^2 + (1/2)\,M\omega_{\parallel}^2x^2 + c_0\tilde{\rho}\,, \tag{4.17}$$

where $\tilde{\rho} = |\psi_1|^2 + |\psi_0|^2 + |\psi_{-1}|^2$ is the total density. The parameter $\tilde{q}$ denotes the quadratic

Zeeman energy shift and the effective 1D coupling constants read

$$c_0^{(1\mathrm{D})} = \frac{c_0}{2\pi a_\perp^2}, \qquad c_1^{(1\mathrm{D})} = \frac{c_1}{2\pi a_\perp^2}, \tag{4.18}$$

with $a_\perp = \sqrt{\hbar/(M\omega_\perp)}$ being the transverse harmonic oscillator length of the system. The coupling constants c_0 and c_1 are given by $c_0 = 4\pi\hbar^2 (a_0 + 2a_2)/(3M)$ and $c_1 = 4\pi\hbar^2 (a_2 - a_0)/(3M)$, with the s-wave scattering lengths a_0 and a_2, see Eq. (3.26).

Measuring time, length and density in units of $\hbar/(c_0^{(1\mathrm{D})}\rho_\mathrm{p})$, $[\hbar^2/(Mc_0^{(1\mathrm{D})}\rho_\mathrm{p})]^{1/2}$ and ρ_p respectively with ρ_p being the peak density of the system, we can write Eqs. (4.15) and (4.16) in dimensionless form as

$$i\partial_t\psi_{\pm1} = H_0\psi_{\pm1} + q\psi_{\pm1} + \delta\left(|\psi_{\pm1}|^2 + |\psi_0|^2 - |\psi_{\mp1}|^2\right)\psi_{\pm1} + \delta\,\psi_0^2\psi_{\mp1}^*, \tag{4.19}$$

$$i\partial_t\psi_0 = H_0\psi_0 + \delta\left(|\psi_1|^2 + |\psi_{-1}|^2\right)\psi_0 + 2\delta\,\psi_{-1}\psi_0^*\psi_1, \tag{4.20}$$

where $H_0 = -(1/2)\,\partial_x^2 + (1/2)\,\Omega^2 x^2 + \rho$ with $\rho = \tilde{\rho}/\rho_\mathrm{p}$ and $q = \tilde{q}/(c_0^{(1\mathrm{D})}\rho_\mathrm{p})$. The normalized trap strength is

$$\Omega = \frac{3}{2\,(a_0 + 2a_2)\,\rho_\mathrm{p}}\left(\frac{\omega_\parallel}{\omega_\perp}\right) \tag{4.21}$$

and we define

$$\delta = \frac{c_1^{(1\mathrm{D})}}{c_0^{(1\mathrm{D})}} = \frac{a_2 - a_0}{a_0 + 2a_2}. \tag{4.22}$$

Typical values of $\delta \approx -5\cdot10^{-3}$ and $\delta \approx 3\cdot10^{-2}$ can be found in ^{87}Rb and ^{23}Na respectively, see, e.g., Refs. [148, 149].

We make use of this particular unit system as it allows us to characterize a broad range of trapped spinor systems. Varying the coupling ratio δ gives access to different species of atoms. Normalizing the trap strength to the transversal trapping frequency enables us to directly tune the effective dimensionality of the system. This is useful to determine a regime of trapping geometries that show the same physical properties as a homogeneous one-dimensional setup.

4.3. Ground states and phase diagram of the trapped spin-1 Bose gas

In Sect. 3.2.2, we introduced the ground states and the corresponding mean-field phase diagram of the homogeneous spin-1 Bose gas. Note again that in the unit system used here, the parameter c_1 has to be replaced by the coupling ratio δ. As we aim at analyzing the stability properties of the ground states in presence of a trapping potential, we first have to map out the phase diagram in presence of the trap. Therefore, we make use of a continuous-time Nesterov (CTN) scheme. We present an extension of the scheme, previously applied to one-component systems, to our multi-component system in Sect. 4.3.2. Finally, we show numerical results obtained with this method for the one-dimensional trapped spin-1 Bose gas in Sect. 4.3.3.

4.3.1. Time-independent equations of motion

In the course of this section, we want to determine the ground states of the system in presence of a trapping potential, i.e., we aim to identify the stationary states of the trapped system with the lowest eigenenergy. By choosing the general ansatz $\psi_m(x,t) = \psi_m(x)e^{-i\mu_m t}$ with $m = 0, \pm 1$ and μ_m being the chemical potential of each spinor component, Eqs. (4.19) and (4.20) turn into

$$\begin{aligned}\mu_{\pm1}\psi_{\pm1} = H_0\psi_{\pm1} + q\psi_{\pm1} + \delta\left(|\psi_{\pm1}|^2+|\psi_0|^2-|\psi_{\mp1}|^2\right)\psi_{\pm1} \\ + \delta\,\psi_0^2\psi_{\mp1}^* e^{-i(2\mu_0-\mu_1-\mu_{-1})t},\end{aligned} \tag{4.23}$$

$$\mu_0\psi_0 = H_0\psi_0 + \delta\left(|\psi_1|^2+|\psi_{-1}|^2\right)\psi_0 + 2\delta\,\psi_{-1}\psi_0^*\psi_1 e^{-i(\mu_1+\mu_{-1}-2\mu_0)t}. \tag{4.24}$$

A stationary state resulting from Eqs. (4.23) and (4.24) has to fulfill the phase matching condition $2\mu_0 - \mu_1 - \mu_{-1} = 0$. As a population imbalance between the $m_\mathrm{F} = \pm1$ components is not favored, independent of the choice of the couplings in the equations of motion, we assume that $\mu_1 = \mu_{-1}$ for all stationary states considered in this thesis. This implies that $\mu_0 = \mu_1 = \mu_{-1} \equiv \mu$. The time-independent equations of motion thus read:

$$\begin{aligned}\mathcal{F}_{\pm1}(\psi_1,\psi_0,\psi_{-1},\psi_1^*,\psi_0^*,\psi_{-1}^*) \equiv &-\mu\psi_{\pm1} + H_0\psi_{\pm1} + q\psi_{\pm1} \\ &+ \delta\left(|\psi_{\pm1}|^2+|\psi_0|^2-|\psi_{\mp1}|^2\right)\psi_{\pm1} \\ &+ \delta\,\psi_0^2\psi_{\mp1}^* \\ &= 0,\end{aligned} \tag{4.25}$$

$$\begin{aligned}\mathcal{F}_0(\psi_1,\psi_0,\psi_{-1},\psi_1^*,\psi_0^*,\psi_{-1}^*) \equiv &-\mu\psi_0 + H_0\psi_0 \\ &+ \delta\left(|\psi_1|^2+|\psi_{-1}|^2\right)\psi_0 \\ &+ 2\delta\,\psi_{-1}\psi_0^*\psi_1 \\ &= 0.\end{aligned} \tag{4.26}$$

Here, we introduced functions $\mathcal{F}_{0,\pm1}$ as abbreviations for the time-independent equations of motion which will be of practical use in Sect. 4.4.2.

Various first- and second-order methods can be applied to find solutions to the above stated equations of motion. A commonly used method for such a problem is an exact Newton scheme. It is a second-order method involving the explicit calculation of the Jacobian. A major advantage of the Newton scheme is that it is not restricted to finding ground states (i.e., the global energy minimum) of a physical system. On the other hand, a disadvantage of this scheme is that an adequate initial guess for the wave functions, proximal to the true solution, is needed to ensure convergence.

For the trapped spin-1 system, however, a priori, we do not know where the quantum phase transition (QPT) between the easy-plane and polar phase is located. Moreover, our initial guesses in the trapped case may not be sufficiently accurate. Thus, the Newton method might fail to converge to the true ground state. In that light, we first focus on a method which is able to map out the spin-1 phase diagram *independently* of the

specifics of the initial guess. Nonetheless, we will make use of the Newton method lateron in order to find a specific state of interest also within a phase where it is not the ground state anymore. This is required to perform the stability analysis for a given state throughout the whole (δ, q)-plane of the spin-1 phase diagram. The Newton scheme for the spin-1 system will be discussed in detail in Sect. 4.4.1.

4.3.2. Continuous-time Nesterov scheme

For simplicity, let us assume that we are interested in the variational problem of minimizing the function $G(x)$. Following the classical discrete-time Nesterov (mirror descent) algorithm [150], it has been shown in the work presented in Ref. [151] that one can formulate a continuous-time analogue. This involves a second-order ordinary differential equation (ODE), which in some sense generalizes standard gradient descent schemes. The ODE is given by

$$\ddot{x} + \frac{3}{t}\dot{x} + \frac{d}{dx}G(x) = 0, \tag{4.27}$$

where the dots denote derivatives with respect to the continuous time variable t. We refer to this scheme as the continuous-time Nesterov (CTN) method. In general, Eq. (4.27) can be viewed as describing the damped motion of a particle in a potential $G(x)$. In contrast to standard gradient descent schemes, we are dealing with a second-order differential equation resulting in the "acceleration vector" pointing into the direction of the steepest descent. The strength of the damping $\sim t^{-1}$ explicitly depends on the evolution time, i.e., the damping is large at small times when the particle is, comparatively, further away from the fixed point solution and decreases as the fixed point solution is approached, which is ensured by choosing an appropriate time step as well as a proper preconditioner when solving Eq. (4.27) numerically. The preconditioner is an operator (or upon discretization, a matrix) that helps solving the linear system at hand by reducing its condition number.

The CTN method can be optimized by introducing a gradient restarting scheme, see Refs. [151, 152]. Following that scheme in two or three spatial dimensions, the time t is reset to 1 when the angle between the negative gradient $-\nabla G(\mathbf{x})$ of the function G that we are trying to extremize and $\dot{\mathbf{x}}$ is larger than 90 degrees and a pre-specified amount of time t_{res} has elapsed. In one spatial dimension this geometrical condition boils down to the inner product of $-dG(x)/dx$ and $\dot{x}$ being smaller than 0. Gradient restarting ensures that the CTN is sufficiently damped in all stages of the evolution. This can be intuitively understood when thinking again of the motion of a particle in a potential. The inner product of $-dG/dx$ and $\dot{x}$ being smaller than 0 means that our particle is moving in the direction of the fixed point solution. To avoid possible oscillations of the solution in the vicinity of the fixed point in case of weak damping, we then reset the time which results in a large damping of the motion. Note that gradient restarting is only useful when the specific geometrical condition stated above is fulfilled. We refer to the optimized scheme as accelerated continuous-time Nesterov (ACTN) method.

In Ref. [152], it has recently been shown that the CTN method and its accelerated version can also be applied to functionals and can be used for finding stationary states of partial differential equations (PDEs). In particular, the CTN method was utilized for analyzing stationary states in a one-component Bose gas in one and two spatial dimensions. Here, we extend the CTN method to a multi-component system, illustrating its ability to capture ground states in a wide range of parametric regimes and rather independently

of the specifics of the initial guess. Following the steps of [152], which are based on the replacements $x \to \psi(x)$ and $dG/dx \to \mathcal{F}(\psi(x))$, i.e., replacing derivatives with respect to the spatial coordinate x by functional derivatives with respect to the field $\psi(x)$, we obtain a PDE for the evolution (towards equilibrium) of the field ψ in space and time. Generalizing the replacements for all hyperfine components, the CTN scheme for the spin-1 system assumes the form:

$$\begin{aligned} 0 = \ddot{\psi}_{\pm1} + \frac{3}{t}\dot{\psi}_{\pm1} - [-H_0\psi_{\pm1} - q\psi_{\pm1} \\ - \delta\left(|\psi_{\pm1}|^2+|\psi_0|^2-|\psi_{\mp1}|^2\right)\psi_{\pm1} - \delta\,\psi_0^2\psi_{\mp1}^* + \mu\psi_{\pm1}\Big], \end{aligned} \tag{4.28}$$

$$\begin{aligned} 0 = \ddot{\psi}_0 + \frac{3}{t}\dot{\psi}_0 - \Big[-H_0\psi_0 - \delta\left(|\psi_1|^2+|\psi_{-1}|^2\right)\psi_0 \\ - 2\delta\,\psi_{-1}\psi_0^*\psi_1 + \mu\psi_0\Big]. \end{aligned} \tag{4.29}$$

Note that the overdot denotes a partial derivative with respect to time as we are performing a distributed minimization by solving the partial differential equations of the above system. We use a second-order center difference scheme for approximating the second derivative and a first-order backward difference scheme for approximating the first derivative with respect to time. This leads to the following evolution equations

$$\begin{aligned} \psi_{\pm1}^{n+1} = \left(2-\frac{3}{n}\right)\psi_{\pm1}^n + (\Delta t)^2\Big[-H_0\psi_{\pm1}^n - q\psi_{\pm1}^n \\ - \delta\left(|\psi_{\pm1}^n|^2+|\psi_0^n|^2-|\psi_{\mp1}^n|^2\right)\psi_{\pm1}^n - \delta\left(\psi_0^n\right)^2\left(\psi_{\mp1}^n\right)^* \\ + \mu\psi_{\pm1}^n\Big] - \left(1-\frac{3}{n}\right)\psi_{\pm1}^{n-1}, \end{aligned} \tag{4.30}$$

$$\begin{aligned} \psi_0^{n+1} = \left(2-\frac{3}{n}\right)\psi_0^n + (\Delta t)^2\Big[-H_0\psi_0^n - \delta\left(|\psi_1^n|^2+|\psi_{-1}^n|^2\right)\psi_0^n \\ - 2\delta\,\psi_{-1}^n\left(\psi_0^n\right)^*\psi_1^n + \mu\psi_0^n\Big] - \left(1-\frac{3}{n}\right)\psi_0^{n-1}, \end{aligned} \tag{4.31}$$

where $t = n\Delta t$ with time step Δt and n being the number of iterations made. Naturally, we mean by the superscript that $\psi_i^n = \psi_i(n\Delta t) = \psi_i(t)$.

Making use of gradient restarting, the ACTN scheme for the spin-1 system is given by

$$\begin{aligned} \psi_{\pm1}^{n+1} = \left(2-\frac{3}{\tilde{n}}\right)\psi_{\pm1}^n + (\Delta t)^2\Big[-H_0\psi_{\pm1}^n - q\psi_{\pm1}^n \\ - \delta\left(|\psi_{\pm1}^n|^2+|\psi_0^n|^2-|\psi_{\mp1}^n|^2\right)\psi_{\pm1}^n - \delta\left(\psi_0^n\right)^2\left(\psi_{\mp1}^n\right)^* \\ + \mu\psi_{\pm1}^n\Big] - \left(1-\frac{3}{\tilde{n}}\right)\psi_{\pm1}^{n-1}, \end{aligned} \tag{4.32}$$

$$\begin{aligned} \psi_0^{n+1} = \left(2-\frac{3}{\tilde{n}}\right)\psi_0^n + (\Delta t)^2\Big[-H_0\psi_0^n - \delta\left(|\psi_1^n|^2+|\psi_{-1}^n|^2\right)\psi_0^n \\ - 2\delta\,\psi_{-1}^n\left(\psi_0^n\right)^*\psi_1^n + \mu\psi_0^n\Big] - \left(1-\frac{3}{\tilde{n}}\right)\psi_0^{n-1}. \end{aligned} \tag{4.33}$$

Here, $\tilde{n}$ starts at 1 and is increased by 1 in each iteration step. $\tilde{n}$ is then reset to 1 when the (discretized in time) multicomponent generalization of the gradient restarting condition for functionals

$$\begin{aligned}
0 < &\left\langle -H_0\psi_1^n - q\psi_1^n - \delta\left(|\psi_1^n|^2+|\psi_0^n|^2-|\psi_{-1}^n|^2\right)\psi_1^n \right. \\
&\left. - \delta\left(\psi_0^n\right)^2\left(\psi_{-1}^n\right)^* + \mu\psi_1^n\,,\,\psi_1^{n+1}-\psi_1^n\right\rangle \\
&+ \left\langle -H_0\psi_0^n - \delta\left(|\psi_1^n|^2+|\psi_{-1}^n|^2\right)\psi_0^n \right. \\
&\left. - 2\delta\,\psi_{-1}^n\left(\psi_0^n\right)^*\psi_1^n + \mu\psi_0^n\,,\,\psi_0^{n+1}-\psi_0^n\right\rangle \\
&+ \left\langle -H_0\psi_{-1}^n - q\psi_{-1}^n - \delta\left(|\psi_{-1}^n|^2+|\psi_0^n|^2-|\psi_1^n|^2\right)\psi_{-1}^n \right. \\
&\left. - \delta\left(\psi_0^n\right)^2\left(\psi_1^n\right)^* + \mu\psi_{-1}^n\,,\,\psi_{-1}^{n+1}-\psi_{-1}^n\right\rangle
\end{aligned} \tag{4.34}$$

is satisfied and $n > n_{\text{res}}$ holds. Here, $\langle a\,,b\rangle = \sum_i a_i^* b_i$ denotes the complex inner product.

To successfully apply the ACTN method, a preconditioner has to be included. We choose the preconditioner to be $P = c - d^2/dx^2$, with the variable x being the argument of the fields $\psi_m(x)$ and the constant c being a real number. Due to the damping term in the ACTN scheme, we additionally need to normalize the wave functions to the total particle number N after each iteration step. The chemical potential μ is treated as a Lagrange multiplier and can be calculated from either Eqs. (4.25) or (4.26). The full ACTN scheme with μ being calculated from Eq. (4.26) can be written as

$$\mu_n = \frac{\left\langle -H_0\psi_0^n - \delta\left(|\psi_1^n|^2+|\psi_{-1}^n|^2\right)\psi_0^n - 2\,\delta\psi_{-1}^n\left(\psi_0^n\right)^*\psi_1^n\,,\,P^{-1}\psi_0^n\right\rangle}{\left\langle\psi_0^n\,,\,P^{-1}\psi_0^n\right\rangle}, \tag{4.35}$$

$$\begin{aligned}
\tilde{\psi}_{\pm1}^{n+1} = &\left(2-\frac{3}{\tilde{n}}\right)\psi_{\pm1}^n + (\Delta t)^2\,P^{-1}\left[-H_0\psi_{\pm1}^n - q\psi_{\pm1}^n \right. \\
&- \delta\left(|\psi_{\pm1}^n|^2+|\psi_0^n|^2-|\psi_{\mp1}^n|^2\right)\psi_{\pm1}^n - \delta\left(\psi_0^n\right)^2\left(\psi_{\mp1}^n\right)^* \\
&\left. +\mu_n\psi_{\pm1}^n\right] - \left(1-\frac{3}{\tilde{n}}\right)\psi_{\pm1}^{n-1},
\end{aligned} \tag{4.36}$$

$$\begin{aligned}
\tilde{\psi}_0^{n+1} = &\left(2-\frac{3}{\tilde{n}}\right)\psi_0^n + (\Delta t)^2\,P^{-1}\left[-H_0\psi_0^n - \delta\left(|\psi_1^n|^2+|\psi_{-1}^n|^2\right)\psi_0^n \right. \\
&\left. - 2\delta\,\psi_{-1}^n\left(\psi_0^n\right)^*\psi_1^n + \mu_n\psi_0^n\right] - \left(1-\frac{3}{\tilde{n}}\right)\psi_0^{n-1},
\end{aligned} \tag{4.37}$$

$$\psi_{0,\pm1}^{n+1} = \frac{\tilde{\psi}_{0,\pm1}^{n+1}\sqrt{N}}{\left[\left\langle\tilde{\psi}_1^{n+1}\,,\,\tilde{\psi}_1^{n+1}\right\rangle + \left\langle\tilde{\psi}_0^{n+1}\,,\,\tilde{\psi}_0^{n+1}\right\rangle + \left\langle\tilde{\psi}_{-1}^{n+1}\,,\,\tilde{\psi}_{-1}^{n+1}\right\rangle\right]^{1/2}}. \tag{4.38}$$

The convergence of the method depends on the choice of the constant c in the preconditioner P, the time step Δt as well as the minimum number of iterations that have to be performed before applying the gradient restarting n_{res}. Note that the ACTN scheme can also be carried out in Fourier space which allows for a straightforward compu-

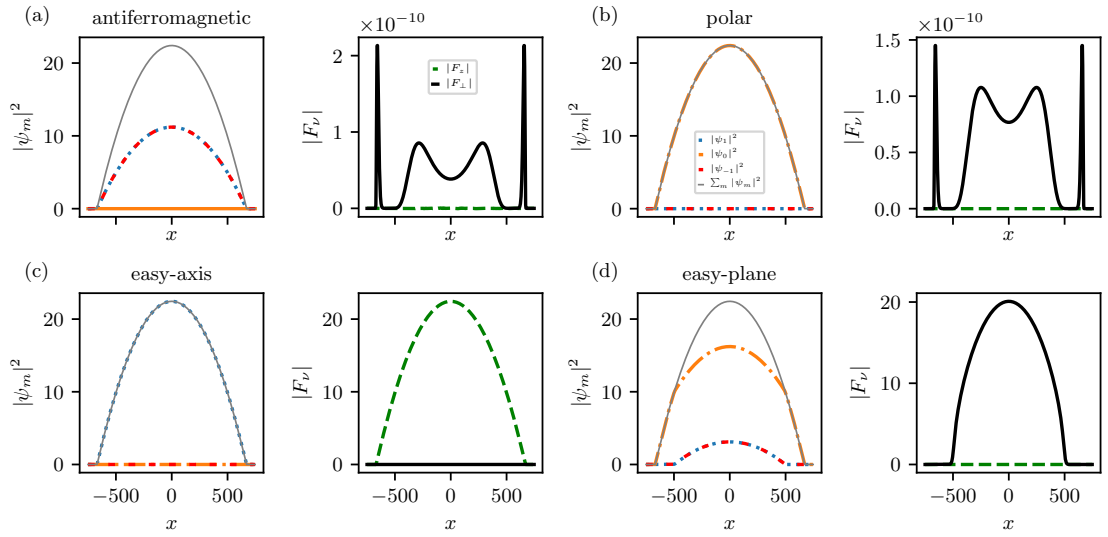

Figure 4.1.: Absolute value squared of the ground state wave functions, $|\psi_m(x)|^2$, with $m = 0, \pm 1$ and the corresponding spin configurations, $|F_\nu(x)|$, with $\nu = z, \perp$ as a function of the spatial position x obtained by means of the ACTN method for a trapped spin-1 Bose gas. The four panels correspond to values of (δ, q) of (a) $(5 \cdot 10^{-3}, -0.1)$, (b) $(5 \cdot 10^{-3}, 0.1)$, (c) $(-5 \cdot 10^{-3}, -0.1)$ and (d) $(-5 \cdot 10^{-3}, 0.1)$. The wave function of the $m_\mathrm{F} = 0$ component is depicted by a dash-dotted orange line. The $m_\mathrm{F} = \pm 1$ components are shown with blue dots and red dashes respectively. The total density $\sum_m |\psi_m(x)|^2$ is illustrated by the grey solid line. The amplitude of the transversal spin $|F_\perp|$ is given by the solid black line and the amplitude of the F_z-magnetization by the green dashes. The analysis is performed for parameters $\Omega = 10^{-2}$ and $N = 20000$ to mimic experimental settings. The associated phases of the spin-1 system are shown in the titles of the subplots. Note the scale of the amplitude of the spin in panels (a) and (b), which illustrates the numerical error arising from the error tolerance used for the ACTN scheme. Figure taken and adapted from Ref. [129].

tation of the action of the inverse of the preconditioner on Fourier modes $P^{-1} e^{ikx} = [1/(c + k^2)] e^{ikx}$.

4.3.3. Numerical results

In this subsection, we apply the ACTN method to map out the phase diagram for our trapped spin-1 Bose gas. Motivated by considerations of experimentally accessible regimes, see, e.g., Refs. [148, 149], we choose $|\delta| = 5 \cdot 10^{-3}$, $\Omega = 10^{-2}$ and $N = 20000$. The numerics is performed on a one-dimensional grid with $N_\mathrm{g} = 512$ grid points and the error tolerance of the ACTN is set to 10^{-10}. The choice of parameters can correspond to a 1D condensate with peak density $\rho_\mathrm{p} \approx 93 \cdot 10^6 \mathrm{m}^{-1}$ confined in a trap with $\omega_\perp = 100\, \omega_\parallel = 2\pi \cdot 200$ Hz.

To provide a specific example, we now discuss the numerically obtained ground states for a quadratic Zeeman energy of $|q| = 0.1$ (using the dimensionless units introduced in Sect. 4.2). Our initial guess of the wave function is a Gaussian, centered around the

middle of the trap, with width $\sigma = 500/\sqrt{2}$ in each of the m_F components. To converge to the ground state in the easy-axis phase, we need to explicitly break the symmetry between the $m_\mathrm{F} = \pm 1$ components. As the equations of motion are symmetric in the $m_\mathrm{F} = \pm 1$ components we have to impose a slight imbalance between them in the initial wave function. We find that an imbalance of 0.2% is sufficient to let the system converge to either one or the other degenerate easy-axis ground state. Note that this does not affect the generality of the method to find ground states of the system without the need of an accurate initial guess.

The absolute value squared of the ground state wave functions and the corresponding spin configurations are depicted in Fig. 4.1. We start by discussing the results for antiferromagnetic spin interactions, which in our study corresponds to $\delta = 5 \cdot 10^{-3}$.

(i) *polar phase* – Convergence to the ground state at $q = 0.1$ within our preset tolerance is reached after $\simeq 700$ iterations. The corresponding absolute value squared of the wave functions only being non-zero for the $m_\mathrm{F} = 0$ component as well as the vanishing spin (see Fig. 4.1(b)) clearly shows that the system is in the polar phase. The chemical potential of the ground state is $\mu = 22.4$. This value corresponds to $\mu = \rho_\mathrm{p} c_0$ obtained within the Thomas-Fermi approximation.

(ii) *antiferromagnetic phase* – In case of $q = -0.1$, the ACTN method needs $\simeq 600$ iterations to converge to the ground state. The data in Fig. 4.1(a), showing an equal non-zero absolute value squared of the wave functions of the $m_\mathrm{F} = \pm 1$ components and a vanishing spin, confirms that the system is in the antiferromagnetic phase. The chemical potential here is $\mu = 22.3$.

For both settings (i) and (ii) we find that taking the parameters $\Delta t = 0.5$, $c = 7$ and $n_\mathrm{res} = 50$ leads to an efficient convergence of the numerical scheme.

In the following, we present the results obtained for ferromagnetic spin interactions, which in our case is represented by $\delta = -5 \cdot 10^{-3}$.

(iii) *easy-axis phase* – At $q = -0.1$, we find two degenerate ground states after $\simeq 10000$ iterations. The system is in the easy-axis phase which is validated by the non-zero F_z-magnetization (see Fig. 4.1(c)). The chemical potential is $\mu = 22.23$. Efficient convergence of the ACTN is reached for parameters $\Delta t = 0.5$, $c = 15$ and $n_\mathrm{res} = 100$.

(iv) *easy-plane phase* – At $q = 0.1$, it takes $\simeq 2000$ iterations to converge to the ground state. The transversal spin depicted in Fig. 4.1(d) clearly shows that the system is in the easy-plane phase. The chemical potential is found to be $\mu = 22.38$. Taking the ACTN parameters to be $\Delta t = 0.5$, $c = 7$ and $n_\mathrm{res} = 200$ leads to an efficient convergence of the scheme in this case.

The zero-temperature phase transition between the easy-plane and the polar phase occurs at $q = q_0$. In a homogeneous system described on the level of mean-field equations the transition is determined by $q_0 = 2\rho_\mathrm{h}|\delta|$, where ρ_h is the homogeneous total density of the system. In a trapped system it is a priori not clear which density, if any, might enter this type of critical-point relation.

Using the ACTN method, we are able to numerically determine the position of the phase transition within our mean-field approximation. To do so, we continuously increase the quadratic Zeeman energy starting at $q = 0$ and let the ACTN converge to the corresponding ground state. We then calculate the amplitude of the transverse spin $|F_\perp(x)|$ for the ground-state configuration. Crossing the phase transition, the transverse spin should drop to zero as the system enters the unmagnetized polar phase. We define the phase transition to occur when $|F_\perp(x)|_\infty < 10^{-2}$, where $|\cdot|_\infty$ denotes the L^∞ norm. We find $q_0 = 0.2236$ to mark the phase transition in the trapped system. This value is

in good agreement with $q_0^{\mathrm{p}} = 2\rho_{\mathrm{p}}|\delta| = 0.224$ corresponding to the peak density. The position of the phase transition is thus determined by the peak density of the trapped system. Note that the ACTN method needs $\simeq 4 \cdot 10^5$ iterations to converge to the ground state in the vicinity of the phase transition. Hence, we observe that the number of iterations needed to converge to the ground state increases significantly close to the phase transition. Nevertheless, the method is still able to converge to the relevant ground state.

Choosing a value of $q > q_0$, i.e., being again in the polar phase, the same parameters Δt, c and n_{res} as for the polar phase with antiferromagnetic spin interactions can be used to achieve an efficient convergence of the ACTN scheme, i.e., the convergence of the numerical scheme is independent of the sign of δ as this term vanishes for an unmagnetized state.

4.4. Stability analysis of the trapped spin-1 Bose gas

In this section, we perform the stability analysis for the spin-1 ground states throughout the (δ, q)-plane of the spin-1 phase diagram. The stability properties are extracted by numerically solving the Bogoliubov de-Gennes (BdG) equations in presence of a trapping potential. The BdG equations are obtained by considering small perturbations about a possible stationary state of the system to linear order.

We compare numerical results for the trapped setup with Bogoliubov theory in a homogeneous spin-1 system discussed in Sect. 4.1. Solving the BdG equations describing the linear excitations about a particular stationary state, requires to first determine the wave functions of this state. To find the desired stationary state for any parameter set (δ, q), we employ a highly accurate Newton scheme, which we introduce in Sect. 4.4.1. We then derive the BdG equations for the one-dimensional trapped spin-1 Bose gas in Sect. 4.4.2. Finally, we discuss the numerically obtained stability properties of the spin-1 ground states in Sect. 4.4.3.

4.4.1. Determining the wave functions of stationary states within the (δ, q)-plane using an exact Newton method

Performing the stability analysis of the different states discussed above within the (δ, q)-plane of the spin-1 phase diagram, i.e., especially in regions where they are not the ground state anymore, requires to first numerically determine their wave functions for any given set of parameters (δ, q). To achieve this goal, we employ an exact Newton method which is also capable of converging to excited states of the system. However, as highlighted above, this requires an initial guess for the wave function which is close to the desired state. The Newton scheme for the spin-1 system can be cast into the form of a six-dimensional matrix equation:

$$J\Delta\psi = \mathcal{F}, \tag{4.39}$$

where $\mathcal{F} = (\mathcal{F}_1, \mathcal{F}_0, \mathcal{F}_{-1}, \mathcal{F}_1^*, \mathcal{F}_0^*, \mathcal{F}_{-1}^*)^T$ is a vector that contains the time-independent equations of motion (see Eqs. (4.25) and (4.26)) as well as their complex conjugated versions and $\Delta\psi$ gives the correction to the wave function of the previous iteration of the Newton scheme with $\psi = (\psi_1, \psi_0, \psi_{-1}, \psi_1^*, \psi_0^*, \psi_{-1}^*)^T$ being a vector of all spinor fields.

The Jacobian J is given by the matrix

$$J_{ij} = \frac{\partial \mathcal{F}_i}{\partial \psi_j}, \tag{4.40}$$

where $i, j \in \{0, \ldots, 5\}$ and the partial derivative is evaluated at the current wave function ψ. Note that we end up with a $6N_\mathrm{g} \times 6N_\mathrm{g}$ matrix when taking N_g grid points to discretize the wave functions.

As we wish to converge to a state with fixed particle number, we introduce a Lagrange multiplier λ for the chemical potential μ. This adds the following constraint to our Newton scheme

$$\mathcal{F}_\lambda \equiv \int \left(|\psi_1|^2 + |\psi_0|^2 + |\psi_{-1}|^2\right) \mathrm{d}x - N = 0. \tag{4.41}$$

Consequently, we get an additional row and column in the Jacobian such that we are dealing with $6N_\mathrm{g} + 1$ equations in the Newton scheme. The modified scheme can be written as

$$\tilde{J}\Delta\tilde{\psi} = \tilde{\mathcal{F}}, \tag{4.42}$$

with $\tilde{\psi} = (\psi_1, \psi_0, \psi_{-1}, \psi_1^*, \psi_0^*, \psi_{-1}^*, \lambda)^T$. Note that all $\psi_m^{(*)}$ are vectors containing the wave function at grid points $1, \ldots, N_\mathrm{g}$. In each iteration step, we calculate $\tilde{\mathcal{F}}$ and evaluate the Jacobian $\tilde{J}$ of the system. The second derivative occurring in the equations of motion is obtained by means of a second-order center difference scheme. By solving the eigenvalue equation (4.42), we obtain the correction to the wave function $\Delta\tilde{\psi}$. The Newton scheme terminates if the correction is smaller than a preset tolerance.

4.4.2. Bogoliubov de-Gennes equations

The stability properties of a specific stationary state are deduced from numerically solving the corresponding Bogoliubov de-Gennes (BdG) equations. In this subsection, we present the derivation of the BdG equations for the trapped spin-1 system and elaborate on how to subsequently solve them.

As a first step, we have to linearize the equations of motion about the stationary state of interest. Thus we take the ansatz

$$\psi_m(x,t) = \left[\Phi_m(x) + \epsilon\delta\psi_m(x,t)\right] e^{-i\mu t}, \tag{4.43}$$

with $m = 0, \pm 1$ labeling the three hyperfine components and $\Phi_m(x)$ being the wave function of each component at the stationary state; μ is the corresponding chemical potential; ϵ is a (formal) small parameter with $\epsilon \ll 1$ and $\delta\psi_m$ is the perturbation about the stationary state.

Note that a "δ" is used here as a symbol to differentiate between the wave function of the stationary state and its fluctuations and should not be confused with the coupling parameter in the Hamiltonian of the model.

Plugging this ansatz into Eqs. (4.19) and (4.20) we obtain

$$\begin{aligned} i\epsilon\partial_t\delta\psi_m = \mathcal{F}_m\,(&\Phi_1 + \epsilon\delta\psi_1, \Phi_0 + \epsilon\delta\psi_0, \Phi_{-1} + \epsilon\delta\psi_{-1}, \\ &\Phi_1^* + \epsilon\delta\psi_1^*, \Phi_0^* + \epsilon\delta\psi_0^*, \Phi_{-1}^* + \epsilon\delta\psi_{-1}^*)\,. \end{aligned} \tag{4.44}$$

Here, the $\mathcal{F}_m$ are the functions introduced in Eqs. (4.25) and (4.26).

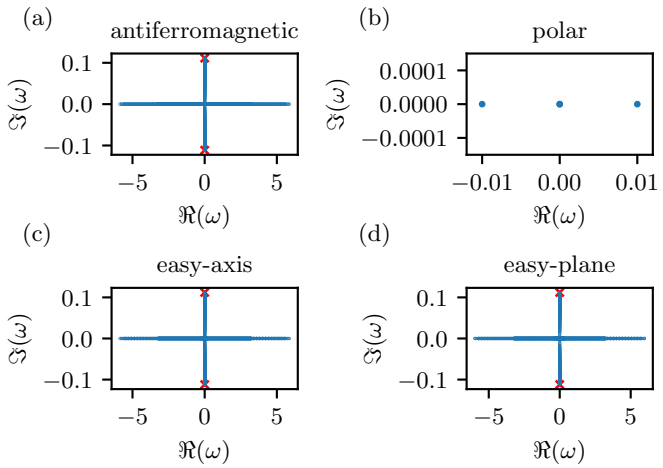

Figure 4.2.: Real ($\mathfrak{R}$) and imaginary ($\mathfrak{I}$) parts of the mode frequencies ω resulting from the BdG analysis of the *polar* state $\psi \sim (0,1,0)^T$ within the (a) antiferromagnetic $(\delta, q) = (5 \cdot 10^{-3}, -0.1)$, (b) polar $(5 \cdot 10^{-3}, 0.1)$, (c) easy-axis $(-5 \cdot 10^{-3}, -0.1)$ and (d) easy-plane $(-5 \cdot 10^{-3}, 0.1)$ phase. In panels (a), (c) and (d) we see a continuum band of mode frequencies along the real and the imaginary axis indicating that the frequencies are either purely real or purely imaginary. The red crosses mark the predicted mode frequency with the largest imaginary part within the given parameter regime derived from homogeneous Bogoliubov theory by replacing the homogeneous density by the peak density of the trapped system. The prediction is in good agreement with the largest imaginary part of the numerically obtained mode frequencies. In panel (b) we only show the neutral and the dipolar mode of the system. Their appearance as the lowest eigenmodes confirms that our BdG method is working properly. Figure taken and adapted from Ref. [129].

Linearization of the equations of motion (4.44) boils down to a Taylor expansion of $\mathcal{F}_m$ to first order in ϵ. The expansion for $\mathcal{F}_m$ reads

$$\begin{aligned}\mathcal{F}_m(\dots) = \mathcal{F}_m(\Phi) + \epsilon \Bigg\{ &\left(\frac{\partial \mathcal{F}_m}{\partial \Phi_1}\right)_{|\Phi} \delta\psi_1 + \left(\frac{\partial \mathcal{F}_m}{\partial \Phi_0}\right)_{|\Phi} \delta\psi_0 \\ &+ \left(\frac{\partial \mathcal{F}_m}{\partial \Phi_{-1}}\right)_{|\Phi} \delta\psi_{-1} + \left(\frac{\partial \mathcal{F}_m}{\partial \Phi_1^*}\right)_{|\Phi} \delta\psi_1^* + \left(\frac{\partial \mathcal{F}_m}{\partial \Phi_0^*}\right)_{|\Phi} \delta\psi_0^* \\ &+ \left(\frac{\partial \mathcal{F}_m}{\partial \Phi_{-1}^*}\right)_{|\Phi} \delta\psi_{-1}^* \Bigg\} + \mathcal{O}\left(\epsilon^2\right). \end{aligned} \tag{4.45}$$

Here, $\Phi = (\Phi_1, \Phi_0, \Phi_{-1}, \Phi_1^*, \Phi_0^*, \Phi_{-1}^*)$ is a vector containing the wave functions at the stationary state. Note that $\mathcal{F}_m(\Phi) = 0$ for all components as Φ is a stationary state of the system. The partial derivatives of $\mathcal{F}_m$ are taken with respect to the stationary fields

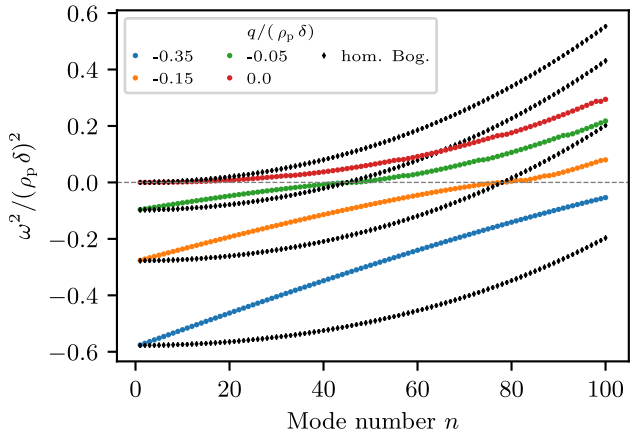

Figure 4.3.: Squared mode frequencies ω^2 as a function of the mode number n for the trapped system (colored dots) as compared to the homogeneous setting (black diamonds). The depicted data points for the trapped case are obtained by means of the BdG analysis of the *polar* state using the parameters $-0.35 \leq q/\rho_p\delta \leq 0$, $\delta = 5\cdot 10^{-3}$ and $\Omega = 10^{-2}$. Data points for the homogeneous case result from Eq. (4.2) using momenta $k_n = \pi n/L_b$ associated with the n-th eigenmode in a one-dimensional box of length $L_b = 2\,R_{TF}$, where R_{TF} is the Thomas-Fermi radius of the corresponding trapped system. The presence of the trap leads to a reduction of the growth rates for all unstable modes except the most unstable one. However, it appears to have no effect on the crossing point to the stable regime. The mode frequencies are given in units of $n_p\delta$. The grey dashed line marks the transition between the unstable ($\omega^2 < 0$) and the stable ($\omega^2 > 0$) regime of modes. Figure taken and adapted from Ref. [129].

and are then evaluated at Φ. To order ϵ we thus obtain

$$\begin{aligned} i\partial_t \delta\psi_m = &\left(\frac{\partial \mathcal{F}_m}{\partial \Phi_1}\right)_{|\Phi} \delta\psi_1 + \left(\frac{\partial \mathcal{F}_m}{\partial \Phi_0}\right)_{|\Phi} \delta\psi_0 + \left(\frac{\partial \mathcal{F}_m}{\partial \Phi_{-1}}\right)_{|\Phi} \delta\psi_{-1} \\ &+ \left(\frac{\partial \mathcal{F}_m}{\partial \Phi_1^*}\right)_{|\Phi} \delta\psi_1^* + \left(\frac{\partial \mathcal{F}_m}{\partial \Phi_0^*}\right)_{|\Phi} \delta\psi_0^* + \left(\frac{\partial \mathcal{F}_m}{\partial \Phi_{-1}^*}\right)_{|\Phi} \delta\psi_{-1}^*. \end{aligned} \tag{4.46}$$

To solve the BdG equations, we make use of the ansatz

$$\delta\psi_m(x,t) = \left(u_m(x)e^{-i\omega t} + v_m^*(x)e^{i\omega^* t}\right), \tag{4.47}$$

with mode functions u_m, v_m and mode frequency ω. Inserting the ansatz into Eq. (4.46) and matching the phase factors to obtain a time-independent description, we end up with a system of six coupled equations. We can write the BdG equations as an eigenvalue problem of the form

$$\bar{J}\mathcal{M} = -\omega\mathcal{M}. \tag{4.48}$$

Here, $\mathcal{M} = (u_1, u_0, u_{-1}, v_1, v_0, v_{-1})^T$ is a vector that contains all eigenmodes of the system. Note again that the vector has $6N_g$ entries after the discretization on a grid with N_g grid points. The matrix $\bar{J}$ turns out to be the Jacobian introduced in Eq. (4.40) whose

lower half of entries is multiplied by a factor of -1. We can formally write it as

$$\bar{J}_{ij} = [1 - 2\Theta(i-3)]\,(J_{ij})_{|\Phi}\,, \tag{4.49}$$

where $i, j \in \{0, \ldots, 5\}$ and the Heaviside theta function Θ is defined as $\Theta(z) = 1$ for $z \geq 0$.

The mode frequencies ω correspond to the eigenvalues of $\bar{J}$ and the mode functions u_m, v_m are given by the eigenvectors. We numerically solve the eigenvalue problem in Eq. (4.48) using the standard _geev LAPACK routines in python. Eigenmodes corresponding to mode frequencies with a non-zero imaginary part are dynamically unstable as they grow in time. Their growth rate is given by the magnitude of the imaginary part.

4.4.3. Numerical results

In the following, we discuss the stability properties of the spin-1 ground states in presence of a trapping potential. We investigate those properties for the polar, antiferromagnetic, easy-plane and easy-axis state, respectively. The numerical settings are taken to be the same as in Sect. 4.3.3, i.e., we take parameters $|\delta| = 5 \cdot 10^{-3}$ for the spin coupling and $\Omega = 10^{-2}$ for the normalized trap strength. We finally study the dependence of the stability properties on the strength of the spin coupling δ and the normalized trap strength Ω for the example case of the polar state.

Excitations about the polar state

We investigate the dynamical stability of the polar state $\psi \sim (0, 1, 0)^T$ throughout the different phases of our trapped spin-1 system. To get an overview of the stability properties of the polar state, we discuss results of the BdG analysis obtained for the case example of $|q| = 0.1$. The initial guess for the wave functions used in the Newton scheme is taken to be a Gaussian, centered around the middle of the trap, with width $\sigma = 500/\sqrt{2}$ in the $m_\mathrm{F} = 0$ component and 0 in the $m_\mathrm{F} = \pm 1$ components. The Newton method converges to the polar state in any of the phases within 10 iterations when setting the error tolerance to 10^{-10}. Due to a finite accuracy of the eigenvalue solver, we only consider eigenmodes with imaginary part larger than 10^{-4} as modes with non-zero imaginary part.

(i) *polar phase* – To check whether our numerical BdG analysis is working properly, we first study the stability of the polar state inside the polar phase, i.e., at the parameter pair $(\delta, q) = (5 \cdot 10^{-3}, 0.1)$. As the polar state is the ground state in this phase it has to be stable. This corresponds to all mode frequencies ω being real. Performing the BdG analysis, we find the imaginary parts of all obtained eigenmodes to be zero within our tolerance. This confirms the expected stability of the polar state within the polar phase. Fig. 4.2(b) shows the imaginary ($\Im(\omega)$) and real ($\Re(\omega)$) part of the two energetically lowest eigenmodes. The mode with eigenvalue $\omega = 0$ is the neutral mode. In addition, we observe that the first mode on the real axis is located at $|\omega| = 0.01$. This mode is called the dipolar mode with mode frequency given by the normalized trap strength Ω (c.f. Eq. (4.21)). Both characteristics are expected for the ground state within the polar phase and thus corroborate the accuracy of our numerical BdG analysis.

(ii) *antiferromagnetic phase* – The real and imaginary parts of all mode frequencies for the polar state in the antiferromagnetic phase, i.e., at parameters $(\delta, q) = (5 \cdot 10^{-3}, -0.1)$, are depicted in Fig. 4.2(a). We find that the polar state is dynamically unstable in this

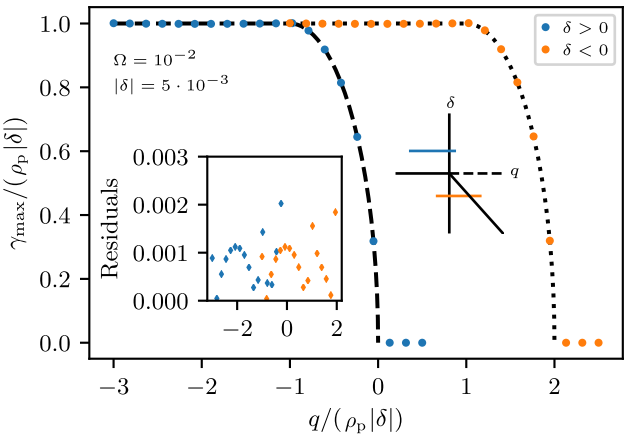

Figure 4.4.: Maximal growth rate $\gamma_{\max} = \max|\Im(\omega)|$ of the eigenmodes obtained by means of the BdG analysis of the *polar* state as a function of q and the sign of δ. The investigated parameter regime is indicated by the blue and orange solid lines in the schematic representation of the spin-1 phase diagram (c.f. Fig. 3.1). The analysis is performed for parameters $\Omega = 10^{-2}$ and $|\delta| = 5 \cdot 10^{-3}$. The growth rate as well as the quadratic Zeeman energy are given in units of $\rho_p|\delta|$. For $\delta > 0$, the growth rate follows the homogeneous prediction (dashed line) for the whole parameter range. The same feature is found in case of $\delta < 0$ where the data agrees with the dotted lines. The inset shows the residuals $|\gamma_{\max,h} - \gamma_{\max}|/\gamma_{\max,h}$, with $\gamma_{\max,h}$ being the growth rate calculated from the homogeneous prediction. The deviation of the numerically extracted growth rates from the homogeneous prediction is less than 0.2% for all parameters considered. The color coding is as in the main frame. Figure taken and adapted from Ref. [129].

parameter regime as a continuum band of modes exhibits $|\Im(\omega)| > 10^{-4}$. The most unstable mode has a growth rate of $\gamma_{\max} = 0.1112$ which equals $0.995\rho_p|\delta|$. Note that we use $\rho_p|\delta| = 0.1118$ extracted by means of the ACTN method in Sect. 4.3.3 for comparison. We find that this growth rate coincides with the growth rate for the homogeneous system resulting from Eq. (4.3) when replacing the homogeneous density ρ_h by the peak density ρ_p of the trapped system. This indicates that the peak density plays a crucial role in characterizing the stability properties of the trapped spin-1 system. We will investigate this key observation in more detail below.

The above stated property might suggest that the trap has no influence at all on the stability properties of the ground states. Nevertheless, we observe that the trap introduces new features in the system. To give an illustrative example, we perform the BdG analysis of the polar state within the antiferromagnetic phase for parameters $-0.35 \leq q/\rho_p\delta \leq 0$. For each value of q, we extract the squared mode frequencies ω^2 of the lowest n eigenmodes of the trapped system. To compare the numerically obtained results with the homogeneous setting, we calculate the squared mode frequencies by means of Eq. (4.2) using momenta $k_n = \pi n/L_b$, with $n \geq 1$, associated with the n-th eigenmode in a one-dimensional box of length $L_b = 2R_{TF}$, where R_{TF} is the Thomas-Fermi radius of the corresponding trapped system. Fig. 4.3 shows the squared frequencies for both settings in units of $\rho_p\delta$ as a function of the mode number n. Except for the most unstable momentum mode, we observe strong deviations when the trap is present. Most strikingly the

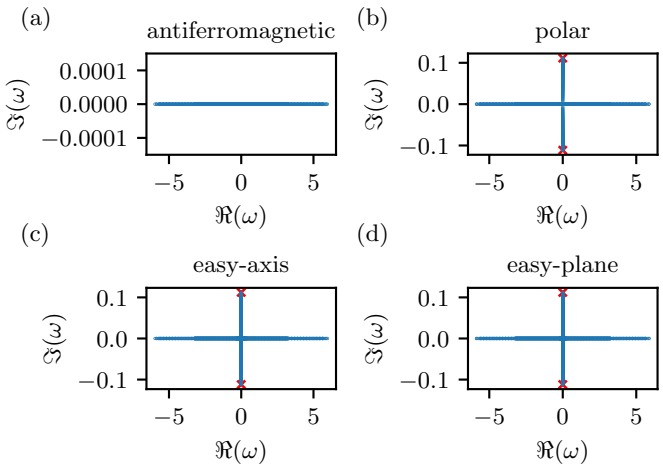

Figure 4.5.: Real ($\mathfrak{R}$) and imaginary ($\mathfrak{I}$) parts of the mode frequencies ω resulting from the BdG analysis of the *antiferromagnetic* state $\psi \sim (1,0,1)^T$ within the (a) antiferromagnetic $(\delta, q) = (5 \cdot 10^{-3}, -0.1)$, (b) polar $(5 \cdot 10^{-3}, 0.1)$, (c) easy-axis $(-5 \cdot 10^{-3}, -0.1)$ and (d) easy-plane $(-5 \cdot 10^{-3}, 0.1)$ phase. In panels (b), (c) and (d) we see a continuum band of mode frequencies along the real and the imaginary axis indicating that the frequencies are either purely real or purely imaginary. The red crosses mark the predicted mode frequency with the largest imaginary part within the given parameter regime derived from homogeneous Bogoliubov theory by replacing the homogeneous density by the peak density of the trapped system. The prediction is in good agreement with the largest imaginary part of the numerically obtained mode frequencies. Figure taken and adapted from Ref. [129].

growth rates of unstable modes are smaller than in the homogeneous case. However, the crossing point to the stable regime is not altered by the trap. We remark that our findings are in agreement with recent results obtained for the squared mode frequencies in a one-dimensional trapped spin-1 system using parameters $q/(\rho_p \delta) \in \{-0.05, 0, 0.05\}$ [153].

As the goal here is to mainly investigate the overall structure of the stability of the spin-1 ground states we will, in the following, focus on discussing the maximal growth rates allowing us to distinguish between stable and unstable regimes as well as to determine the dominant contribution to the growth of mode occupations in case of an instability.

(iii) *easy-plane phase* – Fig. 4.2(d) shows the results of the BdG analysis for the polar state in the easy-plane phase, i.e., at parameters $(\delta, q) = (-5 \cdot 10^{-3}, 0.1)$. We observe once again a band of unstable modes fulfilling the criterion $|\mathfrak{I}(\omega)| > 10^{-4}$. In this case, the most unstable mode has a growth rate of $\gamma_{\max} = 0.1118 = \rho_p |\delta|$. The trapped system exhibits exactly the growth rate expected in a homogeneous system given by Eq. (4.4) when replacing the homogeneous density with the peak density of the trapped system.

(iv) *easy-axis phase* – The real and imaginary parts of the mode frequencies for the polar state in the easy-axis phase, i.e., at parameters $(\delta, q) = (-5 \cdot 10^{-3}, -0.1)$, are presented in Fig. 4.2(c). Once again, in agreement with theory, we find the polar state to be dynamically unstable due to a band of modes with $|\mathfrak{I}(\omega)| > 10^{-4}$. As in the case above, the most unstable mode has a growth rate of $\gamma_{\max} = \rho_p |\delta|$. Furthermore, in the easy-axis phase, as well, the growth rate corresponds to the homogeneous case (see Eq. (4.4)) with the peak density replacing the homogeneous density.

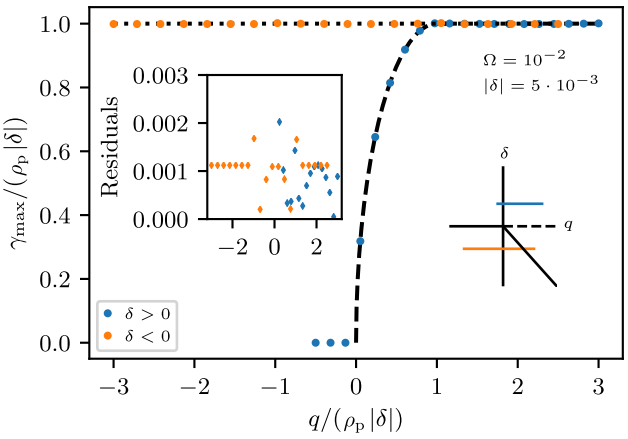

Figure 4.6.: Maximal growth rate $\gamma_{\max} = \max|\Im(\omega)|$ of the eigenmodes obtained by means of the BdG analysis of the *antiferromagnetic* state as a function of q and the sign of δ. The investigated parameter regime is indicated by the blue and orange solid lines in the schematic representation of the spin-1 phase diagram (c.f. Fig. 3.1). The analysis is performed for parameters $\Omega = 10^{-2}$ and $|\delta| = 5 \cdot 10^{-3}$. The growth rate as well as the quadratic Zeeman energy are given in units of $\rho_p|\delta|$. For $\delta > 0$, the growth rate follows the homogeneous prediction (dashed line) for the whole parameter range. In case of $\delta < 0$, we observe a constant growth rate of 1 irrespective of q. The growth rate coincides with the homogeneous setting (dotted line). The antiferromagnetic state is always dynamically unstable for $\delta < 0$. The inset shows the residuals $|\gamma_{\max,h} - \gamma_{\max}|/\gamma_{\max,h}$, with $\gamma_{\max,h}$ being the growth rate calculated from the homogeneous prediction. The deviation of the numerically extracted growth rates from the homogeneous prediction is less than 0.2% for all parameters considered. The color coding is as in the main frame. Figure taken and adapted from Ref. [129].

Hence, we find that the stability properties of the most unstable mode, characterized by the maximal growth rate $\gamma_{\max}$, coincide with the homogeneous prediction in the above shown example. To show that this property is indeed valid over variations of parameters, we carry out the BdG analysis of the polar state at various quadratic Zeeman energies. We perform the relevant continuations for fixed spin coupling δ, but for both types of spin interactions.

The maximal growth rate $\gamma_{\max} = \max|\Im(\omega)|$ as a function of q and different signs of δ is shown in Fig. 4.4. To allow for a direct comparison to the homogeneous predictions, the growth rates and the quadratic Zeeman energies are given in units of $n_p|\delta|$. For $\delta > 0$, the growth rate follows the homogeneous prediction for the whole parameter range. The same feature is found in case of $\delta < 0$. The observed behavior for $\delta > 0$ coincides with the one for $\delta < 0$ when shifting the quadratic Zeeman energy by two units. This is in exact agreement with the shift of the phase transition from $q/(\rho_p|\delta|) = 0$ to $q/(\rho_p|\delta|) = 2$ which shows that the exact same properties are found irrespective of the sign of δ.

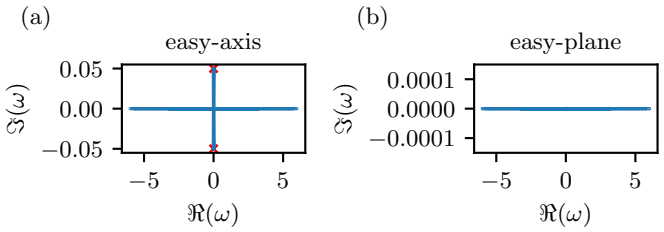

Figure 4.7.: Real ($\mathfrak{R}$) and imaginary ($\mathfrak{I}$) parts of the mode frequencies ω resulting from the BdG analysis of the *easy-plane* state $\psi \sim \left(\sqrt{1-q/q_0}, \sqrt{2(1+q/q_0)}, \sqrt{1-q/q_0}\right)^T$ within the (a) easy-axis $(\delta, q) = (-5 \cdot 10^{-3}, -0.1)$ and (b) easy-plane $(-5 \cdot 10^{-3}, 0.1)$ phase. In panel (a) we see a continuum band of mode frequencies along the real and the imaginary axis indicating that the frequencies are either purely real or purely imaginary. The red crosses mark the predicted mode frequency with the largest imaginary part within the given parameter regime derived from homogeneous Bogoliubov theory. The numerically obtained largest imaginary part of the mode energies is in good agreement with the homogeneous prediction given by $|q|/2 = 0.05$. Figure taken and adapted from Ref. [129].

Excitations about the antiferromagnetic state

We continue by investigating the dynamical stability of the antiferromagnetic state $\psi \sim (1, 0, 1)^T$ throughout the phases of our trapped spin-1 system. The initial state for the wave functions used in the Newton scheme is taken to be a Gaussian, centered around the middle of the trap, with width $\sigma = 500/\sqrt{2}$ in the $m_F = \pm 1$ components and 0 in the $m_F = 0$ component. The Newton method converges to the antiferromagnetic state in all phases within 9 iterations. The error tolerance is set to 10^{-10} as before.

(i) *antiferromagnetic phase* – Fig. 4.5(a) shows the real and imaginary parts of the mode frequencies obtained by means of the BdG analysis in the antiferromagnetic phase. We find no dynamically unstable modes. As before, this is the consistency check of the method as the antiferromagnetic state is the ground state in this phase and thus has to be stable.

(ii) *polar phase* – Within the polar phase (see real and imaginary parts of the mode frequencies depicted in Fig. 4.5(b)) the antiferromagnetic state is dynamically unstable as we observe a band of eigenfrequencies with $|\mathfrak{I}(\omega)| > 10^{-4}$. The growth rate of the most unstable mode is $\gamma_{\max} = 0.995\rho_p|\delta|$, once again coinciding with the growth rate for the homogeneous system obtained through Eq. (4.9) by replacing the homogeneous density ρ_h with the peak density ρ_p of the trapped system.

(iii) *easy-axis phase* – Fig. 4.5(c) shows the real and imaginary parts of the mode frequencies resulting from the BdG analysis of the antiferromagnetic state in the easy-axis phase, where again a band of unstable eigenmodes arises. The most unstable one exhibits a growth rate of $\gamma_{\max} = \rho_p|\delta|$. In this parameter regime, the growth rate equals the homogeneous prediction given in Eq. (4.7) when exchanging the homogeneous density with the trapped problem peak density.

(iv) *easy-plane phase* – Last, we present the real and imaginary parts of the mode frequencies for the antiferromagnetic state in the easy-plane phase in Fig. 4.5(d). The instability here is found to possess a maximal growth rate of $\gamma_{\max} = \rho_p|\delta|$, in line with Eq. (4.7).

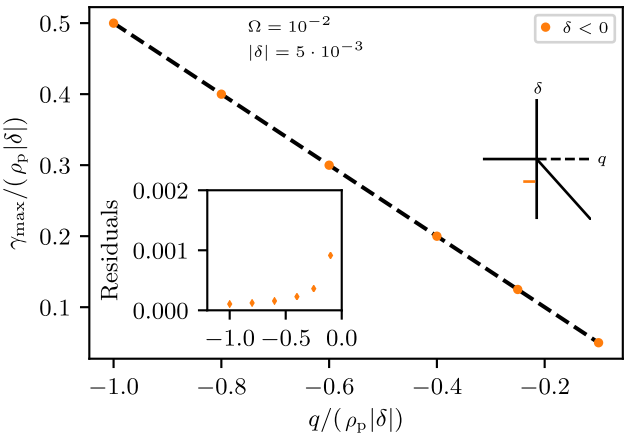

Figure 4.8.: Maximal growth rate $\gamma_{\max} = \max|\Im(\omega)|$ of the eigenmodes obtained by means of the BdG analysis of the *easy-plane* state as a function of q and $\delta < 0$. The investigated parameter regime is indicated by the orange solid line in the schematic representation of the spin-1 phase diagram (c.f. Fig. 3.1). The analysis is performed for parameters $\Omega = 10^{-2}$ and $|\delta| = 5 \cdot 10^{-3}$. The growth rate as well as the quadratic Zeeman energy are given in units of $\rho_p|\delta|$. The growth rate follows the homogeneous prediction (dashed line) given by $\gamma_{\max} = |q|/2$ over the whole parameter range. The inset shows the residuals $|\gamma_{\max,h} - \gamma_{\max}|/\gamma_{\max,h}$, with $\gamma_{\max,h}$ being the growth rate calculated from the homogeneous prediction. The deviation of the numerically extracted growth rates from the homogeneous prediction is less than 0.1% for all parameters considered. The color coding is as in the main frame. Figure taken and adapted from Ref. [129].

Furthermore, we investigate the stability properties of the antiferromagnetic state for various quadratic Zeeman energies and different signs of δ. The maximal growth rate $\gamma_{\max} = \max|\Im(\omega)|$ as a function of q and both signs of δ is shown in Fig. 4.6. To allow for a direct comparison to the homogeneous predictions, the growth rates and the quadratic Zeeman energies are given in units of $\rho_p|\delta|$. For $\delta > 0$, the growth rate follows the homogeneous prediction for the whole parameter range. In case of $\delta < 0$, we observe a constant growth rate of 1 throughout the whole parameter range. This coincides with the homogeneous setting where the maximal growth rate is always 1 in the units used here for $\delta < 0$ (c.f. Eqs. (4.7) and (4.10)).

Furthermore, our BdG analysis shows that the antiferromagnetic state is always dynamically unstable for $\delta < 0$.

Excitations about the easy-plane state

We proceed by investigating the dynamical stability of the easy-plane state given by $\psi \sim \left(\sqrt{1-q/q_0}, \sqrt{2(1+q/q_0)}, \sqrt{1-q/q_0}\right)^T$ within the easy-plane and the easy-axis phase of our trapped spin-1 system. The BdG analysis for $\delta > 0$ is not shown here as we were not able to converge to the easy-plane state in the antiferromagnetic and polar phase by means of a standard Newton method. The initial state for the wave functions used in the Newton scheme within the easy-axis phase is taken to be a Gaussian, centered around the middle of the trap, with width $\sigma = 500/\sqrt{2}$ where the amplitude in the

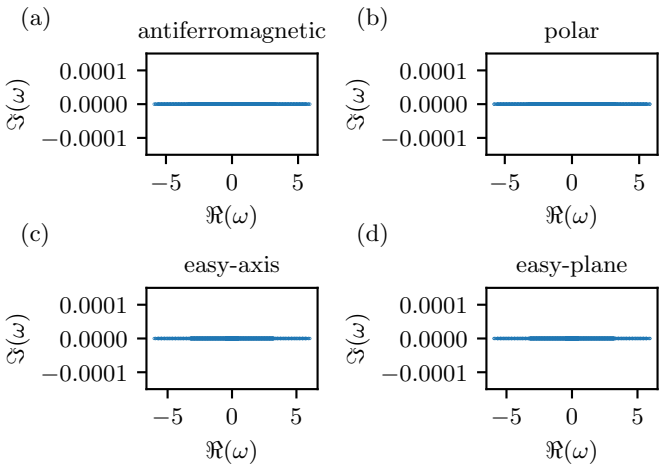

Figure 4.9.: Real ($\mathfrak{R}$) and imaginary ($\mathfrak{I}$) parts of the mode frequencies ω resulting from the BdG analysis of the *easy-axis* state $\psi \sim (1,0,0)^T$ within the (a) antiferromagnetic $(\delta, q) = (5 \cdot 10^{-3}, -0.1)$, (b) polar $(5 \cdot 10^{-3}, 0.1)$, (c) easy-axis $(-5 \cdot 10^{-3}, -0.1)$ and (d) easy-plane $(-5 \cdot 10^{-3}, 0.1)$ phase. The easy-axis state is stable in all phases. This result agrees with the prediction for the homogeneous system in case of $|\delta| = 5 \cdot 10^{-3}$. Figure taken and adapted from Ref. [129].

$m_F = 0$ component is a factor of $1/\sqrt{2}$ smaller than in the $m_F = \pm 1$ components. Within the easy-plane phase the initial Gaussian also has a width of $\sigma = 500/\sqrt{2}$, however, the amplitudes in the $m_F = \pm 1$ components are a factor of two smaller than in the $m_F = 0$ component. The Newton method converges to the easy-plane state in both phases within 18 iterations. The error tolerance is again set to 10^{-10}. It is relevant to mention here that this easy-plane state is the *only* one which we are not able to converge to throughout the parametric variations that we considered (due to the absence of convergence in the $\delta > 0$ regime).

(i) *easy-plane phase* – The real and imaginary parts of the mode frequencies of the easy-plane state in the easy-plane phase are depicted in Fig. 4.7(b). The state is dynamically stable in this parameter regime as expected from its ground state nature in this regime.

(ii) *easy-axis phase* – Fig. 4.7(a) shows the real and imaginary parts of the mode frequencies resulting from the BdG analysis of the easy-plane state in the easy-axis phase. In this case, a band of dynamically unstable modes with $|\mathfrak{I}(\omega)| > 10^{-4}$ arises. The growth rate of the most unstable mode is given by $\gamma_{\max} = 0.05 = |q|/2$. This coincides with the prediction for the homogeneous system stated in Eq. (4.12).

To confirm that the maximal growth rate indeed follows a linear function in $|q|$, we perform the BdG analysis for various negative quadratic Zeeman energies. We present the results obtained for $-\rho_p|\delta| \leq q \leq -0.1\rho_p|\delta|$. The initial guess for the Newton method has to be adjusted to reflect the final population of the three components. The maximal growth rate $\gamma_{\max} = \max|\mathfrak{I}(\omega)|$ agrees exactly with $|q|/2$ (see dashed line in Fig. 4.8). The growth rates and the quadratic Zeeman energies are again given in units of $\rho_p|\delta|$.

Excitations about the easy-axis state

We finally study the stability properties of the easy-axis state $\psi \sim (1,0,0)^T$ throughout the different phases of our trapped spin-1 system. The initial state of the wave function of

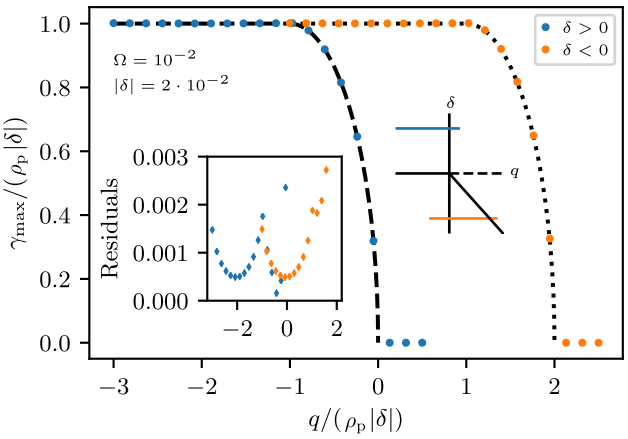

Figure 4.10.: Maximal growth rate $\gamma_{\max} = \max|\Im(\omega)|$ of the eigenmodes obtained by means of the BdG analysis of the *polar* state as a function of q and the sign of δ. The investigated parameter regime is indicated by the blue and orange solid lines in the schematic representation of the spin-1 phase diagram (c.f. Fig. 3.1). The analysis is performed for parameters $\Omega = 10^{-2}$ and $|\delta| = 2 \cdot 10^{-2}$, i.e., the strength of the spin coupling is increased by a factor of 4 as compared to Fig. 4.4. The growth rate as well as the quadratic Zeeman energy are given in units of $\rho_p|\delta|$. For $\delta > 0$, the growth rate follows the homogeneous prediction (dashed line) for the whole parameter range. The same characteristics appear in case of $\delta < 0$ where the data is matched by the dotted lines showing the homogeneous case. The inset shows the residuals $|\gamma_{\max,h} - \gamma_{\max}|/\gamma_{\max,h}$, with $\gamma_{\max,h}$ being the growth rate calculated from the homogeneous prediction. The deviation of the numerically extracted growth rates from the homogeneous prediction is less than 0.3% for all parameters considered. The color coding is as in the main frame. Figure taken and adapted from Ref. [129].

the $m_F = 1$ component used in the Newton scheme is taken to be a Gaussian, centered around the middle of the trap, with width $\sigma = 500/\sqrt{2}$. In addition, we start with a vanishing wave function in the $m_F = 0, -1$ components. The Newton method converges to the easy-axis state in all phases within 9 iterations. The error tolerance is again set to 10^{-10}.

Fig. 4.9 shows the real and the imaginary parts of the mode frequencies obtained by means of the BdG analysis of the easy-axis state in the different phases. We find that the easy-axis state is stable in all phases. This agrees with the prediction for the homogeneous system in the case of $|\delta| = 5 \cdot 10^{-3}$.

Role of spin coupling strength δ

As we observe the stability properties of the ground states in the trapped system to match the homogeneous setting, we wish to investigate the dependence of those properties on the strength of the spin coupling δ. This is of particular interest as different magnitudes of the spin coupling are realized in experiments. Therefore, we increase the spin coupling by a factor of 4 such that $|\delta| = 2 \cdot 10^{-2}$ which is close to the experimental coupling for sodium. To resolve all unstable momentum modes on our numerical grid properly,

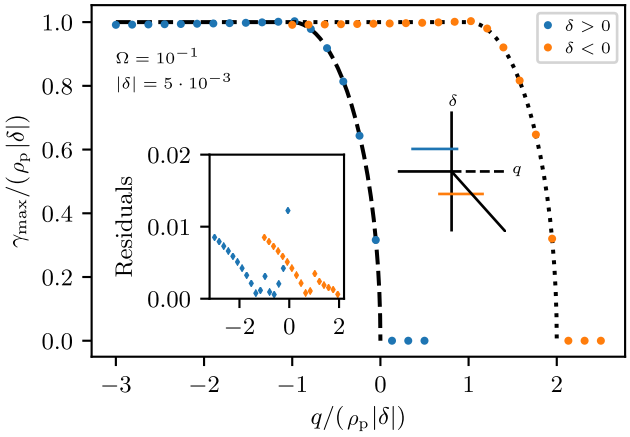

Figure 4.11.: Maximal growth rate $\gamma_{\max} = \max|\Im(\omega)|$ of the eigenmodes obtained by means of the BdG analysis of the *polar* state as a function of q and the sign of δ. The investigated parameter regime is indicated by the blue and orange solid lines in the schematic representation of the spin-1 phase diagram (c.f. Fig. 3.1). The analysis is performed for parameters $\Omega = 10^{-1}$ and $|\delta| = 5 \cdot 10^{-3}$, i.e., the normalized trap strength is increased by a factor of 10 as compared to Fig. 4.4. The growth rate as well as the quadratic Zeeman energy are given in units of $\rho_p|\delta|$. For $\delta > 0$, the growth rate follows the homogeneous prediction (dashed line) for $q > -1$. For $q < -1$ the growth rate tends to attain smaller values than in the homogeneous case (dashed line) showing a maximal deviation of about 1%. The same phenomenon appears in case of $\delta < 0$ where the data is matched by the dotted lines for $q > 1$. The growth rate again shows a maximal deviation of about 1% from the homogeneous case (dotted line) for $q < 1$. The deviations are more clearly visible in the inset which shows the residuals $|\gamma_{\max,h} - \gamma_{\max}|/\gamma_{\max,h}$, with $\gamma_{\max,h}$ being the growth rate calculated from the homogeneous prediction. The color coding is as in the main frame. Increasing the normalized trap strength by an order of magnitude only causes minor changes of the stability properties. However, such changes are expected because we are about to leave the one-dimensional regime as the transversal trapping frequency becomes comparable to the longitudinal trapping frequency. Figure taken and adapted from Ref. [129].

we have to increase the number of grid points to $N_g = 1024$. All other parameters remain unchanged. As a prototypical example, we investigate the maximal growth rates obtained by means of the BdG analysis of the polar state as a function of the quadratic Zeeman energy q and different signs of δ.

Fig. 4.10 shows the maximal growth rate $\gamma_{\max} = \max|\Im(\omega)|$ for $|\delta| = 2 \cdot 10^{-2}$. The growth rate as well as the quadratic Zeeman energy are given in units of $\rho_p|\delta|$. The growth rate follows the homogeneous prediction for the whole parameter range, both for the positive and for the negative value of δ (see dashed and dotted line respectively).

Our analysis indicates that the stability properties of the ground states do not change when increasing the spin coupling strength. Thus, we expect to observe the same dynamical instabilities in systems with different spin couplings when choosing the quadratic Zeeman energy q in the corresponding units of $\rho_p|\delta|$.

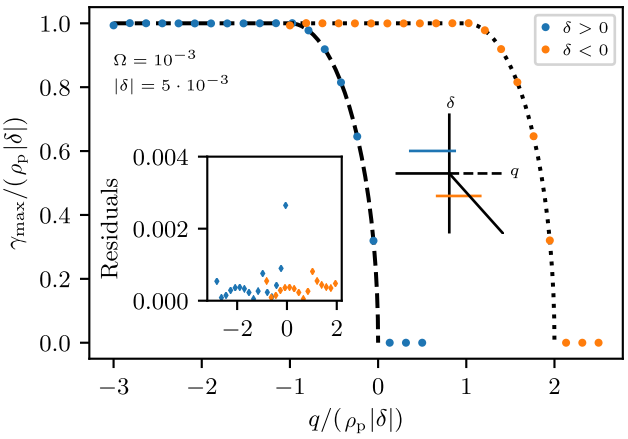

Figure 4.12.: Maximal growth rate $\gamma_{\max} = \max|\Im(\omega)|$ of the eigenmodes obtained by means of the BdG analysis of the *polar* state as a function of q and the sign of δ. The investigated parameter regime is indicated by the blue and orange solid lines in the schematic representation of the spin-1 phase diagram (c.f. Fig. 3.1). The analysis is performed for parameters $\Omega = 10^{-3}$ and $|\delta| = 5 \cdot 10^{-3}$, i.e., the normalized trap strength is decreased by a factor of 10 as compared to Fig. 4.4. The growth rate as well as the quadratic Zeeman energy are given in units of $\rho_p|\delta|$. For $\delta > 0$, the growth rate follows the homogeneous prediction (dashed line) for the whole parameter range. The same phenomenon appears in case of $\delta < 0$ where the data is matched by the dotted line. Decreasing the normalized trap strength by an order of magnitude does not change the stability properties (c.f. Fig. 4.4). The observed behavior is expected as we are further approaching the homogeneous setting when lowering Ω. The inset shows the residuals $|\gamma_{\max,h} - \gamma_{\max}|/\gamma_{\max,h}$, with $\gamma_{\max,h}$ being the growth rate calculated from the homogeneous prediction. The deviation of the numerically extracted growth rates from the homogeneous prediction is less than 0.3% for all parameters considered. Color coding as in the main frame. Figure taken and adapted from Ref. [129].

Role of normalized trap strength Ω

In the following, we want to study the role of the normalized trap strength Ω on the stability properties. All results discussed in this part are obtained for a spin coupling of $|\delta| = 5 \cdot 10^{-3}$. The homogeneous setting is recovered as $\Omega \to 0$. On the other hand, when Ω is increased, we progressively depart from the 1D regime as the condition $\omega_\perp \gg \omega_\parallel$ is not fulfilled anymore. When the transverse and longitudinal trapping frequencies become comparable in magnitude, we expect deviations of the stability properties from the previously shown ones as we have to include additional transversal degrees of freedom. Therefore, we choose the parameter Ω to be sufficiently far away from unity, so as to remain within a quasi-1D realm. To resolve the relevant momentum modes, we again use $N_g = 1024$.

We start by increasing Ω by a factor of 10 such that $\Omega = 10^{-1}$. Fig. 4.11 shows the maximal growth rate $\gamma_{\max} = \max|\Im(\omega)|$ of the eigenmodes as a function of q and the sign of δ. The growth rate as well as the quadratic Zeeman energy are given in units of

$\rho_{\mathrm{p}}|\delta|$. For $\delta > 0$, the growth rate follows the homogeneous prediction (dashed line) for $q > -1$. For $q < -1$ the growth rate is slightly smaller than in the homogeneous case (dashed line) with a maximal deviation of about 1%. The same feature appears in case of $\delta < 0$. Here, the growth rate agrees with the homogeneous prediction (dotted line) for $q > 1$. The rate also shows a maximal deviation of about 1% from the homogeneous case (dotted line) for $q < 1$.

We continue with analyzing the stability properties of the polar state when decreasing the normalized trap strength by a factor of 10 such that $\Omega = 10^{-3}$. The maximal growth rate $\gamma_{\mathrm{max}} = \max|\Im(\omega)|$ of the eigenmodes obtained by means of the BdG analysis as a function of q and the sign of δ is depicted in Fig. 4.12. The growth rate as well as the quadratic Zeeman energy are given in units of $\rho_{\mathrm{p}}|\delta|$. For $\delta > 0$, the growth rate follows the homogeneous prediction (dashed line) for the whole parameter range. The same characteristics appear in case of $\delta < 0$ (see dotted line).

We conclude that increasing the normalized trap strength by an order of magnitude leads to small deviations from the homogeneous predictions when $q < -1$ for $\delta > 0$ and $q < 1$ for $\delta < 0$. Beyond this trapping strength, one progressively departs from the one-dimensional regime as the transversal trapping frequency becomes comparable to the longitudinal one. We find no deviations of the stability properties from the previously discussed setting where $\Omega = 10^{-2}$ when decreasing the normalized trap strength by an order of magnitude. This is expected as we are approaching the homogeneous setting even further by lowering the normalized trap strength.

Our analysis shows that the principal stability properties of the ground states agree with the homogeneous setting over several orders of magnitude of the normalized trap strength Ω. Thus, we expect the characteristics of dynamical instabilities to agree in various one-dimensional trapping geometries. The trapping potential is found to not alter the overall stability properties calculated for homogeneous settings. It solely introduces the peak density of the trapped system which appears in the equations for the maximal growth rates instead of the homogeneous density. Deviations will naturally appear progressively as the trapping strength increases towards values closer to $\Omega \to 1$.

4.5. Summary and outlook

In this chapter, we elaborated on potential scenarios that can be employed to generate far-from-equilibrium states via quenches in spin-1 Bose gases. The key feature is to make use of instabilities that arise when performing parameter quenches between different phases. The exponential growth of the respective dynamically unstable momentum modes then drives the system away from equilibrium during the early-time evolution. Whether the system features an instability and is driven out of equilibrium depends on the state prior to the quench and can be inferred from investigating its dynamical stability within the post-quench phase.

We first discussed the stability properties of ground states in homogeneous spin-1 Bose gases and elaborated on the instabilities that we will use in Chpt. 5 and Chpt. 6 to generate the out-of-equilibrium configurations that subsequently lead to universal scaling dynamics in one- and two-dimensional spin-1 systems.

In the main part of this chapter, we studied the stability properties of the ground states of a trapped one-dimensional spin-1 Bose gas. We started by mapping out the ground state phase diagram of the trapped system. Therefore, we made use of the accelerated continuous-time Nesterov (ACTN) method which we extended to our multi-component

system. We revealed that the ACTN method is a robust and powerful tool for finding the ground states of a physical system as it does not require a highly accurate initial guess for the wave function of the different components. This makes the method extremely useful to explore systems with unknown phase diagrams in the future.

We numerically performed a stability analysis of the spin-1 ground states by solving the BdG equations for the trapped system. We found that the principal stability conclusions for the ground states coincide with the predictions made in absence of a trapping potential, although as shown in Fig. 4.3, the spectrum is not identical and the growth rates of modes other than the most unstable one are indeed altered. The maximal growth rates obtained in the trapped system match the homogeneous predictions when replacing the homogeneous density with the peak density of the trapped system in the corresponding equations. The near-independence of the stability conclusions is valid within the regime of quasi-1D values of the normalized trap strength (representing the ratio of longitudinal to transverse trapping frequencies). It should be noted that we explored each of the possible states (polar, antiferromagnetic, easy-plane and easy-axis) in almost each of the possible regimes, identifying the states in the regimes where they are no longer the ground state via Newton iterations. In the latter cases, potential instabilities of the states were elucidated.

Naturally, the stability analysis of the trapped spin-1 Bose gas paves the way for numerous additional investigations of interest for the near future. For instance, an obvious question that was raised through our studies is whether the easy-plane state can be found to exist in the half-plane with $\delta > 0$. Moreover, for the 1D setting, we tackled the ground states of the system and their stability over the (δ, q)-plane. However, there are numerous intriguing excited states, including ones involving solitary waves that are experimentally accessible [123]. It would be particularly relevant to extend our techniques to the latter context. Finally, while we focused on the quasi-1D setting here, adapting such techniques to 2D and 3D spinorial states would be of interest in its own right.

5. Bidirectional universal scaling dynamics in a one-dimensional spin-1 Bose gas

In this chapter, we numerically study the universal scaling dynamics of an isolated one-dimensional ferromagnetic spin-1 Bose gas. Preparing the system in an initial state far from equilibrium by means of a sudden quench into the easy-plane ferromagnetic phase, bidirectional universal scaling is found to enable and characterize the dynamics close to a non-thermal fixed point. The observed universal scaling is governed by quasi-topological excitations in the spin degree of freedom of the system. A macroscopic length scale which scales in time according to $L_\Lambda(t) \sim t^{\beta}$, with $\beta \simeq 1/4$, quantifies the coarsening of the size of spin textures. At the same time, kink-like defects populating these textures undergo a refining process measured by a shrinking microscopic length scale $L_\lambda \sim t^{\beta'}$, with $\beta' \simeq -0.17$. The combination of these scaling evolutions enables particle and energy conservation in the isolated system and constitutes the bidirectional transport in momentum space. The value of the scaling exponent β suggests the dynamics to belong to the universality class of diffusive coarsening of the one-dimensional XY-model. However, the universal momentum distribution function exhibiting non-linear transport marks the distinction between diffusive coarsening and the self-similar evolution at a non-thermal fixed point in the isolated system. This underlines the importance of the universal scaling function in classifying non-thermal fixed points.

This chapter is organized as follows: In Sect. 5.1, we elaborate on the numerical parameters as well as the applied quench protocol. With this at hand, we examine the bidirectional universal scaling dynamics of the system in Sect. 5.2. Then, we discuss the spatio-temporal scaling regime and the insensitivity of the scaling exponents with respect to the reference time in Sect. 5.3. Furthermore, we investigate the features of the bidirectional scaling in position-space correlation functions in Sect. 5.4. As universal scaling dynamics at a non-thermal fixed is a transient phenomenon in the non-equilibrium time evolution of the system, we study the departure from the scaling regime in Sect. 5.5. In Sect. 5.6 and Sect. 5.7, we then comment on the extracted scaling exponents and compare our findings to experimental observations. Finally, we summarize our results and give an outlook to future work in Sect. 5.8.

The content of this chapter is taken and adapted from Ref. [102]. I stress that the majority of the parts are taken verbatim from the publication. However, I reordered the overall structure of the presentation. I further added and/or modified formulations to embed the work into the broader context of this thesis.

5.1. Numerical methods and parameter quench

We consider a homogeneous one-dimensional spin-1 Bose gas described by the Hamiltonian in Eq. (3.24) with $d = 1$. We work in the regime of ferromagnetic spin interactions

($c_1 < 0$) and positive quadratic Zeeman energy q.

Apart from the trapping potential and a larger total density, we here perform numerical simulations in the parameter regime realized in the experiment in Ref. [35] on ^{87}Rb in the $F = 1$ hyperfine manifold. In particular, we set the ratio of the density and spin coupling to $c_0/|c_1| = 100$. We compare our findings to the experimental observations reported in Ref. [35] in Sect. 5.6.

Assuming a constant homogeneous mean density $\rho_0 = \langle\rho\rangle$, we can express the Hamiltonian in Eq. (3.24) in terms of the dimensionless length $\tilde{x} = x/\xi_s$, with spin healing length $\xi_s = \hbar/\sqrt{2M\rho_0|c_1|}$, and time $\tilde{t} = t/\tau_s$, with spin-changing collision time $\tau_s = t_s/(2\pi) = \hbar/(\rho_0|c_1|)$. The quadratic Zeeman energy is quantified by the dimensionless field strength $\tilde{q} = q\tau_s/\hbar$, the field operators become $\tilde{\psi}_m = \psi_m/\sqrt{\rho_0}$, the density $\tilde{\rho} = \rho/\rho_0$, the spin vector $\tilde{\mathbf{F}} = \mathbf{F}/\rho_0$, and the dimensionless couplings read $\tilde{c}_0 = c_0/|c_1|$ and $\tilde{c}_1 = c_1/|c_1| = \mathrm{sgn}(c_1)$. Throughout this chapter, all quantities are expressed in the above units and the tilde will be suppressed.

We consider far-from-equilibrium dynamics after a quench exerted on a homogeneous condensate in the polar phase, i.e., an initial state with $\langle\psi_0(x)\rangle \equiv 1$, by means of a sudden change of the quadratic Zeeman energy shift to the parameter range $0 < q_f < 2$. As introduced in Sect. 3.3, we compute the time evolution of observables using truncated Wigner simulations, starting each run with a field configuration for $q_i \gg 2$, with additional quantum noise added to the Bogoliubov modes [86, 87] of the polar condensate. The initial state is thus given by

$$\boldsymbol{\psi}(x) = \begin{pmatrix}0\\1\\0\end{pmatrix} + \sum_k \begin{pmatrix} a_{k,1}e^{ikx} \\ a_{k,0}u_k e^{ikx} - a^*_{k,0}v_k e^{-ikx} \\ a_{k,-1}e^{ikx}\end{pmatrix}. \tag{5.1}$$

We again omit the tilde on the rescaled quantities $\tilde{k} = k\xi_s$, $\tilde{a}_{\tilde{k},m} = a_{k,m}/(\xi_s\sqrt{\rho_0})$. The mode functions $a_{k,m}$ are complex Gaussian random variables with

$$\langle a^\dagger_{k,m} a_{k',m'}\rangle = \frac{1}{2}\delta_{mm'}\delta_{k,k'}, \tag{5.2}$$

which corresponds to adding an average occupation of half a particle in each mode k. The Bogoliubov mode functions are given by

$$u_k = \sqrt{\frac{\epsilon_k + c_0}{2\sqrt{\epsilon_k\,(\epsilon_k + 2c_0)}} + \frac{1}{2}}, \qquad v_k = \sqrt{u_k^2 - 1}, \tag{5.3}$$

with mode energy $\epsilon_k = k^2$.

For the numerical simulations, we choose the initial condensate density to be $\rho_0 = 4.5 \cdot 10^4\,\xi_s^{-1}$. The simulations are performed on a one-dimensional grid with $N_g = 4096$ grid points and periodic boundary conditions. The corresponding physical length is $\mathcal{L} = 554\,\xi_s$. We remark that a sufficient convergence of the observables is reached after averaging over $\gtrsim 10^3$ trajectories.

The quench into the easy-plane ferromagnetic phase induces transversal spin modes in the system to become unstable (see the respective highlighted instabilities in Table 4.1 and the corresponding discussion in Sect. 4.1.1), leading to the formation of a spin-wave pattern during the early-time evolution after the quench. Non-linear interactions subsequently give rise to the formation of a flat, relatively smooth background spin length

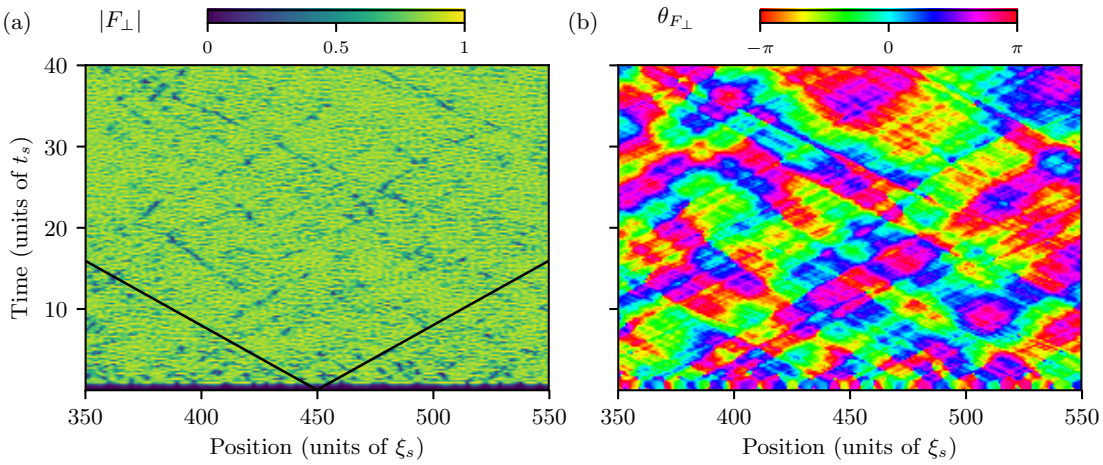

Figure 5.1.: Space-time evolution of the transversal spin $F_\perp = |F_\perp| \exp\{i\theta_{F_\perp}\}$. Quenching the system across the quantum phase transition, here to $q_f = 0.9$, introduces exponentially growing unstable modes which, after a few characteristic time scales t_s, lead to the formation of a flat background transversal spin, with textures on top. The spin textures, with size given by the distance over which a 2π phase winding occurs in the phase angle $\theta_{F_\perp}$, are populated by kink-like defects. The defects are characterized by a dip in the amplitude and a corresponding phase jump as depicted in panels (a) and (b). The solid black lines in panel (a) indicate a sound cone associated with the sound velocity of the spin degree of freedom $c_s = \sqrt{\rho_0|c_1|} = 1$. The size of the spin textures grows in time which is associated with the dilution of kink-like defects leading to long-range order developing in the phase field (see panel (b)). Each panel only shows an excerpt of the total grid of length $\mathcal{L} = 554\,\xi_s$. Figure taken and adapted from Ref. [102].

(Fig. 5.1(a)) with patches in the transversal spin orientation (Fig. 5.1(b)). Within each patch, the phase angle of the complex order-parameter field $F_\perp = |F_\perp| \exp\{i\theta_{F_\perp}\}$ is approximately constant in space. At the same time, kink-like defects, represented by a dip in the amplitude and a corresponding phase jump, are traveling across the system at roughly the speed $c_s = \sqrt{\rho_0|c_1|} = 1$ associated with the sound velocity of the spin degree of freedom (see solid lines in Fig. 5.1(a)). Spin patches in combination with phase jumps form spin textures whose size is given by the distance over which a 2π phase winding occurs. The so-formed spin structure sets the stage for the subsequent universal ordering process in which the distribution of defects dilutes. According to the evolution charts in Fig. 5.1, the average size of the textures appears to grow in time.

5.2. Bidirectional universal scaling

While we got some qualitative impression of the non-equilibrium time evolution from the single realizations of the transversal spin, we aim at a quantitative investigation of the universal scaling dynamics of the spin-1 system in this section. In particular, we lay out the important steps to extract the key features of the scaling behavior such as the spatio-temporal scaling regime, the scaling exponents, the scaling function and potential (emergent) conserved quantities that constrain the exponents.

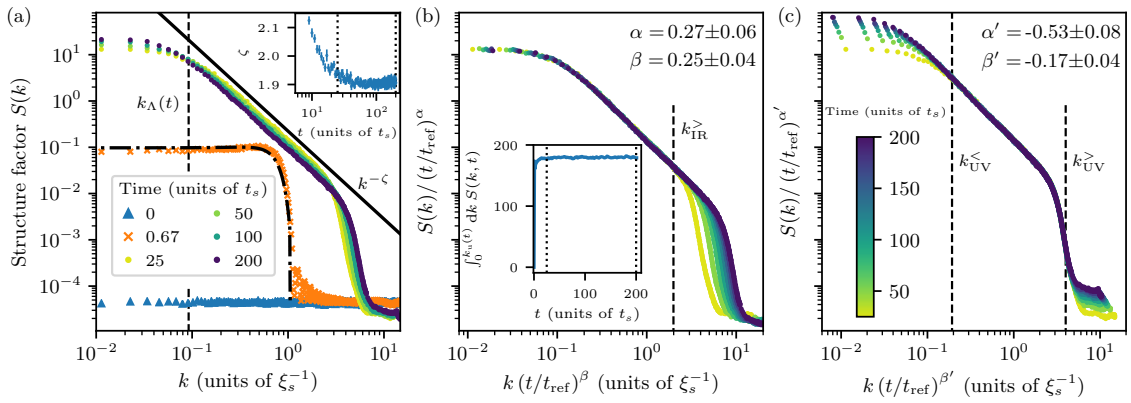

Figure 5.2.: Bidirectional self-similar evolution of the structure factor $S(k,t)$. (a) Overview of the time evolution. The initial polar condensate at $t = 0$ shows ground-state fluctuations around zero spin (blue triangles). At $t = 0.67\,t_s$ (orange crosses), the population of the momentum modes is well approximated by the Bogoliubov prediction stated in Eq. (5.4) (dash-dotted line). For times $25\,t_s \leq t \leq 200\,t_s$, the system is in the spatio-temporal scaling regime and evolves in a self-similar manner (dots). Three qualitatively different momentum regimes emerge: A plateau below a characteristic momentum scale $k_\Lambda(t)$ (which is more clearly seen in panel (b); the dashed line exemplarily marks the scale extracted by means of fitting the scaling function in Eq. (5.9) to the infrared regime of the data at time $t = 25\,t_s$), a $k^{-\zeta}$ power-law fall-off at momenta up to a scale k_λ(t) and a steeper power-law decay at large momenta. The inset shows the extracted exponent ζ (cf. solid line in main frame). (b) Structure factor in the temporal scaling regime rescaled according to Eq. (5.7) with scaling exponents $\alpha = 0.27 \pm 0.06$ and $\beta = 0.25 \pm 0.04$ extracted via a least-square fit. Within the infrared scaling regime, $k \leq k_{\mathrm{IR}}^{>}$ (dashed line), all curves collapse onto a single one. The inset shows that, within this momentum regime, the local spin fluctuations are conserved (up to $\sim 2\%$) for times $25\,t_s \leq t \leq 200\,t_s$ (dotted lines). The corresponding upper bound for the integral is set by $k_u(t) = k_{\mathrm{IR}}^{>} \cdot (t/t_{\mathrm{ref}})^{-1/4}$ with $t_{\mathrm{ref}} = 25\,t_s$. Within errors, the scaling exponents are consistent with $\alpha = \beta$. (c) Structure factor in the temporal scaling regime rescaled according to Eq. (5.7) with $\alpha' = -0.53 \pm 0.08$ and $\beta' = -0.17 \pm 0.04$. Within the ultraviolet scaling regime, $k_{\mathrm{UV}}^{<} \leq k \leq k_{\mathrm{UV}}^{>}$ (marked by dashed lines), all curves collapse onto a single one. Figure taken and adapted from Ref. [102].

For the quantitative analysis of the observed phase-ordering dynamics, we consider the structure factor of the transversal spin $S(k,t) = \langle |F_\perp(k,t)|^2 \rangle$, see Eq. (3.33). Fig. 5.2(a) shows the time evolution of the structure factor $S(k,t)$ for a quench to $q_\mathrm{f} = 0.9$ in the easy-plane ferromagnetic phase. The polar condensate at $t = 0$ has no magnetization. At $t = 0.67\, t_\mathrm{s}$, the population of the momentum modes of the structure factor within the instability regime fits the Bogoliubov prediction given by

$$S(k,t) = 4 \sinh^2 (\gamma_k t) / \gamma_k^2. \tag{5.4}$$

Here, the growth rate of unstable momentum modes determined by

$$\gamma_k = \sqrt{(\epsilon_k + q)\,(2 - \epsilon_k - q)}\,, \tag{5.5}$$

with mode energy $\epsilon_k = k^2$, is obtained as the imaginary part of the complex Bogoliubov mode energy [130]. In the course of the subsequent non-linear redistribution of the excitations, the system is found to enter a spatio-temporal scaling regime where the structure factor evolves in a self-similar manner. During this period of the relaxation process, we observe three qualitatively different momentum regions which reflect the patterns seen in the single spatial realizations in Fig. 5.1.

Below a characteristic momentum scale $k_\Lambda(t)$, the structure factor $S(k,t)$ shows a plateau. Kink-like defects account for the power-law fall-off of the structure factor $S(k,t) \sim k^{-\zeta}$ for momenta $k \lesssim k_\lambda(t)$ [69]. The exponent $\zeta = d + n$ depends on the dimensionality of the system and the defect structure. For kink-like defects ($n = 1$) in one spatial dimension, the resulting exponent $\zeta = 2$ is close to the value $\zeta = 1.91 \pm 0.02$ which we extract by fitting the scaling form

$$f_\mathrm{fit}(k) = A/[1 + (k/k_\Lambda)^{\zeta}] \tag{5.6}$$

to the infrared (IR) part of $S(k,t)$. For large momenta $k \gtrsim k_\lambda(t)$, the structure factor shows a steeper fall-off, before saturating at the level of ground-state fluctuations, $S(k \to k_a) \simeq 0.5 \times 10^{-4}$, where k_a denotes the lattice cutoff.

Fig. 5.2(a) indicates that the structure factor exhibits scaling according to

$$S(k,t) = (t/t_\mathrm{ref})^{\alpha}\, f_\mathrm{s}\left([t/t_\mathrm{ref}]^{\beta}\, k \right)\,, \tag{5.7}$$

see Eq. (3.34), within a region of IR momenta below the ultraviolet (UV) end of the $k^{-\zeta}$ power-law fall-off, i.e., for $k \lesssim k_\lambda(t)$. Taking the structure factor at time $t_\mathrm{ref} = 25\, t_\mathrm{s}$ as a reference and performing a least-square fit of the data up to $t = 200\, t_\mathrm{s}$ yields $\alpha = 0.27 \pm 0.06$ and $\beta = 0.25 \pm 0.04$. The performed least-square analysis is based on the method described in the Appendix of Ref. [34]. The errors are determined from the width of a Gaussian distribution used to fit the marginal-likelihood functions of both scaling exponents [34]. These errors can become relatively large due to statistical uncertainties and systematic deviations caused by the limited scaling window. To get some further insights into the temporal scaling regime, we discuss the scaling exponents as a function of the reference time in Sect. 5.3.

Rescaling the structure factor in time by making use of the scaling form in Eq. (5.7) yields the collapse onto a single curve below the momentum scale $k_\mathrm{IR}^{>}$, as shown in Fig. 5.2(b). The inset in Fig. 5.2(b) demonstrates that the local spin fluctuations are conserved in time (up to a relative error of 2%) within the IR scaling regime. Hence, we

find, to a good approximation, that $\partial_t \int_0^{k_u(t)} \mathrm{d}k\, S(k,t) = 0$, with $k_u(t) = k_{IR}^{>} \cdot (t/t_{ref})^{-1/4}$ and $t_{ref} = 25\, t_s$. Using the scaling form in Eq. (5.7) for the structure factor $S(k,t)$ results in the scaling relation $\alpha = \beta$. The numerically extracted exponents are consistent with this scaling relation. As a consequence of the conserved local spin fluctuations, we can describe the time evolution of the system for momenta $k \lesssim k_\lambda(t)$ by a single scaling exponent and thus a single characteristic IR length $L_\Lambda(t) \sim t^{\beta}$ with $\beta \simeq 0.25$. This macroscopic length scale corresponds to the size of the spin textures in the system.

We further note that the flat background spin length seen in bright green color in Fig. 5.1(a) reflects the approximate conservation of the integrated spin structure factor, $\langle |F_\perp|^2 \rangle (k = 0) = \sum_p \langle F_\perp^*(p) F_\perp(p) \rangle$, cf. inset of Fig. 5.2(b), which governs the scaling evolution towards the non-thermal fixed point and quickly assumes a near-equilibrium value. On top of that, week amplitude fluctuations are seen which, to linear order, are expected to include the gapped excitations of the spin length.

In the UV range of momenta, the structure factor additionally suggests a second characteristic length $L_\lambda(t)$ which shrinks in time. Fig. 5.2(c) shows that the rescaled structure factor collapses onto a single curve for momenta $k_\Lambda(t) \lesssim k \lesssim k_{UV}^{>}$ when choosing the scaling exponents $\alpha' = -0.53 \pm 0.08$ and $\beta' = -0.17 \pm 0.04$.

Being able to rescale the structure factor in the IR as well as in the UV regime of momenta clearly shows the bidirectional nature of the numerically observed universal scaling. Hence, we find that the structure factor, in a range of momenta with strong spin-wave excitations, obeys the extended scaling form [56]

$$S(k,t) = L_\Lambda(t)^{\alpha/\beta} f_s(L_\Lambda(t)k, L_\Lambda(t)/L_\lambda(t)), \tag{5.8}$$

with the scaling function being well approximated by

$$f_s(x,y) = f_0[1 + x^{\zeta} + x^{\zeta'} y^{\zeta - \zeta'}]^{-1}\,. \tag{5.9}$$

Here, $\zeta' \simeq 12 \gg \zeta$ characterizes the large-k fall-off. For the bidirectional scaling behavior shown in Fig. 5.2, the scaling function f_s follows, to a good approximation, the form in Eq. (5.9), with a single power-law exponent ζ in between the IR and UV scales $k_\Lambda(t)$ and $k_\lambda(t)$, respectively.

For the scaling function in Eq. (5.9), the temporal scaling evolution of $L_\Lambda(t)$ and $L_\lambda(t)$ implies that the exponents are related by

$$\alpha - \alpha' = (\beta - \beta')\zeta\,. \tag{5.10}$$

Moreover, imposing kinetic energy conservation in the ultraviolet scaling regime, i.e., $\partial_t \int_{k_l(t)}^{k_u(t)} \mathrm{d}k\, k^z\, S(k,t) = 0$ within a corresponding UV momentum interval $[k_l(t), k_u(t)]$, yields $\alpha' = (1+z)\,\beta'$. Taking the additional conservation of local spin fluctuations in the IR, $\alpha = \beta$, one obtains the dynamical exponent z, characterizing the dispersion $\omega(k) \sim k^z$, to be

$$z = (\zeta - 1)\,(1 - \beta/\beta')\,. \tag{5.11}$$

Inserting the extracted parameters $\beta = 0.25 \pm 0.04$, $\beta' = -0.17 \pm 0.04$ and $\zeta = 1.91 \pm 0.02$, we find $z = 2.24 \pm 0.38$.

To cross-check this result, we numerically determine the dispersion for which the kinetic energy $\int_{k_l(t)}^{k_u(t)} \mathrm{d}k\, \omega(k)\, S(k,t)$ shows the minimal deviation from being conserved within the UV scaling regime set by $k_l(t) = k_{UV}^{<} \cdot (t/t_{ref})^{0.17}$ and $k_u(t) = k_{UV}^{>} \cdot (t/t_{ref})^{0.17}$

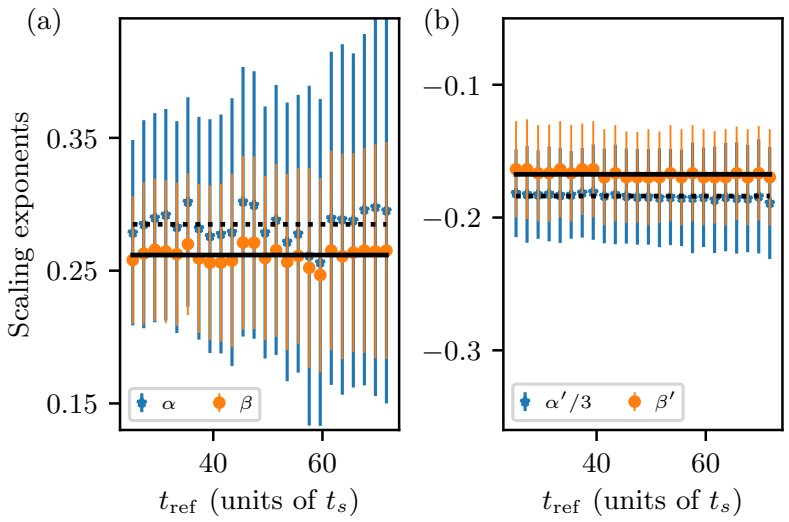

Figure 5.3.: (a) Scaling exponents α (blue stars) and β (orange circles) obtained from least-square rescaling fits to $S(k,t)$ within the time window $[t_{\mathrm{ref}}, t_{\mathrm{ref}} + \Delta t]$ with $\Delta t = 120\,t_{\mathrm{s}}$. The scaling exponents are independent of the reference time t_{ref}. A constant fit to the data reveals $\alpha = 0.284 \pm 0.013$ (dashed line) and $\beta = 0.261 \pm 0.008$ (solid line). The error is given by the standard deviation of all data points as they are not statistically independent. (b) Scaling exponents $\alpha'/3$ (blue stars) and β' (orange circles) obtained by the same method and within the same time window as in (a). A constant fit to the data yields $\alpha'/3 = -0.183 \pm 0.002$ (dashed line) and $\beta' = -0.168 \pm 0.004$ (solid line). Error computed as in (a). Figure taken and adapted from Ref. [102].

with $t_{\mathrm{ref}} = 25\,t_{\mathrm{s}}$. This method yields $z = 2.15 \pm 0.05$ consistent with the dynamical exponent directly calculated from the extracted scaling parameters.

5.3. Scaling regime

To study universal scaling dynamics, it is inevitable to identify the spatio-temporal scaling regime during the non-equilibrium time evolution of the system. A key feature of this regime is a constant scaling function which we identified in Sect. 5.2 by means of a fit as stated in Eq. (5.6) to the structure factor of the transversal spin at different evolution times. Furthermore, self-similar scaling is characterized by scaling exponents that are independent of the reference time t_{ref} within the spatio-temporal scaling period. In this section, we confirm this property of the system by performing the least-square rescaling analysis for different reference times t_{ref}, within the constant time window $[t_{\mathrm{ref}}, t_{\mathrm{ref}} + \Delta t]$ with $\Delta t = 120\,t_{\mathrm{s}}$. We find that the scaling exponents settle to a constant value at $t_{\mathrm{ref}} \simeq 25\,t_{\mathrm{s}}$ which marks the onset of the scaling regime (see Fig. 5.3).

A constant fit to the extracted IR scaling exponents for $25\,t_{\mathrm{s}} \leq t_{\mathrm{ref}} \leq 74\,t_{\mathrm{s}}$ yields $\alpha = 0.284 \pm 0.013$ and $\beta = 0.261 \pm 0.008$ (see Fig. 5.3(a)). For the UV scaling exponents we find $\alpha' = -0.549 \pm 0.006$ and $\beta' = -0.168 \pm 0.004$ (see Fig. 5.3(b)). The error is given by the standard deviation of all data points, which are not statistically independent. Making use of analyzing the scaling exponents for various reference times incorporates fluctuations of the scaling exponents caused by statistical errors in each reference spectrum thus leading to a potentially more accurate determination of the universal exponents.

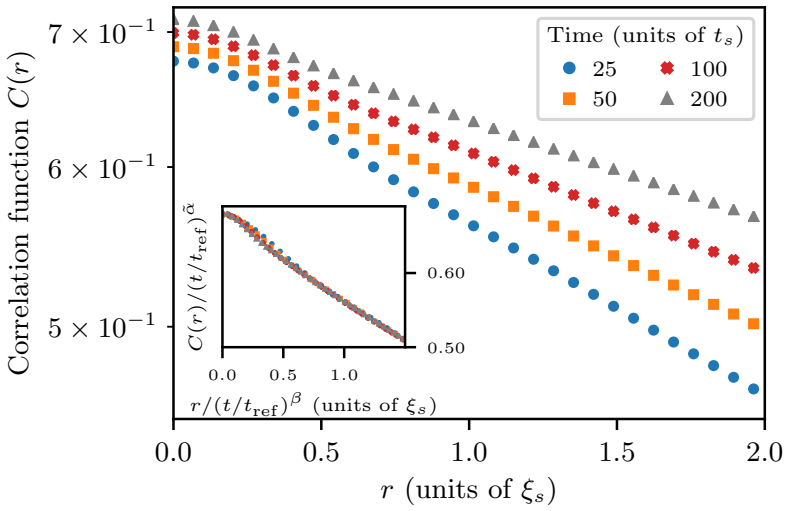

Figure 5.4.: Spatial first-order coherence function $C(r,t)$ within the temporal scaling regime. $C(r,t)$ is calculated by applying a Fourier transform to the structure factor $S(k,t)$. At larger distances the correlation function decays exponentially $C(r,t) \sim \exp(-r/L_\Lambda)$, with time-evolving correlation length $L_\Lambda(t) \sim t^{\,\beta}$. The inset shows $C(r,t)$ rescaled with $\tilde{\alpha} = 0.02$ and $\beta = 0.25$ for reference time $t_{\mathrm{ref}} = 25\, t_{\mathrm{s}}$ such that the data collapses at large distances. This enables us to observe the shrinking of the characteristic UV length scale $L_\lambda(t)$ occurring at distances below $r \simeq 0.5$. Note the semi-log scale of the inset. Figure taken and adapted from Ref. [102].

5.4. Spatial correlation function

The two different characteristic length scales that undergo universal scaling dynamics in the system can also be studied by means of the position-space correlation function $C(r,t)$ which is calculated by applying a Fourier transform to the structure factor $S(k,t)$. Note that $r = x - x'$ denotes the distance between positions x and x' on the one-dimensional grid. Fig. 5.4 shows the position-space correlation function for distances $0 \leq r \leq 2$ within the temporal scaling regime.

The shrinking of the characteristic UV length scale $L_\lambda(t) \sim t^{\,\beta'}$ is found below distances $r \simeq 0.5$. It is related to the quadratic part of the correlation function at short distances becoming steeper (see inset of Fig. 5.4). Note that the effect is small due to the slow scaling with $\beta' \simeq -0.17$.

At larger distances, the correlation function is given by

$$C(r,t) \sim \exp\left(-\frac{r}{L_\Lambda}\right), \tag{5.12}$$

with time-evolving correlation length $L_\Lambda(t) \sim t^{\,\beta}$. The growth of the correlation length in time is associated with the decrease of the slope of the correlation function drawn in semi-logarithmic representation. The data collapses onto a single curve at large distances when rescaling the argument of the correlation function with the IR scaling exponent $\beta = 0.25$ (see inset of Fig. 5.4). To account for small variations in the amplitude of the correlation function we introduce an exponent $\tilde{\alpha} = 0.02$.

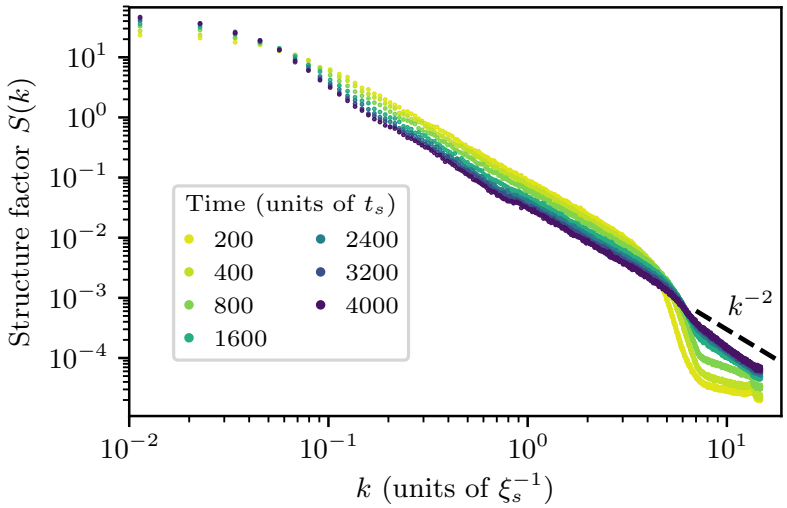

Figure 5.5.: Time evolution of the structure factor $S(k,t)$ on time scales up to $t = 4000\,t_s$ indicating the departure from the scaling regime. Bidirectional self-similar dynamics can be observed even up to $t \simeq 400\,t_s$ as the scaling function remains the same as in Fig. 5.2. For $t \geq 800\,t_s$, a thermal tail given by an approximate k^{-2} power law (see black dashed line) is present in the UV regime of momenta. The mean kinetic energy in the tail gradually increases as time evolves up to $t = 4000\,t_s$. Note that the final equilibration process is beyond the time scales considered in our numerical simulations. Figure taken and adapted from Ref. [102].

5.5. Departure from the scaling regime

Self-similar evolution within a spatio-temporal scaling regime during the phase-ordering process of a non-equilibrium system is understood to generally occur as a transient phenomenon on the way to equilibrium. Indications of this behavior become visible in the time evolution of the structure factor $S(k,t)$ on time scales beyond $t = 400\,t_s$ (see Fig. 5.5). To study the transient nature in more detail, we extract the time evolution of the characteristic momentum scales $k_\Lambda(t) \sim L_\Lambda(t)^{-1}$ and $k_\lambda(t) \sim L_\lambda(t)^{-1}$ by means of fitting the scaling form in Eq. (5.9) to the structure factor $S(k,t)$ for evolution times up to $t = 2000\,t_s$. We find that the IR scale $L_\Lambda(t)$ shows scaling with $\beta \simeq 0.25$ for all times considered for the extraction (see Fig. 5.6(a)). To retain the IR scaling, energy has to be transported to the UV. In the case of the bidirectional scaling evolution, the energy transported to the UV leads to the sharpening of kink-like defects. However, defects in the spin degree of freedom are expected to have a natural minimal width on the order of the spin healing length. As the UV scale approaches this length scale, i.e., as $L_\lambda(t) = 2\pi/k_\lambda(t) \to 1$, we thus observe that the UV scaling exponent starts to deviate from $\beta' \simeq -0.17$ (see Fig. 5.6(b)) causing the system to leave the regime of bidirectional universal scaling dynamics. The deviation of the scaling exponent becomes clearly visible around $t \simeq 500\,t_s$. This behavior is accompanied by a build-up of a thermal tail in the range of momenta larger than $k_{\mathrm{UV}}^{>}$, which instead stores the transported energy (cf. Fig. 5.5).

Although the system leaves the regime of bidirectional universal scaling dynamics at $t \simeq 500\,t_s$, it remains close to the non-thermal fixed point as the IR scaling exponent is unaffected for evolution times up to $t = 2000\,t_s$. At a later point in time, which is

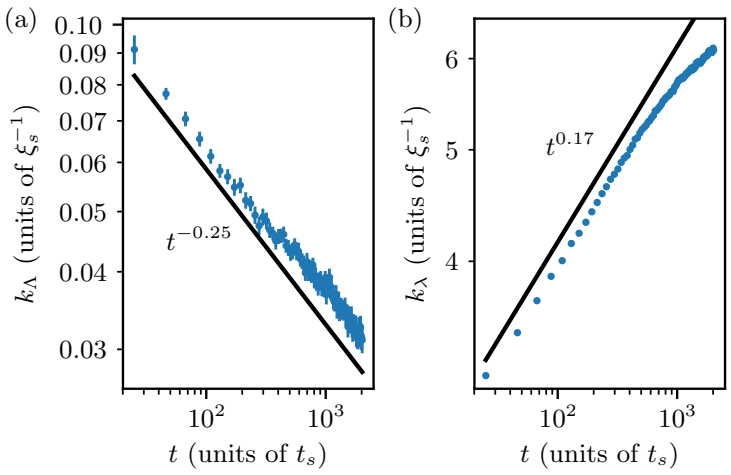

Figure 5.6.: Time evolution of the characteristic IR scale $k_\Lambda(t)$ (panel (a)), as well as the UV scale $k_\lambda(t)$ (panel (b)). While the IR scale decreases algebraically as $k_\Lambda(t) \sim L_\Lambda(t)^{-1} \sim t^{-0.25}$ over the whole range of evolution times considered (see solid line in (a)), the UV scale starts to deviate from $k_\lambda(t) \sim L_\lambda(t)^{-1} \sim t^{0.17}$ (see solid line in (b)) at $t \simeq 500\, t_s$. The deviation arises as the corresponding UV length scale approaches the spin healing length, i.e., as $L_\lambda(t) = 2\pi/k_\lambda(t) \to 1$. While this causes the system to leave the regime of bidirectional universal dynamics, it stays close to the non-thermal fixed point as the IR scaling behavior remains unchanged. The characteristic scales $k_\Lambda(t)$ and $k_\lambda(t)$ are obtained by means of fitting the scaling form in Eq. (5.9) to the structure factor up to a maximum momentum given by $k_{\mathrm{UV}}^{>}$ (see Fig. 5.2(c)). We remark that the scaling function in Eq. (5.9) does not appropriately capture the data in the UV regime of momenta anymore for evolution times $t \gtrsim 2000\, t_s$, which strongly influences the extraction of the UV scale $k_\lambda(t)$. Hence, we restrict our analysis to the time window $25\, t_s \leq t \leq 2000\, t_s$. For all times considered, $k_\Lambda(t)$ is comfortably larger than the momentum scale $k_{\mathcal{L}} = 2\pi/\mathcal{L} = 0.011$ associated with the system size $\mathcal{L}$. Error bars correspond to the fit error of the extracted scales. Note the double-log scale. Figure taken and adapted from Ref. [102].

presently beyond the reach of our simulations, we expect the rising mean kinetic energy in the thermal tail as well as the finite size of the system to induce the system to move away from the fixed point and towards final equilibrium.

5.6. Discussion of scaling exponents

So far, we presented our numerical findings that characterize the bidirectional scaling behavior of the one-dimensional spin-1 system. In this section, we discuss the extracted infrared scaling in the context of related one-dimensional models.

As the scaling dynamics of the spinor system takes place in the transversal spin, it is instructive to compare with similar behavior known for the 1D XY model. Considering an open system coupled to a heat bath and applying a temperature quench into the ordered phase leads to phase-ordering kinetics with a temporal scaling exponent $\beta = 1/4$ [138]. At first sight, this appears to provide the universality classification for the self-similar

dynamics seen in our system. However, the nature of the respective evolutions turns out to be qualitatively very different. Coarsening in the 1D XY model with non-conserved order parameter can be described as free phase diffusion of the order-parameter phase angle. As the topological charge is locally conserved in the system, the position-space correlation function at large distances r is given by $C(r,t) \to \exp(-r/\xi_0)$, where ξ_0 is the initial correlation length of the system. Thus, the characteristic IR length scale does not change in time. Instead, the scaling takes place in the UV giving rise to a broadening Gaussian spatial correlation function during the ordering dynamics, and thus to a sharpening Gaussian momentum-space structure factor [138].

In contrast, the universal scaling dynamics in our isolated spinor gas is driven by nonlinear dynamics of the spinor field, leading to a bidirectional transport of excitations in momentum space. This transport redistributes spin-wave excitations from an intermediate scale to both, smaller and larger wave numbers. Thereby, the correlation length $L_\Lambda(t) \sim k_\Lambda(t)^{-1}$ grows in time as $L_\Lambda(t) \sim t^{1/4}$. Note that a similar behavior of the correlation length has been reported in the one-dimensional p-state clock model for a moderate-sized $p > 4$ in Ref. [154]. We expect the coarsening dynamics described by this model to be closer to that of our system where the kink-like defects in the transversal spin are accompanied by phase jumps similar to the phase steps occurring in the p-state clock model.

5.7. Comparison to experimental observations

In this section, we compare our findings with the experimental observations made in Ref. [35]. In the experiment, we study the non-equilibrium dynamics of a spin-1 Bose gas consisting of ^{87}Rb atoms confined in a quasi-one-dimensional cigar-shaped trapping geometry with trapping frequencies $\omega_\parallel \simeq 2\pi \cdot 2.2$ Hz and $\omega_\perp \simeq 2\pi \cdot 250$ Hz. The mean atom number in the experiment is $N \approx 70000$ leading to a one-dimensional peak density of $\rho_\mathrm{p} \approx 250\,\mu m^{-1}$. This renders the system to be one-dimensional in the spin degree of freedom as the spin-healing length is larger than the transversal extension of the atomic cloud. However, the system appears quasi-one-dimensional in the density degree of freedom as the corresponding healing length is smaller than the transversal extension.

The experimental system is initially prepared as a polar condensate deep in the polar phase at a quadratic Zeeman energy $q \gg 2\rho_\mathrm{p}|c_1|$. Using microwave dressing, we perform a sudden quench of the quadratic Zeeman energy into the easy-plane ferromagnetic phase. The post-quench magnetic field is adjusted such that $q \approx \rho_\mathrm{p}|c_1|$, with $\rho_\mathrm{p}|c_1| \approx 2\pi\cdot 2$ Hz. This choice ensures that the system remains in the easy-plane phase throughout the entire time evolution irrespective of small fluctuations of the microwave dressing.

After four seconds of evolution time, which is on the order of ten spin-changing collision times in our numerical simulations, the system enters a universal scaling regime indicated by a constant power law of the momentum-space correlation function of the transversal spin. Note that due to a decaying amplitude of the spin on time scales beyond four seconds, we considered the correlator of the phases of the transversal spin in this work. This observable contains equivalent information about the scaling dynamics as the complex transversal spin in case of a flat distribution of the spin amplitude which holds for the performed experiments.

Rescaling the momentum-space correlator in the IR momentum regime leads to a scaling exponent $\beta \simeq 1/2$. Due to an approximate conservation of fluctuations we find a value of $\alpha \simeq \beta$ consistent with an emergent conserved quantity in one spatial dimension.

The experimentally observed IR scaling exponent $\beta \simeq 1/2$ differs distinctly from the numerically obtained exponent $\beta \simeq 1/4$. We attribute the different scaling exponent observed in the experiment to the absence of quasi-topological excitations in the transversal spin degree of freedom. While the strictly one-dimensional system studied by means of numerical simulations features spin textures and kink-like defects that characterize the scaling dynamics, the cigar-shaped trapping geometry seems to inhibit the creation of such types of excitations during the non-equilibrium time evolution. The experimentally observed scaling dynamics is thus much closer to $U(N)$-symmetric systems which show a scaling evolution governed by $\beta = 1/2$, see Chpt. 7 for a detailed discussion of the scaling properties of the $U(N)$-symmetric Bose gas. For further information concerning the experimental observations see Refs. [35, 155].

5.8. Summary and outlook

In this chapter, we have numerically demonstrated universal self-similar dynamics in a one-dimensional ferromagnetic spin-1 Bose gas characterized by two separate time-evolving scales. The corresponding bidirectional self-similar evolution of the structure factor of the transversal spin is determined by the algebraic growth of an infrared scale $L_\Lambda(t) \sim t^{\beta}$ associated with the conservation of local spin fluctuations as well as an algebraic decrease of a second scale $L_\lambda(t) \sim t^{\beta'}$ connected to kinetic energy conservation in the ultraviolet. The growth of $L_\Lambda(t)$ is observed to be associated with the dilution of kink-like defects separating patches of approximately uniform spin orientation, while $L_\lambda(t)$ is set by the decreasing microscopic width of the defects.

Simulating the system in a strictly one-dimensional homogeneous setting, we extracted the IR scaling exponent $\beta \simeq 0.25$. Although the value of the scaling exponent β suggests the dynamics to belong to the universality class of diffusive coarsening of the one-dimensional XY-model, we showed that this is indeed not the case as both systems feature distinctly different universal scaling functions. We remark that the value of $\beta \simeq 0.25$ is considerably smaller than the standard exponent $\beta = 1/2$ found in isolated systems for universal scaling transport towards the IR [34, 35, 37, 42, 45, 50, 56, 61], associated with near-Gaussian fixed points [45, 61], and, in open systems in two and three dimensions, for diffusive coarsening of a non-conserved order-parameter field [69].

Furthermore, we compared our findings to the experimental observation of universal scaling dynamics reported in Ref. [35]. The distinct deviation from the experimentally observed exponent $\beta \simeq 1/2$ is attributed to the presence of quasi-topological excitations in the numerical simulations.

Note that our results show that universal scaling dynamics associated with a non-thermal fixed point is possible in a purely one-dimensional geometry in contrast to the case of a one-dimensional single-component gas where no scaling evolution is expected due to kinematic constraints on elastic $2 \to 2$ scattering from energy and particle-number conservation and $\beta \simeq 0.1$ has been observed experimentally [36].

There are a number of interesting prospects for future research arising from the numerical as well as experimental studies discussed in this chapter. First of all, it is so far unknown whether there is the possibility to generate a far-from-equilibrium configuration in the strictly one-dimensional numerical setting that exhibits universal scaling dynamics in the easy-plane ferromagnetic phase which is not dominated by quasi-topological excitations. This naturally raises the question whether we then observe the same scaling exponents as in the experimental quasi-one-dimensional geometry or no scaling at all

due to the absence of a transversal degree of freedom.

We can also turn the problem around and ask whether a scaling exponent of $\beta = 1/4$ is observed experimentally in presence of quasi-topological excitations. Due to the recently developed ability of performing local manipulations to clouds of bosonic quantum gases in experiments, it is possible to imprint distributions of quasi-topological excitations in a controlled and reproducible fashion. This allows investigating the interactions of potential quasi-topological excitations in the easy-plane phase of the spin-1 system experimentally. Such studies might also give access to an explanation for the numerically observed value of the scaling exponent β, which is lacking so far.

6. Violation of single-length-scaling dynamics via spin vortices in a two-dimensional spin-1 Bose gas

In this chapter, we consider the universal scaling dynamics at a non-thermal fixed point within the phase-ordering process of an isolated quasi-two-dimensional spin-1 Bose gas quenched into the easy-plane ferromagnetic phase. Preparing the initial system in an unmagnetized anti-ferromagnetic state, the subsequent ordering involves both polar core and Mermin-Ho spin vortices, with the ratio between the different vortices controllable by the quench parameter. Ferromagnetic domain growth occurs as these vortices annihilate. The distinct dynamics of the two types of vortices means that the domain growth law is determined by two macroscopic length scales, violating the standard dynamical scaling hypothesis characterizing the self-similar evolution of correlation functions in the universal scaling regime. Nevertheless, we find that universality of the ordering process manifests in the decay laws for the spin vortices. To provide a full picture of the phase ordering dynamics, we present results for the scaling of the order parameter correlation function and the hydrodynamic decomposition of the kinetic energy of the system.

This chapter is organized as follows: In Sect. 6.1, we elaborate on the numerical parameters as well as the applied quench protocol. In Sect. 6.2, we introduce the relevant topological excitations of the system in the easy-plane ferromagnetic phase, which in this case are polar core and Mermin-Ho spin vortices. Then, we present an algorithm for the detection of different types of spin vortices in Sect. 6.3. With this at hand, we examine the universal phase ordering dynamics of the system. The main numerical results are presented in Sect. 6.4 and Sect. 6.5. We first extract the universal decay laws of the spin vortices and show the violation of single-length scaling. Furthermore, we investigate the origin of the shape of the scaling function characterizing the momentum-space correlations of the order-parameter field during the phase ordering by performing a hydrodynamic decomposition of the kinetic energy density. Finally, we summarize our findings and give an outlook to future work in Sect. 6.6.

The content of this chapter is taken and adapted from Ref. [109]. I stress that the majority of the parts are taken verbatim from the publication. However, I reordered the overall structure of the presentation. I further added and/or modified formulations to embed the work into the broader context of this thesis.

6.1. Numerical methods and parameter quench

We consider a homogeneous quasi-two-dimensional (2D) spin-1 Bose gas described by the Hamiltonian in Eq. (3.24) with $d = 2$. We again work in the regime of ferromagnetic spin interactions given by $c_1 < 0$.

Starting from a polar condensate at $q \gg q_0 = 2\rho_0|c_1|$, where we denote the total condensate density by ρ_0, it has been shown that after a sudden quench across the quantum phase transition, separating the polar and the easy-plane phase, the system undergoes universal scaling dynamics within the easy-plane ferromagnetic phase [35, 102, 104]. Here, we investigate the phase ordering dynamics occurring when quenching the system into the easy-plane ferromagnetic phase starting from the state

$$\psi_{\mathrm{AF}} = \sqrt{\frac{\rho_0}{2}} \begin{pmatrix} e^{i\phi_1} \\ 0 \\ e^{i\phi_{-1}} \end{pmatrix}, \tag{6.1}$$

where $\phi_{\pm 1}$ denote arbitrary phases which we choose to be zero for our simulations. This unmagnetized state is a mean-field ground state for the case of anti-ferromagnetic interactions ($c_1 > 0$), see Sect. 3.2.2. It can be easily generated experimentally by applying a $\pi/2$ radio-frequency (rf)-rotation to a polar condensate [156].

Quenching into the easy-plane ferromagnetic phase gives the system an excess energy (relative to the easy-plane ground state) of $\Delta\epsilon_{\mathrm{AF}} = q + \frac{1}{4}q_0\,(1 - q/q_0)^2$. This is larger than the excess energy for a polar initial condition ($\Delta\epsilon_{\mathrm{P}} = \Delta\epsilon_{\mathrm{AF}} - q$), indicating that more heating in the form of thermal excitations will occur for the initial condition we employ. However, the degree of extra heating will be less for smaller q and here we focus on the regime $q \lesssim 0.3\,q_0$.

To seed the growth of unstable modes due to the quench, and the subsequent formation of symmetry breaking domains, it is crucial to account for fluctuations beyond mean-field order. We implement this by adding noise to the initial state according to the truncated Wigner prescription, see Sect. 3.3 and Refs. [86, 87, 105]. The time evolution of this initial state is then given by the spin-1 Gross-Pitaevskii equations (GPEs) stated in Eq. (3.27).

Our quasi-2D simulations are performed for the case of $c_0/|c_1| = 3$, and $\rho_0 = 10^4\,\xi_{\mathrm{s}}^{-2}$, where $\xi_{\mathrm{s}} = \hbar/\sqrt{Mq_0}$ is the spin healing length of the system. Throughout this chapter, we express length scales in units of the healing length ξ_{s} and measure time in units of the characteristic spin time $t_s = \hbar/q_0$. Note that this definition differs from the time scale used for the one-dimensional setting (see Sect. 5.1) by a factor of 4π. Each component of the spinor field is represented on a 2D grid of 2048×2048 points of spatial extent $l \times l = 1600\,\xi_{\mathrm{s}} \times 1600\,\xi_{\mathrm{s}}$, and subject to periodic boundary conditions.

We consider a sudden quench made by setting q to a value in the range $[0, q_0]$ at the start of the simulation. In the early time evolution, the dynamics is dominated by the growth of unstable modes leading to the formation of transverse magnetization (see Refs. [157, 158] and the respective highlighted instabilities in Table 4.1). Spin vortices develop between the small magnetized domains that form with a length scale comparable to ξ_s. Once the (local) ferromagnetic order is established, these defects are topologically stabilized and can only decay by mutual annihilation when the appropriate vortex-antivortex pair meets. This process is relatively slow compared to the initial growth of local order and dominates the long-time ordering dynamics of the system [69]. The mean distance between spin vortices is proportional to the average size of the magnetic domains, and is generally taken as the key length scale for the universal phase ordering process.

6.2. Spin vortices

In two-dimensional systems, vortices often play a dominant role in the phase-ordering process and thus determine the observed universal scaling behavior. For our spin-1 system, we find that two types of spin vortices have a crucial effect on the scaling dynamics after the sudden quench. Therefore, we briefly introduce the structure of single spin vortices in the easy-plane ferromagnetic phase. We write its wave function in polar coordinates with origin taken at the vortex core. Sufficiently far from the core the general vortex state vector is of the form

$$\psi_V = \frac{\sqrt{n_0}}{2} e^{i\sigma_\phi \varphi} \begin{pmatrix} e^{-i\sigma_\alpha \varphi}\sqrt{1-q/q_0} \\ \sqrt{2(1+q/q_0)} \\ e^{i\sigma_\alpha \varphi}\sqrt{1-q/q_0}. \end{pmatrix}. \tag{6.2}$$

Here, φ is the azimuthal angle, σ_ϕ and σ_α are integers accounting for the directions of the mass and spin flow around the vortex, respectively. Different types of spin vortices arise from different combinations of σ_ϕ and σ_α. We only discuss elementary vortices given by $\sigma_\phi = 0, \pm 1$ and $\sigma_\alpha = \pm 1$ as they will be long-lived configurations in the system.

Polar core vortices (PCVs) exhibit spin circulation ($\sigma_\alpha = \pm 1$) but no mass circulation ($\sigma_\phi = 0$), and have an unmagnetized (i.e. polar) core. The two types of PCVs can be distinguished by the phase winding in the order parameter field, i.e., $F_\perp \sim e^{i\sigma_\alpha \varphi}$. Here, we refer to these as positive (p) $\sigma_\alpha = 1$ and negative (n) $\sigma_\alpha = -1$ PCVs, and note that these two types constitute a vortex-antivortex pair and can annihilate.

There are four types of elementary Mermin-Ho vortices (MHVs) which exhibit both mass ($\sigma_\phi = \pm 1$) and spin ($\sigma_\alpha = \pm 1$) circulation, and the vortex core is magnetized. The winding number of the m_F-th component is given by $w_{m_\mathrm{F}} = \sigma_\phi - m_\mathrm{F}\sigma_\alpha$. Thus, a MHV is characterized by a double winding in either the $m_\mathrm{F} = 1$ or -1 component, a single winding in $m_\mathrm{F} = 0$, and no winding in the remaining component. We denote the four types of MHVs as $(\sigma_\phi, \sigma_\alpha)$ = (p,p), (n,n), (p,n), (n,p) where p $\equiv +1$ and n $\equiv -1$. The spin circulation σ_α can be determined from the phase winding of the transverse spin whereas σ_ϕ can directly be inferred from the phase winding of the $m_\mathrm{F} = 0$ component. This unambiguously characterizes all types of MHVs. The two MHVs (p,p) and (n,n) constitute a vortex-antivortex pair, and similarly for (p,n) and (n,p).

6.3. Detection of spin vortices

Compared to the case of quenches from the polar initial state, where only PCVs emerge, our initial state gives rise to a rich ensemble of different vortices. In this section, we present an algorithm that allows us to detect the different types of spin vortices in the system enabling to investigate the universal scaling properties of both types of vortices. An example of the vortex configuration in a subregion of the system is shown in Fig. 6.1. This example is taken at a time sufficiently long after the quench such that the average domain size is much larger than the microscopic length scales of the system set by spin healing length ξ_s.

Each spin vortex is located by finding a vortex in the phase field of the transversal spin (see Fig. 6.1(d)). The spin vortex type is identified as follows: We count the number and the corresponding winding of vortices occurring in the phase fields of the three

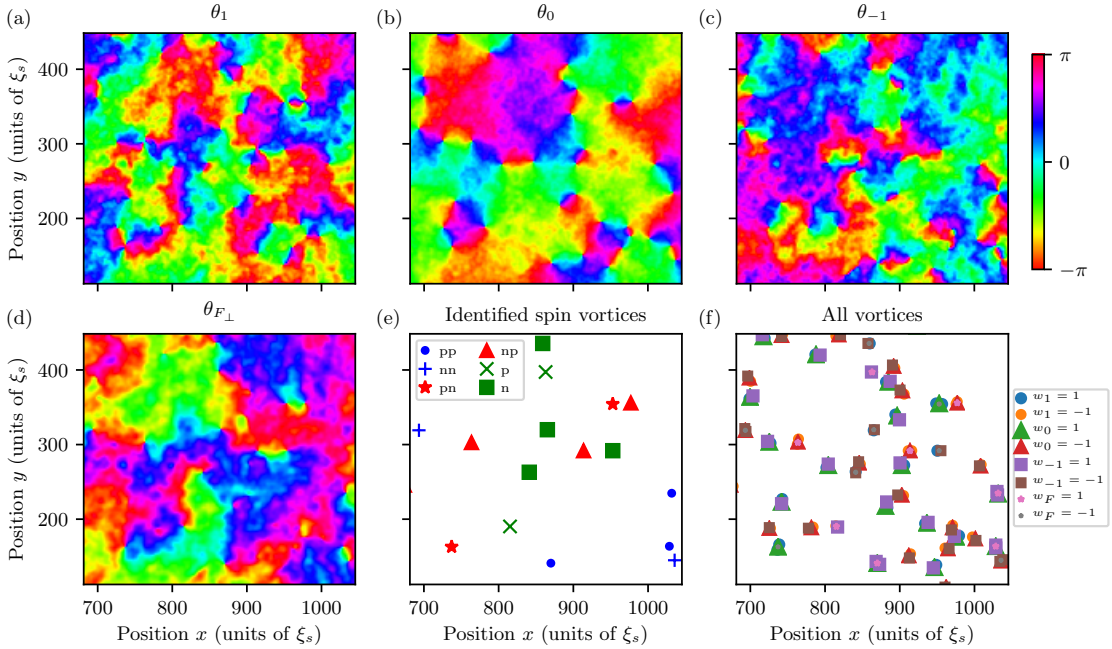

Figure 6.1.: Image of a $336\,\xi_s \times 336\,\xi_s$ subregion of the system at time $t = 2485\,t_s$, where $t_s = \hbar/q_0$ is the characteristic spin time, for a quench to $q = 0.15\,q_0$. (a)-(c) Phase profiles $\theta_{m_\mathrm{F}} = \mathrm{Arg}(\psi_{m_\mathrm{F}})$ of the three m_F-components. (d) Phase field of the transversal spin revealing the spin circulations. (e) Identified spin vortices: Vortex-antivortex pairs are shown with the same color code. All types of Mermin-Ho vortices (MHVs) (blue pluses/dots and red stars/triangles) and polar core vortices (PCVs) (green crosses/squares) are present. Vortex labeling and details of the identification procedure are given in the main text. (f) All vortices detected in the phase profiles depicted in (a)-(d) including their winding numbers indicated by w_δ with $\delta = 0, \pm 1, F$, where w_F denotes the winding identified in $\theta_{F_\perp}$. The pure vortex detection is performed as in Ref. [159]. Comparison of (e) and (f) shows that our algorithm for the spin vortex identification (see main text) is able to identify all PCVs and MHVs in the system with a high accuracy. A Gaussian blur filter with 2 grid point width is applied to the data in (a)-(c) and 3 grid point width to the data in (d) to reduce short length scale noise. Figure taken and adapted from Ref. [109].

m_F-components in a specified detection area around the spin vortex (see Fig. 6.1(a)-(c) and (f)). The initial detection area is taken to be 3×3 grid points. After extracting all the information from the phase fields, we are usually able to unambiguously determine the type of the spin vortex. We find that some of the spin vortices are stretched (i.e., the vortices in the different m_F components are spatially separated) due to the heating from the energy released by the quench. Such vortices cannot be identified if they extend beyond the initial detection area, so we repeat the identification step using a larger detection area in an iterative procedure. In each iteration step, we increase each side of the detection area by one grid point. We terminate the algorithm when the spin vortex has been identified or the detection area has grown to include a vortex number exceeding a threshold value of four vortices. This accounts for our algorithm to detect a doubly quantized vortex in the $m_\mathrm{F} = \pm 1$ components as two separate singly quantized vortices with equal winding number. Note that a small systematic error can arise in our identifi-

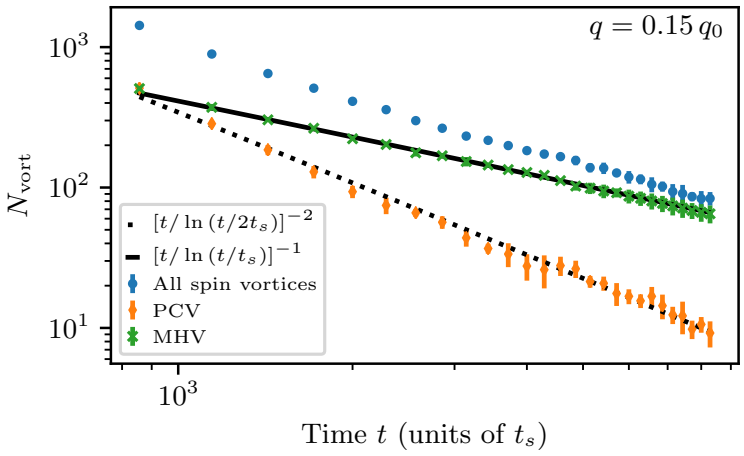

Figure 6.2.: Vortex number N_{vort} as a function of time within the universal scaling regime for $q = 0.15\,q_0$. We show the decay of PCVs (orange diamonds) and a fit of Eq. (6.3) (dotted line) to the PCV data as well as the decay of MHVs (green crosses) and a fit of Eq. (6.4) (solid line) to the MHV data. The total number of spin vortices is depicted by blue dots. The data is averaged over 5 trajectories and the error bars correspond to the standard deviation of the results. Figure taken and adapted from Ref. [109].

cation analysis when a vortex-antivortex pair is separated by less than three grid points, which can, for example, happen when they are about to annihilate. The result of the vortex identification analysis is shown in Fig. 6.1(e). We observe all types of PCVs and MHVs to be present in the system (see Fig. 6.1(e) and (f)), and that our algorithm is able to identify them accurately. In addition to spin vortices, free vortices occur in each of the m_{F}-components and tend to cluster into small groups with the same phase winding.

6.4. Universal decay laws of spin vortices

To characterize the universal scaling dynamics within the phase-ordering process following the quench, we quantify the evolution of the spin vortex number in the system. Fig. 6.2 shows the total number of PCVs (orange diamonds) and MHVs (green crosses) at times $850\,t_s \lesssim t \lesssim 8300\,t_s$ for a quench to $q = 0.15\,q_0$. There is approximately an equal number of PCVs and MHVs at the earliest time presented. However, the decay rate of each type of vortex is distinctly different, with the PCVs decaying faster than the MHVs. This leads to qualitatively different regimes for the phase ordering dynamics: As the MHVs become dominant at later times, the rate of decay of the total number of spin vortices changes (and hence the magnetic domain growth law) approaching that of the MHVs.

We quantitatively determine the decay laws for the two types of spin vortices. The PCV decay is consistent with

$$N_{\mathrm{vort}} \sim [t/\ln(t/t_0)]^{-2}\,, \tag{6.3}$$

where t_0 is a short-time cutoff [136] (see dotted line in Fig. 6.2). This result agrees with the domain growth law and vortex decay rate found in earlier work on the polar to easy-

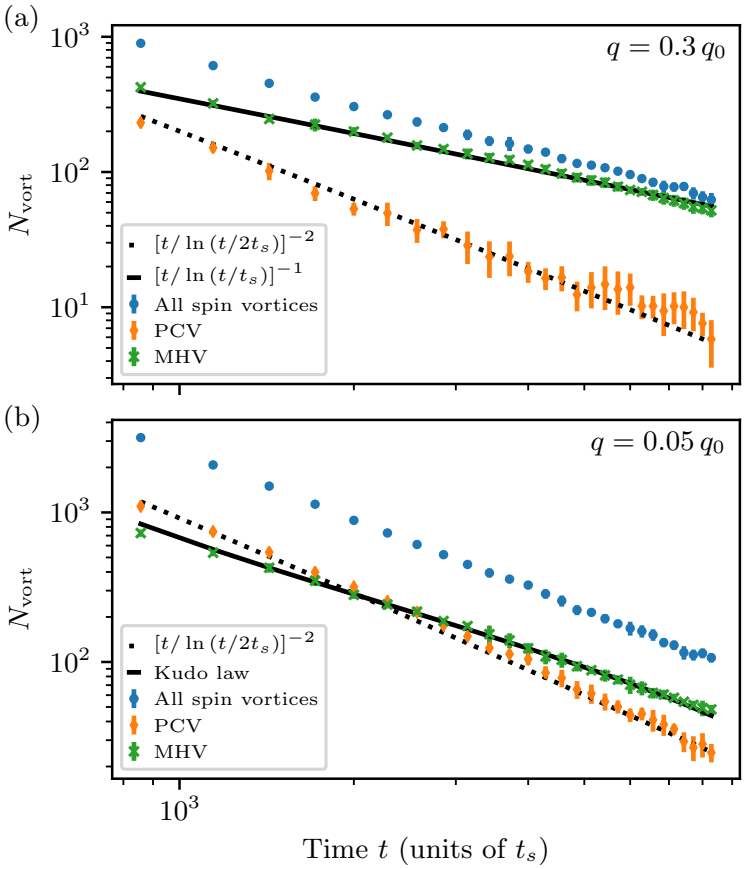

Figure 6.3.: Vortex number N_{vort} as a function of time within the universal scaling regime for quenches to (a) $q = 0.3\,q_0$ and (b) $q = 0.05\,q_0$. We show the decay of PCVs (orange diamonds) and a fit of Eq. (6.3) (dotted lines) to the PCV data as well as the decay of MHVs (green crosses) and (a) a fit of Eq. (6.4) (solid line); (b) a fit of a Kudo decay law (solid line) according to Ref. [124] to the MHV data. The total number of spin vortices is depicted by blue dots. The data is averaged over 5 trajectories and the error bars correspond to the standard deviation of the results. Figure taken and adapted from Ref. [109].

plane quench where only PCVs emerge [104]. The MHVs decay more slowly, consistent with XY-like scaling [136, 137, 139]

$$N_{\mathrm{vort}} \sim [t/\ln(t/t_0)]^{-1}\,, \tag{6.4}$$

(see solid line in Fig. 6.2).

We further consider quenches to other values of q, and present results for two other cases in Fig 6.3. These results reveal that the respective decay laws we have identified for the PCVs and MHVs are universal. For the quench to $q = 0.05\,q_0$, we find that we have to modify the XY decay law stated in Eq. (6.4) taking into account the possible difference in the number of vortices between the two subclasses of MHVs. The decay is well fit[1] by a decay law found for MHVs in a similar parameter regime ($q/q_0 \ll 1$, close to the

[1]We fit to Eq. (39) of Ref. [124] with $a = 30957 \pm 1433$, $c = 312 \pm 69$ and $d = 17 \pm 2$. We take the parameter $b = l^2/\xi_s^2 = 2.56 \times 10^6$ as an estimate for the maximal number of vortices. The curve in Fig. 6.3(b) is then obtained by numerically inverting Eq. (39) for the vortex number.

isotropic phase at $q = 0$) by Kudo *et al.* [124]. This Kudo decay law is governed by the XY universality class. Consequently, this does not indicate a change in the universality of the MHV decay.

A key feature we observe is, that varying the quadratic Zeeman energy we can engineer the proportion of PCVs and MHVs that are present when the system enters the scaling regime. Increasing the quadratic Zeeman energy, the ratio of PCVs to MHVs decreases (see Figs. 6.2 and 6.3).

We have also studied quenches for a larger interaction parameter ratio of $c_0/|c_1| = 12$ and find the number and the ratio of spin vortices as well as their decay to be consistent with the results presented above. This supports our expectation that the decay laws of the vortices are independent of the interaction parameter ratio as long as $|c_1|$ is sufficiently smaller than c_0 such that the excitations of the total density and phase do not significantly disturb the spin dynamics. Hence, we expect the same dynamics to occur in various experiments using spin-1 Bose gases such as in Refs. [35, 97, 146].

6.5. Violation of single-length scaling

Due to the distinctly different universal decay laws of the two types of spin vortices, we find that our system evolution violates the dynamical scaling hypothesis, which underlies standard universal scaling behavior within the phase-ordering process. As aforementioned, the dynamical scaling hypothesis [69] states that correlation functions of the order parameter collapse (i.e., become time independent) when spatial coordinates are scaled by the (single) macroscopic length scale $L(t)$. Our system instead has two distinct macroscopic length scales which have different scaling with time: the mean distance between PCVs

$$L_{\mathrm{PCV}}(t) \sim t/\ln t \tag{6.5}$$

and the mean distance between MHVs

$$L_{\mathrm{MHV}}(t) \sim (t/\ln t)^{1/2}. \tag{6.6}$$

Only in the limit of one spin vortex type being much more numerous than the other, pure single length scaling according to the dynamic scaling hypothesis will hold.

We verify the above mentioned properties by studying the momentum-space correlation function of the transversal spin as introduced in Eq. (3.33). To ensure a proper normalization of the transversal spin, we consider the correlation function

$$S(k,t) = \langle |f_\perp(k,t)|^2 \rangle, \tag{6.7}$$

where $f_\perp = F_\perp/\rho_0$. As before, the brackets denote an average over different trajectories of the simulation. Note that $k = |\mathbf{k}|$ denotes the radial momentum as we calculate angle-averaged momentum-space correlators in the two-dimensional setting.

According to the scaling hypothesis, a self-similar evolution of the correlation function, involving a single macroscopic length scale $L(t)$ only, is given by the scaling form

$$S(k,t) = [L(t)]^{\alpha/\beta} f_s\left(L(t)\, k\right), \tag{6.8}$$

where f_s is a universal scaling function and α, β are the corresponding scaling exponents. As the single length scale $L(t)$ evolves in time according to $L(t) \sim t^{\beta}$, we can write

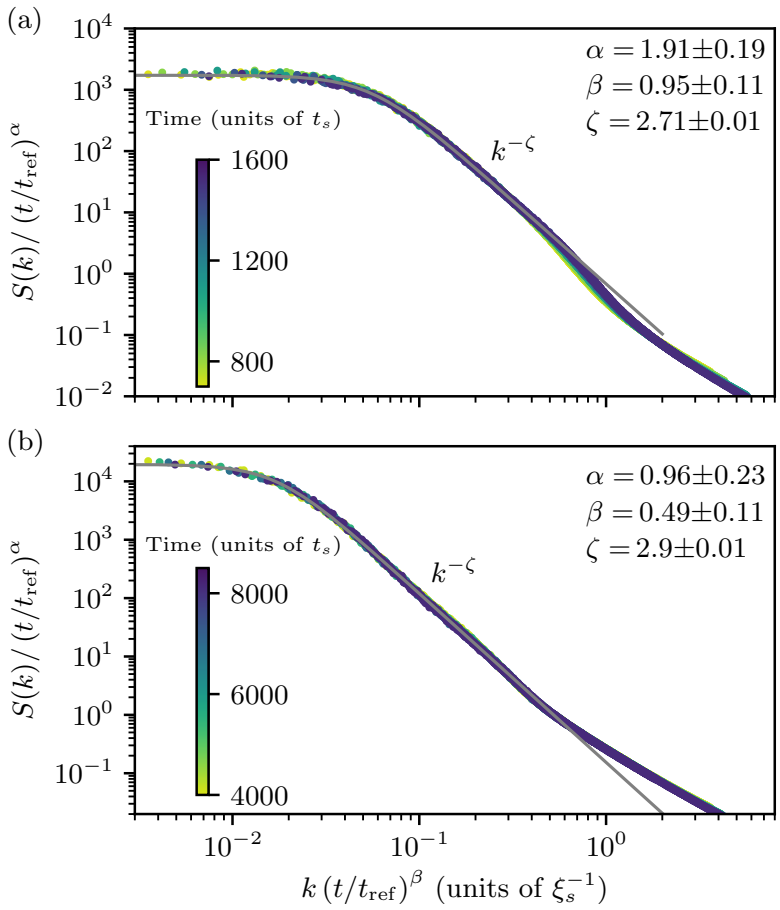

Figure 6.4.: Universal scaling dynamics of the momentum-space correlation function of the transversal spin, $S(k,t)$ (see Eq. (6.7)), according to Eq. (6.9) for a quench to $q = 0.15\,q_0$. (a) Using the scaling exponents $\alpha = 1.91 \pm 0.19$ and $\beta = 0.95 \pm 0.11$ and taking the reference time to be $t_{\mathrm{ref}} = 690\,t_s$ (i.e., the evolution time which corresponds to the data of the earliest time shown), the data collapses to a universal scaling function for times $650\,t_s \lesssim t \lesssim 1700\,t_s$. The scaling exponents are consistent with the scaling law obtained for PCVs (see Eq. (6.5)). The power-law fall-off of the distribution as $S(k,t) \sim k^{-\zeta}$ is given by $\zeta = 2.71 \pm 0.01$, which differs from the exponent $\zeta = 2.45$ reported for a system containing PCVs only [104]. (b) Using the scaling exponents $\alpha = 0.96 \pm 0.23$ and $\beta = 0.49 \pm 0.11$ and taking the reference time to be $t_{\mathrm{ref}} = 4137\,t_s$ (i.e., the evolution time which corresponds to the data of the earliest time shown), the data collapses to a universal scaling function for times $4100\,t_s \lesssim t \lesssim 8300\,t_s$. The scaling exponents are consistent with the scaling law obtained for MHVs (see Eq. (6.6)). The power-law fall-off of the distribution as $S(k,t) \sim k^{-\zeta}$ is given by $\zeta = 2.90 \pm 0.01$. All scaling exponents are obtained by means of a least-square fit to the corresponding data within the infrared momentum regime below the scale $k_{\mathrm{max}}\xi_s = 0.4$ and $k_{\mathrm{max}}\xi_s = 0.2$ for the cases (a) and (b), respectively. The exponent ζ results from fitting the scaling form $A/[1 + (k/k_\Lambda)^\zeta]$ (see Eq. (6.10)), with characteristic momentum scale $k_\Lambda \sim L(t)^{-1}$, to the above stated infra-red regime of the rescaled data. The solid grey lines show the best fit of the scaling form. All data depicted is averaged over 64 trajectories. Figure taken and adapted from Ref. [109].

Eq. (6.8) in the more general form (see Eq. (3.34))

$$S(k,t) = (t/t_{\mathrm{ref}})^{\alpha}\, f_{\mathrm{s}}\left([t/t_{\mathrm{ref}}]^{\beta}\, k\right) , \tag{6.9}$$

with t_{ref} being some reference time within the scaling regime. If the integral over the correlations is conserved in time within the infrared momentum regime obeying the scaling evolution, one finds the constraint $\alpha = 2\beta$ for a two-dimensional system.

Fig. 6.4 shows the momentum-space correlation function of the transversal spin rescaled according to Eq. (6.9) for two different regimes of the time evolution in case of a quench to $q = 0.15\, q_0$. For times $650\, t_s \lesssim t \lesssim 1700\, t_s$, the correlation function exhibits approximate scaling with scaling exponents $\alpha = 1.91 \pm 0.19$ and $\beta = 0.95 \pm 0.11$ (see Fig. 6.4(a)), whereas for times $4100\, t_s \lesssim t \lesssim 8300\, t_s$, we extract scaling exponents $\alpha = 0.96 \pm 0.23$ and $\beta = 0.49 \pm 0.11$ (see Fig. 6.4(b)). The exponents result from performing a least-square fit of the data using the reference times $t_{\mathrm{ref}} = 690\, t_s$ and $t_{\mathrm{ref}} = 4137\, t_s$, respectively. The errors are deduced from the width of the marginal-likelihood functions of the scaling exponents [34]. The extracted scaling exponents are consistent with the integral of the correlation function being conserved in time within the infrared scaling regime as we find $\alpha \approx 2\beta$. Note that we do not take into account a possible logarithmic correction entering the scaling forms in Eq. (6.8) and (6.9) in our analysis. As the time window considered for the scaling analysis of the correlation function is comparatively small, we expect the effects of logarithmic corrections to not be detectable within the error of the extraction method.

We clearly observe two distinct scaling regimes for the time evolution of our spin-1 system. The scaling exponents for the early stage of the phase ordering are consistent with the scaling law obtained for PCVs (see Eq. (6.5)), whereas we find good agreement with the scaling of MHVs (see Eq. (6.6)) within the late-time regime. For times $1700\, t_s \lesssim t \lesssim 4100\, t_s$, we are not able to collapse the data with a single set of exponents α, β. This indicates the violation of single-length scaling in the system. While the decay of each of the underlying spin vortices obeys a universal scaling law during the whole process of phase ordering, the correlation function measuring the evolution of the order parameter does not. Nonetheless, in the late-time regime where MHVs are much more numerous than PCVs (see Fig. 6.2), we find the phase ordering process to be well described by a single length scale only corresponding to the decay of MHVs (see Fig. 6.4(b)). Due to the fast decay of PCVs as compared to MHVs, the scaling behavior is dominated by the PCV scaling law at early stages (see Fig. 6.4(a)), although there is an approximate equal number of PCVs and MHVs in the system (see Fig. 6.2).

However, the phase ordering for evolution times $t \lesssim 1700\, t_s$ is not purely characterized by the dynamics and the properties of PCVs. This becomes visible when investigating the scaling function associated with the scaling evolution in Fig. 6.4(a). The momentum-space correlation function of the transversal spin shows a plateau below the characteristic momentum scale $k_\Lambda \sim L(t)^{-1}$, followed by a power-law fall-off $S(k,t) \sim k^{-\zeta}$. Using all rescaled data, we determine the exponent ζ by means of fitting the scaling form

$$f_{\mathrm{fit}}(k) = A/[1 + (k/k_\Lambda)^{\zeta}] \tag{6.10}$$

to the infrared momentum regime. We extract an exponent $\zeta = 2.71 \pm 0.01$ from the fit, which is considerably larger than the exponent $\zeta = 2.45$ found for a system containing PCVs only [104]. We expect the deviation to arise from the approximately equal number of MHVs being present in the system. In contrast, in the late-time regime, we extract an

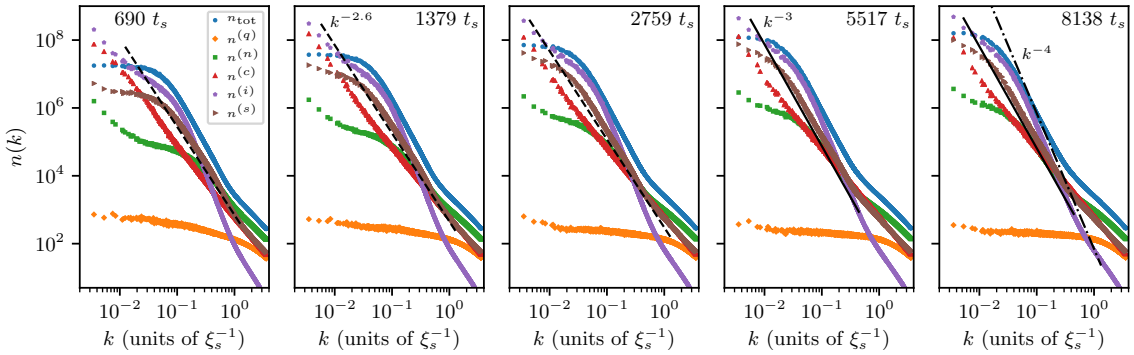

Figure 6.5.: Momentum distributions $n^{(\delta)}(k)$ derived from the hydrodynamic decomposition of the kinetic energy density into $\varepsilon^{(\delta)}(k) = k^2 n^{(\delta)}(k)/(2M)$ at five different evolution times during the phase ordering process. The momentum distributions representing the quantum pressure $n^{(q)}$ (orange diamonds), nematic $n^{(n)}$ (green squares), compressible $n^{(c)}$ (red triangles), incompressible $n^{(i)}$ (purple pentagons) and the spin $n^{(s)}$ (brown arrows) parts of the decomposition are compared to the total occupation number $n_{\mathrm{tot}} = \sum_m |\psi_m|^2$ (blue dots). See Sect. 3.4 for a detailed definition of each of the parts. The two leftmost panels correspond to the time regime depicted in Fig. 6.4(a). The power-law fall-off of the spin part $n^{(s)}(k) \sim k^{-\zeta}$ with exponent $\zeta \simeq 2.6$ (dashed line) is consistent with the one extracted for the correlation function of the transversal spin. The two rightmost panels correspond to the time regime depicted in Fig. 6.4(b). Here, the power-law fall-off of the spin part with exponent $\zeta \simeq 3$ (solid line) is also consistent with the one extracted for the correlation function. This indicates that the spin part plays the dominant role for the shape of the universal scaling function describing the scaling evolution of the transversal spin. The occupation number spectrum $n_{\mathrm{tot}}(k)$, however, is dominated, in the infrared momentum regime, by the incompressible part arising from the vortices in the system. It shows a power-law behavior with $\zeta \simeq 4$ (dash-dotted line in the rightmost panel) which is consistent with $\zeta = d+2$ predicted for an ensemble of randomly distributed vortices in a d-dimensional system [69]. Figure taken and adapted from Ref. [109].

exponent of $\zeta = 2.90 \pm 0.01$. This indicates that not only the scaling exponents but also the shape of the scaling function differs for the two types of spin vortices causing the associated universal dynamics to belong to clearly distinct universality classes.

We emphasize that the power-law fall-off of the correlation function of the transversal spin does not characterize the flow fields induced by the vortices detected in the system. For an ensemble of randomly distributed vortices, one generally expects a steeper power-law fall-off of the order parameter correlation function with exponent $\zeta = d + 2$ [40, 62, 69].

Investigating the origin of the observed power-law fall-off thus requires to separate the flow field induced by vortices from other contributions such as sound excitations or additional structure in the spin degree of freedom of the system. For this, we make use of a hydrodynamic decomposition of the kinetic energy density as defined in Sect. 3.4. Fig. 6.5 shows the momentum distributions $n^{(\delta)}(k)$ derived from such a decomposition. In particular, note the (purple pentagons) curve $n^{(i)}(k)$ which depicts the contribution

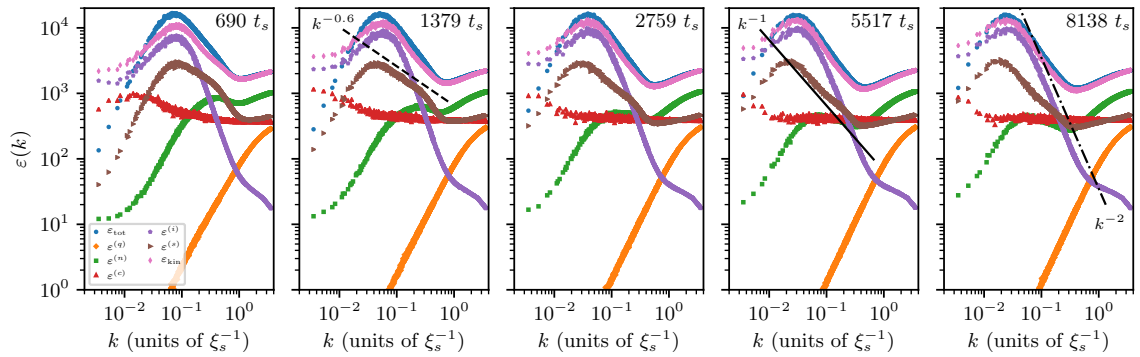

Figure 6.6.: Hydrodynamic decomposition of the kinetic energy density into $\varepsilon^{(\delta)}(k)$ for the same evolution times as in Fig. 6.5. The contributions representing the quantum pressure $\varepsilon^{(q)}$ (orange diamonds), nematic $\varepsilon^{(n)}$ (green squares), compressible $\varepsilon^{(c)}$ (red triangles), incompressible $\varepsilon^{(i)}$ (purple pentagons) and the spin $\varepsilon^{(s)}$ (brown arrows) parts of the decomposition are compared to $\varepsilon_{\text{tot}}(k) = k^2 n_{\text{tot}}(k)/(2M)$ (blue dots). The sum of all parts of the decomposition $\varepsilon_{\text{kin}} = \sum_\delta \varepsilon^{(\delta)}$ (pink thin diamonds) reveals expected deviations between the hydrodynamic decomposition and ε_{tot} for infrared momenta [40]. While the spin part is characterized by a single power law according to $\varepsilon^{(s)}(k) \sim k^{-\zeta+2}$ with $\zeta \simeq 2.6$ (dashed line) in the early stage of the phase ordering, a bimodal distribution with a steeper power-law fall-off consistent with $\zeta \simeq 3$ (solid line) within the low momentum region arises in the late-time regime. The incompressible part shows a power-law behavior consistent with $\zeta \simeq 4$ (dash-dotted line). We remark that the power-law fall-off of ε_{tot} arises from contributions of both, the incompressible and the spin part. Hence, it neither gives direct access to the vortices characterizing the scaling evolution nor to the surface structure of the spin domains determining the shape of the universal scaling function of the transversal spin correlator. Figure taken and adapted from Ref. [109].

of the incompressible, i.e., the divergence-free part of the velocity field to the kinetic energy spectrum. This part arises from both, spin and free vortices (c.f. Fig. 6.1(f)) and falls off as $n^{(i)}(k) \sim k^{-\zeta}$ with $\zeta \simeq 4$ during the late-time regime of the phase ordering. We remark that for the early stage we observe a slightly steeper power-law consistent with $\zeta \simeq 4.3$.

As a result, while the total kinetic energy spectrum is dominated by the contribution from the incompressible part within the infrared momentum region below $k\xi_s \lesssim 0.2$, the power-law fall-off of the spin correlator $S(k,t)$ is closer to that of the spin part of the decomposition ($n^{(s)}$, brown arrows in Fig. 6.5), for which we find an exponent consistent with $\zeta \simeq 2.6$ for times $650\,t_s \lesssim t \lesssim 1700\,t_s$, and an exponent $\zeta \simeq 3$ in the late-time regime $4100\,t_s \lesssim t \lesssim 8300\,t_s$ (see dashed and solid lines respectively in Fig. 6.5). Both exponents can be related to the surface structure of the transversal spin domains present in the system. For domains in a d-dimensional system, one generally expects a power-law behavior of the associated momentum-space correlator with exponent $\zeta = -2d + d_s$, where d_s denotes the surface fractal dimension [160]. For smooth surfaces, the fractal dimension is $d_s = d - 1$ [160], which results in an exponent $\zeta = 3$. Hence, the late-time scaling regime dominated by the annihilation of MHVs can be interpreted in terms of the spin domains having a rather smooth surface structure. However, within the early

stage of the phase ordering, the scaling is consistent with the spin domains having a fractal surface structure with fractal dimension $d_s \approx 1.4$. Note that a fractal dimension of this size has been found for the phase-ordering process involving PCVs only [104]. Our results thus seem to indicate that each type of spin vortex is accompanied by a specific surface structure of the attached spin domain boundaries.

The spectrum of the kinetic energy gives additional insights into the results presented in Fig. 6.5. Fig. 6.6 shows the hydrodynamic decomposition of the kinetic energy density during the phase ordering process. As we have already seen in Fig. 6.5, for the early stage of the phase ordering the spin part of the decomposition exhibits a power-law behavior according to $\varepsilon^{(s)}(k) \sim k^{-\zeta+2}$ with $\zeta \simeq 2.6$. In the late-time regime, the single power law transitions into a bimodal distribution characterized by a steeper power-law fall-off consistent with $\zeta \simeq 3$ in the low momentum region, while the high momentum region is still characterized by an exponent $\zeta \simeq 2.6$. In contrast, for the incompressible part of the kinetic energy, $\varepsilon^{(i)}(k)$, a single power-law consistent with $\zeta \simeq 4$ prevails throughout the whole evolution. Note that the power-law fall-off of the total kinetic energy $\varepsilon_{\text{tot}}(k) = k^2 n_{\text{tot}}(k)/(2M)$ results from both, the incompressible and the spin part such that it neither provides direct access to the vortices characterizing the scaling evolution nor to the surface structure of the spin domains determining the shape of the universal scaling function of the order parameter correlator.

6.6. Summary and outlook

In this chapter, we studied the universal scaling dynamics during the phase-ordering process of a two-dimensional spin-1 system quenched into the easy-plane ferromagnetic phase. Our choice of initial condition allowed both, polar core vortices (PCVs) and Mermin-Ho vortices (MHVs) to form during the quench and we observed that both types of spin vortices play a crucial role for the universal scaling characterizing the phase-ordering process.

We found that the ratio of PCVs and MHVs produced can be varied by quenching to different quadratic Zeeman energies q. The subsequent decay of each type of spin vortex appeared to be described by a universal scaling law. Because the two types of vortices have different decay laws, the standard (i.e., single macroscopic length scale) dynamical scaling hypothesis characterizing the infrared self-similar evolution of correlations in the universal scaling regime cannot hold for the order parameter of the system. We thus believe that our numerical studies present an extension of the dynamical scaling hypothesis to systems supporting multiple defects relevant to the order parameter.

Our results for the scaling of the order-parameter correlation function support the interpretation of two distinct macroscopic length scales and importantly demonstrate that in the PCV dominated regime, the scaling function deviates from the one found for a system containing PCVs only [104]. Performing a hydrodynamic decomposition of the kinetic energy density, we identified the spin part of the decomposition to determine the shape of the scaling function of the order-parameter correlations.

We remark that earlier work studying spin-1 quench dynamics found that only PCVs played a role in the phase ordering process [104]. Phase ordering of a (non-quenched) spin-1 system containing only MHVs was investigated in Ref. [124], with the initial vortices inserted randomly into the initial equilibrium state. Hence, our studies unraveled a neat choice of initial condition to generate multiple topological excitations that show universal scaling in the subsequent dynamical evolution of the system.

A practical feature of our system is that it can be realized in experiments with spin-1 Bose gases. The initial state production and tuning of q are common place experimental manipulations. The main challenges lie in producing a large quasi-2D system, ideally in a flat bottomed trap, and subsequently monitoring the evolution for long time scales.

Note that the initial condition considered here is a $\pi/2$-spin rotation of the one studied in Ref. [104], yet the ordering dynamics proceeds in a different manner involving two classes of topological defects. An interesting future direction is to vary the spin rotation angle continuously to produce a family of initial states to explore the crossover between the two different transient ordering processes.

Within the framework of non-thermal fixed points, our findings indicate that the system approaches two different such fixed points simultaneously during the time evolution. As this sounds counter-intuitive in the first place and hard to connect to the standard scaling properties of correlation functions at the fixed point, one could think of the idea that one has to identify observables that only contain information about one particular type of spin vortex. Those observables would incorporate the two relevant low-energy excitations separately and allow for a proper rescaling of the corresponding correlations.

The numerical results presented in this chapter raise numerous fundamental questions for the classification of non-thermal fixed points dominated by multiple topological excitations. In particular, one could think of a classification in terms of excitations such that scaling properties at non-thermal fixed points are assigned to the present excitations rather than the physical system itself. This idea could be further investigated in higher-order spin systems, where individual phases of the system feature an even larger number of potential topological excitations.

Part III.

Non-thermal fixed points dominated by collective excitations

7. Universal scaling dynamics in a $U(N)$-symmetric Bose gas

In the previous part of this thesis, we considered universal scaling dynamics at a non-thermal fixed point dominated by topological excitations. In this chapter, we focus on scaling behavior dominated by collective excitations. To illustrate this type of non-thermal fixed point scaling, we investigate the non-equilibrium dynamics of a $U(N)$-symmetric Bose gas.

In Sect. 7.1, we elaborate on analytical predictions of the spatio-temporal scaling of the $U(N)$-symmetric Bose gas within a kinetic theory approach. In particular, we perform the scaling analysis within the large-N limit of the model by making use of the effective action derived by means of the low-energy effective field theory outlined in Sect. 3.1.2. As we consider low-energy fluctuations on top of a homogeneous background condensate, topological excitations are not included in the effective field theory. Thus, the analytical treatment solely allows us to extract the scaling behavior resulting from collective excitations in the system. Hence, we perform numerical simulations of a $U(3)$-symmetric Bose gas in three spatial dimensions to corroborate our analytical predictions and to show that the scaling behavior is dominated by the collective excitations discussed within the analytical framework. We present the numerical results in Sect. 7.2. We find that the numerically extracted scaling exponents and scaling function are in good agreement with the scaling behavior predicted in the large-N limit. Making use of higher-order correlators of the fundamental Bose fields and the hydrodynamic decomposition of the flow field allows us to identify that the universal scaling is dominated by relative-phase excitations which are predicted to be the relevant low-energy degree of freedom in the large-N limit of the underlying model. The hydrodynamic decomposition further reveals that topological excitations are indeed present in the system but play a subdominant role in the scaling evolution.

7.1. Analytical predictions for the $U(N)$-symmetric Bose gas

In this section, we discuss analytical predictions for the scaling behavior at a non-thermal fixed point in $U(N)$-symmetric Bose gases. We make use of a kinetic-theory description to perform a scaling analysis from which we extract the universal scaling exponents. Therefore, we briefly outline the derivation of the kinetic equations that govern the scaling behavior at the fixed point in Sect. 7.1.1. We proceed by investigating the spatio-temporal scaling of the quasiparticle distribution characterizing the phase-angle excitations within the large-N limit in Sect. 7.1.2. To do so, we make use of the low-energy effective field theory derived in Sect. 3.1.2. Note that the spatio-temporal scaling of the particle number distribution of the $U(N)$-symmetric Bose gas within the large-N limit has been studied within the framework of non-perturbative resummed kinetic theory in

Refs. [34, 50, 56]. Finally, we comment on how to relate the scaling behavior obtained for the quasiparticle distribution to the particle number distribution measurable in experimental systems in Sect. 7.1.3.

The content of this section is taken and adapted from Refs. [37, 52, 61]. I stress that the majority of the parts are taken verbatim from the publications. I further added and/or modified formulations to embed the work into the broader context of this thesis.

7.1.1. From Kadanoff-Baym to kinetic equations in a nutshell

In Sect. 2.2, we outlined that the non-equilibrium time evolution of a quantum many-body system can be computed within the Schwinger-Keldysh description [77–80]. In that framework, the dynamical evolution of unequal-time two-point correlators is given by the Kadanoff-Baym equations [81]. Following Ref. [56], we briefly explain how to proceed from the Kadanoff-Baym equations in order to derive a kinetic equation that governs the scaling behavior at a non-thermal fixed point.

As a first step, the two-point correlators are decomposed into a symmetric and anti-symmetric part. For bosons, the symmetric part, which is termed the statistical function, is given by the anti-commutator of the field operators at two points in space and time, whereas the spectral function, defined by the commutator, represents the antisymmetric part. To obtain a kinetic equation, it is necessary to introduce a quasiparticle ansatz for the spectral function. In a next step, a gradient expansion of the Kadanoff-Baym equations with respect to the evolution time is performed. As universal scaling is reminiscent of a loss of memory about the initial condition, we can formally put the initial time to minus infinity and thus forget about contributions to the equations coming from the initial state.

Taking the gradient expansion to leading order and performing the equal-time limit, we obtain a Boltzmann-type kinetic equation for the time evolution of the (quasi)particle occupation number. This equation is termed generalized quantum Boltzmann equation (QBE).

7.1.2. Spatio-temporal scaling in the large-N limit

As discussed above, the kinetic description focuses on the evolution of equal-time two-point correlators. To analyze the universal scaling behavior of the $U(N)$-symmetric Bose gas at a non-thermal fixed point, we evaluate the QBE associated with the two-point correlator of the phase-excitation quasiparticles $f_a(\mathbf{k},t) = \langle \theta_a(\mathbf{k},t)\theta_a(-\mathbf{k},t)\rangle$ as introduced in Eq. (3.19). This is a natural choice as phases are the relevant low-energy degree of freedom due to the suppression of density fluctuations as explained in Sect. 3.1.2. We remark that analytical predictions for the scaling behavior at a non-thermal fixed point made by means of two-particle irreducible (2PI) resummation treatments usually consider the distribution of particles instead of quasiparticles. We will give a relation between the scaling of the quasiparticle and particle distribution in Sect. 7.1.3.

The kinetic equation that governs the time evolution of the momentum spectrum $f_{\mathbf{k}} \equiv f(\mathbf{k},t) \equiv f_a(\mathbf{k},t)$ of phase excitations reads

$$\partial_t f(\mathbf{k},t) = I[f](\mathbf{k},t)\,, \qquad I[f](\mathbf{k},t) = I_3(\mathbf{k},t) + I_4(\mathbf{k},t)\,. \tag{7.1}$$

The scattering integral $I[f](\mathbf{k},t)$ has two contributions arising from respective 3- and 4-wave interactions. The form of the 3- and 4-point scattering integrals $I_3(\mathbf{k},t)$ and $I_4(\mathbf{k},t)$

can be directly inferred from the low-energy effective action derived in Sect. 3.1.2. From the effective action in the large-N limit (see Eq. (3.18)), we obtain the scattering integrals to be given by [61]

$$I_3(\mathbf{k},t) \sim \int_{\mathbf{p},\mathbf{q}} |T_3(\mathbf{k},\mathbf{p},\mathbf{q})|^2\, \delta(\mathbf{k}+\mathbf{p}-\mathbf{q})\, \delta(\omega_{\mathbf{k}}+\omega_{\mathbf{p}}-\omega_{\mathbf{q}}) \\ \times \Big[(f_{\mathbf{k}}+1)(f_{\mathbf{p}}+1)f_{\mathbf{q}} - f_{\mathbf{k}} f_{\mathbf{p}} (f_{\mathbf{q}}+1)\Big]\,, \tag{7.2}$$

$$I_4(\mathbf{k},t) \sim \int_{\mathbf{p},\mathbf{q},\mathbf{r}} |T_4(\mathbf{k},\mathbf{p},\mathbf{q},\mathbf{r})|^2\, \delta(\mathbf{k}+\mathbf{p}-\mathbf{q}-\mathbf{r})\, \delta(\omega_{\mathbf{k}}+\omega_{\mathbf{p}}-\omega_{\mathbf{q}}-\omega_{\mathbf{r}}) \\ \times \Big[(f_{\mathbf{k}}+1)(f_{\mathbf{p}}+1)f_{\mathbf{q}} f_{\mathbf{r}} - f_{\mathbf{k}} f_{\mathbf{p}} (f_{\mathbf{q}}+1)(f_{\mathbf{r}}+1)\Big]\,. \tag{7.3}$$

The scattering T-matrices read

$$|T_3(\mathbf{k},\mathbf{p},\mathbf{q})|^2 = |\gamma(\mathbf{k},\mathbf{p},\mathbf{q})|^2 \frac{g_{\mathrm{G}}(\mathbf{k})\, g_{\mathrm{G}}(\mathbf{p})\, g_{\mathrm{G}}(\mathbf{q})}{8\,\omega(\mathbf{k})\,\omega(\mathbf{p})\,\omega(\mathbf{q})}\,, \tag{7.4}$$

$$|T_4(\mathbf{k},\mathbf{p},\mathbf{q},\mathbf{r})|^2 = |\lambda(\mathbf{k},\mathbf{p},\mathbf{q},\mathbf{r})|^2 \frac{g_{\mathrm{G}}(\mathbf{k})\cdots g_{\mathrm{G}}(\mathbf{r})}{2\omega(\mathbf{k})\cdots 2\omega(\mathbf{r})}\,, \tag{7.5}$$

with interaction couplings

$$\gamma(\mathbf{k},\mathbf{p},\mathbf{q}) = \frac{(\mathbf{k}\cdot\mathbf{p})\,\omega(\mathbf{q})}{M\, g_{\mathrm{G}}(\mathbf{q})} + \mathrm{perm}^{\mathrm{s}}\,, \tag{7.6}$$

$$\lambda(\mathbf{k},\mathbf{p},\mathbf{q},\mathbf{r}) = \frac{(\mathbf{k}\cdot\mathbf{p})(\mathbf{q}\cdot\mathbf{r})}{2M^2\, g_{\mathrm{G}}(\mathbf{k}-\mathbf{p})} + \mathrm{perm}^{\mathrm{s}}\,. \tag{7.7}$$

Here, the terminology 'perm$^{\mathrm{s}}$' denotes permutations of the sets of momentum arguments. The dispersions $\omega(\mathbf{k}) \sim k^z$ are characterized by the dynamical exponent z. In the large-N limit we obtain $z = 2$ as the corresponding quasiparticles are Goldstone excitations with quadratic, free-particle-like dispersion. Recall that the index G of the coupling $g_{\mathrm{G}}(\mathbf{k}) = Ng\mathbf{k}^2/(2k_\Xi^2)$ refers to the relevant Goldstone excitations in the large-N limit.

Now, we use the kinetic equations derived above to obtain a prediction for the scaling exponents α and β at the non-thermal fixed point. The fixed point is defined by the quasiparticle distribution obeying the scaling form

$$f(\mathbf{k},t) = s^{\alpha/\beta} f(s\mathbf{k}, s^{-1/\beta}t), \tag{7.8}$$

with s being a general scale parameter. Choosing $s = (t/t_{\mathrm{ref}})^\beta$ one obtains the scaling form

$$f(\mathbf{k},t) = (t/t_{\mathrm{ref}})^\alpha f_{\mathrm{s}}([t/t_{\mathrm{ref}}]^\beta \mathbf{k}) \tag{7.9}$$

of the distribution function. For the general scaling analysis of the kinetic equation performed in this section, we keep the parameter s, whereas for the discussion of the numerical results it is more convenient to use the form stated in Eq. (7.9).

Since the coupling $g_{\mathrm{G}}(\mathbf{k}) = s^{-2} g_{\mathrm{G}}(s\mathbf{k})$ scales quadratically in momentum, the T-matrices scale as

$$|T_l(\mathbf{k}_1,\ldots,\mathbf{k}_l;t)| = s^{-m_l} |T_l(s\mathbf{k}_1,\ldots,s\mathbf{k}_l; s^{-1/\beta}t)|, \tag{7.10}$$

with $l \in \{3, 4\}$ and $m_3 = m_4 = 2$.

This causes the scattering integrals to scale according to

$$I_l[f](\mathbf{k}, t) = s^{-\mu_l} I_l[f](s\mathbf{k}, s^{-1/\beta} t)\,, \tag{7.11}$$

with

$$\mu_l = 2 + (l-2)\,d - (l-1)\,\alpha/\beta. \tag{7.12}$$

At the non-thermal fixed point, the scaling quasiparticle distribution function f obeys the scaling form stated in Eq. (7.8). For it to be a solution of the kinetic equation in Eq. (7.1) for a given $\mu = \mu_l$, the scaling exponents need to satisfy the relation

$$\alpha = 1 - \beta\mu. \tag{7.13}$$

In addition, in the presence of a global conservation of the quasiparticle number given by the integral $\int_{\mathbf{k}} f(\mathbf{k}, t)$, the scaling exponents are subject to the constraint $\alpha = \beta d$ such that both scattering integrals, I_3 and I_4, scale with $\mu_l \equiv \mu = 2 - d$. Note that this relation implies that the relative importance of the two scattering integrals should remain throughout the evolution of the system. Collecting the above results, we obtain

$$\beta = 1/2\,, \qquad \alpha = d/2\,. \tag{7.14}$$

So far, we elaborated on the spatio-temporal scaling of the correlation function determining the scaling exponents α and β. In addition, we can also analyze the purely spatial momentum scaling which characterizes the form of the scaling function. The scaling of the QBE at a fixed evolution time $t = t_0$ implies $\kappa = -\mu_{\kappa,l}$, where $\mu_{\kappa,l}$ is the spatial scaling exponent of the corresponding scattering integral, $I_l(\mathbf{k}, t_0) = s^{-\mu_{\kappa,l}} I_l(s\mathbf{k}, t_0)$. Power-counting of the scattering integrals, together with the above stated scaling relation and inserting $z = 2$ for the large-N limit, gives

$$\kappa_3 = -\mu_{\kappa,3} = d + 2, \tag{7.15}$$

$$\kappa_4 = -\mu_{\kappa,4} = d + 1. \tag{7.16}$$

For a given κ_l, one additionally finds that

$$\mu_{\kappa,3} - \mu_{\kappa,4} = \kappa_l - d \geq 1. \tag{7.17}$$

Hence, the 4-wave scattering integral is expected to dominate at low momenta, $k \to 0$. This implies that, at the non-thermal fixed point, the quasiparticle distribution $f(\mathbf{k}, t) \sim k^{-\kappa}$ is characterized by the momentum scaling exponent $\kappa = \kappa_4 = d + 1$. From first sight, the result appears to contradict the previous analysis of the spatio-temporal scaling which revealed an equal importance of I_3 and I_4. We emphasize, however, that the scaling exponents α and β corresponding to the spatio-temporal scaling properties are obtained from relations which are independent of the precise form of $f(\mathbf{k}, t)$ but only require the scaling relation $f(\mathbf{k}, t) = (t/t_{\mathrm{ref}})^{\alpha} f_s([t/t_{\mathrm{ref}}]^{\beta}\mathbf{k})$. Hence, the questions, which of the scattering integrals is responsible for the shape of the scaling function and which dominates the transport, can be answered independently of each other, see Ref. [61] for details.

7.1.3. Relation between the scaling of particle and quasiparticle distributions

Making use of the low-energy effective field theory, we analyzed the spatio-temporal scaling of the quasiparticle distribution $f_a(\mathbf{k}, t)$ characterizing the phase-angle excitations. We find the scaling exponents to agree with results obtained from non-perturbatively resummed kinetic theory [56]. However, in the latter approach, one studies the spatio-temporal scaling of the particle number distribution $n_a(\mathbf{k}, t)$ encoded in the fundamental Bose fields. We remark that a priori there is no reason for the scaling properties of the two distributions to coincide since they correspond to different degrees of freedom.

Hence, one needs a translation between the scaling of the quasiparticle and particle number distribution. Under the assumption that the non-thermal fixed point is Gaussian with respect to quasiparticle excitations in the phase degree of freedom, it can be shown that the scaling properties derived in the large-N limit of the low-energy effective theory, defined by the exponents $z = 2$, $\alpha = d/2$, $\beta = 1/2$, and $\kappa = d + 1$, are consistent with the scaling properties derived within the non-perturbative approach, for the case of a dynamical exponent $z = 2$, and a vanishing anomalous dimension $\eta = 0$.

This relation enables us to extract scaling properties of the phase-angle excitations from the scaling behavior of the particle number distribution which is directly accessible in experiments. Additionally, due to the phase being compact, it is technically much more involved to even evaluate the phase correlator from numerical data. Therefore, we solely study correlators of the fundamental Bose fields in the following section where we discuss numerical results obtained by simulating the non-equilibrium dynamics after a strong cooling quench in a $U(3)$-symmetric Bose gas.

7.2. Numerical simulation of the $U(3)$-symmetric Bose gas

In this section, we corroborate the analytical predictions made for the scaling behavior of the $U(N)$-symmetric Bose gas with numerical simulations. Therefore, we consider the non-equilibrium time evolution of a $U(3)$-symmetric Bose gas in three spatial dimensions after a strong cooling quench. We introduce the numerical parameters used for the simulations in Sect. 7.2.1. Then, we discuss the spatio-temporal scaling of the system in Sect. 7.2.2. We focus especially on extracting that the scaling behavior is dominated by excitations of relative phases which are predicted to characterize the universal scaling in the large-N limit. Therefore, we make use of higher-order correlators of the fundamental fields and the hydrodynamic decomposition of the flow field.

The content of this section is taken and adapted from Ref. [61]. I stress that some parts are taken verbatim from the publication. However, I reordered the overall structure of the presentation. I further added and/or modified formulations to embed the work into the broader context of this thesis.

7.2.1. Numerical parameters

The three-dimensional $U(3)$-symmetric Bose gas is described by the Hamiltonian introduced in Eq. (3.1) with $N = 3$ and $d = 3$. Note that we use units of $\hbar = 1$. We

start with a far-from-equilibrium initial condition given by a 'box' particle number distribution $n_a(\mathbf{k}, t_0) = n_0\,\Theta(k_\mathrm{q} - |\mathbf{k}|)$, where one can express the occupation number as $n_0 = (4\pi k_q^3)^{-1}\rho^{(0)}$. Additionally, we choose all phases $\theta_a(\mathbf{k}, t_0)$ randomly on the circle such that no significant coherence prevails. Note that we use the label $a = 1, 2, 3$ to enumerate the three components. We take the momentum cutoff for the initial condition to be $k_\mathrm{q} = 1.4\,k_\Xi$ leading to an initial occupation number of $n_0 \simeq 2350$. Here, $k_\Xi = [2Mg\,\rho^{(0)}]^{1/2}$ is a momentum scale set by the inverse healing length corresponding to the total particle density $\rho^{(0)}$ present in the system.

Our initial configuration has an extreme out-of-equilibrium form as the modes are strongly occupied, on the order of $n_0 \sim \zeta_\mathrm{d}^{-1}$. Here, $\zeta_\mathrm{d} = [\rho^{(0)}a^3]^{1/2}$ is the diluteness parameter which measures the s-wave scattering length $a = gM/(4\pi)$ in units of the inverse mean total density. In physical terms, this means that all particles are placed, predominantly, at a momentum scale with kinetic energy equal to the interaction energy or chemical potential $\mu = g\rho^{(0)}$ the gas has stored if it was fully Bose condensed. In practice, one may prepare such an initial state, e.g., by applying a strong cooling quench to an equilibrated system as already outlined in Sect. 2.1.

All simulations are performed on a grid with $N_\mathrm{g} = 256^3$ grid points using periodic boundary conditions. The corresponding physical volume of our system is $V = N_\mathrm{g}\Xi^3$. The total particle number is $\mathcal{N} = \rho^{(0)}V = 6.7\cdot 10^9$, i.e., we have $\mathcal{N}_a = 2.23\cdot 10^9$ particles in each of the three components. The correlation functions, obtained by solving the equations of motion stated in Eq. (3.3) within the truncated Wigner approximation, are averaged over 144 trajectories.

Throughout this section, we express length scales in units of the healing length $\Xi = k_\Xi^{-1}$ and measure time in units of the characteristic time scale $t_\Xi = 2\pi/(g\rho^{(0)})$.

7.2.2. Spatio-temporal scaling

Starting from the extreme out-of-equilibrium initial configuration discussed above, the system can approach a non-thermal fixed point and show universal scaling. In particular, the occupation numbers $n_a(\mathbf{k}, t) = \langle|\psi_a(\mathbf{k}, t)|^2\rangle$ of the Bose fields in each component a in momentum space, see Eq. (3.20), can obey a scaling evolution according to

$$n_a(\mathbf{k}, t) = (t/t_\mathrm{ref})^\alpha f_{\mathrm{s},a}([t/t_\mathrm{ref}]^\beta \mathbf{k}) \tag{7.18}$$

within a range of modes $0 < k \lesssim k_\Xi$.

Fig. 7.1(a) shows that, within a regime of low momenta, the evolution of the angle-averaged momentum distribution $n_1(k, t) = (4\pi)^{-1}\int d\Omega_\mathbf{k}\, n_1(\mathbf{k}, t)$, where $n_1(\mathbf{k}, t) = \langle\psi_1^\dagger(\mathbf{k}, t)\psi_1(\mathbf{k}, t)\rangle$, exhibits scaling in time t and radial momentum $k = |\mathbf{k}|$ according to Eq. (7.18). While the inset shows the evolution of the particle number distribution at different instances of time, the data shown in the main frame demonstrates the rather precise scaling collapse in momentum space, up to the scale on the order of the healing-length wave number k_Ξ above which a near-thermal tail characterizes the higher-energetic particles.

For a quantitative analysis of the scaling behavior, we determine the respective scaling exponents α and β by means of least-square rescaling fits of the occupation number spectra within a time window $[t_\mathrm{ref}, t_\mathrm{ref} + \Delta t]$ with $\Delta t = 146\,t_\Xi$. The resulting t_ref-dependent exponents are shown in Fig. 7.2(a). The extracted exponents confirm, within errors, the relation $\alpha = \beta\,d$ in $d = 3$ dimensions which results form the particle number conserva-

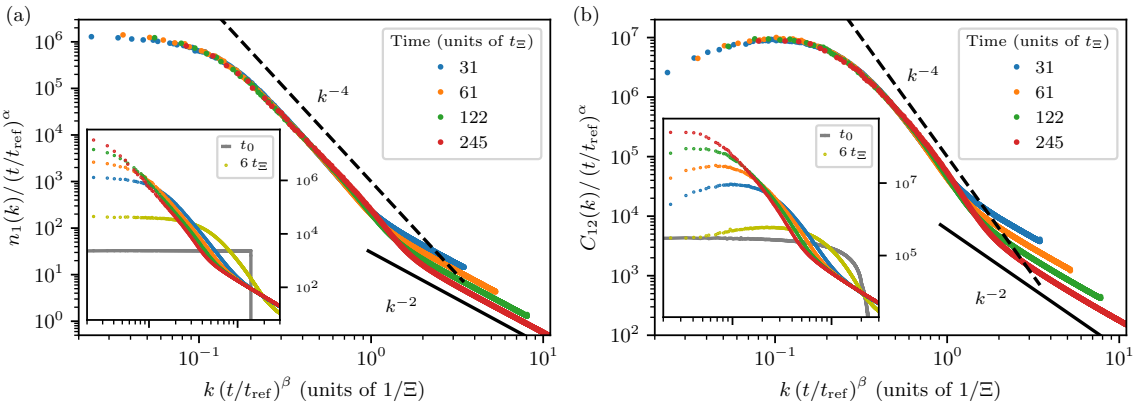

Figure 7.1.: (a) Universal scaling of the angle-averaged occupation number distribution $n_1(k) \equiv n_1(k,t) = (4\pi)^{-1}\int d\Omega_{\mathbf{k}}\, n_1(\mathbf{k},t)$, where $n_1(\mathbf{k},t) = \langle\psi_1^\dagger(\mathbf{k},t)\psi_1(\mathbf{k},t)\rangle$. Inset: Evolution starting from a 'box' momentum distribution $n_1(k,t_0) = n_0\,\Theta(k_{\rm q}-|\mathbf{k}|)$, identical in all three components a (grey line), with $n_0 = (4\pi k_q^3)^{-1}\rho^{(0)}$, $k_{\rm q} = 1.4\,k_\Xi$, at five different times (colored dots). The collapse of the data to a universal scaling function, with reference time $t_{\rm ref} = 31\,t_\Xi$, shows the scaling in space and time according to Eq. (7.18). Within the time window $t_{\rm ref} = 200\,t_\Xi \le t \le 350\,t_\Xi$, we extract exponents $\alpha = 1.62 \pm 0.37$, $\beta = 0.53 \pm 0.09$, see Fig. 7.2(a). At momenta $k \gg k_\Lambda(t)$, we find a power-law fall-off of the distribution as $n_1(k) \sim k^{-\zeta}$ with $\zeta \simeq 4$. (b) Universal scaling dynamics of the angle-averaged correlator measuring the spatial fluctuations of the relative phases $C_{12}(k) \equiv C_{12}(k,t) = (4\pi)^{-1}\int d\Omega_{\mathbf{k}}\, C_{12}(\mathbf{k},t)$, where $C_{12}(\mathbf{k},t) = \langle|(\psi_1^\dagger\psi_2)(\mathbf{k},t)|^2\rangle$, for the same system. While no plateau prevails in the infrared, a similar fall-off at higher momenta is seen as for $n_1(k)$ with only slightly modified power law. Within the same time window as stated in (a), we extract scaling exponents $\alpha = 1.48 \pm 0.18$, $\beta = 0.51 \pm 0.06$, see Fig. 7.2(b). The scaling exponents characterizing the evolution of $C_{12}(k)$ are closer to the predicted fixed-point exponents $\beta = 1/2$, $\alpha = 3/2$ than for $n_1(k)$. Figure taken and adapted from Ref. [37].

tion within the infrared regime of momenta. We find similar results (not shown) for the other components.

During the late period, $t_{\rm ref} = 200\,t_\Xi \le t \le 350\,t_\Xi$, one obtains the scaling exponents $\alpha = 1.62 \pm 0.37$, $\beta = 0.53 \pm 0.09$ for the scaling of $n_1(k)$, with a trend towards a smaller β, cf. similar results found in Ref. [34]. For all three components, the exponent β is slightly larger than the value $\beta = 1/2$ analytically predicted in the large-N limit as discussed in Sect. 7.1.2.

Note that we previously defined the scaling regime associated with a non-thermal fixed point to be characterized by the scaling exponents becoming independent of the chosen reference time. Fig. 7.2(a) thus indicates that we are about to enter this scaling regime during the late period of the numerical simulation. However, the evolution of the extracted scaling exponents towards the fixed-point value is of interest in its own right as it offers the possibility to study how the system actually approaches the non-thermal fixed point. We use these observations to illustrate the concept of prescaling in Chpt. 8.

The scaling form of the occupation number distribution, as stated in Eq. (7.18), allows

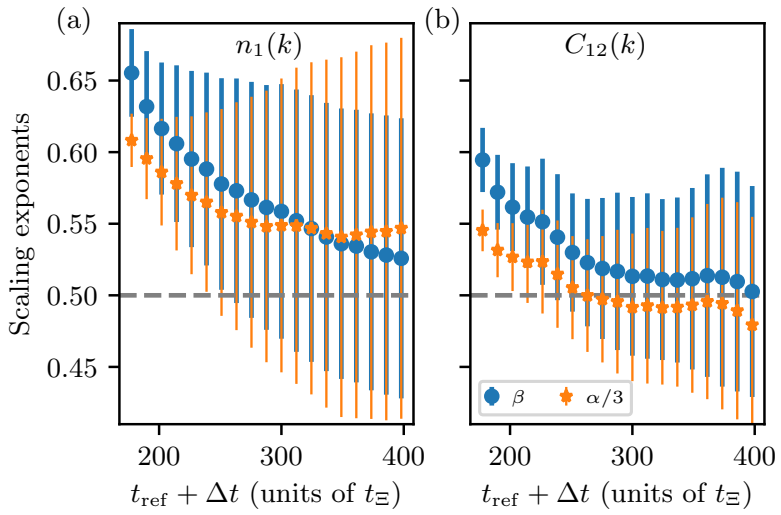

Figure 7.2.: (a) Scaling exponents $\alpha/3$ and β obtained from least-square rescaling fits of the angle-averaged occupation number distribution $n_1(k,t)$ shown in Fig. 7.1(a). The exponents correspond to the mean required to collapse the spectra within the time window $[t_{\mathrm{ref}}, t_{\mathrm{ref}} + \Delta t]$ with $\Delta t = 146\, t_\Xi$, and the momentum window $[k_{\mathrm{min}}, k_{\mathrm{max}}]$, with k_{min} set by the lowest non-zero radial momentum at $t = t_{\mathrm{ref}}$ and $k_{\mathrm{max}} = 0.45\,\Xi^{-1}$, such that the slight bend of $n_1(k)$ to a steeper power law is excluded. Error bars denote the least-square fit error. (b) Exponents extracted from the collapse of $C_{12}(k,t)$, shown in Fig. 7.1(b), for the same time window. While $n_1(k)$ is about to enter the scaling regime in the late period of the simulation, $C_{12}(k)$ already exhibits approximate scaling at $t_{\mathrm{ref}} + \Delta t \gtrsim 300\, t_\Xi$ as the scaling exponents have settled in to stationary values. The scaling exponents are in good agreement with the analytically predicted values of $\beta = 1/2$ and $\alpha = 3/2$, see Sect. 7.1.2. Figure taken and adapted from Ref. [37].

for a straightforward consistency check of the extracted scaling exponents. Analyzing the time evolution of the zero-momentum mode occupation $n_1(k = 0, t)$ gives direct access to the scaling exponent α as the universal dynamics according to Eq. (7.18) reduces to $n_1(k = 0, t) = (t/t_{\mathrm{ref}})^\alpha f_{s,1}(k = 0)$. Fig. 7.3 shows that at late times, $t \gtrsim 200\, t_\Xi$, the evolution is governed by $\alpha \simeq d/2 = 3/2$ consistent with our analytic prediction in the case of a conserved quasiparticle number and the numerical extraction by means of the least-square fits.

So far, we elaborated on the scaling exponents that govern the time evolution of the particle number distribution. As we are also able to make analytical predictions for the form of the scaling function, we briefly comment on this in the following. The numerically observed scaling function is characterized by a plateau up to an inverse coherence-length scale $k_\Lambda(t)$, which rescales in time according to $k_\Lambda(t) \sim t^{-\beta}$. At momenta larger than this inverse coherence-length scale, $|\mathbf{k}| = k \gg k_\Lambda(t)$, the scaling function takes the power-law form $n_a(k) \sim k^{-\zeta}$, with $\zeta \simeq d + 1 = 4$, confirming earlier predictions [34, 56, 161] and the result obtained in Sect. 7.1.3.

When deriving the low-energy effective field theory for the $U(N)$-symmetric Bose gas in Sect. 3.1.2, we found the phase fields to be the relevant low-energy degree of freedom. In the large-N limit of the model, we then identified Goldstone excitations of relative phases to play the dominant role in the low-energy regime. This means that

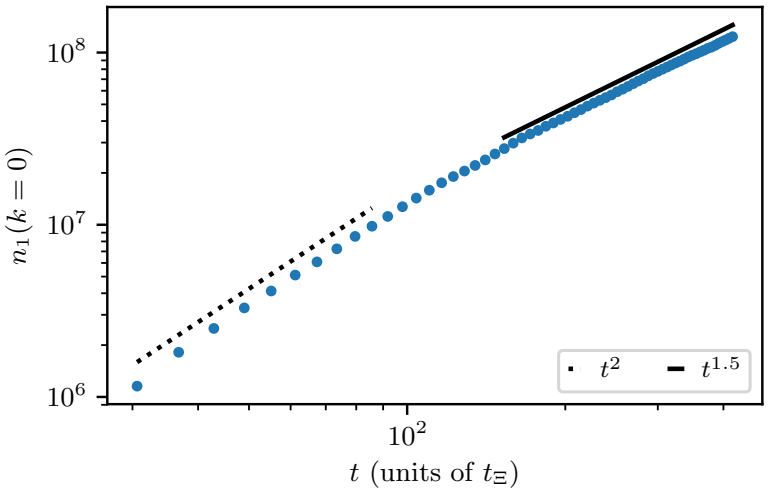

Figure 7.3.: Zero-momentum mode of the single-component occupation number $n_1(k = 0, t)$ (blue dots). According to Eq. (7.18) the universal time evolution is given by $n_1(k = 0, t) = (t/t_{\text{ref}})^\alpha f_{\text{s},1}(k = 0)$. At late times, $t \gtrsim 200\, t_\Xi$, we find $\alpha \simeq d/2 = 3/2$ (black solid line) consistent with the analytical prediction within our low-energy effective field theory, see Sect. 7.1.2. Figure taken and adapted from Ref. [61].

universal scaling dynamics is expected to be predominantly seen in observables sensitive to relative phases as we increase the number of components. As the particle number distribution is insensitive to such phases, we consider additionally the coherence function $C_{ab}(\mathbf{k}, t) = \langle |(\psi_a^\dagger \psi_b)(\mathbf{k}, t)|^2 \rangle$ as introduced in Eq. (3.21). This momentum-space correlator measures the fluctuations of the relative phases between components a and b. Fig. 7.1(b) shows the time evolution of the angle-averaged correlator for $a = 1$ and $b = 2$. We also find a scaling collapse onto a scaling function according to Eq. (7.18) revealing the same kind of universal scaling as the particle number distribution.

Extracting the scaling exponents by means of least-square fits reveals $\alpha = 1.48 \pm 0.18$ and $\beta = 0.51 \pm 0.06$ within the time window $t_{\text{ref}} = 200\, t_\Xi \leq t \leq 350\, t_\Xi$, see Fig. 7.2(b). These findings are considerably closer to the exponents $\beta = 1/2$ and $\alpha = 3/2$ predicted for the fixed point, see Sect. 7.1.2. We stress that the extracted relation between the scaling exponents α and β shows that the scaling evolution of the correlator $C_{ab}(k, t)$ is characterized by an emergent conservation law within the infrared regime of momenta. We discuss this conservation law in more detail in the framework of prescaling in Sect. 8.5.

Our observation for the scaling behavior of the coherence function clearly indicates the dominant role of relative-phase excitations for the universal scaling dynamics of the system. To support this conclusion further, we investigate the hydrodynamic flows of the system.

In order to obtain information on the character of the hydrodynamic flows corresponding to the phase field θ_a, we analyze the time evolution of the total momentum distribution $n_{\text{tot}}(k, t) = \sum_{a=1}^{3} n_a(k, t)$ in hydrodynamic decomposition. This is obtained by decomposing the kinetic energy distribution in momentum space into quantum-pressure (q), spin (s), nematic (n), incompressible (i) and compressible (c) parts, as defined in detail in Sect. 3.4. The numerically extracted time evolution is depicted in Fig. 7.4.

We point to the observation that the incompressible flow arising from vortical mo-

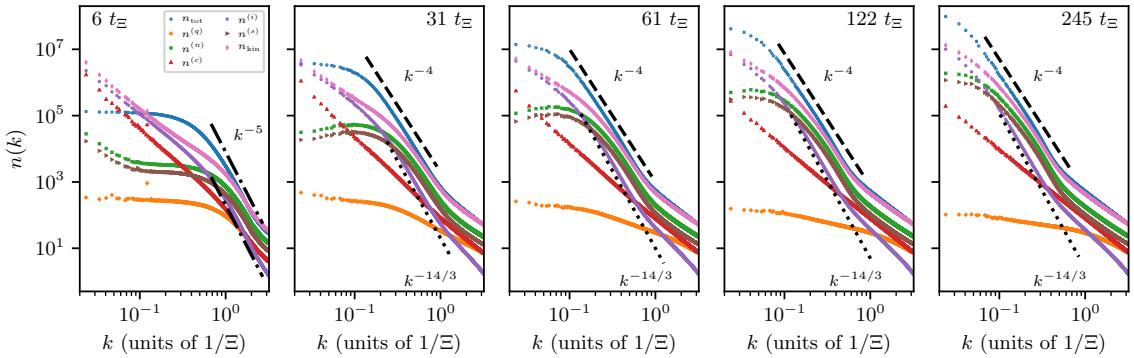

Figure 7.4.: Hydrodynamic decomposition of the flow pattern encoded in the phase-angle field θ_a at an early time as well as for the four evolution times in the universal scaling regime. Shown are momentum distributions $n^{(\delta)}(k)$ derived from the decomposition of the kinetic energy density into $\varepsilon^{(\delta)}(k) = k^2\, n^{(\delta)}(k)$. The total occupation number n_{tot} (blue dots) is compared to the distributions representing the quantum pressure part $n^{(q)}$ (orange diamonds), the nematic $n^{(n)}$ (green squares), compressible $n^{(c)}$ (red triangles), incompressible $n^{(i)}$ (purple pentagons) and spin $n^{(s)}$ (brown arrows) parts, as well as their sum n_{kin} (pink thin diamonds). The incompressible part arising from vorticity in the system exhibits a power law decay with $n^{(i)}(k) \sim k^{-14/3}$ (see dotted line). The total occupation number is dominated by the nematic and the spin parts except for momenta deep in the infrared regime where the decomposition is expected to fail. The interplay of the dominant parts with the steep power law in the incompressible part leads to an overall power-law decay of $n_{\mathrm{tot}}(k) \sim k^{-4}$ (see dashed line) at intermediate momenta. Figure taken and adapted from Ref. [61].

tion is subdominant as compared to the nematic and spin parts which determine the leading scaling of the occupation number as $n_{\mathrm{tot}}(k) \sim k^{-4}$. The vortex flow contributes significantly only at very low momenta, where the plateau appears in the total number distribution. In this regime, as is seen at times $t/t_\Xi = 31, 61$, the nematic and spin parts fall off towards zero momentum but this is compensated for by the incompressible part. Note that the distributions shown in Fig. 7.4 result from the tensor decomposition of the current which is a four-point function of the Bose fields. Hence, $n_{\mathrm{kin}}(k,t)$, which is the sum of the hydrodynamic parts, deviates from $n_{\mathrm{tot}}(k,t)$ in the infrared momentum regime [40].

We emphasize that the spin and nematic fluctuations are determined by the fluctuations of the relative phases between the field components $a = 1, 2, 3$. The corresponding momentum distributions take the same form as the scaling function shown in Fig. 7.1(b). The universal scaling of $C_{12}(k,t)$ together with the hydrodynamic decomposition thus confirms our hypothesis that the scaling behavior is dominated by the relative phases between different components.

Additionally, we find that the incompressible as well as the spin and nematic parts of the hydrodynamic decomposition also exhibit universal scaling according to Eq. (7.18), which is shown in Fig. 7.5. The late-time value of $\beta \simeq 0.5$ extracted for the universal scaling of the spin and nematic parts (see insets of Fig. 7.5(b) and (c)) demonstrates the crucial role of the relative phases for the scaling behavior of the system. Interestingly, the scaling behavior of the subdominant vortical flow in the system seems to be charac-

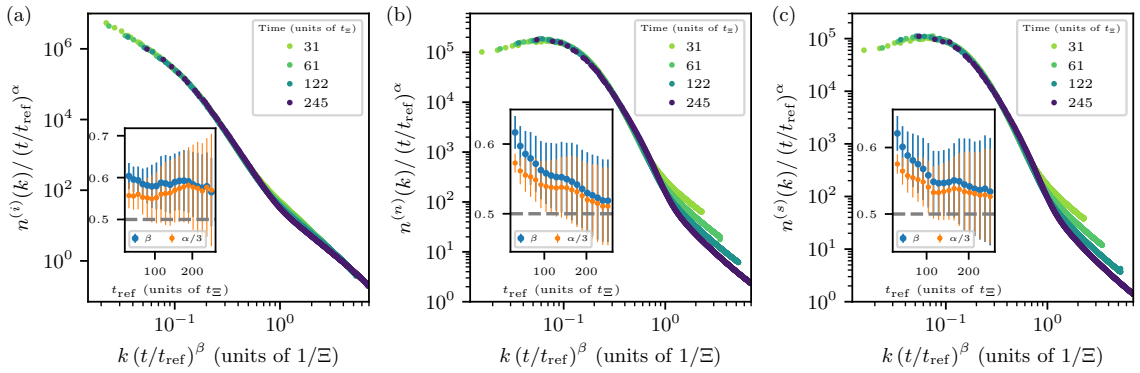

Figure 7.5.: Universal scaling dynamics of the occupation numbers representing the (a) incompressible, $n^{(i)}$, (b) nematic, $n^{(n)}$, and (c) spin, $n^{(s)}$, parts of the hydrodynamic decomposition (see Fig. 7.4) according to Eq. (7.18). The collapse of the data to the universal scaling functions $f_{\rm s}^{(\delta)}(k)$, with reference time $t_{\rm ref} = 31\,t_\Xi$, shows, in each case $\delta = i, n, s$, the scaling in space and time as stated in Eq. (7.18) . The universal scaling exponents $\alpha/3$ (orange stars) and β (blue dots) obtained by means of a least-square fit to the data within the time window $[t_{\rm ref}, t_{\rm ref} + \Delta t]$ with $\Delta t = 146\,t_\Xi$ are depicted in the insets of each panel. For late times, we find that the scaling exponent β extracted for the nematic and spin part approaches $\beta \simeq 0.5$ while for the incompressible part it settles in to $\beta \simeq 0.58$. The scaling exponents corresponding to the time evolution of the nematic and spin part corroborate our hypothesis that the scaling behavior is dominated by the relative phases of the components. Figure taken and adapted from Ref. [61].

terized by a scaling exponent $\beta \simeq 0.58$ nearly unaffected by variations of the reference time (see inset of Fig. 7.5(a)). For smaller N, in particular $N = 1$, vortices are expected to play a more prominent role [39, 40, 42–45, 57] in the evolution following a quench of the type considered here.

Finally, we stress that during the approach of the scaling regime associated with the non-thermal fixed point, the system shows prescaling [37], which will be discussed in detail in Chpt. 8. Our analysis here demonstrates that, cf. in particular Fig. 7.4, effects of topological excitations such as vortices, contributing to the incompressible flow, can induce scaling violations of the single-component occupation numbers and coherence functions. Nevertheless, also other contributions such as $1/N$ corrections to the scaling analysis could explain certain systematic deviations of the exponents found at the largest simulation times from the analytical predictions presented in Sect. 7.1.

7.3. Summary and outlook

In this chapter, we discussed universal scaling dynamics at a non-thermal fixed point dominated by collective excitations. To illustrate this type of scaling behavior, we considered a $U(N)$-symmetric Bose gas far from equilibrium.

To obtain analytical predictions for the universal scaling, we performed a scaling analysis of the corresponding kinetic equation. The scattering matrices entering the kinetic equation were extracted from the low-energy effective field theory of the model. We focussed on the large-N limit, where Goldstone excitations of the relative-phase degree

of freedom play the dominant role at low energies. In this case, we found the scaling exponents to be $\beta = 1/2$ and $\alpha = d\beta = d/2$, in agreement with predictions resulting from non-perturbatively resummed kinetic theory [56]. The scaling relation between α and β reflects the conservation of the quasiparticle number within the regime of infrared momenta where the universal scaling dynamics occurs.

We remark that the analytical treatment solely allows us to predict the scaling properties of the system resulting from collective excitations. This results from the fact that we consider low-energy fluctuations on top of a homogeneous background condensate within our low-energy effective field theory. Hence, topological excitations and their influence on the scaling behavior of the system are not included. This naturally raised the question whether the predicted scaling is observed when performing numerical simulations of the non-equilibrium time evolution, where topological excitations are expected to be present.

We find that numerical simulations of a $U(3)$-symmetric Bose gas in three spatial dimensions corroborate the analytical predictions. Making use of higher-order correlators sensitive to relative-phase excitations and performing a hydrodynamic decomposition of the flow field allowed us to show that topological excitations are subdominant and that the universal scaling is dominated by the collective low-energy excitations. In the late period of the time evolution, the numerical results for the scaling exponents and the form of the scaling function are in good agreement with the large-N predictions. This suggests that the universality class of the model is independent of the number of components N, reflecting that the dispersion of the dominating Goldstone relative-phase modes does not depend on N.

Recall that a similar value for the scaling exponent β has also been found in experiments employing a quasi-one-dimensional spin-1 Bose gas [35], see the discussion in Sect. 5.7. In this experiment, additional spin interactions and the quadratic Zeeman energy break the $U(3)$ symmetry, freezing out one of the relative-phase degrees of freedom at low momenta. Nonetheless, given the experimental parameters, the measured momentum range is within a regime well described by the $U(3)$-symmetric model such that a similar scaling behavior of correlations sensitive to the relative-phase degree of freedom can be observed in both systems.

As the non-thermal fixed-point scaling relation $\alpha = d\beta$ also holds for the relative-phase correlators $C_{ab}(k,t)$ shown in Fig. 7.1(b) as well as for the spin-contributions to the energy spectrum seen in Fig. 7.5, an additional emerging symmetry is expected to play an important role in the universal time evolution. Gaining a deeper understanding of such emergent conserved quantities and their general role in the framework of non-thermal fixed points is of particular interest in future research.

Numerically studying the non-equilibrium dynamics of the $U(3)$-symmetric Bose gas further revealed that the extracted scaling exponents only slowly approach the constant universal value predicted at the non-thermal fixed point. This offers the possibility to study how the system actually approaches the associated non-thermal fixed point.

A major future challenge from an analytical perspective is to make predictions for the scaling behavior at a non-thermal fixed point in presence of topological excitations. This is lacking so far as it is not known how to properly derive a low-energy effective description in presence of a non-equilibrium ensemble of topological excitations. An expansion about a single stationary topological background solution has already been performed for the case of a kink defect in one spatial dimension [111]. However, this simply provides low-energy excitations on top of that stationary background solution,

which does not resemble the non-equilibrium configuration in the numerically studied systems.

In addition, the analytical scaling analysis of the kinetic equation solely provides information about the power-law fall-off of the scaling function. Relevant information characterizing the entire scaling function, such as the bending over from a plateau to the power-law fall-off, are not directly accessible.

From a numerical perspective it is an interesting question whether we can generate initial configurations in the $U(N)$-symmetric model for which topological excitations are either completely absent or become dominant in the non-equilibrium evolution of the system. While the former case should lead to a clean observation of non-thermal fixed point scaling governed by the collective excitations, the latter case might reveal a different set of scaling exponents associated with the annihilation of topological excitations. In addition, we are able to study the role of dimensionality on the scaling evolution of the system. A natural question arising straightforwardly is whether collective excitations can dominate the fixed point scaling in two spatial dimensions or whether vortices always play the dominant role as for the spin-1 Bose gases discussed in Chpt. 6. Furthermore, it is possible to numerically study the case of $N = 2$ to investigate a system that features one Bogoliubov and one Goldstone mode in the low-energy regime. It is then of particular interest which mode determines the scaling properties of the system, i.e., which scaling exponents and scaling functions are observed for the two-point as well as higher-order correlators in the universal scaling regime.

Finally, extracting the pure phase correlators from the numerical data is of interest in its own right as it would allow us to directly compare the predictions of our low-energy effective theory to the numerical simulations. The main challenge lies in dealing with the compact nature of the phase fields. Finding suitable tools to properly extract the pure phase correlators is part of ongoing research.

8. Prescaling

At this point, it is worthwhile to recapitulate the conceptual aspects of the phenomena discussed in the course of this thesis. In all cases, we started with an isolated quantum many-body system that we prepared in a far-from-equilibrium state. For long evolution times, we then found the system to show universal scaling dynamics associated with a non-thermal fixed point. This immediately poses conceptual questions related to the intermediate non-equilibrium time evolution. Especially, we can ask how in general quantum many-body systems evolve from a given far-from-equilibrium initial state to such a fixed point. In this chapter, we elaborate on the possibility of *prescaling* as a generic feature of that evolution.

While the fixed point and thus full scaling in space and time, characterized by a fixed set of scaling functions and exponents, is generically reached at very long evolution times, we propose that systems can show prescaling much earlier in time. During the prescaling evolution, some well-measurable properties of spatial correlations already scale with the universal exponents of the fixed point while others still show scaling violations. Prescaling is characterized by the evolution obeying conservation laws associated with the remaining symmetry which also defines the universality class of the asymptotically reached non-thermal fixed point.

To illustrate the concept and the existence of prescaling, we consider a $U(3)$-symmetric Bose gas in three spatial dimensions. In particular, we reinvestigate the numerical data presented in Chpt. 7, where we have already seen indications of prescaling during the early stages of the evolution of momentum-space correlations. During the stage of prescaling, the system evolves according to a remaining $U(N-1)$ symmetry of the underlying $U(N)$-symmetric model. Furthermore, we find that the conserved transport, reflecting explicit and emerging symmetries, leads to the buildup of rescaling quasicondensate distributions.

This chapter is organized as follows: In Sect. 8.1, we give a motivation and a basic introduction to the concept of prescaling. As prescaling is more easily detected in position space, we discuss the relevant position-space correlations in Sect. 8.2. The main part of this chapter is devoted to the extraction of prescaling which is laid out in Sect. 8.3. Then, we continue with a brief discussion of the numerical results obtained from the extraction procedure in Sect. 8.4. We investigate the conservation laws obeyed during prescaling in Sect. 8.5. Furthermore, we elaborate on the build-up of the scaling function and present scaling violations in Sect. 8.6. Finally, we summarize our findings and give an outlook to future work in Sect. 8.7.

The content of this chapter is taken and adapted from Ref. [37]. I stress that the majority of the parts are taken verbatim from the publication. However, I reordered the overall structure of the presentation. I further added and/or modified formulations to embed the work into the broader context of this thesis.

8.1. Motivation and introduction

Universal scaling dynamics associated with a non-thermal fixed point is characterized by the scaling evolution of correlation functions. For example, the occupation number $n_a(\mathbf{k},t) = \langle \psi_a^\dagger(\mathbf{k},t)\psi_a(\mathbf{k},t)\rangle$ of an N-component Bose field $\psi_a(\mathbf{k},t)$ described by means of a $U(N)$-symmetric Gross-Pitaevskii model, *at* the fixed point, evolves in a self-similar manner according to

$$n_a(\mathbf{k},t) = (t/t_{\mathrm{ref}})^\alpha f_{\mathrm{s},a}([t/t_{\mathrm{ref}}]^\beta \mathbf{k})\,, \tag{8.1}$$

with universal scaling function $f_{\mathrm{s},a}$, scaling exponents α, β, and some reference time t_{ref} within the temporal scaling regime. In particular, the scaling exponent β defines the time evolution of a single characteristic length scale $L_\Lambda(t) \sim 1/k_\Lambda(t) \sim t^\beta$, where $k_\Lambda(t)$ is the associated characteristic momentum scale.

In the previous chapter, we showed that universal scaling of the $U(N)$-symmetric Bose gas at the non-thermal fixed point can be described analytically in terms of a low-energy effective theory for the phase-angle excitations of the Bose fields. Performing a scaling analysis of the kinetic equations within the large-N limit of the model (see Sect. 7.1.2), we obtained the scaling exponents $\beta = 1/2$ and $\alpha = \beta\, d = 3/2$ [52, 61]. Note that this set of exponents characterizes the self-similar evolution of the respective phase correlators $f_a(\mathbf{k},t) = \langle \theta_a(\mathbf{k},t)\theta_a(-\mathbf{k},t)\rangle$. However, as we find that the particular fixed point has Gaussian character, correlation functions factorize in the limit $t \to \infty$ and the scaling of $f_a(\mathbf{k},t)$ implies the scaling of $n_a(\mathbf{k},t)$ as well as of higher-order correlators of the fundamental Bose fields $\psi_a(\mathbf{k},t)$ [61].

Strictly speaking, the non-thermal fixed point itself is reached only in a certain scaling limit, such as, for $\beta > 0$, at asymptotic times and infinite volume. However, the question arises how the scaling limit is reached and to what extent and when scaling is already seen at finite times.

In equilibrium, fixed points of renormalization-group flows describe correlations at a continuous phase transition. They correspond to a pure rescaling of the correlations, in momentum or position space, under the change of the flow parameter such as a scale beyond which fluctuations are averaged over (see Sect. 2.1). In the context of critical phenomena as well as fundamental particle physics, renormalization flows are known which are first attracted to a partial fixed point [162]. In such situations, still away from the actual fixed point, scaling violations can occur for some quantities while others already show scaling and the further flow can be strongly constrained by a symmetry the system is subject to.

Motivated by the general concept of partial fixed points [12], we proposed the existence of *prescaling* [1] in Ref. [37]. This means that certain correlation functions, already at comparatively early times and within a limited range of distances, scale with the universal exponents predicted for the fixed point which itself is reached only much later in time and in a finite-size system may not be reached at all. During the stage of prescaling, (weak) scaling violations occur in correlations at distances outside this range. Such violations only slowly vanish as time evolves. In analogy to the case of partial fixed points, we expect the underlying symmetries of the system to play a key role for the realization of prescaling. While part of the symmetries can be broken, symmetries reflecting the conservation laws associated with the non-thermal fixed point remain intact during prescaling.

[1] C. Wetterich, private communication.

To reveal the existence of prescaling, we reinvestigate the early stages of the time evolution of the three-dimensional $U(3)$-symmetric Bose gas, discussed in Sect. 7.2.2, from a new perspective. Recall that, in the previous chapter, we focussed on corroborating the analytical predictions for the fixed-point scaling by means of analyzing the scaling behavior of momentum-space correlators in the late-time regime of our numerical simulations. In the course of this chapter, we are interested in the quantitative properties of the scaling functions and the respective exponents as the system approaches the non-thermal fixed point. To unravel the properties defining the stage of prescaling, we study the evolution of spatial correlations.

For details about the numerical parameters as well as the initial state of the simulations, see Sect. 7.2.1. Note that we again express length scales in units of the healing length $\Xi = [2Mg\rho^{(0)}]^{-1/2}$ and measure time in units of the characteristic time scale $t_\Xi = 2\pi/(g\rho^{(0)})$.

As symmetries play an important role for the realization of prescaling, we remark that already the chosen initial state does not obey the full $U(3)$ symmetry but breaks it to $U(2) \simeq [SU(2) \times U(1)]/Z_2$ as does the evolving state. The $U(3)$ symmetry of Eq. (3.1) gives rise to conservation laws, consistent with the reduced $U(2)$ symmetry, which will be obeyed during prescaling [61].

In case of the $U(3)$-symmetric Bose gas, we find prescaling to become visible in the short-distance properties of correlation functions that measure, for example, the spatial coherence of the local phase-angle differences between different components. We emphasize that scaling violations do not only affect the scaling exponents but in particular also the shape of the scaling functions.

8.2. Position-space correlations

While the scaling behavior *at* a non-thermal fixed point is commonly extracted from momentum-space correlators, we find that prescaling is more clearly seen in position-space correlations. Based on momentum-space treatments of non-thermal fixed point scaling, it is intuitive to study the first-order spatial coherence function $g_a^{(1)}(\mathbf{r}, t) = \langle \psi_a^\dagger(\mathbf{x}+\mathbf{r}, t)\, \psi_a(\mathbf{x}, t)\rangle$, as introduced in Eq. (3.22), which is obtained as the Fourier transform of the occupation number $n_a(\mathbf{k})$. At large evolution times, close to the non-thermal fixed point, the coherence function is expected to be spherically symmetric and characterized by a universal function $f_s(x)$ as $g_a^{(1)}(\mathbf{r}, t) = f_s(k_\Lambda(t)\, r)$, with $r = |\mathbf{r}|$. The inverse coherence length scales as $k_\Lambda(t) \sim t^{-\beta}$.

The time evolution of the angle-averaged first-order coherence function, for the component $a = 1$, is shown in Fig. 8.1(a). The coherence function takes, to a good approximation, an exponential form at short distances $r \gtrsim \Xi$. Similar results are found (not shown) for the components $a = 2, 3$. We stress that this behavior is in agreement with the analytical predictions derived from the low-energy effective field theory of non-thermal fixed points discussed in Sect. 7.1.2 and Ref. [61]. The exponential form of the coherence function is reminiscent of that of a quasicondensate in an equilibrium gas in one spatial dimension [128]. Hence, the coherence function signals the buildup of a non-equilibrium quasicondensate in three spatial dimensions, rescaling in time and space towards a longer-range coherence.

However, we observe that the numerically extracted form at larger distances clearly differs from a pure exponential, $g_a^{(1)}(\mathbf{r}, t) \sim \exp\{-k_\Lambda(t) r\}$. Instead, on top of an approximately exponential fall-off, the coherence function also shows oscillatory behavior in

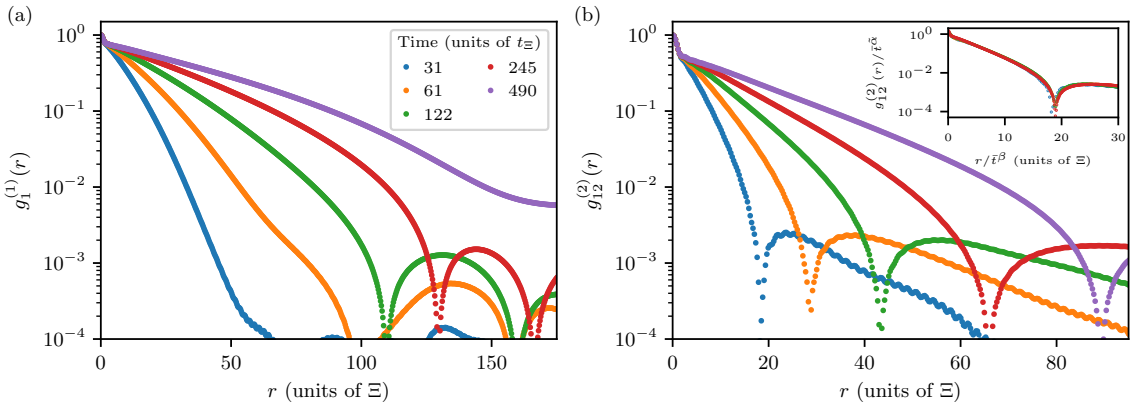

Figure 8.1.: (a) Time evolution of the angle-averaged first-order coherence function $g_1^{(1)}(r) \equiv g_1^{(1)}(r,t) = (4\pi)^{-1}\int d\Omega_{\mathbf{r}}\, g_1^{(1)}(\mathbf{r},t)$, where $g_1^{(1)}(\mathbf{r},t) = \langle\psi_1^\dagger(\mathbf{x}+\mathbf{r},t)\psi_1(\mathbf{x},t)\rangle$, at five different times (colored dots). The shape of the correlation function is reminiscent of an exponential with a multiplicative oscillatory contribution. It clearly exhibits violations of universal scaling at larger distances, which become weaker in time but still prevail even at long evolution times. At the latest time shown, finite-size effects appear. (b) Corresponding angle-averaged second-order coherence function measuring the spatial fluctuations of the relative phases between components 1 and 2, $g_{12}^{(2)}(r) \equiv g_{12}^{(2)}(r,t) = (4\pi)^{-1}\int d\Omega_{\mathbf{r}}\, g_{12}^{(2)}(\mathbf{r},t)$, where $g_{12}^{(2)}(\mathbf{r},t) = \langle\psi_1^\dagger(\mathbf{x}+\mathbf{r},t)\psi_2(\mathbf{x}+\mathbf{r},t)\psi_2^\dagger(\mathbf{x},t)\psi_1(\mathbf{x},t)\rangle$, for the same evolution times as in (a) (colored dots). The inset shows the rescaled coherence function $\bar{t}^{-\tilde{\alpha}} g_{12}^{(2)}(\bar{t}^{-\beta}r, t_{\mathrm{ref}})$, with $\beta = 0.6$, $\tilde{\alpha} = -0.2$, and $\bar{t} = t/t_{\mathrm{ref}}$, with reference time $t_{\mathrm{ref}} = 31\, t_\Xi$. The collapse of the data onto a single function, especially at short distances where $g_{12}^{(2)}(r,t) \gtrsim 10^{-2}$, indicates that violations of scaling are considerably weaker than for $g_1^{(1)}$. Note that we show absolute values of the angle-averaged coherence functions and normalize to unity at distance $r = 0$ to visualize all features of the data on a semi-logarithmic scale. Figure taken and adapted from Ref. [37].

r. Note that the low-energy effective field theory description does not allow us to make predictions for the functional form of the first-order coherence function in this regime. The oscillations indicate a structure developing in the system that causes excitations of the field to switch its sign over a distance on the order the inverse coherence length k_Λ, i.e., the phase strongly varies on that characteristic scale. Scaling violations at larger distances are clearly indicated by the change of the shape of the first-order coherence function at different evolution times.

We stress that, as the non-linear term in Eq. (3.1) couples the total densities, it suppresses total-density fluctuations but not fluctuations of the local density differences between the components. Hence, the spatial Goldstone excitations of the inter-component phase differences are predicted to become the relevant low-energy degree of freedom (see Sect. 3.1.2). As the first-order coherence function is insensitive to the relative phases $\theta_a - \theta_b$, we additionally study the second-order coherence function $g_{ab}^{(2)}(\mathbf{r},t) = \langle\psi_a^\dagger(\mathbf{x}+\mathbf{r},t)\,\psi_b(\mathbf{x}+\mathbf{r},t)\,\psi_b^\dagger(\mathbf{x},t)\,\psi_a(\mathbf{x},t)\rangle$ as introduced in Eq. (3.23).

The time evolution of the angle-averaged second-order correlation function for the

case of $(a, b) = (1, 2)$ is shown in Fig. 8.1(b). The second-order coherence function shows a form reminiscent of an exponential decay comparable to the first-order coherence function at short distances whereas a clear oscillatory behavior is seen at larger distances. As compared to the first-order coherence function, scaling violations at larger distances are much weaker for the second-order coherence function. This is clearly seen by the approximate rescaling collapse of the data in the inset of Fig. 8.1(b).

Note that we present the data in Fig. 8.1 on a semi-logarithmic scale to emphasize the exponential form at short distances. In order to additionally show the oscillatory behavior of the angle-averaged coherence functions, we take the absolute value at each position r. Furthermore, we normalize the correlators to unity at distance $r = 0$ for a better comparison.

8.3. Extraction of prescaling

A temporal scaling analysis of the numerically determined coherence functions $g_1^{(1)}(r, t)$ and $g_{12}^{(2)}(r, t)$ provides a direct way to extract the scaling exponent β via the single scale $k_\Lambda(t)$. However, as long as the fixed-point scaling is not yet fully developed, the time evolution of the correlations is not given by such a single scale. To account for that, we provide a general scheme for determining how the scaling behavior is being approached.

In order to approximate the correlation functions, within a certain regime of distances r, without any restriction to a particular scaling form, we expand them into a general Taylor series such that they take the form

$$g^{(l)}(r, t) = c_0^{(l)} + \sum_{n=1}^{\infty} c_n^{(l)}(t)\,(r - r_0)^n\,. \tag{8.2}$$

Here, $r_0 \geq 0$ marks the expansion point, and $l = 1, 2$ denotes the two different types of correlators. The time-dependent coefficients of the series, dropping the l-index, are written as

$$c_n(t) = c_n[k_{\Lambda,n}(t)]^n\,, \tag{8.3}$$

rescaling in time according to $k_{\Lambda,n}(t) \sim t^{-\beta_n}$. In consequence, the coefficients of the expansion rescale as

$$c_n(t) \sim t^{-n\,\beta_n}\,. \tag{8.4}$$

Each order of the expansion can be seen as a probe for the scaling of the correlations at a different distance r. The corresponding scaling exponents can be written as

$$\beta_n(t) = \beta + \delta\beta_n(t)\,. \tag{8.5}$$

A particular order of the expansion shows scaling with the fixed-point exponent β, when $\delta\beta_n(t)$ becomes small and approximately constant in time.

The system prescales when

$$\beta_n \approx \beta \tag{8.6}$$

for at least one order n of the expansion. The fixed point itself is, in a strict sense, only reached if the statement holds for all orders of the expansion.

For our system, we expect prescaling to emerge on short distances and to subsequently spread towards longer distances. Therefore, we truncate the expansion at the fourth

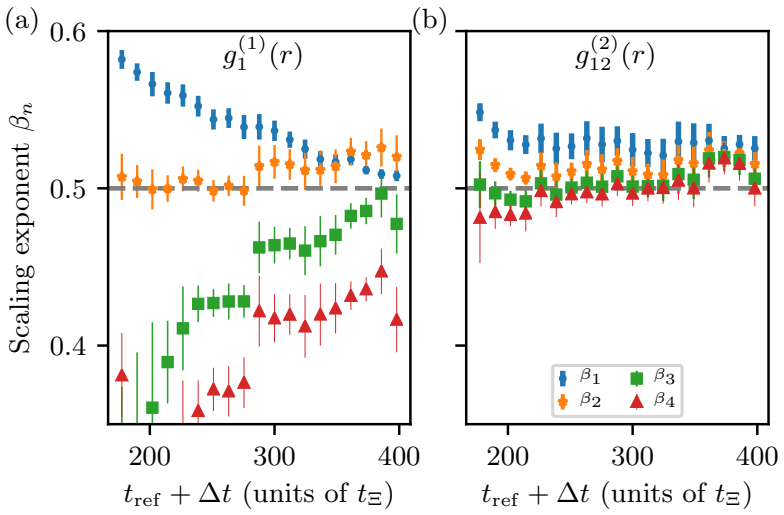

Figure 8.2.: Prescaling of position-space correlations. (a) Scaling exponents β_n describing the time evolution of $k_{\Lambda,n}(t) \sim t^{-\beta_n}$ with $n = 1, 2, 3, 4$. The different exponents are deduced from Taylor series coefficients $c_n(t) = c_n[k_{\Lambda,n}(t)]^n$ which are obtained by means of a fit of the first-order coherence function $g_1^{(1)}(r, t)$, see Fig. 8.1(a), at small distances r. The index n marks the corresponding order of the Taylor series. The jump of the exponents at $t_{\mathrm{ref}} + \Delta t \approx 285\, t_\Xi$ results from a sign change of the fitted third and fourth order coefficients. This indicates that the shape of the scaling form is altered more significantly on large distances as compared to short distances as can already be expected from Fig. 8.1(a). (b) Scaling exponents β_n deduced from an analogous Taylor series fit of $g_{12}^{(2)}(r, t)$ (see Fig. 8.1(b)). Prescaling is quantitatively seen by the scaling exponents β_n settling in to, within errors, equal stationary values for the lower orders of the fit. While $g_1^{(1)}(r)$, up to order r^4 shows scaling violations, $g_{12}^{(2)}(r)$ already scales, to a good approximation, with the predicted exponent $\beta = 1/2$ for $t_{\mathrm{ref}} + \Delta t \gtrsim 250\, t_\Xi$. For an individual fit, the β_n result from averaging over times $[t_{\mathrm{ref}}, t_{\mathrm{ref}} + \Delta t]$ with $\Delta t = 146\, t_\Xi$. The final data points shown are obtained by additionally averaging over a set of fits with different fit ranges. Errors are given by the corresponding standard deviation of the exponents of the set. Figure taken and adapted from Ref. [37].

order and extract the coefficients $c_n(t)$, with $n = 1, 2, 3, 4$, from a fit of the expansion to the data at various instances of time t. To focus on short-distance scaling properties of the system, the fit is applied at distances $5\,\Xi \lesssim r \ll \mathcal{L}$, with linear system size $\mathcal{L}$. By this choice, we exclude the non-universal regime at distances $r \lesssim 5\,\Xi$ which arises from contributions of the thermal tail in the region of large momenta (see Fig. 7.1).

As a consistent fitting procedure of a time series of curves is a somewhat challenging task, we briefly comment on the precise procedure applied in order to extract the time-resolved coefficients $c_n(t)$.

Due to the presence of the non-universal thermal peak at very short distances, we choose the fit range to be limited by the lower bound $r_{\mathrm{l.b.}}$. This lower bound is furthermore taken to be the expansion point of the Taylor series, $r_{\mathrm{l.b.}} = r_0$. In order to stay consistent during the scaling evolution of the coefficients, r_0 is changed in time according to $r_0(t) \sim t^{\beta}$. This is achieved by taking a fixed value of the correlation function at

all considered instances of time and determining the distance associated with this value, i.e., solving $g^{(l)}(r_0(t),t) = g^{(l)}_{\text{l.b.}}$ for $r_0(t)$. Analogously, we choose the fit to be limited by an upper bound $r_{\text{u.b.}}$, which is defined by the relation $g^{(l)}(r_{\text{u.b.}}(t),t) = g^{(l)}_{\text{u.b.}}$. The upper bound of the fit is chosen in a range sensitive to the highest order of the expansion used to fit the numerical data.

To ensure equal quality of the fit on short distances, independent of the evolution time and of the choice of the lower bound of the fit, we optimize the residuals defined as $|g^{(l)}(r,t)/g^{(l)}_{\text{fit}}(r,t)|$ of each fit at distances close to r_0 in a way that they symmetrically scatter around 1 with a maximum deviation of 1%, i.e., we keep $0.99 \leq |g^{(l)}(r,t)/g^{(l)}_{\text{fit}}(r,t)| \leq 1.01$ in a range of distances $d^{(l)}_{\text{min}}(t) \leq r(t) - r_0(t) \leq d^{(l)}_{\text{max}}(t)$. The length of the interval $[d^{(l)}_{\text{min}}(t),\, d^{(l)}_{\text{max}}(t)]$ is given by $d^{\,(l)} \cdot (t/t_{\text{ref}})^{1/2}$, with reference time $t_{\text{ref}} = 31\, t_{\Xi}$. The parameter $d^{\,(l)}$, characterizing the length of the interval at the reference time $t = t_{\text{ref}}$, is chosen to be $d^{\,(1)} = 6\,\Xi$ and $d^{\,(2)} = 4\,\Xi$. At each instance of time, the minimal distance $d^{(l)}_{\text{min}}(t) = r^{(l)}_{0,\text{min}}(t) - r_0(t)$ is given by the difference between the lowest expansion point of all fit ranges used for a particular correlation function, $r^{(l)}_{0,\text{min}}(t)$, and the lower bound of the current fit $r_0(t)$. Hence, $d^{(l)}_{\text{min}}(t) = 0$ for the fit corresponding to the expansion point $r^{(l)}_{0,\text{min}}(t)$, whereas $d^{(l)}_{\text{min}}(t) < 0$ for all other fits. This means that, for fits belonging to the latter class, we ensure that it matches the data well even at distances below the expansion point $r_0(t)$. The maximal distance $d^{(l)}_{\text{max}}(t)$ then directly follows from $d^{(l)}_{\text{min}}(t)$ and from the fixed length of the interval $[d^{(l)}_{\text{min}}(t), d^{(l)}_{\text{max}}(t)]$.

Applying this procedure to the numerical data, we are able to extract the Taylor coefficients as a function of the evolution time. Taking the negative of the logarithmic derivative of the fitted $c_n(t)$ with respect to t and dividing by n, gives the scaling exponent β_n at a particular instance in time. To reduce fluctuations of the locally in time extracted exponents, we average the β_n over a fixed time window. Taking into account possible fluctuations of the scaling exponents arising from the choice of the fit range, we furthermore average over different fit ranges, which are given by $0.55 \leq g^{(1)}_{\text{l.b.}} \leq 0.65$, $0.03 \leq g^{(1)}_{\text{u.b.}} \leq 0.08$ for the first-order coherence function, and $0.25 \leq g^{(2)}_{\text{l.b.}} \leq 0.40$, $0.005 \leq g^{(2)}_{\text{u.b.}} \leq 0.010$ for the second-order coherence function, respectively. This defines $r^{(1)}_{0,\text{min}}(t)$, at each instance of time and for all fits of the first-order coherence function, as the solution of $g^{(1)}(r^{(1)}_{0,\text{min}}(t),t) = 0.65$. Analogously, $r^{(2)}_{0,\text{min}}(t)$ is determined by the solution of $g^{(2)}(r^{(2)}_{0,\text{min}}(t),t) = 0.40$ for all fits of the second-order coherence function.

Performing the whole analysis procedure gives the scaling exponents β_n shown in Fig. 8.2, for $n = 1,2,3,4$, for both coherence functions $g^{(1)}_1$ and $g^{(2)}_{12}$.

8.4. Discussion of numerical results

The extraction of the time series of the scaling exponents β_n by means of the analysis procedure presented in the previous section reveals that the system indeed shows prescaling. This is quantitatively seen by the scaling exponents settling in to, within errors, equal stationary values for the lower orders of the fit, see Fig. 8.2. We stress that the particular value $\beta_n \simeq 0.5$ found in the late time regime for the scaling of $k_{\Lambda,n}(t)$, for $n = 1,2$, parameterizing $g^{(1)}_1$, and for $n = 1,2,3,4$ in the case of $g^{(2)}_{12}$, is in good

agreement with the analytically predicted fixed-point value of $\beta = 1/2$, see Sect. 7.1.2 and Refs. [34, 56, 61]. Note that the finite size of the system does not lead to continued scaling beyond an evolution time of $t \simeq 400\, t_\Xi$.

For the first-order coherence function $g_1^{(1)}$, we find that scaling in the higher orders of the expansion ($n = 3, 4$) is not yet fully developed within our numerical time window. This causes the scaling violations on larger distances observed in Fig. 8.1. The converging flow of the scaling exponents indicates the slow approach of a full scaling form. In consequence, the system appears on some scales already close to the non-thermal fixed point but is still away from it.

Comparing Figs. 8.2(a) and (b), we conclude that different correlators can enter the stage of prescaling on different time scales. Therefore, establishing the full scaling function and the associated scaling exponents is observable-dependent. This can also be intuitively concluded from comparing Figs. 8.1(a) and (b). In general, we expect the scaling applying at the fixed point to first show up in correlators of observables that are most sensitive to the relevant degrees of freedom of the underlying universal behavior.

Hence, our results indicate that the fixed-point scaling of the considered model is dominated by relative-phase fluctuations, forming the Goldstone modes of the broken $U(3)$ symmetry [61]. This further supports the discussion of the dominant role of relative-phase excitations for the universal scaling behavior of the system in Sect. 7.2.2. Note that these excitations are much less energetically constrained than the sound-like excitations of the total density, which are suppressed by the interaction term in Eq. (3.1) and associated with the overall $U(1)$ symmetry. If N is large, the relative-phase fluctuations, corresponding to the spatial re-shuffling of the local density differences between the different components, will in general dominate the non-equilibrium evolution of the system, also of the single-component correlators $g_1^{(1)}$. However, as in our case we are dealing with the comparatively small number of components $N = 3$, a clear difference in the scaling violations for $g_1^{(1)}$ and $g_{12}^{(2)}$ is seen.

8.5. Conservation laws during prescaling

We emphasize that the evolution during the stage of prescaling already obeys the conservation laws associated with the non-thermal fixed point. This can be inferred from the scaling behavior of the previously discussed momentum-space correlators $n_a(\mathbf{k}, t)$ and $C_{ab}(\mathbf{k}, t)$, associated with the position-space correlators $g_a^{(1)}(\mathbf{r}, t)$ and $g_{ab}^{(2)}(\mathbf{r}, t)$. The scaling collapse according to Eq. (8.1), as depicted in Fig. 7.1 for the occupation number $n_1(k, t)$ and the coherence function $C_{12}(k, t)$, revealed that the scaling along the k-axis quantified by the exponent β is coupled to the scaling along the vertical axis set by the exponent α. The relation, within errors, is found to be given by $\alpha = d\,\beta$, with $d = 3$ being the spatial dimension of the system. In consequence, the self-similar scaling leaves the d-dimensional volume, enclosed by the curves within the infrared scaling regime, approximately constant and thus, in each case, reflects a conserved symmetry during the prescaling evolution.

We emphasize that, due to the steep power law $n_a(k) \sim k^{-4}$ in the infrared (IR) scaling region, the particle number density is concentrated in this region of low momenta, where spatio-temporal scaling according to Eq. (8.1) is seen. In contrast, the energy density is concentrated in the high-momentum tail exhibiting semi-classical Rayleigh-Jeans distributions $n_a(k) \sim k^{-2}$. Hence, during the scaling evolution, the scales at which par-

ticles and energy are concentrated, separate continuously further in time and thus, in the IR region of momenta, this process is increasingly dominated by quasi-local particle number conservation only, see, e.g., Ref. [56].

This conservation law is due to the $U(3)$ symmetry of the model describing the dynamics of the system: The initial state as well as the state during the ensuing prescaling evolution break the full $U(N)$ symmetry of the model to $U(N-1) \simeq SU(N-1) \times U(1)/Z_{N-1}$, where the $SU(N-1)$ symmetry describes rotations of the resulting state leaving the symmetry-broken mean-density vector invariant, and the $U(1)$ is the additional total phase symmetry, also applying in the case of a vanishing mean-density vector. The Z_{N-1} factor accounts for the non-isomorphic centers of $U(N-1)$ and $SU(N-1)$ but is irrelevant for the conservation laws considered here. As a result, there is a remaining global $U(1)$ symmetry corresponding to the local conservation of the total particle density in the N components of the gas. Furthermore, our model does not allow for particle exchange between the different components, such that the particle numbers are actually conserved separately for each component. Stated differently, taking the generators of the $U(3)$ group, one finds that each of the components carries a separate $U(1)$ symmetry which is conserved also in the broken state and its further evolution. For the prescaling of $n_a(k,t)$, this implies the relation $\alpha = d\,\beta$.

Note that our numerics exhibits the same type of conservation law and power-law behavior for the coherence function $C_{12}(k,t)$, see Figs. 7.1(b) and 7.2(b). Here, the conservation law does not only refer to the conservation of the single-component and total particle numbers. Furthermore, it reflects that the local density fluctuations are small. This can be seen by considering the integral of $C_{12}(\mathbf{k})$ over all momenta $\mathbf{k}$, which corresponds to the density-density correlation function,

$$\begin{aligned}\int_{\mathbf{k}} C_{ab}(\mathbf{k},t) = \; & g_{ab}^{(2)}(0,t) = \langle \psi_a^\dagger(\mathbf{x},t)\psi_b(\mathbf{x},t)\psi_b^\dagger(\mathbf{x},t)\psi_a(\mathbf{x},t)\rangle \\ & = \langle \delta\rho_a(\mathbf{x},t)\delta\rho_b(\mathbf{x},t)\rangle + \rho_a^{(0)}\rho_b^{(0)} + (\delta_{ab}-1)\Omega\rho_a^{(0)}\,, \end{aligned} \tag{8.7}$$

where Ω is a constant representing the momentum-space volume. As a result of the suppression of density fluctuations, $\delta\rho_a(\mathbf{k})/\rho_a^{(0)} \sim |\mathbf{k}|/k_\Xi\theta_a(\mathbf{k}) \ll \theta_a(\mathbf{k})$ as compared to phase fluctuations $\theta_a(\mathbf{k})$ in the IR region of momenta $k \ll k_\Xi$, see Sect. 3.1.2 and Ref. [61], one may neglect the fluctuation contribution which implies an approximate conservation of the momentum integral of $C_{12}(\mathbf{k},t)$ in the scaling region, as seen in the relation $\alpha = d\,\beta$ between the scaling exponents characterizing the evolution of $C_{12}(\mathbf{k},t)$.

Note that this symmetry is an emerging approximate symmetry which is established during the stage of prescaling. The associated conservation law is expected to quantitatively improve the closer the system approaches the final fixed point.

8.6. Scaling function and scaling violations

In Sect. 8.3, we discussed the form of the spatial first-order coherence function $g_a^{(1)}(\mathbf{r},t)$ at comparatively short distances, larger than the extent of the thermal-peak and smaller than the scale of the first zero of the oscillating function. In order to obtain more quantitative insights about the scaling function beyond the low-r, near-exponential fall-off, we study the infrared regime of the corresponding momentum-space correlator $n_a(\mathbf{k},t)$. In the following, we exemplarily compare the numerical data with two idealized limiting

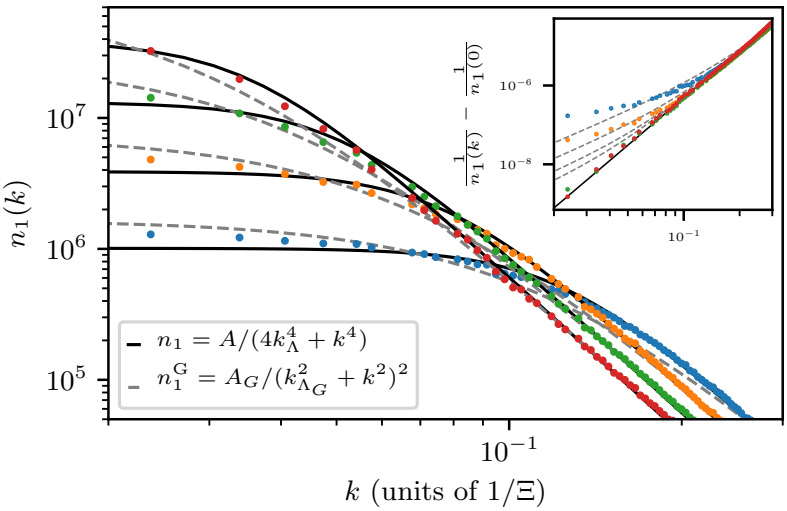

Figure 8.3.: Enlarged representation of the infrared prescaling evolution of the single-component occupation number $n_1(k) \equiv n_1(k,t)$ for the same evolution times as shown in Fig. 7.1(a) (same color coding). The solid black and dashed grey lines show the results obtained by fitting the corresponding scaling functions to the infrared part of the distribution. The extracted parameters for the fit of n_1 are $(A/C_3 k_\Lambda,\, k_\Lambda,\, t) = (0.82 \pm 0.02,\, 0.088 \pm 0.001$, blue), $(0.77 \pm 0.02,\, 0.055 \pm 0.001$, orange), $(0.76 \pm 0.02,\, 0.036 \pm 0.001$, green), and $(0.75 \pm 0.02,\, 0.025 \pm 0.001$, red). Analogously, the results for the fit of n_G are $(A_G/C_3 k_{\Lambda_G},\, k_{\Lambda_G},\, t) = (0.82 \pm 0.02,\, 0.118 \pm 0.002$, blue), $(0.76 \pm 0.02,\, 0.070 \pm 0.001$, orange), $(0.71 \pm 0.02,\, 0.044 \pm 0.001$, green), and $(0.69 \pm 0.02,\, 0.030 \pm 0.001$, red). We emphasize that the thermal tail present in the regime of large momenta, see Fig. 7.1(a), leads to an effective decrease of the extracted constant C_3 as compared to the analytical treatment, where a thermal tail is absent, such that the ratio $A/C_3 k_\Lambda$ differs from the analytically expected value of 1. Extrapolating the position-space correlation functions shown in Fig. 8.1(a) from distances larger than the thermal peak back to distance $r = 0$, yields a factor of ≈ 0.8 consistent with the ratios stated above from the fits. At late times (green and red), the data is close to the scaling function $n_1(\mathbf{k}, t)$, defined in Eq. (8.8), which corresponds to the first-order coherence function with exponential times cardinal-sine form in Eq. (8.9). For all evolution times, the data distinctly differs from the scaling function $n_1^{\mathrm{G}}(\mathbf{k}, t)$ defined in Eq. (8.10) which corresponds to the purely exponential first-order coherence function in Eq. (8.11). This supports the observation of the presence of an oscillatory contribution in the first-order coherence function. The fact that the quadratic term in the denominator gradually scales away is more clearly seen in the inset where we show $n_1(k)^{-1} - n_1(0)^{-1}$, with the respective extrapolated fit value inserted for $n_1(k = 0)$ in order to be independent of possible deviations due to the buildup of a condensate in the zero mode. The solid black line in the inset corresponds to the fit of Eq. (8.8) to the data for the latest time shown (red dots). Figure taken and adapted from Ref. [37].

cases of the momentum-space scaling form. Taking into account the extracted conservation law as well as the power-law fall-off, the momentum-space distribution $n_a(\mathbf{k}, t)$, as presented in Fig. 7.1 in the previous chapter, is approximately consistent with a scaling form given by

$$n_a(\mathbf{k}, t) = \frac{C_3\, k_\Lambda(t)}{4k_\Lambda^4(t) + |\mathbf{k}|^4}\,, \tag{8.8}$$

with normalization constant $C_3 = 8\pi\rho_a^{(0)}$ and $k_\Lambda(t) \sim t^{-\beta}$, for $k \lesssim k_\Xi$. Fourier transforming the function in Eq. (8.8) gives an exponential × cardinal-sine form of the first-order coherence function,

$$g_a^{(1)}(\mathbf{r}, t) = \rho_a^{(0)} \exp\Big(- k_\Lambda(t)\, |\mathbf{r}|\Big)\, \mathrm{sinc}\Big(k_\Lambda(t)\, |\mathbf{r}|\Big)\,, \tag{8.9}$$

($\mathrm{sinc}(x) = \sin(x)/x$) with uniform particle density $\rho_a^{(0)}$. An alternative functional form, which is also approximately compatible with the numerically determined momentum distribution, reads

$$n_a^{\mathrm{G}}(\mathbf{k}, t) = \frac{C_3 k_\Lambda(t)}{[k_\Lambda(t)^2 + |\mathbf{k}|^2]^2} = \frac{C_3 k_\Lambda(t)}{k_\Lambda(t)^4 + 2k_\Lambda(t)^2|\mathbf{k}|^2 + |\mathbf{k}|^4}\,, \tag{8.10}$$

with normalization constant C_3 as above. In contrast to the functional form in Eq. (8.8), a quadratic term $\propto |\mathbf{k}|^2$ is added to the denominator. Note that the function in Eq. (8.10) corresponds to the spatial first-order coherence function of the Bose fields having the form of a pure exponential,

$$g_a^{(1)}(\mathbf{r}, t) = \rho_a^{(0)} \exp\Big(- k_\Lambda(t)|\mathbf{r}|\Big)\,. \tag{8.11}$$

A comparison of the numerical data and the above mentioned two different functional forms is shown in Fig. 8.3. We find that, at late times, the data is close to the function in Eq. (8.8). In contrast, our data differs from the function in Eq. (8.10) for all evolution times, which is in accordance with the observation of the presence of an oscillatory contribution in the first-order coherence function.

Due to the rescaling of the inverse coherence length as $k_\Lambda(t) \sim t^{-\beta}$, the quadratic term in the denominator sets in below a decreasing momentum scale during prescaling. This can be clearly seen in the inset, where, in the late-time scaling regime and within the region of momenta relevant in the finite-size system, a single power law prevails in the inverse of the momentum distribution after subtracting a constant. Moreover, note that the precise form of the function during the scaling evolution is in between both limiting cases, i.e., the quadratic term in the denominator is found to have a prefactor smaller than 2. This results in a scaling function of the form of an exponential × cardinal-sine, with the argument $k_\Lambda(t)\, |\mathbf{r}|$ of the sine being multiplied with a different factor than that of the exponential.

The scaling violations in $n_1(k, t)$, corresponding to those discussed for $g_1^{(1)}(r, t)$ in Sect. 8.4, are seen as a gradual change in time of the form of the distribution at low momenta, see Fig. 8.3. In contrast, scaling violations are again weaker for the case of the relative-phase fluctuations, as is quantitatively seen in comparing Figs. 7.2(a) and (b).

8.7. Summary and outlook

In this chapter, we introduced and discussed the concept of prescaling, a generic feature of the evolution of an out-of-equilibrium quantum many-body system towards a non-thermal fixed point. During the prescaling evolution, some well-measurable properties of spatial correlations already scale with the universal exponents of the fixed point while others still show scaling violations.

We illustrated the concept and the existence of prescaling by investigating the non-equilibrium time evolution of a $U(3)$-symmetric Bose gas in three spatial dimensions. We presented a general approach for the extraction of the scaling exponents characterizing the prescaling evolution of the system and applied the procedure to the numerically obtained position-space correlation functions of the $U(3)$-symmetric model. Furthermore, we showed that already during the stage of prescaling, the evolution of the system obeys conservation laws associated with the non-thermal fixed point. Such conservation laws can either result from remaining symmetries in the system or emerge during the the non-equilibrium time evolution. Studying the scaling function of momentum-space correlators of the $U(3)$-symmetric model enabled us to characterize scaling violations present during the stage of prescaling and allowed us to elaborate on the oscillatory behavior seen in the position-space correlators at larger distances.

At this point, it is worth highlighting once again, that it is remarkable, that the $N = 3$ prescaling exponents β_i found for $g_a^{(1)}$ and $g_{ab}^{(2)}$, as shown in Fig. 8.2, are in good agreement with the analytically predicted fixed-point value $\beta = 1/2$ obtained within the large-N limit of the model. This further supports our suggestion that the universality class of the model is independent of the number of components N, reflecting that the $U(N)$ symmetry is broken during prescaling to $U(N-1)$ and that the dispersion of the dominating Goldstone relative-phase modes is independent of N.

In a broader sense, as prescaling emerges in the relatively early evolution after a quench far from equilibrium, it is expected to play an important role in the universal scaling evolution and its accessibility in experiments with ultracold atomic gases. Furthermore, from a renormalization-group perspective and with respect to the given underlying symmetries, we expect prescaling during the time evolution of various types of quantum many-body systems.

The notion of prescaling was also introduced on the basis of numerical studies of the spatio-temporal evolution of a quark-gluon plasma [163]. In this case, prescaling is characterized as a far-from-equilibrium phenomenon that describes the rapid establishment of a universal scaling form of distributions much before the universal values of the respective scaling exponents are realized. This means that the dynamical evolution of the investigated gluon distribution within the prescaling regime is fully encoded in a few time-dependent scaling exponents. This is different from the prescaling observed in the $U(3)$-symmetric Bose gas, where we find a systematic build-up of the scaling function connected to the respective scaling exponents approaching the associated fixed-point value. Nonetheless, the underlying conceptual ideas of the reported types of prescaling are very closely related corroborating the existence of prescaling in a variety of quantum many-body systems.

A future prospect is to make use of recently developed methods within the framework of temporal functional renormalization group (t-fRG) which allows studying the temporal flow of correlators induced by fluctuations in the system [164–166]. The aim is to choose a suitable initial condition and see the emergence of prescaling with the ability

to directly follow the respective dynamical flow. Eventually, the t-fRG flow stops and reaches a fixed point. Such a fixed point is then expected to have a correspondence to the non-thermal fixed point of the investigated model.

Part IV.

Concluding Remarks

9. Summary

In this thesis, we studied universal scaling dynamics associated with non-thermal fixed points of multi-component Bose gases far from equilibrium. We investigated the key features of the evolution by means of numerical simulations as well as analytical calculations.

To enable universal scaling and the approach of a non-thermal fixed point, the system has to be prepared in an extreme out-of-equilibrium initial configuration. We elaborated on potential scenarios to generate such configurations by means of parameter quenches. In particular, we discussed the generation process for one-dimensional spin-1 Bose gases, where we considered instantaneous parameter quenches between different phases of the model. Such quenches lead to instabilities which subsequently drive the system out of equilibrium in the early-time evolution. Whether the system is subject to an instability is inferred from the dynamical stability properties of the pre-quench state within the post-quench phase. We made use of Bogoliubov theory to investigate the respective stability properties. In addition to homogeneous systems, we analyzed the dynamical stability in presence of a trapping potential, which is common in experiments with ultracold quantum gases.

With this at hand, we numerically studied universal scaling dynamics of spin-1 Bose gases in one and two spatial dimensions. Irrespective of the dimensionality of the system, we found the scaling behavior to be driven by the annihilation and dissolution of (quasi)topological excitations. Numerical simulations of a one-dimensional spin-1 Bose gas revealed bidirectional universal scaling. While the growth of an infrared length scale with scaling exponent $\beta \simeq 0.25$ was associated with the dilution of kink-like defects separating patches of approximately uniform spin orientation, the refining ultraviolet length scale was determined by the decreasing width of the defects. We compared our findings to the experimental observation of universal scaling dynamics reported in Ref. [35]. The distinct deviation from the experimentally observed infrared scaling exponent $\beta \simeq 1/2$ was attributed to the presence of quasi-topological excitations in the numerical simulations. Furthermore, we discussed universal scaling involving the growth of two macroscopic length scales determined by the mutual annihilation of two types of spin vortices in a two-dimensional spin-1 Bose gas. As both vortices exhibited distinctly different decay laws, the standard, single-length-scale dynamical scaling hypothesis describing the self-similar evolution of correlation functions at the non-thermal fixed point could not hold for the correlations of the order-parameter field. However, we found that universality of the scaling behavior manifests in the decay laws for the individual spin vortices.

While universal scaling in the numerically simulated spin-1 Bose gases was driven by (quasi)topological excitations, we found collective excitations to dominate the scaling dynamics of $U(N)$-symmetric Bose gases. Deriving a low-energy effective field theory for the model revealed the phases of the complex bosonic fields as the relevant low-energy degree of freedom. Taking the large-N limit of the model, we showed that the respective excitations are Goldstone modes with free-particle dispersion characterizing the

excitations of relative phases between different components. Performing a scaling analysis of the respective kinetic equations enabled us to extract the scaling exponents and to determine the power-law fall-off of the corresponding phase correlator. We corroborated our analytical predictions by means of numerical simulations of a $U(3)$-symmetric Bose gas in three spatial dimensions. By making use of higher-order correlation functions and a decomposition of the hydrodynamic flow field, we showed that relative-phase excitations play the dominant role in the scaling evolution, as predicted within the large-N limit of the model, while topological excitations are present but subdominant. This suggests the universality class of the model to be independent of the number of components N.

As studies of universal scaling commonly focus on the scaling behavior at the non-thermal fixed point it was not known how a quantum many-body system generally approaches such a fixed point. This left a gap in the time evolution between the far-from-equilibrium initial configuration of the system and the actual fixed-point scaling. We conceptually bridge this gap by proposing prescaling as a phenomenon that occurs as a quantum many-body system approaches a non-thermal fixed point. During the prescaling evolution, some well-measurable properties of spatial correlations already scale with the universal exponents of the fixed point while others still show scaling violations. Prescaling is further characterized by the evolution obeying conservation laws associated with the remaining symmetry, which also defines the universality class of the asymptotically reached non-thermal fixed point. We illustrated and showed the existence of prescaling by means of numerical simulations of a $U(3)$-symmetric Bose gas in three spatial dimensions. While the extraction of prescaling was performed by analyzing position-space correlations, the conservation laws associated with the prescaling evolution could be deduced from respective momentum-space correlators.

The research presented in this thesis contributes to a deeper understanding of universal scaling dynamics far from equilibrium and unravels important key aspects for establishing out-of-equilibrium universality classes. In particular, our numerical studies showed the decisive role of excitations for the resulting scaling behavior of the system. Additionally, the variety of presented scaling evolutions suggests that the realized configuration of excitations and their interaction processes finally characterize the dynamics in the vicinity of the associated non-thermal fixed point. This hints to the fact that a classification of universal scaling dynamics far from equilibrium requires more than the underlying symmetries of the investigated microscopic model. From this point of view, it will be essential to identify the specifically relevant symmetries and the corresponding effective models that enable determining the respective out-of-equilibrium universality classes.

In addition, introducing the concept of prescaling enables us to shed light on the non-equilibrium evolution from the initial state to the associated non-thermal fixed point. As prescaling occurs in the short time dynamics of the evolution, it is expected to be detectable in state-of-the-art experiments with ultracold quantum gases.

10. Outlook

The main goal for the future is to establish a full classification of universal scaling far from equilibrium. Therefore, one has to unravel further key features that allow us to group many-body systems into distinct out-of-equilibrium universality classes.

One potential direction is to get analytical predictions for the scaling behavior at non-thermal fixed points in the presence of an ensemble of topological excitations. These predictions would give access to further investigate the decisive role of excitations for the realized universal dynamics. Another opportunity is to study high-order correlation functions and extract the building blocks of the quantum effective action of the many-body system [89, 90]. In particular, calculating four-point correlators of fields associated with the relevant low-energy degrees of freedom of the system offers the possibility to deduce momentum-dependent interaction properties of these objects. These properties can then be employed to explain the observed scaling behavior at the non-thermal fixed point.

As state-of-the-art experiments are able to access spatio-temporal scaling regimes and observe universal dynamics [35, 36], we can make use of experimental platforms in combination with numerical and analytical tools to tackle the overarching research question of classifying universal dynamics far from equilibrium.

For example, local manipulations, such as spin rotations, are a promising tool to imprint distributions of quasi-topological excitations in a controlled and reproducible fashion in (quasi) one-dimensional experimental settings. This technique provides the opportunity to study the influence of (quasi)topological excitations on the universal scaling behavior of the system as compared to the case where such excitations are absent. This is particularly relevant for a more complete understanding of the scaling evolution of the (quasi) one-dimensional spin-1 Bose gases discussed in the course of this thesis.

In two-dimensional experimental settings, one can think of producing tailored configurations of vortices and anti-vortices by means of the controlled generation of shock waves with external potentials. This allows investigating the scaling behavior of a particular type of topological excitation with respect to the underlying spatial configuration of these excitations.

At this point, we would like to stress that we have solely studied universal scaling in an equal-time framework in this thesis. In general, quantum-field-theoretical descriptions are formulated in terms of unequal-time quantities. Hence, further information about the nature of the scaling behavior can be stored in unequal-time correlators. While such observables are notoriously hard to extract experimentally, numerical simulations generally allow investigating such types of correlations, see Refs. [51, 167]. In the latter case, it was possible to unravel the nature of universal dynamics in $O(N)$-symmetric models by means of numerically analyzing unequal-time correlators. In particular, such correlators allow disentangling the dominant excitations in the universal scaling of highly-occupied N-component scalar systems. In that light, investigating unequal-time quantities is of strong interest for future research related to universal scaling dynamics associated with non-thermal fixed points.

Analytical treatments for the extraction of scaling behavior at non-thermal fixed points commonly make use of effective descriptions such as low-energy effective field theories and non-perturbative resummation schemes that are then employed to perform a scaling analysis of the respective kinetic equation. A different approach is to apply functional renormalization group techniques in order to derive flow equations for correlators, which can then be used to search for fixed point solutions that are expected to be connected to non-thermal fixed points of the investigated model.

The plethora of potential future research directions shows that a substantial amount of joint theoretical and experimental effort is still needed to shed far-reaching light on the extensive possibilities nature reserves for the structure and states of quantum many-body systems far from equilibrium.

Bibliography

[1] L. Kofman, A. D. Linde, and A. A. Starobinsky, "Reheating after inflation," Phys. Rev. Lett. **73**, 3195 (1994).

[2] R. Micha and I. I. Tkachev, "Relativistic Turbulence: A Long Way from Preheating to Equilibrium," Phys. Rev. Lett. **90**, 121301 (2003).

[3] R. Baier, A. H. Mueller, D. Schiff, and D. T. Son, "'Bottom up' thermalization in heavy ion collisions," Phys. Lett. **B502**, 51 (2001).

[4] J. Berges, K. Boguslavski, S. Schlichting, and R. Venugopalan, "Turbulent thermalization process in heavy-ion collisions at ultrarelativistic energies," Phys. Rev. D **89**, 074011 (2014).

[5] I. Bloch, J. Dalibard, and W. Zwerger, "Many-body physics with ultracold gases," Rev. Mod. Phys. **80**, 885 (2008).

[6] A. Polkovnikov, K. Sengupta, A. Silva, and M. Vengalattore, "Colloquium: Nonequilibrium dynamics of closed interacting quantum systems," Rev. Mod. Phys. **83**, 863 (2011).

[7] T. Kinoshita, T. Wenger, and D. S. Weiss, "A quantum Newton's cradle," Nature **440**, 900 (2006).

[8] S. Hofferberth, I. Lesanovsky, B. Fischer, T. Schumm, and J. Schmiedmayer, "Non-equilibrium coherence dynamics in one-dimensional Bose gases," Nature **449**, 324 (2007).

[9] S. Trotzky, Y.-A. Chen, A. Flesch, I. P. McCulloch, U. Schollwöck, J. Eisert, and I. Bloch, "Probing the relaxation towards equilibrium in an isolated strongly correlated one-dimensional Bose gas," Nature Phys. **8**, 325 (2012).

[10] P. Calabrese, F. H. L. Essler, and G. Mussardo, "Introduction to 'Quantum Integrability in Out of Equilibrium Systems'," J. Stat. Mech.: Theor. Exp. **2016**, 064001 (2016).

[11] L. M. A. Bettencourt and C. Wetterich, "Time evolution of correlation functions in non-equilibrium field theories," Phys. Lett. **B430**, 140 (1998).

[12] G. Aarts, G. F. Bonini, and C. Wetterich, "Exact and truncated dynamics in nonequilibrium field theory," Phys. Rev. D **63**, 025012 (2000).

[13] J. Berges, S. Borsanyi, and C. Wetterich, "Prethermalization," Phys. Rev. Lett. **93**, 142002 (2004).

[14] M. Gring, M. Kuhnert, T. Langen, T. Kitagawa, B. Rauer, M. Schreitl, I. Mazets, D. A. Smith, E. Demler, and J. Schmiedmayer, "Relaxation and Prethermalization in an Isolated Quantum System," Science **337**, 1318 (2012).

[15] T. Langen, T. Gasenzer, and J. Schmiedmayer, "Prethermalization and universal dynamics in near-integrable quantum systems," J. Stat. Mech. **1606**, 064009 (2016).

[16] E. T. Jaynes, "Information Theory and Statistical Mechanics," Phys. Rev. **106**, 620 (1957).

[17] E. T. Jaynes, "Information Theory and Statistical Mechanics. ii," Phys. Rev. **108**, 171 (1957).

[18] M. Rigol, V. Dunjko, V. Yurovsky, and M. Olshanii, "Relaxation in a Completely Integrable Many-Body Quantum System: An Ab Initio Study of the Dynamics of the Highly Excited States of 1D Lattice Hard-Core Bosons," Phys. Rev. Lett. **98**, 050405 (2007).

[19] T. Langen, S. Erne, R. Geiger, B. Rauer, T. Schweigler, M. Kuhnert, W. Rohringer, I. E. Mazets, T. Gasenzer, and J. Schmiedmayer, "Experimental observation of a generalized Gibbs ensemble," Science **348**, 207 (2015).

[20] L. Vidmar and M. Rigol, "Generalized Gibbs ensemble in integrable lattice models," J. Stat. Mech.: Theor. Exp. **6**, 064007 (2016).

[21] S. Braun, M. Friesdorf, S. S. Hodgman, M. Schreiber, J. P. Ronzheimer, A. Riera, M. del Rey, I. Bloch, J. Eisert, and U. Schneider, "Emergence of coherence and the dynamics of quantum phase transitions," PNAS **112**, 3641 (2015).

[22] E. Nicklas, M. Karl, M. Höfer, A. Johnson, W. Muessel, H. Strobel, J. Tomkovic, T. Gasenzer, and M. K. Oberthaler, "Observation of scaling in the dynamics of a strongly quenched quantum gas," Phys. Rev. Lett. **115**, 245301 (2015).

[23] N. Navon, A. L. Gaunt, R. P. Smith, and Z. Hadzibabic, "Critical dynamics of spontaneous symmetry breaking in a homogeneous Bose gas," Science **347**, 167 (2015).

[24] C. Eigen, J. A. P. Glidden, R. Lopes, E. A. Cornell, R. P. Smith, and Z. Hadzibabic, "Universal Prethermal Dynamics of Bose Gases Quenched to Unitarity," Nature **563**, 221 (2018).

[25] M. Schreiber, S. S. Hodgman, P. Bordia, H. P. Lüschen, M. H. Fischer, R. Vosk, E. Altman, U. Schneider, and I. Bloch, "Observation of many-body localization of interacting fermions in a quasirandom optical lattice," Science **349**, 842 (2015).

[26] R. Vasseur and J. E. Moore, "Nonequilibrium quantum dynamics and transport: from integrability to many-body localization," J. Stat. Mech.: Theor. Exp. **6**, 064010 (2016).

[27] F. H. L. Essler and M. Fagotti, "Quench dynamics and relaxation in isolated integrable quantum spin chains," J. Stat. Mech.: Theor. Exp. **6**, 064002 (2016).

[28] M. A. Cazalilla and M.-C. Chung, "Quantum quenches in the Luttinger model and its close relatives," J. Stat. Mech.: Theor. Exp. **6**, 064004 (2016).

[29] V. E. Zakharov, V. S. L'vov, and G. Falkovich, *Kolmogorov Spectra of Turbulence I: Wave Turbulence* (Springer, Berlin, 1992).

[30] S. Nazarenko, *Wave turbulence*, Lecture Notes in Physics No. 825 (Springer, Heidelberg, 2011) pp. XVI, 279.

[31] N. Navon, A. L. Gaunt, R. P. Smith, and Z. Hadzibabic, "Emergence of a turbulent cascade in a quantum gas," Nature **539**, 72 (2016).

[32] B. Rauer, S. Erne, T. Schweigler, F. Cataldini, M. Tajik, and J. Schmiedmayer, "Recurrences in an isolated quantum many-body system," Science **360**, 307 (2018).

[33] J. Berges, A. Rothkopf, and J. Schmidt, "Non-thermal fixed points: Effective weak-coupling for strongly correlated systems far from equilibrium," Phys. Rev. Lett. **101**, 041603 (2008).

[34] A. Piñeiro Orioli, K. Boguslavski, and J. Berges, "Universal self-similar dynamics of relativistic and nonrelativistic field theories near nonthermal fixed points," Phys. Rev. D **92**, 025041 (2015).

[35] M. Prüfer, P. Kunkel, H. Strobel, S. Lannig, D. Linnemann, C.-M. Schmied, J. Berges, T. Gasenzer, and M. K. Oberthaler, "Observation of universal quantum dynamics far from equilibrium," Nature **563**, 217 (2018).

[36] S. Erne, R. Bücker, T. Gasenzer, J. Berges, and J. Schmiedmayer, "Universal dynamics in an isolated one-dimensional Bose gas far from equilibrium," Nature **563**, 225 (2018).

[37] C.-M. Schmied, A. N. Mikheev, and T. Gasenzer, "Prescaling in a far-from-equilibrium Bose gas," Phys. Rev. Lett. **122**, 170404 (2019).

[38] J. Berges, K. Boguslavski, S. Schlichting, and R. Venugopalan, "Universality far from equilibrium: From superfluid Bose gases to heavy-ion collisions," Phys. Rev. Lett. **114**, 061601 (2015).

[39] B. Nowak, D. Sexty, and T. Gasenzer, "Superfluid turbulence: Nonthermal fixed point in an ultracold Bose gas," Phys. Rev. B **84**, 020506(R) (2011).

[40] B. Nowak, J. Schole, D. Sexty, and T. Gasenzer, "Nonthermal fixed points, vortex statistics, and superfluid turbulence in an ultracold Bose gas," Phys. Rev. A **85**, 043627 (2012).

[41] M. Schmidt, S. Erne, B. Nowak, D. Sexty, and T. Gasenzer, "Nonthermal fixed points and solitons in a one-dimensional Bose gas," New J. Phys. **14**, 075005 (2012).

[42] J. Schole, B. Nowak, and T. Gasenzer, "Critical dynamics of a two-dimensional superfluid near a non-thermal fixed point," Phys. Rev. A **86**, 013624 (2012).

[43] M. Karl, B. Nowak, and T. Gasenzer, "Tuning universality far from equilibrium," Sci. Rep. **3**, 2394 (2013).

[44] M. Karl, B. Nowak, and T. Gasenzer, "Universal scaling at non-thermal fixed points of a two-component Bose gas," Phys. Rev. A **88**, 063615 (2013).

[45] M. Karl and T. Gasenzer, "Strongly anomalous non-thermal fixed point in a quenched two-dimensional Bose gas," New J. Phys. **19**, 093014 (2017).

[46] J. Berges and G. Hoffmeister, "Nonthermal fixed points and the functional renormalization group," Nucl. Phys. **B813**, 383 (2009).

[47] C. Scheppach, J. Berges, and T. Gasenzer, "Matter-wave turbulence: Beyond kinetic scaling," Phys. Rev. A **81**, 033611 (2010).

[48] J. Berges and D. Sexty, "Strong versus weak wave-turbulence in relativistic field theory," Phys. Rev. D **83**, 085004 (2011).

[49] J. Berges, K. Boguslavski, S. Schlichting, and R. Venugopalan, "Universal attractor in a highly occupied non-Abelian plasma," Phys. Rev. D **89**, 114007 (2014).

[50] J. Berges, "Nonequilibrium Quantum Fields: From Cold Atoms to Cosmology," in *Proc. Int. School on Strongly Interacting Quantum Systems Out of Equilibrium, Les Houches*, edited by T. Giamarchi et al. (OUP, Oxford, 2016).

[51] A. Piñeiro Orioli and J. Berges, "Breaking the fluctuation-dissipation relation by universal transport processes," Phys. Rev. Lett. **122**, 150401 (2019).

[52] C.-M. Schmied, A. N. Mikheev, and T. Gasenzer, "Non-thermal fixed points: Universal dynamics far from equilibrium," Int. J. Mod. Phys. A **34**, 1941006 (2019).

[53] P. C. Hohenberg and B. I. Halperin, "Theory of Dynamic Critical Phenomena," Rev. Mod. Phys. **49**, 435 (1977).

[54] N. Goldenfeld, *Lectures on phase transitions and the renormalization group*, Frontiers in physics (Addison-Wesley, 1992).

[55] J. Zinn-Justin, *Quantum Field Theory and Critical Phenomena*, International series of monographs on physics (Clarendon Press, Oxford, UK, 2004).

[56] I. Chantesana, A. Piñeiro Orioli, and T. Gasenzer, "Kinetic theory of nonthermal fixed points in a Bose gas," Phys. Rev. A **99**, 043620 (2019).

[57] B. Nowak, J. Schole, and T. Gasenzer, "Universal dynamics on the way to thermalisation," New J. Phys. **16**, 093052 (2014).

[58] J. Berges and D. Sexty, "Bose condensation far from equilibrium," Phys. Rev. Lett. **108**, 161601 (2012).

[59] M. J. Davis, T. M. Wright, T. Gasenzer, S. A. Gardiner, and N. P. Proukakis, "Formation of Bose-Einstein condensates," in *Universal Themes of Bose-Einstein Condensation*, edited by D. W. Snoke, N. P. Proukakis, and P. B. Littlewood (CUP, Cambridge, 2017).

[60] B. Svistunov, "Highly nonequilibrium Bose condensation in a weakly interacting gas," J. Mosc. Phys. Soc. **1**, 373 (1991).

[61] A. N. Mikheev, C.-M. Schmied, and T. Gasenzer, "Low-energy effective theory of nonthermal fixed points in a multicomponent Bose gas," Phys. Rev. A **99**, 063622 (2019).

[62] B. Nowak, S. Erne, M. Karl, J. Schole, D. Sexty, and T. Gasenzer, "Non-thermal fixed points: universality, topology, & turbulence in Bose gases," in *Proc. Int. School on Strongly Interacting Quantum Systems Out of Equilibrium, Les Houches*, edited by T. Giamarchi et al. (OUP, Oxford, 2016).

[63] C. Ewerz, T. Gasenzer, M. Karl, and A. Samberg, "Non-Thermal Fixed Point in a Holographic Superfluid," JHEP **05**, 070 (2015).

[64] J. Berges, K. Boguslavski, A. Chatrchyan, and J. Jaeckel, "Attractive versus repulsive interactions in the Bose-Einstein condensation dynamics of relativistic field theories," Phys. Rev. D **96**, 076020 (2017).

[65] J. Deng, S. Schlichting, R. Venugopalan, and Q. Wang, "Off-equilibrium infrared structure of self-interacting scalar fields: Universal scaling, Vortex-antivortex superfluid dynamics and Bose-Einstein condensation," Phys. Rev. A **97**, 053606 (2018).

[66] J. Berges and J. Jaeckel, "Far from equilibrium dynamics of Bose-Einstein condensation for Axion Dark Matter," Phys. Rev. D **91**, 025020 (2015).

[67] G. D. Moore, "Condensates in Relativistic Scalar Theories," Phys. Rev. D **93**, 065043 (2016).

[68] J. Berges, K. Boguslavski, S. Schlichting, and R. Venugopalan, "Nonequilibrium fixed points in longitudinally expanding scalar theories: infrared cascade, Bose condensation and a challenge for kinetic theory," Phys. Rev. D **92**, 096006 (2015).

[69] A. J. Bray, "Theory of phase-ordering kinetics," Adv. Phys. **43**, 357 (1994).

[70] R. Kraichnan, "Inertial Ranges in Two-Dimensional Turbulence," Phys. Fl. **10**, 1417 (1967).

[71] B. Svistunov, E. Babaev, and N. Prokof'ev, *Superfluid States of Matter* (CRC Press, 2015).

[72] S. Ma, *Modern Theory of Critical Phenomena*, Advanced book classics (Perseus, 2000).

[73] S. Sachdev, *Quantum Phase Transitions* (Cambridge University Press, 2000).

[74] M. Henkel, H. Hinrichsen, and S. Lübeck, *Non-Equilibrium Phase Transitions: Volume 1: Absorbing Phase Transitions*, Theoretical and Mathematical Physics (Springer Netherlands, 2008).

[75] U. C. Täuber, *Critical Dynamics. A Field Theory Approach to Equilibrium and Non-Equilibrium Scaling Behaviour* (Cambridge University Press, 2014).

[76] J. Berges, "Introduction to nonequilibrium quantum field theory," AIP Conf. Proc. **739**, 3 (2005).

[77] J. Schwinger, "Brownian Motion of a Quantum Oscillator," J. Math. Phys. **2**, 407 (1961).

[78] K. T. Mahanthappa, "Multiple Production of Photons in Quantum Electrodynamics," Phys. Rev. **126**, 329 (1962).

[79] P. M. Bakshi and K. T. Mahanthappa, "Expectation Value Formalism in Quantum Field Theory. I," J. Math. Phys. **4**, 1 (1963).

[80] P. M. Bakshi and K. T. Mahanthappa, "Expectation Value Formalism in Quantum Field theory. II," J. Math. Phys. **4**, 12 (1963).

[81] L. P. Kadanoff and G. Baym, *Quantum Statistical Mechanics* (Benjamin, 1962).

[82] M. Lindner and M. M. Müller, "Comparison of Boltzmann equations with quantum dynamics for scalar fields," Phys. Rev. D **73**, 125002 (2006).

[83] H. Georgi, "Effective field theory," Ann. Rev. Nucl. Part. Sci. **43**, 209 (1993).

[84] A. Pich, "Effective field theory: Course," in *Probing the standard model of particle interactions. Proceedings, Summer School in Theoretical Physics, NATO Advanced Study Institute, 68th session, Les Houches, France, July 28-September 5, 1997. Pt. 1, 2* (1998) pp. 949–1049.

[85] J. Berges and T. Gasenzer, "Quantum versus classical statistical dynamics of an ultracold Bose gas," Phys. Rev. A **76**, 033604 (2007).

[86] P. B. Blakie, A. S. Bradley, M. J. Davis, R. J. Ballagh, and C. W. Gardiner, "Dynamics and statistical mechanics of ultra-cold Bose gases using c-field techniques," Adv. Phys. **57**, 363 (2008).

[87] A. Polkovnikov, "Phase space representation of quantum dynamics," Ann. Phys. **325**, 1790 (2010).

[88] T. Gasenzer, "Ultracold gases far from equilibrium," Eur. Phys. J. ST **168**, 89 (2009).

[89] M. Prüfer, T. V. Zache, P. Kunkel, S. Lannig, A. Bonnin, H. Strobel, J. Berges, and M. K. Oberthaler, "Experimental extraction of the quantum effective action for a non-equilibrium many-body system," (2019), arXiv:1909.05120 [cond-mat.quant-gas] .

[90] T. V. Zache, T. Schweigler, S. Erne, J. Schmiedmayer, and J. Berges, "Extracting the field theory description of a quantum many-body system from experimental data," (2019), arXiv:1909.12815 [cond-mat.quant-gas] .

[91] J. Berges, "Controlled nonperturbative dynamics of quantum fields out of equilibrium," Nucl. Phys. **A699**, 847 (2002).

[92] A. X. Arrizabalaga, *Quantum field dynamics and the 2PI effective action*, PhD thesis, University of Amsterdam (2004).

[93] A. Branschädel and T. Gasenzer, "2PI nonequilibrium versus transport equations for an ultracold Bose gas," J. Phys. B **41**, 135302 (2008).

[94] T. Gasenzer, J. Berges, M. G. Schmidt, and M. Seco, "Non-perturbative dynamical many-body theory of a Bose-Einstein condensate," Phys. Rev. A **72**, 063604 (2005).

[95] J. Stenger, S. Inouye, D. Stamper-Kurn, H. Miesner, A. Chikkatur, and W. Ketterle, "Spin domains in ground-state Bose-Einstein condensates," Nature **396**, 345 (1998).

[96] T.-L. Ho, "Spinor Bose condensates in optical traps," Phys. Rev. Lett. **81**, 742 (1998).

[97] L. E. Sadler, J. M. Higbie, S. R. Leslie, M. Vengalattore, and D. M. Stamper-Kurn, "Spontaneous symmetry breaking in a quenched ferromagnetic spinor Bose-Einstein condensate," Nature **443**, 312 (2006).

[98] E. M. Bookjans, A. Vinit, and C. Raman, "Quantum phase transition in an antiferromagnetic spinor Bose-Einstein condensate," Phys. Rev. Lett. **107**, 195306 (2011).

[99] D. M. Stamper-Kurn and M. Ueda, "Spinor Bose gases: Symmetries, magnetism, and quantum dynamics," Rev. Mod. Phys. **85**, 1191 (2013).

[100] K. Fujimoto, R. Hamazaki, and M. Ueda, "Unconventional universality class of one-dimensional isolated coarsening dynamics in a spinor Bose gas," Phys. Rev. Lett. **120**, 073002 (2018).

[101] K. Fujimoto, R. Hamazaki, and M. Ueda, "Flemish strings of magnetic solitons and a nonthermal fixed point in a one-dimensional antiferromagnetic spin-1 Bose gas," Phys. Rev. Lett. **122**, 173001 (2019).

[102] C.-M. Schmied, M. Prüfer, M. K. Oberthaler, and T. Gasenzer, "Bidirectional universal dynamics in a spinor Bose gas close to a nonthermal fixed point," Phys. Rev. A **99**, 033611 (2019).

[103] J. Pietraszewicz, A. Seweryn, and E. Witkowska, "Multifaceted phase ordering kinetics of an antiferromagnetic spin-1 condensate," (2019), arXiv:1905.00662 [cond-mat.quant-gas] .

[104] L. A. Williamson and P. B. Blakie, "Universal coarsening dynamics of a quenched ferromagnetic spin-1 condensate," Phys. Rev. Lett. **116**, 025301 (2016).

[105] L. A. Williamson and P. B. Blakie, "Coarsening and thermalization properties of a quenched ferromagnetic spin-1 condensate," Phys. Rev. A **94**, 023608 (2016).

[106] L. A. Williamson and P. B. Blakie, "Coarsening dynamics of an isotropic ferromagnetic superfluid," Phys. Rev. Lett. **119**, 255301 (2017).

[107] L. M. Symes and P. B. Blakie, "Nematic ordering dynamics of an anti-ferromagnetic spin-1 condensate," Phys. Rev. A **96**, 013602 (2017).

[108] A. Bourges and P. B. Blakie, "Different growth rates for spin and superfluid order in a quenched spinor condensate," Phys. Rev. A **95**, 023616 (2017).

[109] C.-M. Schmied, T. Gasenzer, and P. B. Blakie, "Violation of single-length-scaling dynamics via spin vortices in an isolated spin-1 Bose gas," Phys. Rev. A **100**, 033603 (2019).

[110] L. P. Pitaevskii and S. Stringari, *Bose-Einstein Condensation* (Clarendon Press, Oxford, 2003).

[111] E. J. Weinberg, *Classical Solutions in Quantum Field Theory: Solitons and Instantons in High Energy Physics*, Cambridge Monographs on Mathematical Physics (Cambridge University Press, 2012).

[112] M. Henkel and M. Pleimling, *Non-Equilibrium Phase Transitions: Volume 2: Ageing and Dynamical Scaling Far from equilibrium*, Theoretical and Mathematical Physics (Springer Netherlands, 2010).

[113] V. E. Zakharov and A. B. Shabat, "Exact theory of two-dimensional self-focusing and one-dimensional self-modulation of waves in nonlinear media," JETP **34**, 62 (1972).

[114] D. J. Frantzeskakis, "Dark solitons in atomic Bose–Einstein condensates: from theory to experiments," J. Phys. A **43**, 213001 (2010).

[115] B. P. Anderson, P. C. Haljan, C. A. Regal, D. L. Feder, L. A. Collins, C. W. Clark, and E. A. Cornell, "Watching dark solitons decay into vortex rings in a Bose-Einstein condensate," Phys. Rev. Lett. **86**, 2926 (2001).

[116] P. G. Kevrekidis and D. J. Franteskakis, "Pattern forming dynamical instabilities of Bose-Einstein condensates," Mod. Phys. Lett. B **18**, 173 (2004).

[117] P. Kevrekidis and D. Frantzeskakis, "Solitons in coupled nonlinear Schrödinger models: A survey of recent developments," Rev. Phys. **1**, 140 (2016).

[118] S. Middelkamp, J. Chang, C. Hamner, R. Carretero-González, P. Kevrekidis, V. Achilleos, D. Frantzeskakis, P. Schmelcher, and P. Engels, "Dynamics of dark-bright solitons in cigar-shaped Bose-Einstein condensates," Phys. Lett. A **375**, 642 (2011).

[119] D. Yan, J. J. Chang, C. Hamner, P. G. Kevrekidis, P. Engels, V. Achilleos, D. J. Frantzeskakis, R. Carretero-González, and P. Schmelcher, "Multiple dark-bright solitons in atomic Bose-Einstein condensates," Phys. Rev. A **84**, 053630 (2011).

[120] C. Hamner, J. J. Chang, P. Engels, and M. A. Hoefer, "Generation of dark-bright soliton trains in superfluid-superfluid counterflow," Phys. Rev. Lett. **106**, 065302 (2011).

[121] M. Vijayajayanthi, T. Kanna, and M. Lakshmanan, "Bright-dark solitons and their collisions in mixed N-coupled nonlinear Schrödinger equations," Phys. Rev. A **77**, 013820 (2008).

[122] B. Prinari, F. Vitale, and G. Biondini, "Dark-bright soliton solutions with non-trivial polarization interactions for the three-component defocusing nonlinear Schrödinger equation with nonzero boundary conditions," J. Math. Phys. **56**, 071505 (2015).

[123] T. M. Bersano, V. Gokhroo, M. A. Khamehchi, J. D'Ambroise, D. J. Frantzeskakis, P. Engels, and P. G. Kevrekidis, "Three-component soliton states in spinor $F = 1$ Bose-Einstein condensates," Phys. Rev. Lett. **120**, 063202 (2018).

[124] K. Kudo and Y. Kawaguchi, "Coarsening dynamics driven by vortex-antivortex annihilation in ferromagnetic Bose-Einstein condensates," Phys. Rev. A **91**, 053609 (2015).

[125] J. Goldstone, "Field Theories with Superconductor Solutions," Nuovo Cim. **19**, 154 (1961).

[126] H. Watanabe and H. Murayama, "Unified Description of Nambu-Goldstone Bosons without Lorentz Invariance," Phys. Rev. Lett. **108**, 251602 (2012).

[127] D. Pekker and C. M. Varma, "Amplitude/Higgs Modes in Condensed Matter Physics," Ann. Rev. Cond. Mat. Phys. **6**, 269 (2015).

[128] M. A. Cazalilla, R. Citro, T. Giamarchi, E. Orignac, and M. Rigol, "One dimensional bosons: From condensed matter systems to ultracold gases," Rev. Mod. Phys. **83**, 1405 (2011).

[129] C.-M. Schmied, T. Gasenzer, M. K. Oberthaler, and P. G. Kevrekidis, "Stability analysis of ground states in a one-dimensional trapped spin-1 Bose gas," CNSNS **83**, 105050 (2020).

[130] Y. Kawaguchi and M. Ueda, "Spinor Bose-Einstein condensates," Phys. Rep. **520**, 253 (2012).

[131] E. Gross, "Classical theory of boson wave fields," Ann. Phys. **4**, 57 (1958).

[132] W. Bao and Y. Zhang, "Dynamical Laws of the Coupled Gross-Pitaevskii Equations for Spin-1 Bose-Einstein Condensates," Methods Appl. Anal. **17**, 49 (2010).

[133] S. Heupts, *Nonequilibrium dynamics of an ultracold spin-1 Bose gas*, Master thesis, Universität Heidelberg (2014).

[134] K. Geier, *Dynamics of Vector Solitons in Spinor Bose-Einstein Condensates*, Master thesis, Universität Heidelberg (2017).

[135] E. Yukawa and M. Ueda, "Hydrodynamic description of spin-1 Bose-Einstein condensates," Phys. Rev. A **86**, 063614 (2012).

[136] A. J. Bray, A. J. Briant, and D. K. Jervis, "Breakdown of Scaling in the Nonequilibrium Critical Dynamics of the Two-Dimensional XY Model," Phys. Rev. Lett. **84**, 1503 (2000).

[137] A. D. Rutenberg and A. J. Bray, "Energy-scaling approach to phase-ordering growth laws," Phys. Rev. E **51**, 5499 (1995).

[138] A. D. Rutenberg and A. J. Bray, "Unwinding scaling violations in phase ordering," Phys. Rev. Lett. **74**, 3836 (1995).

[139] R. E. Blundell and A. J. Bray, "Phase-ordering dynamics of the $O(n)$ model: Exact predictions and numerical results," Phys. Rev. E **49**, 4925 (1994).

[140] A. J. Bray, "Renormalization-group approach to domain-growth scaling," Phys. Rev. B **41**, 6724 (1990).

[141] S. Puri, A. J. Bray, and F. Rojas, "Ordering kinetics of conserved XY models," Phys. Rev. E **52**, 4699 (1995).

[142] K. Kudo and Y. Kawaguchi, "Magnetic domain growth in a ferromagnetic Bose-Einstein condensate: Effects of current," Phys. Rev. A **88**, 013630 (2013).

[143] T. Simula, M. J. Davis, and K. Helmerson, "Emergence of order from turbulence in an isolated planar superfluid," Phys. Rev. Lett. **113**, 165302 (2014).

[144] A. J. Groszek, T. P. Simula, D. M. Paganin, and K. Helmerson, "Onsager vortex formation in Bose-Einstein condensates in two-dimensional power-law traps," Phys. Rev. A **93**, 043614 (2016).

[145] S. P. Johnstone, A. J. Groszek, P. T. Starkey, C. J. Billington, T. P. Simula, and K. Helmerson, "Evolution of large-scale flow from turbulence in a two-dimensional superfluid," Science **364**, 1267 (2019).

[146] J. Guzman, G.-B. Jo, A. N. Wenz, K. W. Murch, C. K. Thomas, and D. M. Stamper-Kurn, "Long-time-scale dynamics of spin textures in a degenerate $F = 1$ ^{87}Rb spinor Bose gas," Phys. Rev. A **84**, 063625 (2011).

[147] P. G. Kevrekidis, D. J. Frantzeskakis, and R. Carretero-González, *Emergent Nonlinear Phenomena in Bose-Einstein Condensates*, Springer Series on Atomic, Optical, and Plasma Physics, Vol. 45 (Springer, Berlin, 2008).

[148] B. J. Dabrowska-Wüster, E. A. Ostrovskaya, T. J. Alexander, and Y. S. Kivshar, "Multicomponent gap solitons in spinor Bose-Einstein condensates," Phys. Rev. A **75**, 023617 (2007).

[149] H. E. Nistazakis, D. J. Frantzeskakis, P. G. Kevrekidis, B. A. Malomed, and R. Carretero-González, "Bright-dark soliton complexes in spinor Bose-Einstein condensates," Phys. Rev. A **77**, 033612 (2008).

[150] Y. Nesterov, "A method for solving a convex programming problem with convergence rate $O(1/k^2)$," Sov. Math. Dokl. **27**, 372 (1983).

[151] W. Su, S. Boyd, and E. J. Candès, "A differential equation for modeling Nesterov's accelerated gradient method: Theory and insights," J. Mach. Learn. Res. **17**, 1 (2016).

[152] C. B. Ward, N. Whitaker, I. G. Kevrekidis, and P. G. Kevrekidis, "A toolkit for steady states of nonlinear wave equations: Continuous time Nesterov and exponential time differencing schemes," arXiv:1710.05047 [nlin.PS] (2017).

[153] A. Vinit and C. Raman, "Hanbury Brown-Twiss correlations and multi-mode dynamics in quenched, inhomogeneous density spinor Bose-Einstein condensates," New J. Phys. **20**, 095003 (2018).

[154] N. Andrenacci, F. Corberi, and E. Lippiello, "Crossover between Ising and XY-like behavior in the off-equilibrium kinetics of the one-dimensional clock model," Phys. Rev. E **74**, 031111 (2006).

[155] M. Prüfer, *Experimentally testing quantum field theory concepts with spinor Bose gases far from equilibrium*, PhD thesis, Universität Heidelberg (2019).

[156] S. W. Seo, S. Kang, W. J. Kwon, and Y.-i. Shin, "Half-quantum vortices in an antiferromagnetic spinor Bose-Einstein condensate," Phys. Rev. Lett. **115**, 015301 (2015).

[157] H. Saito, Y. Kawaguchi, and M. Ueda, "Kibble-Zurek mechanism in a quenched ferromagnetic Bose-Einstein condensate," Phys. Rev. A **76**, 043613 (2007).

[158] R. Barnett, A. Polkovnikov, and M. Vengalattore, "Prethermalization in quenched spinor condensates," Phys. Rev. A **84**, 023606 (2011).

[159] C. J. Foster, P. B. Blakie, and M. J. Davis, "Vortex pairing in two-dimensional Bose gases," Phys. Rev. A **81**, 023623 (2010).

[160] C. Oh and C. Sorensen, "Scaling approach for the structure factor of a generalized system of scatterers," J. Nanopart. Res. **1** (1999).

[161] R. Walz, K. Boguslavski, and J. Berges, "Large-N kinetic theory for highly occupied systems," Phys. Rev. D **97**, 116011 (2018).

[162] C. Wetterich, "Gauge hierarchy due to strong interactions?" Phys. Lett. B **104**, 269 (1981).

[163] A. Mazeliauskas and J. Berges, "Prescaling and far-from-equilibrium hydrodynamics in the quark-gluon plasma," Phys. Rev. Lett. **122**, 122301 (2019).

[164] T. Gasenzer and J. M. Pawlowski, "Towards far-from-equilibrium quantum field dynamics: A functional renormalisation-group approach," Phys. Lett. **B670**, 135 (2008).

[165] T. Gasenzer, S. Keßler, and J. M. Pawlowski, "Far-from-equilibrium quantum many-body dynamics," Eur. Phys. J. C **70**, 423 (2010).

[166] L. Corell, A. K. Cyrol, M. Heller, and J. M. Pawlowski, "Flowing with the Temporal Renormalisation Group," (2019), arXiv:1910.09369 [hep-th] .

[167] K. Boguslavski and A. Piñeiro Orioli, "Unraveling the nature of universal dynamics in $O(N)$ theories," (2019), arXiv:1911.04506 [hep-ph] .

Danksagung

An dieser Stelle bedanke ich mich bei all denjenigen, die mich auf dem Weg zu meiner Doktorarbeit auf verschiedenste Art und Weise unterstützt haben.

Zuallererst danke ich Thomas Gasenzer, der mir die Möglichkeit gegeben hat an diesem spannenden Forschungsprojekt zu arbeiten. Seine Tür stand mir immer offen für Diskussionen und Fragen zur Physik, aber auch für Themen darüber hinaus. Vor allem während meines Aufenthaltes in Neuseeland hat er sich aufgrund der Zeitverschiebung auch regelmäßig spät abends oder am Wochenende die Zeit für ein Skype-Meeting genommen. Von ihm habe ich gelernt, dass qualitativ hochwertige Forschung sich zuvorderst darin begründet, dass man immer versuchen sollte, die Dinge so genau wie möglich zu verstehen. Seine schier unerschöpfliche Kenntnis der Literatur beeindruckt mich zudem immer wieder aufs Neue. Wie wir im Laufe der Doktorarbeit feststellen konnten, teilen wir eine besondere Leidenschaft für Neuseeland. Die atemberaubende Natur konnten wir dann auch bei einer gemeinsamen Wanderung im Mount Aspiring National Park genießen.

Markus Oberthaler danke ich für die gemeinsamen Projekte und die vielen Diskussionen zum Vergleich von Experimenten und numerischen Simulationen. Seine besondere Art Projekte voranzutreiben und seine Begeisterungsfähigkeit für Neues finde ich beeindruckend. Neben seinen vielen Verpflichtungen nimmt er sich immer auch die Zeit für Anliegen der Gruppe und schafft so ein Grundgerüst für produktive und hochwertige Forschung.

Jörg Jäckel danke ich für die Bereitschaft das Zweitgutachten meiner Doktorarbeit zu übernehmen.

Im Rahmen meiner Doktorarbeit durfte ich auch einen Einblick in die Forschung außerhalb von Heidelberg gewinnen. Das war etwas ganz besonderes für mich und ich danke allen, die mir diese Erfahrung ermöglicht haben. Ein besonderer Dank geht dabei an Panos Kevrekidis, den ich an der University of Massachusetts in Amherst besuchen durfte. In unseren zahlreichen Diskussionen habe ich sehr viel über Solitonen und numerische Methoden zum Lösen von PDEs gelernt. Ich finde es klasse, dass wir auch weiterhin in regelmäßigem Austausch stehen und an gemeinsamen Projekten arbeiten. Des Weiteren möchte ich Blair Blakie danken, in dessen Gruppe an der University of Otago in Dunedin ich für 5 Monate an einem gemeinsamen Forschungsprojekt arbeiten durfte. Seine motivierende Art hat stets eine sehr angenehme und produktive Arbeitsatmosphäre geschaffen. In diesem Rahmen geht auch ein großer Dank an meinen neuseeländischen Kollegen Danny Baillie, der mich mehrfach auf einen ”kleinen” Mountain oder Beach Run mitgenommen hat und mich so zum Langstreckenlaufen gebracht hat.

An dieser Stelle sage ich auch Danke für die finanzielle Unterstützung im Rahmen meiner Doktorarbeit. Insbesondere danke ich der HGSFP für das Stipendium während der ersten Monate im 4+4 Programm. Des Weiteren möchte ich dem DAAD danken für das 5-monatige Forschungsstipendium, welches es mir ermöglicht hat ein Forschungsprojekt an der University of Otago in Dunedin zu machen.

Für das intensive Korrekturlesen meiner gesamten Doktorarbeit danke ich Max und Sandra. Für weitere hilfreiche Kommentare zu Teilen meiner Arbeit danke ich Aleksandr, Anna und Paul.

Ein ganz spezieller Dank gilt meinem Freund und Kollegen Max für die großartige Zusammenarbeit in den letzten drei Jahren. Du hast sehr oft die richtigen Fragen gestellt und dafür gesorgt, dass so mancher Faktor 2π am Ende gefunden wurde. Die vielen Sonntagabende auf dem bequemsten Sitz deiner Couch und die vielen schönen (und teils verrückten) Laufevents bleiben unvergessliche Erlebnisse. An diesem Punkt auch einen großen Dank an seine Frau Mareike dafür, dass du jeden "verdammten" Sonntag mit uns geduldig Football schaust.

Ich danke meinen Bürokollegen Stefanie, Aleksandr, Paul und Sarah für die angenehme Arbeitsatmosphäre und die vielen Diskussionen über die verschiedensten Themen des Lebens. Hervorheben möchte ich hier meinen Kollegen Aleksandr, ohne den die Analytik in dieser Arbeit wohl deutlich kürzer gekommen wäre. Du hast mir immer wieder geduldig meine Fragen zu seinen Rechnungen beantwortet und in vielen Diskussionen dafür gesorgt, dass die zentralen Fragen mathematisch und physikalisch fundiert beantwortet wurden.

Danken möchte ich auch allen Kollegen vom BEC Experiment, mit denen ich im Laufe der Doktorarbeit (und vielfach auch schon während der Bachelor- und Masterarbeit) sehr eng zusammen gearbeitet habe. Ich konnte immer mit Fragen zu euch kommen und wir haben dann gemeinsam überlegt wie wir das Projekt vorantreiben. Herausgreifen möchte ich hier meinen Kollegen Stefan, mit dem ich in letzter Zeit so manche Stunde in der Wohlfühloase verbracht habe, um Doktorhüte zu basteln. Ohne sein enormes technisches Verständnis wäre ich des Öfteren aufgeschmissen gewesen.

Als nächstes geht ein besonderer Dank an das gesamte Matterwave und SynQS Team für die zahlreichen gemeinsamen Aktivitäten, wie das Gruppenfrühstück, Grillen, Paperparties oder auch das gemeinsame Singen, um Geld für die KIP Weihnachtsfeier zu sammeln. Ihr seid ein ganz tolles Team und es freut mich sehr ein Teil davon zu sein.

Ein großer Dank geht an dieser Stelle auch an Dagmar und Christiane. Auf euch ist immer Verlass, wenn es um Organisatorisches oder die liebe Bürokratie geht.

Im Laufe meines Studiums hatte ich das Glück viele tolle Freunde zu finden. Vielen Dank an euch für unzählige gemeinsame Mittagessen, Skiurlaube und Grillabende. Ohne euch würde es diese Arbeit sicherlich nicht in dieser Form geben. Ich freue mich schon auf unseren nächsten "Physiker-Kongress".

Um hin und wieder Abstand von der Arbeit zu gewinnen, habe ich immer wieder gerne meine Freunde aus der Heimat in der Nähe von Köln besucht. Es ist schön, dass uns die Freundschaft teils aus dem Kindergarten erhalten geblieben ist und wir neben unserer Leidenschaft für Gesellschaftsspiele und das Singen auch den Surfsport für uns entdeckt haben.

Ein wichtiger Ausgleich neben der Arbeit ist für mich vor allem der Sport. Daher vielen Dank an meine langjährigen Vereinskollegen und Freunde vom Eppelheimer TC und die neu dazu gewonnenen Langdapper von der TSG Heidelberg.

An dieser Stelle möchte ich nun einen großen Dank an meine Mitbewohnerinnen Doro und Sandra ausrichten. Ihr wart oft die erste Anlaufstelle für Sorgen oder Probleme und habt mich in stressigen Phasen immer rücksichtsvoll unterstützt. Ihr habt das Wohnen in Heidelberg wohnenswert gemacht.

Zum Schluss geht ein ganz besonderer Dank an meine Familie, die mich immer in allen Lebenslagen unterstützt hat. Im Speziellen danke ich meinen Eltern, bei denen ich jederzeit zur Ruhe kommen kann und die immer voll hinter mir stehen. Ebenso danke ich meinem Bruder, mit dem ich gerade während meiner Doktorandenzeit so manche abenteuerliche Reise durch Deutschland und die Welt unternommen habe. Ihr drei seid einfach die Besten!